



**HAL**  
open science

# Ultra-high field diffusion and quantitative MRI with strong gradients to explore the connectivity, cytoarchitecture and myeloarchitecture of animal and human brains at the mesoscale

Raïssa Yebga Hot

► **To cite this version:**

Raïssa Yebga Hot. Ultra-high field diffusion and quantitative MRI with strong gradients to explore the connectivity, cytoarchitecture and myeloarchitecture of animal and human brains at the mesoscale. Medical Physics [physics.med-ph]. Université Paris-Saclay, 2021. English. NNT : 2021UPAST088 . tel-03376306

**HAL Id: tel-03376306**

**<https://theses.hal.science/tel-03376306>**

Submitted on 13 Oct 2021

**HAL** is a multi-disciplinary open access archive for the deposit and dissemination of scientific research documents, whether they are published or not. The documents may come from teaching and research institutions in France or abroad, or from public or private research centers.

L'archive ouverte pluridisciplinaire **HAL**, est destinée au dépôt et à la diffusion de documents scientifiques de niveau recherche, publiés ou non, émanant des établissements d'enseignement et de recherche français ou étrangers, des laboratoires publics ou privés.

Ultra-high field diffusion and quantitative  
MRI with strong gradients to explore the  
connectivity, cytoarchitecture and  
myeloarchitecture of animal and human  
brains at the mesoscale

*IRM de diffusion et quantitative à très haut  
champ et forts gradients pour l'exploration de la  
connectivité, de la cytoarchitecture, et de la  
myéloarchitecture du cerveau de l'animal à  
l'homme à l'échelle mésoscopique*

**Thèse de doctorat de l'Université Paris-Saclay**

École doctorale n° 575, electrical, optical, bio : physics and  
engineering (EOBE)  
Spécialité de doctorat: Imagerie et Physique Médicale  
Unité de recherche: Université Paris-Saclay, CEA, CNRS, BAOBAB,  
91191, Gif-sur-Yvette, France  
Réfèrent: Faculté des sciences d'Orsay

**Thèse présentée et soutenue à Paris-Saclay, le 03/09/2021, par**

**Raïssa YEBGA HOT**

**Composition du Jury**

<b>Thierry DELZESCAUX</b> Directeur de recherche, CEA, MIRCent	Président
<b>Yaniv ASSAF</b> Professeur, Tel Aviv University	Rapporteur & Examineur
<b>Eric JOUVENT</b> Professeur des Universités - Praticien Hospitalier, Université de Paris, INSERM	Rapporteur & Examineur
<b>Samuel SARRAZIN</b> Médecin-Chercheur, Centre Médical Pasteur Chevilly-Larue	Examineur

**Direction de la thèse**

<b>Cyril POUPON</b> Directeur de recherche, CEA, NeuroSpin, BAOBAB	Directeur de thèse
<b>Elodie CHAILLOU</b> Chercheuse, INRAE, CNRS, IFCE	Invitée
<b>Jean-François MANGIN</b> Directeur de recherche, CEA, NeuroSpin, BAOBAB	Invité



# Acknowledgements

An old African proverb says: "It takes a village to raise a child". Well, I believe that it also took a village to succeed my PhD thesis.

Je tiens tout d'abord à remercier mon directeur de thèse Cyril Poupon. Tu as été un excellent chef et encadrant durant mes trois ans et demi à NeuroSpin. Tu m'as fait découvrir le monde de la neuroimagerie IRM, tu m'as donné la chance de faire une thèse dans la géniale équipe que tu diriges avec beaucoup d'enthousiasme, d'écoute et de professionnalisme. Tu m'as également encouragé et accordé ta confiance dans les différents projets que j'ai menés, et tu as su m'accorder du temps malgré toutes tes autres obligations. Tu es une personne que je respecte profondément et que je ne remercierai jamais assez pour toutes les opportunités que j'ai eu durant mon temps passé à NeuroSpin.

I would like to thank Pr Yaniv Assaf and Pr Eric Jouvent for doing me the honor of being my reviewers. You respectively inspired me by your work and the great interest you have expressed for my thesis. Merci également à Thierry Delzescaux, Samuel Sarrazin, Elodie Chaillou et Jean-François Mangin d'avoir accepté de faire partie de mon jury de thèse.

Je souhaite également remercier la super équipe de recherche tourangelle composée de Marine Siwiaszczyk, Elodie Chaillou, Scott Love, Mélody Morisse, Frédéric Andersson et Ludovic Calandreau pour m'avoir accueillie lors de multiples séjours à l'INRAE de Nouzilly et au CHRU Bretonneau de Tours afin d'aboutir à deux articles sur la caille japonaise et une nomination au prix Beauval Nature 2019. Ces sessions de travail avec vous tous ont toujours été agréables et enrichissantes. Je remercie aussi tous les acteurs et collaborateurs du projet Neuro2Co qui a été une belle expérience de partage et d'enseignement avec les collégiens participant à l'atelier Ciboulot.

J'adresse aussi un grand merci aux docteurs Christophe Destrieux et Igor Lima Maldonado qui ont pris le temps de répondre à toutes mes questions sur le cerveau humain, et de m'accueillir dans leur laboratoire ainsi qu'au bloc opératoire. Cela a toujours été un grand plaisir de travailler avec vous à Tours.

J'ai eu la grande chance de faire partie d'une super équipe de post-docs, de thésards et de stagiaires durant mes années à NeuroSpin, cette équipe qui se nomme dorénavant la Ginkgo Team et qui a tenu bon face à la pandémie. Mes pensées vont d'abord aux anciens de l'équipe que j'ai intégrée à mon arrivée, Justine, Kévin, Nicole, Miguel et Ivy. Vous m'avez chaleureusement accueilli dans l'équipe et fait de moi une respectable arbitre de matchs de ping-pong. Merci à toi Justine de m'avoir très bien formée pour que mon stage puis ma thèse se passent pour le mieux. Merci à toi Kévin, le "gourgandin", pour ta bonne humeur et pour m'avoir montré que le ping-pong était effectivement un sport. Merci aux deux adoptés de l'équipe, Nicole, créatrice de la "mignonesse attitude", et Miguel, co-fan de baleines, pour votre sympathie et votre grain de folie. Un grand merci à toi Ivy, notre "marraine la bonne fée" de la Ginkgo Team, qui

t'es rendue disponible pour m'aider et me conseiller durant ces trois ans et demi. Ta gentillesse et ton humour m'ont toujours fait beaucoup de bien. Ne change rien Super Vivy!

Viennent maintenant les "nouveaux" de la Ginkgo Team: Alexandre, David, Maëlig, Gaël, Anaïs, Alexis, Anas, Bastien, Simon et Bosco. Merci à mon co-thésard Alexandre qui a toujours eu le mot pour rire aussi bien en stage qu'en thèse. Merci à toi David pour ta pédagogie scientifique et celle des répliques de Kaamelott. Merci à toi Maëlig, la championne (presque indétronable) des Blind Tests, pour ta bonne humeur et ma remise à niveau sur Harry Potter et les films Disney. Merci à toi Gaël, l'éternel No. 2 à Shabadabada, d'avoir apporté une super énergie dans l'équipe et de m'avoir fait découvrir La Cité de la Peur (mieux vaut tard que jamais!), et redécouvrir Astérix et Obélix: Mission Cléopâtre. Merci à toi Anaïs, la reine du 3T, pour ta gaieté et tes petits conseils de fin de journée. Merci à toi Alexis, le plus fort des outsiders aux Blind Tests, pour ton humour décalé qui redonne le sourire. Merci à toi Anas, le meilleur des saxophonistes (surtout en forêt), pour tes super blagues et ta gentillesse. Merci à toi Bastien, le maître pâtissier de la tarte normande, pour ta (semi-)compassion footballistique, et ton apprentissage express de la neuroanatomie de la caille japonaise. Merci à toi Simon, l'éternel No. 2 aux Blind Tests, pour toute ta sympathie et tout particulièrement pendant l'Euro 2020. Et merci à toi Bosco, le vrai survivor aux Haribo Piratos, pour ta bonne humeur qui fait du bien à l'équipe.

J'ai eu le plaisir de rencontrer pleins de chouettes personnes durant ma thèse, Héloïse, Solène, Cindy, Inès, et tant d'autres que je remercie pour les bons moments passés en déplacement ou au labo. Merci aussi aux membres de NeuroSpin, Fabrice Poupon, Fawzi Boumezbou, Denis Fournier, Luisa Ciobanu, Sébastien Mériaux, Erwan Selingue, Benoît Larrat, Françoise Geoffroy et Jérémy Bernard qui ont toujours su prendre le temps de m'aider en cas de pépin. Je remercie très chaleureusement Maryline et Johanna qui ont été adorables avec moi durant ces trois ans et demi.

Je tiens à remercier du fond du coeur tous mes amis qui m'ont soutenue durant cette thèse. Pour ne citer que la Dr Léna Soun, j'ai eu la chance d'habiter avec deux (et demi?) formidables colocs, Léna, Sabrina et notre squatteuse officielle Emilie, dans notre Manoir, aka la Maison du Chèvre. Je vous remercie les filles pour nos super escape games (un sans faute!), soirées de gourmets et week-ends ensoleillés jusqu'à 2877m d'altitude.

J'adresse un grand merci à ma team Polytech sudiste et tout particulièrement à Justine, Hajar et Khalid, pour tous les moments inoubliables que nous avons vécus en vrai comme en visio, du festin de sushis à la réalisation/production de courts-métrages improbables, et pour tous ceux que nous partagerons encore. J'ai également une pensée particulière à mon squad du lycée, Maryane, Medhi, Karoline, Adrian et Amandine, merci pour votre soutien infaillible et inspirant durant toutes ces années. Un très grand merci à ma plus vieille amie, Amandine, pour ta joie de vivre et ta positivité.

J'aimerais enfin conclure mes remerciements avec mon incroyable famille qui m'a encouragée et aidée tout au long de mes études, et notamment durant ma thèse. Big love à mon grand frère, ma grande sœur et mes nièces chéries. Je ne remercierai jamais assez ma maman, ma supportrice No. 1 et le meilleur modèle qu'on puisse rêver d'avoir.

# Contents

- Acknowledgements** **ii**
  
- List of Figures** **xv**
  
- List of Tables** **xvii**
  
- Acronyms** **xix**
  
- Glossary** **xxiii**
  
- 1 Introduction** **1**
  - 1.1 Context and motivations . . . . . 1
  - 1.2 Thesis organization . . . . . 2
  
- I Background** **5**
  
- 2 Human brain anatomy** **7**
  - 2.1 Macroscopic anatomy . . . . . 7
    - 2.1.1 Global description . . . . . 7
    - 2.1.2 Neurodevelopment . . . . . 8
    - 2.1.3 Cerebral lobes . . . . . 9
    - 2.1.4 Ventricles . . . . . 11
    - 2.1.5 Brain vascular system . . . . . 12

---

2.2	Gray matter . . . . .	13
2.2.1	In the cerebellum and the brainstem . . . . .	14
2.2.2	The diencephalon . . . . .	15
2.2.3	In the cerebrum . . . . .	15
2.3	White matter . . . . .	16
2.3.1	Projection fibers . . . . .	17
2.3.2	Association fibers . . . . .	17
2.3.3	Commissures . . . . .	17
2.4	Microscopic anatomy . . . . .	18
2.4.1	Neurons . . . . .	18
2.4.2	Neuroglia . . . . .	20
2.4.2.1	Macroglia . . . . .	21
2.4.2.2	Microglia . . . . .	22
2.5	Conclusion . . . . .	22
<b>3</b>	<b>Human cerebral cortex</b>	<b>23</b>
3.1	Global description . . . . .	23
3.1.1	Definition and embryogenesis . . . . .	23
3.1.2	Cortex gyri and sulci . . . . .	24
3.1.3	Microstructure of the cerebral cortex . . . . .	25
3.2	The cerebral cortices . . . . .	25
3.2.1	The allocortex . . . . .	26
3.2.1.1	The archicortex . . . . .	26
3.2.1.2	The paleocortex . . . . .	27
3.2.2	The neocortex or isocortex . . . . .	27
3.2.2.1	The heterotypical neocortex . . . . .	27
3.2.2.2	The homotypical neocortex . . . . .	29

---

3.3	Cortex histology . . . . .	30
3.3.1	Cortical layers . . . . .	30
3.3.1.1	The cortex laminar structure . . . . .	30
3.3.1.2	Specific cortical layers . . . . .	31
3.3.2	Cortical cell types . . . . .	32
3.3.2.1	The pyramidal cells . . . . .	32
3.3.2.2	The fusiform cells . . . . .	33
3.3.2.3	The granular cells . . . . .	33
3.3.2.4	Specific cortical cells . . . . .	33
3.3.3	Cortical connections . . . . .	34
3.4	Cytoarchitectonics and myeloarchitectonics . . . . .	34
3.4.1	Pre-Brodmann cytoarchitectonic and myeloarchitectonic maps . . . . .	35
3.4.2	Brodmann areas and further works . . . . .	37
3.5	Cortical vasculature . . . . .	38
3.5.1	Cortex vascular network . . . . .	39
3.5.2	Intracortical vessels . . . . .	40
3.6	Cortex-related diseases . . . . .	40
3.6.1	Neurodegenerative disorders . . . . .	40
3.6.2	Neurodevelopmental pathologies . . . . .	43
3.6.3	Neuropsychiatric disorders . . . . .	43
3.6.4	Neurovascular disorders . . . . .	44
3.7	Conclusion . . . . .	45
<b>4</b>	<b>Ultra-high and extreme fields postmortem MRI to probe cerebral microstructure</b>	<b>47</b>
4.1	Physical principles of magnetic resonance imaging . . . . .	47
4.1.1	Magnetic properties of hydrogen . . . . .	47
4.1.2	Magnetic resonance phenomenon . . . . .	48



---

4.1.2.1	Polarization . . . . .	48
4.1.2.2	Excitation or resonance . . . . .	48
4.1.2.3	Relaxation . . . . .	48
4.1.3	Bloch equations, $T_1$ , $T_2$ and $T_2^*$ relaxation times . . . . .	49
4.1.4	2D image encoding . . . . .	50
4.1.5	Conventional MRI sequences . . . . .	51
4.1.5.1	Image contrast . . . . .	51
4.1.5.2	Spin echo sequence . . . . .	52
4.1.5.3	Gradient echo sequence . . . . .	52
4.1.6	Ultra-high and extreme magnetic fields . . . . .	53
4.2	Postmortem imaging specificity . . . . .	54
4.2.1	Ex vivo brain tissue features . . . . .	54
4.2.2	Considerations for MRI scanner setups . . . . .	56
4.2.3	<i>Ex vivo</i> or <i>in vivo</i> imaging ? . . . . .	56
4.3	Diffusion-weighted MRI . . . . .	57
4.3.1	The diffusion process . . . . .	57
4.3.2	Diffusion NMR signal . . . . .	58
4.3.2.1	Mathematical expression . . . . .	58
4.3.2.2	Noise and artifacts . . . . .	59
4.3.3	Diffusion MRI sequences . . . . .	61
4.3.4	Local modeling of the diffusion process . . . . .	62
4.3.4.1	Diffusion tensor imaging (DTI) . . . . .	62
4.3.4.2	High angular resolution diffusion imaging (HARDI) . . . . .	62
4.3.5	Applications of diffusion-weighted imaging . . . . .	65
4.3.5.1	Tractography to access the structural connectivity . . . . .	65
4.3.5.2	Clinical applications . . . . .	67

4.4	Quantitative MRI . . . . .	68
4.4.1	Quantitative $T_1$ mapping . . . . .	69
4.4.2	Quantitative $T_2$ mapping . . . . .	69
4.4.3	Quantitative $T_2^*$ mapping . . . . .	70
4.4.4	Applications of quantitative MRI . . . . .	70
4.5	Conclusion . . . . .	71
 <b>II Postmortem investigation of the structural connectivity in breeding and wildlife animals</b>		<b>73</b>
<b>5</b>	<b>Structural connectivity atlas of the Japanese quail, a breeding bird to explore emotivity</b>	<b>75</b>
5.1	Introduction . . . . .	75
5.2	Material and methods . . . . .	77
5.2.1	The Japanese quail cohort . . . . .	77
5.2.2	MRI protocol . . . . .	78
5.2.3	Image processing and analysis . . . . .	79
5.2.3.1	Pre-processing . . . . .	79
5.2.3.2	Local modeling of the diffusion process . . . . .	79
5.2.3.3	Fiber tracking . . . . .	80
5.2.3.4	Template creation and normalization . . . . .	80
5.2.3.5	From fibers to bundle segmentation . . . . .	80
5.2.3.6	Statistical analyses along the white matter fibers . . . . .	84
5.3	Results . . . . .	85
5.3.1	Diffusion MRI and inference of the structural connectivity . . . . .	85
5.3.1.1	Noise correction in the pre-processing step . . . . .	85
5.3.1.2	Local modeling at the individual scale . . . . .	85
5.3.1.3	Tractography of quails at the individual scale . . . . .	85

5.3.1.4	The anatomical template and its labeled structures . . . . .	89
5.3.2	Fiber clustering on an individual scale . . . . .	89
5.3.3	Fiber clustering at group level . . . . .	94
5.3.4	Atlas building . . . . .	94
5.3.5	Statistical analyses of the diffusion features along each quail tractogram streamline . . . . .	98
5.4	Discussion . . . . .	103
5.4.1	Connectivity-based comparisons between the two lineages . . . . .	103
5.4.2	The brain lateralization of the Japanese quail . . . . .	103
5.4.3	The fear-related circuit of the Japanese quail . . . . .	105
5.4.4	Methodological optimization . . . . .	106
5.5	Conclusion . . . . .	108
<b>6</b>	<b>Structural connectivities of wildlife specimens from ZooParc de Beauval</b>	<b>109</b>
6.1	Introduction . . . . .	109
6.2	Material and methods . . . . .	110
6.2.1	The wildlife species . . . . .	110
6.2.2	MRI protocol . . . . .	110
6.2.3	Image processing and analysis . . . . .	112
6.3	Results and discussion . . . . .	113
6.3.1	General overview . . . . .	114
6.3.2	Focus on the California sea lion . . . . .	119
6.4	Conclusion . . . . .	125
<b>III</b>	<b>The human cerebral cortex in the Chenonceau project</b>	<b>131</b>
<b>7</b>	<b>Probing the human cortical cytoarchitecture and myeloarchitecture</b>	<b>133</b>
7.1	Introduction to the Chenonceau project . . . . .	134
7.1.1	Ex vivo brain preparation process . . . . .	134

---

7.1.2	Anatomical and diffusion MRI protocol at 11.7T . . . . .	136
7.1.3	Quantitative MRI protocol at 7T . . . . .	139
7.1.3.1	Protocol tuning . . . . .	139
7.1.3.2	Description of the final protocol . . . . .	141
7.1.4	Expectations from the Chenonceau project . . . . .	142
7.2	Quantitative MRI mapping of the Chenonceau brain at 7T and 11.7T . . . . .	143
7.2.1	Pre-processing pipeline . . . . .	143
7.2.2	Relaxometry mapping . . . . .	144
7.2.3	Quantitative mapping from the NODDI model . . . . .	149
7.3	Conclusion . . . . .	149
<b>8</b>	<b>Focus on the Chenonceau cerebral cortex</b>	<b>151</b>
8.1	Inference of the laminar structure of the Chenonceau human cortex . . . . .	151
8.1.1	State of the art . . . . .	151
8.1.2	Segmentation of the neocortex . . . . .	153
8.1.3	Design of a method to segment cortical layers using multi-contrast clustering . . . . .	155
8.1.4	Segmentation of the laminar structure from cytoarchitectural information . . . . .	156
8.1.5	Segmentation of the laminar structure from myeloarchitectural information . . . . .	158
8.1.6	Segmentation of the laminar structure from cytoarchitectural and myeloarchitectural information . . . . .	160
8.2	Towards the inference of the inner connectivity of the isocortex . . . . .	161
8.3	Comparison of 11.7T dMRI to 3D polarized light imaging . . . . .	163
8.4	Discussion . . . . .	166
8.4.1	Comparison to existing studies . . . . .	166
8.4.2	Limitations and future improvements . . . . .	167
8.5	Conclusion . . . . .	168
<b>9</b>	<b>Conclusion</b>	<b>169</b>

---

9.1	Conclusion and contributions . . . . .	169
9.1.1	Structural connectivity atlas of the Japanese quail . . . . .	169
9.1.2	Structural connectivity of wildlife animals . . . . .	170
9.1.3	Inference of the cytoarchitecture and myeloarchitecture of the human cortical ribbon . . . . .	170
9.1.4	Contributions of this thesis . . . . .	170
9.2	Upcoming work . . . . .	171
9.2.1	Towards a mesoscopic structural connectome of the Chenonceau atlas . . . . .	172
9.2.2	Towards new computational models of tissue ultrastructure . . . . .	172
9.2.3	On the importance of validating computational models . . . . .	173
<b>A</b>	<b>Communications</b>	<b>175</b>
	<b>Bibliography</b>	<b>177</b>

# List of Figures

1	Atlas de la connectivité structurelle de la caille japonaise basée sur la méthode de tractographie régularisée par streamline déterministe et représentée sur un maillage 3D du template anatomique . . . . .	xxx
2	Tractogrammes des animaux sauvages provenant du Zooparc de Beauval . . . . .	xxxii
3	Images du clustering de fibres intra-sujet pour l’otarie de Californie . . . . .	xxxiii
4	Cartes quantitatives des temps de relaxation $T_1$ , $T_2$ et $T_2^*$ et de la fraction de myéline locale du cerveau Chenonceau . . . . .	xxxvii
5	Mosaïque des différents types d’images et de cartes éditées pour le projet Chenonceau . . . . .	xxxviii
2.1	Scheme of the brain skull and the meninges . . . . .	8
2.2	Illustrations of the principal regions of the human central nervous system and locating the cerebrospinal fluid . . . . .	9
2.3	Scheme of the human neurodevelopment . . . . .	10
2.4	Images of the human brain lobes . . . . .	12
2.5	Images of the four ventricles in the human brain . . . . .	13
2.6	Schematic visualization of the brain vascular system including the circle of Willis . . . . .	14
2.7	Illustrations of the cerebellar nuclei and the brainstem . . . . .	15
2.8	Images of the basal ganglia and the relationships between the structures forming them . . . . .	16
2.9	Schemes of the association, projection and commissural fibers of the white matter . . . . .	19
2.10	Drawing of a neuronal cell showing its major parts . . . . .	21
2.11	Schematic visualization of the glia located in the central nervous system . . . . .	22
3.1	Illustration of the phylogenetic types of the human cerebral cortex . . . . .	24

---

3.2	Schemes of the main lobes, gyri and sulci of the cerebral left hemisphere . . . . .	25
3.3	Hierarchical graph of the cortices composing the human cortex . . . . .	26
3.4	Representations of the laminar organization of the human cerebral cortex . . . . .	28
3.5	Illustration of the cortical thickness variations of a gyrus . . . . .	29
3.6	Histological images of the Gennari, Baillarger and Exner stripes . . . . .	32
3.7	Photomicrograph of a supragranular pyramidal cell . . . . .	32
3.8	OCT image of granular cells in the hippocampus . . . . .	33
3.9	Major types of cells seen in the cerebral cortex . . . . .	35
3.10	Brodmann's original maps . . . . .	38
3.11	Groups of blood vessels of the cortical vascular system penetrating the six-layer neocortex . . . . .	39
3.12	Drawing of the morphological features of intracortical arteries and veins . . . . .	41
3.13	Drawing of the right-hemisphere cortical pial vessels . . . . .	43
3.14	Image of multiple cortical microinfarcts in the frontal cortex . . . . .	44
3.15	Diffusion-weighted image of a focal brain lesion in Broca's area . . . . .	45
4.1	Illustration of the magnetic resonance phenomenon . . . . .	49
4.2	Description of the three relaxation times $T_1$ , $T_2$ and $T_2^*$ . . . . .	50
4.3	Illustration of a slice selection . . . . .	51
4.4	Image of the output of frequency encoding . . . . .	52
4.5	Image weightings in MRI from a spin echo sequence . . . . .	53
4.6	$T_2$ signal decay and the RF framework of the spin echo sequence . . . . .	54
4.7	The principle of the gradient echo sequence . . . . .	55
4.8	Comparison between unhindered and hindered diffusion . . . . .	58
4.9	Scheme explaining the PGSE sequence and the effects of the application of diffusion gradients . . . . .	59
4.10	Illustration of the DTI diffusion tensor and its matrix . . . . .	63
4.11	Representation of the evolution of the q-space sampling, the diffusion orientation distribution function (dODF) and the fiber orientation distribution function (FOD) . . . . .	65

4.12	Compilation of the major multi-compartment models with the corresponding compartments . . . . .	66
4.13	Human tractogram from the HCP database computed using a streamline regularized deterministic approach . . . . .	68
5.1	Anatomical images of subject 7133 LTI showing three typical reference points used to define the AC-PC frame for each Japanese quail . . . . .	81
5.2	3D mesh image of quail 7426 STI brain and skull and eight pairs of raw diffusion-weighted and filtered diffusion-weighted images in eight different diffusion directions . . . . .	86
5.3	Maps of subject 7426 STI showing its ADC, FA, $D_{\text{parallel}}$ , $D_{\text{transverse}}$ , GFA and color-encoded direction of diffusion, based on the aQBI and DTI local models . . . . .	87
5.4	Orientation distribution function (ODF) maps of subject 7426 STI stemming from the analytical Q-ball model . . . . .	88
5.5	Histogram of generalized fractional anisotropy (GFA) for quail 7412 STI . . . . .	89
5.6a	Images of subject 7167 LTI showing 50% of its SRD tractograms' streamlines . . . . .	90
5.6b	Images of subject 7167 LTI showing 50% of its SRP tractograms' streamlines . . . . .	91
5.7	Histograms of the fiber lengths from the Japanese quails' cohort . . . . .	92
5.8	Template images obtained from the Japanese quail cohort . . . . .	93
5.9a	Results of the intra-subject fiber clustering step based on SRD tractography for 7147 LTI quail . . . . .	95
5.9b	Results of the intra-subject fiber clustering step based on SRP tractography for 7147 LTI quail . . . . .	96
5.10	3D surface plots of the number of clusters obtained at the inter-subject fiber clustering step stemming from the SRD and SRP tractographies for four quails . . . . .	97
5.11a	The structural connectivity atlas of the Japanese quail based on SRD tractography, the first set . . . . .	99
5.11b	The structural connectivity atlas of the Japanese quail based on SRD tractography, the second set . . . . .	100
5.12	Box-plot diagrams realized on the SRD intra-subject fiber clusterings covering the lineage effect for the different brain regions . . . . .	104
5.13	The probable circuit of fear-related behaviors of the Japanese quail . . . . .	107
6.1	$T_2$ -weighted anatomical images of the Java mouse-deer and the ring-tailed lemur in their AC-PC frames . . . . .	114
6.2a	Cerebral tractograms of Beauval animals, the first set . . . . .	116
6.2b	Cerebral tractograms of Beauval animals, the second set . . . . .	117
6.3	Zoom in the intracortical connectivity of the Java mouse-deer and the ring-tailed lemur . . . . .	118



6.4	Time-calibrated phylogeny of mammals . . . . .	120
6.5	3D rendering and anatomical MR images of the California sea lion brain . . . . .	121
6.6	ODFs maps obtained from HARDI data acquired from the California sea lion brain . . . . .	122
6.7	GFA and CED maps of the California sea lion brain . . . . .	123
6.8	3D rendering and tractograms of the California sea lion brain . . . . .	124
6.9	Zoom in the California sea lion tractogram highlighting cortical fibers . . . . .	126
6.10	Histogram of the fiber lengths computed from the California sea lion tractogram . . . . .	127
6.11	Images of the resulting intra-subject fiber clustering step performed on the California sea lion specimen . . . . .	128
6.12	3D rendering of the fiber clusters corresponding to the corpus callosum of the California sea lion . . . . .	129
7.1	Photos of the cutting procedure of the brain sample . . . . .	135
7.2	MRI images of the block-face . . . . .	136
7.3	Classification of the fields of view from the human brain sample . . . . .	137
7.4	Histograms showing the distribution of the $T_2$ and mean diffusivity values of a hippocampus sample . . . . .	138
7.5	Anatomical and diffusion-weighted images from the left-hemisphere C1 field of view . . . . .	139
7.6	Schematic representation of the duration of the two acquisition campaigns . . . . .	140
7.7	Series of $T_2^*$ -weighted images on the right-hemisphere C1 field of view . . . . .	141
7.8	Relaxometric images from the right-hemisphere C1 field of view . . . . .	143
7.9	Schematic representation of the pre-processing pipeline of the Chenonceau project . . . . .	145
7.10	Schematic representation of the diffeomorphic registration step of the Chenonceau project . . . . .	146
7.11	Images of the 7T data of a Chenonceau field of view, before and after Rician noise filter . . . . .	147
7.12	Quantitative $T_1$ , $T_2$ , $T_2^*$ and MWF maps and related histograms of the Chenonceau brain . . . . .	148
7.13	Quantitative maps and related histograms of the intracellular volume fraction and orientation dispersion of the Chenonceau brain . . . . .	149
8.1	Hierarchical graph of the MRI-based approaches for brain parcellation . . . . .	154
8.2	Masking of the Chenonceau neocortex . . . . .	155
8.3	Schematic definition of the multi-contrast cortical layer clustering algorithm . . . . .	157

---

8.4	Cyto-clustering maps of the Chenonceau neocortex . . . . .	158
8.5	Myelo-clustering maps of the Chenonceau neocortex . . . . .	159
8.6	Layer-clustering maps of the Chenonceau neocortex . . . . .	160
8.7	GFA histogram of the Chenonceau brain issued from the aQBI model . . . . .	162
8.8	The SRD tractogram of the Chenonceau brain . . . . .	162
8.9	Intracortical connectivity maps of the Chenonceau brain . . . . .	163
8.10	Comparison between the tractogram and the 3D polarized light image from a microscopic slice of the Chenonceau brain . . . . .	164
8.11	Global presentation of all the images and maps issued for the Chenonceau project so far . . . . .	165



# List of Tables

3.1	Timeline of major cytoarchitectonic discoveries made in the pre-Brodmann era . . . . .	36
3.2	Listing of the neurodegenerative disorders linked to their pathologies, affected brain regions, and noticed symptoms . . . . .	42
4.1	Review of the major HARDI techniques . . . . .	64
5.1	Set of intra-subject fiber clustering parameters used for the Japanese quail cohort . . . . .	83
5.2	Set of inter-subject fiber clustering parameters for the Japanese quail cohort . . . . .	84
5.3	Table showing the number of clusters generated by the two inter-subject fiber clustering steps . . . . .	94
5.4	Table sorting the structural connectivity atlas fiber bundles according to the part of the brain they belong to	101
5.5	Table of the diffusion features from the aQBI and DTI local models, regarding the fiber tracts from the connectivity atlas and the resulting p-values of the statistical tests . . . . .	102
6.1	Table presenting the major information on Beauval specimens . . . . .	111
6.2	Table indicating the spatial resolutions of the MRI data . . . . .	112
6.3	Distinct sets of intra-subject fiber clustering parameters used for each Beauval animal . . . . .	113
6.4	Table showing the number of streamlines and clusters respectively generated by the two tractography methods and intra-subject fiber clustering steps . . . . .	115
7.1	Table of the mean SNRs in the Chenonceau brain for each qMRI sequence before and after filtering . . . . .	144
7.2	Table of the mean relaxation times in the Chenonceau brain for the white matter and the cerebral cortex at 7T . . . . .	147



# Acronyms

**ADC** apparent diffusion coefficient. 55, 58, 59, 77, 79, 87, 102, 112, 114, 151

**ALS** amyotrophic lateral sclerosis. 41

**aQBI** analytical Q-ball imaging. 85, 87, 98, 102, 112, 114, 162, 164, 171

**BIC** Bayesian information criterion. 155

**CADASIL** cerebral autosomal dominant arteriopathy with subcortical infarcts and leukoencephalopathy. 45

**CLARITY** Clear Lipid-exchanged Acrylamide-hybridized Rigid Imaging/immunostaining compatible Tissue hYdrogel.  
37

**CNS** central nervous system. xi, 7, 9, 13, 14, 16, 18, 20–22, 40, 42

**CSF** cerebrospinal fluid. xi, 7, 9, 11, 21, 55, 56, 64, 66, 156

**dMRI** diffusion-weighted magnetic resonance imaging. 1–3, 44, 57, 59, 60, 64, 66–68, 71, 76, 77, 79, 80, 84, 85, 103, 108–110, 112, 115, 118, 125, 133, 134, 136, 138, 139, 142, 143, 146, 149–153, 155, 160, 163, 166, 168, 171, 172

**dODF** diffusion orientation distribution function. 63, 65

**DTI** diffusion tensor imaging. 62, 63, 77, 79, 85, 87, 98, 102, 112, 114, 149, 151, 152, 156, 164, 166, 171

**DW** diffusion weighting. 59, 61

**EPI** echo planar imaging. xxix, 61, 69, 78, 79, 111, 112, 138, 141, 142, 146, 147

**FA** fractional anisotropy. 62, 63, 79, 80, 84, 87, 101, 102, 106, 112, 114, 151, 152, 156, 166

**FID** Free Induction Decay. 49

**FLAIR** fluid attenuated inversion recovery. 67

**FLASH** fast-low-angle shot. 70, 140–144, 146, 147, 153

**fMRI** functional magnetic resonance imaging. 1, 56, 133, 154

- FOD** fiber orientation distribution function. 63–65
- FOV** field of view. 50, 60, 78, 110, 134–137, 139–147, 161, 164
- GFA** generalized fractional anisotropy. 63, 68, 79, 80, 84, 85, 87, 89–91, 95, 96, 101, 102, 106, 112, 114, 116, 117, 120, 121, 123, 161, 162, 164, 166
- GRE** gradient echo. 51, 52, 55, 61, 70
- HARDI** high angular resolution diffusion imaging. 62–64, 78, 79, 111, 112, 122, 161, 166
- HBP** Human Brain Project. 2, 3, 146, 166, 170, 171
- HCP** Human Connectome Project. 66, 68, 133, 153
- IR** inversion recovery. 69, 153
- LTI** long tonic immobility. xxix, 76, 77, 81, 84, 89, 92, 94, 103–108, 169
- MD** mean diffusivity. 62, 84, 151, 152, 156
- MGE** multi-gradient echo. 140, 141
- MNI** Montreal Neurological Institute. 37, 145, 146, 148, 149
- MR** magnetic resonance. 3, 53, 56, 60, 70, 78, 115, 119, 121, 123, 133, 146, 153, 156, 164, 168, 170, 171
- MRI** magnetic resonance imaging. 1–3, 37, 45, 47, 48, 50–58, 60–62, 66–71, 75–80, 82, 106, 109–112, 114, 115, 119, 121, 125, 127, 133–136, 138–144, 146, 147, 149, 151–154, 159, 161, 166, 167, 169–173
- MSME** multi slice multi echo. 69, 138, 140–144, 146, 147
- MWF** myelin water fraction. 70, 144, 145, 148, 152, 155, 156, 158, 164, 166, 170
- NMR** nuclear magnetic resonance. 47, 48, 50, 51, 58, 61, 70, 76, 78–80, 111, 134, 135, 141, 144, 145, 147, 172, 173
- NODDI** neurite orientation dispersion and density imaging. 3, 64–66, 115, 143, 149, 151, 152, 156, 157, 160, 164, 170, 171
- OCT** optical coherence tomography. 33, 37, 168
- OD** orientation dispersion. 149, 155, 156
- ODF** orientation distribution function. 63, 64, 66, 79, 80, 85, 88, 110, 112, 114, 120, 122, 161, 172
- OGSE** oscillating gradient spin echo. 61, 173
- PBS** phosphate-buffered saline. 56, 78, 111, 135, 153, 157, 167
- PFA** paraformaldehyde. 54, 56, 77, 110
- PGSE** pulsed gradient spin echo. xii, 58, 59, 61, 78, 111, 112, 138, 173

- PLI** polarized light imaging. 3, 37, 105, 107, 151, 161, 163, 164, 166, 168
- PMI** post mortem interval. 54–56
- PNS** peripheral nervous system. 7
- qMRI** quantitative magnetic resonance imaging. 2, 3, 67, 68, 70, 71, 139, 142–144, 146, 150, 153, 155, 160, 166–168
- REM** rapid eye movement. 119
- RF** radiofrequency. 48–50, 52, 54, 58, 60, 61, 69, 70
- ROI** region of interest. 78, 81
- SANDI** soma and neurite density imaging. 115, 152
- SAR** specific absorption rate. 53, 56, 57
- SE** spin echo. 51–54, 58, 61, 69, 78, 111, 138, 142, 146
- SLF** superior longitudinal fasciculus. 17
- SNR** signal-to-noise ratio. 2, 51, 53, 55, 57, 59–61, 76–79, 112, 134, 140, 141, 144, 147, 166, 167
- SPGR** spoiled gradient echo. 69, 141–144, 146, 147
- SRD** streamline regularized deterministic. 80, 82, 84, 85, 89, 90, 92, 94, 95, 97, 99, 103, 104, 106, 107, 112–118, 121, 161, 162, 164
- SRP** streamline regularized probabilistic. 80, 82, 84, 85, 89, 91, 92, 94, 96, 97, 112–115
- SSFP** steady state free precession. 61, 69
- STEAM** stimulated echo acquisition mode. 61
- STI** short tonic immobility. xxix, 76, 77, 84, 92, 94, 103–108, 169
- TE** echo time. 51, 52, 55, 79, 136, 137, 142, 143, 147
- TI** inversion time. 69
- TR** repetition time. 51–53, 60, 61, 69
- UHF** ultra-high field. 2, 53, 55, 57, 61, 71, 76, 77, 79, 108–110, 121, 125, 127, 151, 152, 161, 166, 167, 170
- VFA** variable flip angle. 69, 140–144, 146, 147, 153





# Glossary

**alien limb phenomenon** Involuntary motor activity of a limb in conjunction with the feeling of estrangement from that limb. 42

**Ammon's horn** Also known as the hippocampus proper, it is a C-shape white bead that corresponds to one of three strip-like areas of the hippocampal gray matter. It has a trilaminar structures where a cellular layer is trapped between two fiber layers. 18

**anastomosis** Natural communication between two conduits. 12

**aphasia** Partial or complete loss of language function. It is a common consequence of stroke or brain injury. 42, 45

**apraxia** Inability to correctly perform learned skilled movements even though the patient has normal sensation is strong and coordinated, due to a disturbance of elementary sensorimotor functions. 42

**autolysis** Cellular or tissue necrosis due to self-digestion of the cellular components. 54, 55

**autosomal** Designates non-sexual, somal chromosome. It exists 22 pairs of autosomal chromosomes in humans. 42

**bradykinesia** Slowness of movements observed during confusion, stuporous states, or in neurological pathologies such as Parkinson's disease. 42

**chemical shift** Modification in the Larmor frequency for a specific isotope within the image voxels. 53

**chorea** Abnormal movements that are usually generalized, brutal, unpredictable, arrhythmic, and targeting the proximal or distal part of limbs, the trunk, the neck and face muscles. 42

**circle of Willis** A system of communicating arteries that interconnects the anterior and middle cerebral arteries of both sides with the vertebro-basilar system. It is located at the base of the brain and surrounds the infundibulum and the optic chiasm. 12, 14

**collateral** Anatomical element that breaks off or joins a main stem. 10, 11, 24, 30, 33

**commissure** Intertwining or passing point of nerve bundles connecting the hemispheres of the central nervous system. 10, 17

**contralateral** At the opposite side. 17, 60

**cross-linking** Chemical bond formed between adjacent chains of a complex molecule such as a polymer or a protein. 55, 56

- cytoarchitecture** Changes in local layering of cells in the cerebral cortex by patterns of neuronal chemistry. 34, 36, 37
- cytoplasm** Everything contained within the cell membrane, except the nucleus. Cytoplasm consists of 80–97% water and has within a system of microscopic filaments or fibers called the cytoskeleton. The latter maintains cell shape and is responsible for cell locomotion and for movement of the organelles within it. 18
- decussation** Intersection on the median line of motor, sensitive or vegetative fiber bundles of the cerebrospinal axis. It is a synonymous of intertwine. 17
- dystonia** Disorder leading to uncontrolled and sometimes painful muscle movements (spasms). 42
- ectoderm** One of the three primary germ cell layers (the others are the mesoderm and endoderm) that make up the very early embryo. The ectoderm is the outermost of the three layers. It gives rise to many tissues and structures including the brain and spinal cord. 8, 21
- ectopic** Occurring in an abnormal position or in an unusual manner or form. 43
- entorhinal cortex** Cortex of the ambiens gyrus' rostral part, which covers ventrally the amygdala. It provides input to the hippocampus and then disseminate hippocampal output to the cortical mantle. The ambiens gyrus is the lateral segment of the olfactory gyrus, placed outside the annular sulcus. 25, 41
- ferritin** Protein macromolecule which constitutes an iron supply located in some organs, the spleen, the liver, the bone marrow. 70
- fimbria** Little white band bordering the hippocampus composed of a fiber bundle that begins in the alveus and joins in the fornix. It is the only efferent pathway of the hippocampus. 11, 18
- gliosis** Reaction of the central nervous system to injury of the brain or spinal cord that results in the fibrous proliferation of glial cells in the injured areas. 42
- heterotypical** Refers to the isocortex in which one or more layers show functional modification. Not all six layers are recognizable to the point that some are so attenuated that they appear virtually missing. We distinct the agranular and the granulous types. 24, 27
- homotypical** Corresponds to the isocortex that presents readily discernable layers with the same function. There are three structural types of homotypical isocortex: the frontal, the parietal and the polar types that all clearly conserve the basic six-layered arrangement characteristic of the granular isocortex. 24, 27, 29
- hypomania** Personality disposition resulting in a state of permanent subexcitation with activity and often creativity. 44
- infarct** Localized area of ischemic necrosis produced by the absence of oxygen supply (anoxia), following occlusion of the arterial supply or the venous drainage of the tissue or organ. 44, 45, 67
- interneuron** Small neuron characterized by local connections that modulated the sensibility level of the surrounding neurons. 30, 33
- ipsilateral** In the same side. 17
- lobe** Roughly isolated organ territory, which perfusion and innervation allow its autonomization. 10, 12, 17, 18

- magnetic susceptibility** Amplitude to which a tissue gets magnetized when placed within a magnetic field. 53
- mania** Indicative state of a mood disorder manifested by euphoric psychic and motor excitation. 44
- microtubule** Structural, cylindrical element with a 25nm diameter, constituting the cytoskeleton of fibrous proteins. 42
- myeloarchitecture** Changes in local layering of myelination in the cerebral cortex by patterns of absent cells. It relies on measurements on myelin density within cortical layers.. 34, 36
- nerve** Cord linking a nervous center to an organ of the body. It is usually cylindrical, off-white and made of nerve cells expansions. Nerve fibers are ensheathed by blood capillaries and adipose cells. One must distinguish nerve tracts that include spinal nerves from the spinal cord and cranial nerves from the brainstem, from the automatic nerves. Depending on their physiological actions, nerves are sensitive or sensory, motor or secretory. 7, 8, 14
- post mortem interval** Time interval separating the time of death and the time of the brain collection. 54, 56, 134
- proton density** Concentration of mobile hydrogen atoms located in a tissue sample. 51
- Ranvier node** Gaps formed between the myelin sheath where the axons are left uncovered. Nodes of Ranvier allow the generation of a fast electrical impulse along the axon. This rapid rate of conduction is called saltatory conduction. 20, 21
- Schwann sheath** Membrane consisting of Schwann cells and surrounds the axons of peripheral nerves. 20
- spasticity** Muscle contraction showing all the characteristics of a spasm. 42
- stroke** Sudden death of neuronal cells in a localized area due to inadequate blood flow. 45, 55, 67
- tau protein** Intracellular protein taking part to the connection and stabilization of microtubules. 42



# Résumé de la thèse

Le cerveau est un organe qui se distingue de par sa complexité, aussi bien sur le plan structurel que sur le plan fonctionnel. Sa compréhension est un des principaux enjeux de la communauté scientifique. Le cerveau est le chef d'orchestre du corps: il assure la gestion et le fonctionnement de tous les organes, il navigue entre notre conscient et notre inconscient, et il crée notre lien avec le monde qui nous entoure. Le cerveau représente un gigantesque réseau formé de neurones, cellules spécialisées et unités fondamentales, morphologiques, et fonctionnelles du tissu nerveux. Ce sont près de 100 milliards de neurones qui communiquent grâce aux connexions synaptiques. Le cerveau humain est notamment formé du cortex cérébral, une zone continue de substance grise d'environ trois à quatre millimètres d'épaisseur occupant la totalité de la surface cérébrale. Il présente une structure laminaire, tant du point de vue de son organisation cellulaire (cytoarchitecture) que de sa myélinisation (myéloarchitecture). Aboutir à une segmentation automatique des couches corticales à une échelle mésoscopique permettrait de mieux appréhender les corrélats anatomiques des fonctions cérébrales chez le sujet sain, mais également de mieux identifier les anomalies de ces structures dans les pathologies cérébrales, à l'instar des pathologies neurodégénératives (maladies d'Alzheimer, de Parkinson, de Huntington), neurodéveloppementales ou neuropsychiatriques.

Les histologistes tels que l'espagnol Santiago Ramón y Cajal, qui ont imagé les neurones pour la première fois grâce à la coloration de Golgi au début du 20<sup>ème</sup> siècle, ont été les premiers neuroscientifiques et les pionniers des neurosciences modernes. Depuis les prémices de la neuroimagerie qui se limitait à la dissection postmortem de pièces anatomiques, les techniques d'imagerie modernes se sont multipliées pour y inclure des méthodes ionisantes telles que la tomodensitométrie (TDM), la tomographie par émission de positons (TEP) et la tomographie à émission monophotonique (TEMP); ainsi que des méthodes non ionisantes telles que l'électroencéphalographie (EEG), l'échographie, la magnétoencéphalographie (MEG) et l'imagerie par résonance magnétique (IRM). Cette dernière, apparue dans les années 1970, a révolutionné les neurosciences en permettant d'imager le cerveau d'un sujet vivant en utilisant le phénomène de résonance magnétique nucléaire (RMN), dont notamment celui du proton de l'atome d'hydrogène. L'IRM ne génère pas de rayonnements ionisants, elle est non invasive et offre un bon contraste des tissus mous. L'IRM possède différentes modalités telle que l'IRM anatomique qui fournit des coupes 2D ou 3D du corps avec une résolution spatiale et un contraste élevés, et l'IRM fonctionnelle (IRMf) qui se base sur les modulations du débit sanguin cérébral provoquée par l'activité cérébrale et sur l'aimantation de l'hémoglobine des globules rouges pour connaître la localisation des régions fonctionnelles. On compte également l'IRM de diffusion qui est basée sur les modifications du signal RMN induites par les mouvements microscopiques des molécules d'eau dans les tissus, afin de remonter à la connectivité structurale cérébrale et définir ses caractéristiques microstructurales (diamètre axonal, longueur dendritique). Toutefois, l'IRM *in vivo* connaît une résolution spatiale limitée (de l'ordre de 1-3mm), ne permettant pas d'imager avec précision des structures telles que les couches corticales.

L'utilisation jointe de très hauts champs magnétiques ( $\geq 7T$ ), et de puissants gradients ( $\geq 300mT/m$ ), permet d'améliorer le contraste, le rapport signal sur bruit, ainsi que la résolution spatiale des images IRM. Cependant, les imageurs cliniques actuels ne sont pas dotés de cette double technologie, sans compter que la possibilité d'imager le cerveau entier d'un sujet vivant à une résolution mésoscopique reste inatteignable pour des durées d'acquisition cliniquement tolérables.

C'est pour cela que l'objectif de cette thèse est d'étudier *ex vivo* la cytoarchitecture et la myéloarchitecture du cortex cérébral humain en utilisant deux imageurs IRM précliniques à 7T et 11,7T, tous deux dotés de gradients atteignant une forte intensité (respectivement 440mT/m et 780mT/m). Ce duo d'imageurs rend possible la cartographie de la cytoarchitecture et la myéloarchitecture des couches corticales, ainsi que de leur connectivité intracorticale avec une résolution d'une centaine de micromètres. Les travaux menés durant cette thèse ont été divisés en deux projets complémentaires:

- le projet Neuro2Co, en partenariat avec l'INRAE Val de Loire et le ZooParc de Beauval, qui s'intéresse à la comparaison *ex vivo* de la connectivité structurale des circuits socio-émotionnels chez les animaux d'élevage et les animaux sauvages afin de traiter des questions neuroscientifiques et éthologiques. Ce projet implique la participation de collégiens de la région Centre-Val de Loire volontaires dans l'apprentissage des neurosciences et l'utilisation d'outils scientifiques. Le projet se déroule sous la coordination du Dr Elodie Chaillou (Unité de Physiologie de la Reproduction et des Comportements, INRAE, CNRS, IFCE, Université de Tours, Nouzilly).
- le projet Chenonceau qui est en partenariat avec l'unité INSERM U1253, iBrain, sous la coordination du Pr Christophe Destrieux (CHU Bretonneau, Faculté de médecine de Tours), et l'Institut de neuroscience et de médecine 1 du centre de recherche de Jülich en Allemagne (IMN-1, Forschungszentrum, Jülich) impliquant les Pr Katrin Amunts et Markus Axer. Ce projet a été partagé et financé par l'ANR FibrAtlas II-III et le projet phare européen Human Brain Project (HBP) (phases SGA2 et SGA3). Il vise à élaborer une cartographie IRM à l'échelle mésoscopique du cerveau humain post-mortem à 7T et 11,7T. Cette thèse a significativement contribué aux campagnes d'acquisitions ainsi qu'à l'analyse de cet unique jeu de données afin d'explorer la structure laminaire du manteau cortical et sa connectivité intracorticale en utilisant des séquences d'IRM quantitative et de diffusion.

## **Etablissement d'un atlas de la connectivité anatomique de la caille japonaise**

L'émotivité peut être définie comme l'aptitude à s'émouvoir facilement, à réagir trop vivement aux stimuli même très faibles, caractérisée aussi par une insuffisance de l'inhibition, une incapacité à s'adapter aux situations nouvelles, imprévues. En psychologie, l'émotivité est même l'un des critères permettant l'analyse et le classement des caractères. L'émotivité met en relation plusieurs structures cérébrales communicant entre elles par les faisceaux de fibres blanches. L'hypothèse de recherche implique donc que l'émotivité a un impact direct sur les circuits socio-émotionnels du cerveau. Parmi les animaux d'élevage qui présentent une émotivité quantifiable, on compte la caille japonaise (*Coturnix japonica*). Son degré d'émotivité est reflété par le test d'immobilité tonique, une réaction innée, de type réflexe, et donc involontaire. L'animal est comme paralysé, avec les muscles hypertoniques, les yeux fermés de façon intermittente et le rythme cardiaque abaissé. Il s'agit d'une réponse de peur caractéristique de chez l'oiseau lorsque celui-ci est capturé par son prédateur.

Ce critère présente l'avantage de s'exprimer quel que soit le milieu d'élevage. Il constitue une mesure de l'état de peur des cailles non invasive, robuste, et reproductible. Pour provoquer l'immobilité tonique, on place la caille sur son dos et

en la maintenant ainsi pendant 10 secondes. Une fois lâchée, elle peut rester dans cette position, immobile, pendant un temps qui varie de quelques secondes à plusieurs minutes. Dans le cas de notre sélection, on a distingué deux lignées :

- les cailles à courte immobilité tonique (STI), qui restent moins d'une minute en immobilité tonique;
- les cailles à longue immobilité tonique (LTI), qui restent plus d'une minute en immobilité tonique.

De ce fait, les cailles LTI sont considérées comme étant très émotives, tandis que les cailles STI sont jugées peu émotives d'après leur performance au test d'immobilité tonique. Les cailles de cette étude sont le fruit de plusieurs décennies de sélection (65 générations en 33 ans).

Les sujets de travail furent 21 cailles japonaises mâles âgées de 10 semaines lors de leur sacrifice. Elles étaient donc toutes à maturité sexuelle. On comptait 11 cailles de la lignée LTI et 10 cailles de la lignée STI. La fixation du cerveau s'est faite par perfusion intracardiaque de paraformaldéhyde (PFA) à 4%. La boîte crânienne de tous les sujets a été conservée pour des soucis pratiques de manipulation expérimentale. En attente de leur acquisition, les échantillons sont gardés dans un réfrigérateur à une température constante de 4°C.

L'imageur utilisé pour toutes les acquisitions est l'IRM préclinique de 11,7T Bruker BioSpec 117/16 USR de la plateforme d'imagerie de NeuroSpin. L'IRM est équipée d'un puissant gradient pouvant atteindre 780mT/m et avec une vitesse de balayage maximale de 9500T/m/s. L'antenne associée pour ces mesures est une antenne volumique de 40mm de diamètre interne en émission-réception du signal RMN. Chaque échantillon est réhydraté dans une solution tampon de *phosphate buffered saline* (PBS) à 0,1M minima deux jours avant une acquisition.

Le protocole d'acquisition combine IRM de diffusion à une résolution isotrope de 200 $\mu$ m et IRM anatomique à une résolution isotrope de 150 $\mu$ m. Les images anatomiques furent obtenues avec une séquence écho de spin (SE) 2D, pondérée en  $T_2$ . Les images pondérées en diffusion furent obtenues avec une séquence d'imagerie écho planaire (EPI) 3D, segmentée, basée sur de la PGSE (*pulsed gradient spin echo*) ( $b=4500s/mm^2$ , 75 directions).

La pipeline réalisée a impliqué la délimitation manuelle des masques du cerveau de chaque sujet, le débruitage des données de diffusion, l'application de deux modèles locaux du processus de diffusion (DTI et aQBI), l'utilisation des approches de tractographie régularisée par streamline déterministe et probabiliste. Les outils computationnels utilisés sont disponibles dans la toolbox Ginkgo (<https://framagit.org/coupon/gkg>). Les tractogrammes de chaque caille ont permis la réalisation du clustering de fibres intra-sujet puis du clustering de fibres inter-sujet regroupant les 21 cailles japonaises scannées. La réorientation des cerveaux dans un référentiel commun s'est faite grâce aux commissures antérieure et postérieure clairement identifiables, de même qu'un axe interhémisphérique, étant donnée l'absence de corps calleux reliant les deux hémisphères comme chez tous les oiseaux. Ces points de repère se sont avérés essentiels pour l'étape de clustering de fibres inter-sujet préalable à la construction d'un atlas de la connectivité.

L'analyse du résultat du clustering inter-sujet issu de la méthode de tractographie régularisée par streamline déterministe a permis de créer le tout premier atlas de la connectivité structurelle de la caille japonaise (voir Figure 1). Il présente 34 faisceaux de fibres branches, identifiés à l'aide de l'atlas et du template anatomiques développés à partir des images anatomiques pondérées en  $T_2$ , ainsi que de la littérature scientifique sur les oiseaux.

Des différences hémisphériques entre les deux lignées ont été observées pour ces faisceaux grâce à l'analyse statistique de métriques basées sur la diffusion (fraction d'anisotropie généralisée ou non; diffusivités axiale, radiale et moyenne). Ces différences ressortent notamment pour les 6 faisceaux potentiellement responsables des réactions de peur de la caille japonaise: les tractus amygdalo-nidopalliale, les tractus amygdalofuge ventraux, le tractus amyg-



dalofuge dorsal gauche et le tractus amygdalofuge dorsal droit. Cette première étude a été conclue par une publication dans la revue scientifique *Brain Structure And Function* qui est en cours de correction (voir Appendix A).

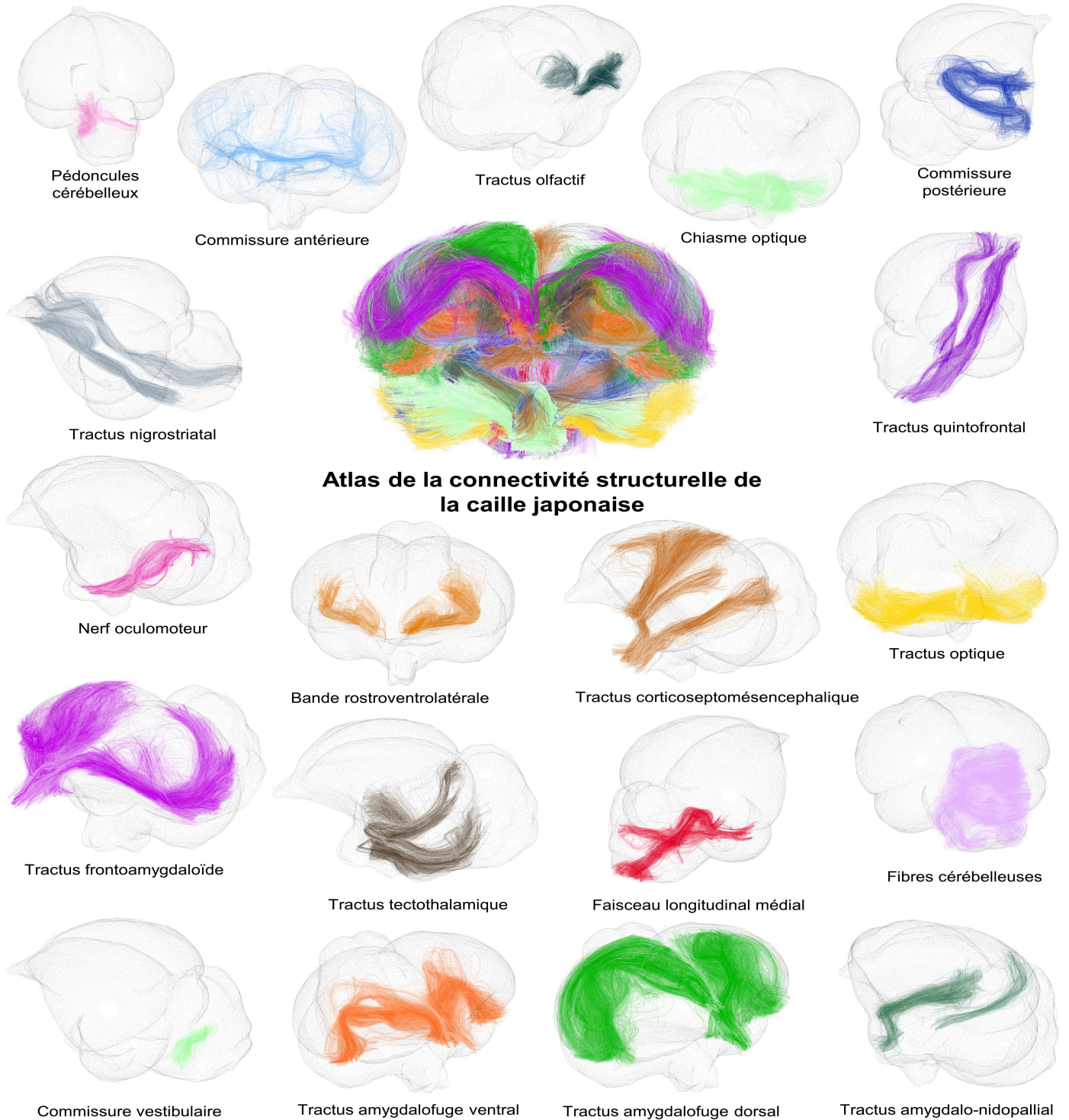


Figure 1: *Atlas de la connectivité structurale de la caille japonaise (Coturnix japonica) basée sur la méthode de tractographie régularisée par streamline déterministe et représentée sur un maillage 3D du template anatomique. Les 34 faisceaux de substance blanche sont montrés avec des couleurs différentes en tant que fibres des clusters auxquelles elles appartiennent.*

# Etude des connectivités anatomiques des animaux sauvages provenant du ZooParc de Beauval

Tous les mammifères possèdent un néocortex et un cervelet au sein de leur système nerveux central. Le néocortex est une structure particulièrement complexe, organisée sous forme de couches cellulaires et myélinisées, et elle permet aux mammifères d'appréhender leur environnement. Partant sur le principe que les comportements sont intégrés dans les circuits socio-émotionnels du cerveau, nous avons cherché à comparer les connectivités anatomiques de deux catégories de mammifères, les proies et les prédateurs. Le but était de définir leurs points communs et leurs différences en rapport avec les faisceaux de fibres blanches impactant la régulation des émotions.

Nous avons donc scanné *ex vivo* à 7T et 11,7T huit animaux sauvages qui vivaient au ZooParc de Beauval (Saint-Aignan, France). On dénombre cinq proies (un bongo femelle, une otarie de Californie mâle, un cerf-souris mâle, un sitatunga femelle et un maki-catta), ainsi que trois prédateurs (un bébé tigre de Sumatra, un bébé jaguar femelle et un puma mâle). Le protocole d'acquisition implique un imageur IRM préclinique à 11,7T pour la quasi-totalité des spécimens et un imageur IRM clinique à 7T pour les pièces les plus volumineuses (le bongo et l'otarie de Californie). Chaque acquisition a été réalisée à une haute résolution spatio-angulaire (150 $\mu$ m à 600 $\mu$ m isotrope). Nous avons procédé à de l'imagerie anatomique pondérée en  $T_2$  avec une séquence 2D SE sur l'imageur 11,7T et une séquence pondérée en  $T_2$  turbo spin écho SPACE sur l'imageur 7T. Le protocole inclut également de l'imagerie de diffusion utilisant une séquence 3D EPI segmentée sur l'imageur 11,7T et une séquence 3D DW TrueFISP/bSSFP sur l'imageur clinique 7T.

En utilisant une pipeline similaire à celle de la cohorte de cailles japonaises et qui fait appel à la toolbox Ginkgo (<https://framagit.org/coupon/gkg>), deux tractogrammes basés sur les approches de tractographie déterministe et probabiliste ont été créés pour chaque animal. La connectivité structurelle de chacun a ensuite été définie grâce au clustering de fibres intra-sujet.

A partir des résultats de clustering intra-sujet issus des tractogrammes régularisés par streamline déterministe (Figure 2), il a été possible de détecter d'une part les plus larges faisceaux de fibres blanches que l'on retrouve chez la plupart des mammifères, tels que le corps calleux, le tractus cortico-spinal, les faisceaux du cingulum, les commissures antérieure et postérieure, les pédoncules cérébelleux, et le tractus optique. D'autre part, des connexions plus fines sous-corticales de forme en U ou cérébelleuses sont également observées.

La haute résolution spatiale des données de diffusion du cerf-souris (250 $\mu$ m) et du maki-catta (200 $\mu$ m) a d'ailleurs permis d'observer la connectivité intracorticale au niveau des lobes frontal et temporal. Ces résultats se sont avérés déterminants pour la suite de la thèse, impliquant l'étude postmortem du cerveau humain et la possibilité d'observer la connectivité cortico-corticale suivant les couches cytoarchitecturales et myéloarchitecturales explorées. Les cartes de connectivité structurelle ont aussi révélé une architecture similaire entre le bongo et le sitatunga qui sont proches sur le plan de la phylogénie. Enfin, l'emphasis a été mise sur l'otarie de Californie qui a la capacité d'adapter son sommeil suivant son lieu de vie (terrestre ou marin) ce qui impacte l'activité cérébrale de ces deux hémisphères. Cette singularité liée au processus de sommeil apporte un angle supplémentaire dans l'étude de la connectivité structurelle de l'otarie de Californie (Figure 3). Une segmentation complète des substrats anatomiques des 8 espèces animales permettra de développer les premières observations pour aboutir à une étude comparative finale de leurs circuits socio-émotionnels.

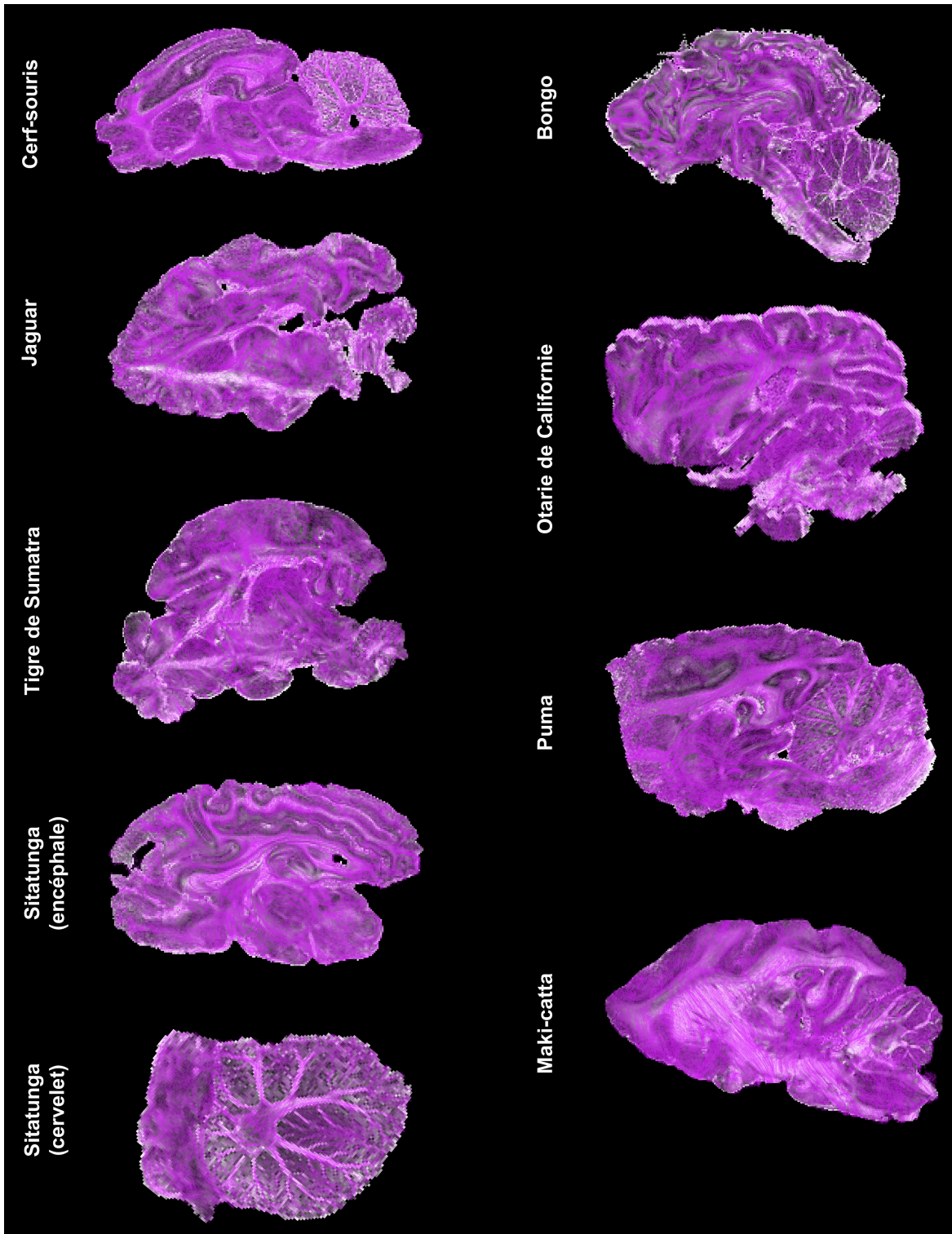


Figure 2: *Tractogrammes des animaux sauvages provenant du Zooparc de Beauval. Il y a d'une part les proies: le cerf-souris, le maki-catta, le sitatunga, le bongo et l'otarie de Californie; et d'autre part les prédateurs: le bébé tigre de Sumatra, le bébé jaguar et le puma. Les images de faisceaux de fibres sont en vue sagittale et superposées sur leur carte de fraction d'anisotropie généralisée (GFA) correspondante.*

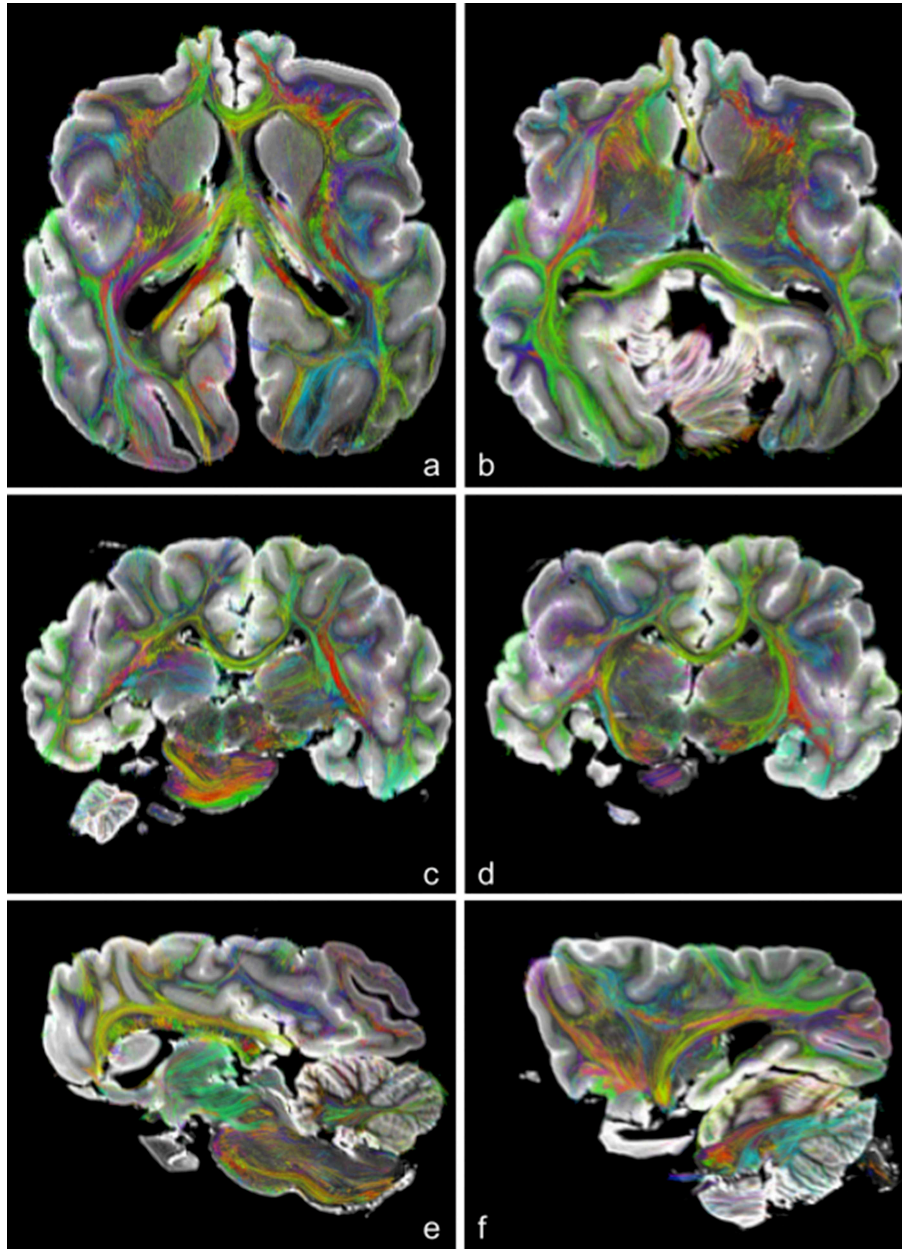


Figure 3: *Images du clustering de fibres intra-sujet pour l'otarie de Californie. Présentation de paires d'images dans les plans axial (a,b), coronal (c,d) et sagittal (e,f). Les clusters de fibres ont une longueur comprise entre 50 et 290mm ce qui correspond aux fibres les plus longues facilement observables. Les clusters de fibres sont superposés à l'image de référence pondérée en  $T_2$ .*

## **Inférence de la cytoarchitecture et de la myéloarchitecture du cortex cérébral humain au sein du projet Chenonceau**

L'objectif des travaux présentés ici portent donc sur le développement de nouvelles approches de cartographie *ex vivo* de la cytoarchitecture et de la myéloarchitecture du cortex cérébral humain grâce à l'imagerie par résonance magnétique (IRM) anatomique, quantitative et de diffusion à très haut champ magnétique (7T et 11,7T). Ils s'inscrivent

dans le cadre du projet Chenonceau qui correspond à la construction d'un atlas à l'échelle mésoscopique du cerveau humain post-mortem.

**L'échantillon de cerveau humain** L'étude porte sur un cerveau entier postmortem d'un homme de 92 ans présentant des antécédents de DMLA et des premiers signes de troubles cognitifs. Le cerveau est fixé 8 heures après la mort du donneur par immersion et perfusion dans du formol concentré à 4% et conservé 5 mois dans cette solution à une température de 5°C. La pièce anatomique est découpée en trois parties: les deux hémisphères et le cervelet. Chaque hémisphère est par la suite découpé en blocs parallélépipédiques (7 pour l'hémisphère gauche et 6 pour l'hémisphère droit) afin de permettre l'acquisition de données IRM à très haut champ (11,7T et 7T) sur deux imageurs IRM précliniques. Chaque bloc est immobilisé dans un gel d'isolation électrique (Biz'gel, BizLine, France) et hydraté régulièrement à l'aide d'une solution de *phosphate buffered saline* (PBS) à 0.1M. Au moment de l'acquisition, la solution de PBS est remplacée par un fluide non-protonique, le Fluorinert (FC-40, 3M, Etats-Unis), qui ne présente aucun signal RMN. Ce fluide protège les tissus de la déshydratation et limite les effets de susceptibilité susceptibles d'induire des distorsions géométriques délétères.

**Protocoles IRM** Chaque bloc de l'encéphale est scanné à 4 reprises sur 4 champs de vue consécutifs permettant de couvrir le champ de vue global (2 champs de vue consécutifs se superposent sur une région de 1.6cm de longueur afin de faciliter le recalage a posteriori). Deux IRM précliniques munies d'antennes volumiques en émission-réception de 60mm de diamètre intérieur sont utilisées: le Bruker BioSpec 11,7T ( $G_{\max}=780\text{mT/m}$ ,  $v_{\text{balayage}}=9500\text{T/m/s}$ ) pour acquérir les données anatomiques et de diffusion et le Bruker BioSpec 7T ( $G_{\max}=440\text{mT/m}$ ,  $v_{\text{balayage}}=3440\text{T/m/s}$ ) pour les données de relaxométrie.

Le protocole appliqué sur l'imageur préclinique 11,7T concerne les imageries anatomique et de diffusion. Ce dernier a été élaboré durant la thèse de Justine Beaujoin [Beaujoin 2018] et il dure 107 heures par champ de vue acquis. La campagne d'acquisition sur l'imageur 11,7T a duré 26 mois pour imager chacun des 45 champs de vue du specimen, par les contributions jointes de Justine Beaujoin, Alexandros Popov et moi-même. Le protocole d'imagerie anatomique à 11,7T inclut deux séquences IRM pondérées en  $T_2$  avec une résolution isotrope de  $100\mu\text{m}$  pour l'une (séquence MSME 3D, TE/TR = 20/500ms, taille de la matrice =  $400 \times 400 \times 560$  coupes, 1 excitation, bande passante de lecture = 50kHz, temps d'acquisition = 22h13min) et  $150\mu\text{m}$  pour l'autre (séquence SE 2D, TE/TR = 16/6647ms, taille de la matrice =  $374 \times 27 \times 256$  coupes, 9 excitations, angle de bascule =  $90^\circ$ , bande passante de lecture = 66kHz, temps d'acquisition = 3h26min).

De plus, le protocole compte un ensemble de séquences IRM pondérées en diffusion de type multiple-shell permettant l'acquisition de données à haute résolution spatiale de  $200\mu\text{m}$  isotrope (séquence EPI 3D segmentée,  $\delta/\Delta = 5/12,3\text{ms}$ , TE/TR = 24,3/250ms,  $16 b = 0\text{s/mm}^2$ , 30 segments, angle de bascule =  $90^\circ$ , taille de la matrice =  $280 \times 212 \times 204$  coupes, 1 excitation, bande passante de lecture = 300kHz, temps d'acquisition = 81h20min), avec un échantillonnage de l'espace q réalisé avec respectivement  $b = 1500/4500/8000\text{s/mm}^2$  et 25/60/90 directions.

Le protocole d'imagerie quantitative à 7T a une résolution spatiale de  $200\mu\text{m}$  isotrope, identique à la résolution des données pondérées en diffusion. La campagne d'acquisition sur l'imageur préclinique 7T a duré 18 mois et a été fortement impactée par une anomalie technique qui est survenue sur l'imageur, ainsi que la pandémie de la COVID-19. La campagne d'acquisition a subi *in fine* un retard de 8 mois. De nombreux tests réalisés sur un corps calleux humain provenant d'un autre sujet ont permis la mise au point du protocole final qui dure 72 heures par champ de vue et inclut:

- une série de séquences d'échos de spin multiples pondérées en  $T_2$  (séquence MSME 3D, 30 échos, TE/TR = 5,56-166,8/1000ms, 3 excitations, taille de la matrice = 280x212x204 coupes, bande passante de lecture = 100kHz, temps d'acquisition = 36h02min);
- une série de séquences d'échos de gradient multiples pondérées en  $T_2^*$  avec une variation du temps d'écho (séquence FLASH 3D SPGR, angle de bascule = 50°, TE/TR=5-100/110,048ms, 10 échos, taille de la matrice = 280x212x204 coupes, 1 excitation, bande passante de lecture = 50kHz, temps d'acquisition = 12h30min);
- une série de séquences d'échos de gradient rapide avec angle de bascule variable pondérées en  $T_1$  (séquence VFA FLASH 3D, TE/TR = 4,99/15ms, angles de bascule = 3-45°, taille de la matrice = 280x212x204 coupes, 65 angles de bascule, 1 excitation, bande passante de lecture = 50kHz, temps d'acquisition = 12h30min);
- Une cartographie du champ  $B_1^+$  par la méthode du double angle de bascule EPI a également été réalisée afin de corriger a posteriori les données pondérées en  $T_1$  du biais de champ radiofréquence (séquence EPI 3D, TE/TR = 13,41/1500ms, angles de bascule = 30/60°, signal de type Spin Echo, 35 segments, taille de la matrice = 280x212x204 coupes, 1 excitation, bande passante de lecture = 300kHz, temps d'acquisition = 5h56min).

**Post-traitement** L'ensemble de la chaîne de traitement des données IRM est disponible sur la toolbox Ginkgo (<https://framagit.org/coupon/gkg>). Les différences de gain en réception ont été corrigées lorsque cela était nécessaire.

Prétraitement des données: les données pondérées en diffusion, anatomiques et relaxométriques ont été corrigées du bruit ricien à l'aide d'un algorithme de débruitage par moyennes non-locales (*non-local means*).

Segmentation du tissu cérébral: un masque correspondant au tissu cérébral a ensuite été construit par combinaison d'opérateurs de seuillage et de morphologie mathématique suivi d'une correction manuelle. Puis un second masque ciblant le cortex a été effectué sur le volume entier.

Calcul des cartographies paramétriques de la cytoarchitecture et de la myéloarchitecture: des routines d'analyse ad hoc ont été programmées en langages C++ et Python afin de reconstruire les cartographies du modèle NODDI permettant d'avoir accès à une estimation de la densité neuritique locale ( $f_{intra}$ ) et de la dispersion angulaire des dendrites ou axones (OD). Les cartographies des paramètres quantitatifs tels que la densité protonique relative, les temps de relaxation  $T_1$ ,  $T_2$ ,  $T_2^*$  mais également celle de la fraction de myéline locale (MWF) ont aussi été créées (Figure 4). Le reconstitution complète du cerveau Chenonceau pour toutes ces cartes quantitatives provient d'un algorithme de recalage difféomorphe 3D ANTs, dont le codage et la mise en application a été faite par Alexandros Popov, membre de l'équipe de recherche. A partir de la carte de densité protonique relative, issue des séquences VFA FLASH 3D, qui offre un bon contraste substance blanche/substance grise, il a été possible de générer un masque de l'ensemble du cortex cérébral du cerveau Chenonceau. Ce masque provient de l'application d'un algorithme de partitionnement en k-moyennes (*k-means*) qui a exploité la différence de contraste tissulaire, ainsi que d'un algorithme de croissance de régions qui a complété les zones non masquées par l'algorithme en k-moyennes (Figure 5).

Classification des couches cellulaires et myélinisées du cortex: en définissant à chaque voxel une combinaison de contrastes issue des cartes préétablies  $T_1$ ,  $T_2$ ,  $T_2^*$ , MWF,  $\kappa$  et  $f_{intra}$ , les cartes de classification à N dimensions ont été établies à l'aide d'un algorithme de partitionnement en k-moyennes de nouveau. La classification des couches cellulaires s'est faite à partir des cartes  $f_{intra}$  et  $\kappa$ , tandis que les couches myélinisées ont été déterminées à partir des cartes  $T_2^*$  et MWF. Ainsi, un morcellement spatial du manteau cortical a été défini sur l'ensemble du cerveau humain. Les cartes de classification résultantes ont été optimisées à l'aide du modèle Potts pour corriger les valeurs aberrantes. Connectivité intracorticale: une tractographie déterministe régularisée a permis la reconstruction virtuelle 3D des fibres présentes dans le cerveau entier *ex vivo*. Elle s'appuie sur le champ des fonctions de distribution des orientations de diffusion (ODFs) calculé suivant le modèle local du Q-ball analytique (harmoniques sphériques d'ordre 8, facteur

de régularisation de Laplace-Beltrami de 0,006). La connectivité intracorticale a ensuite été mise en relation avec la segmentation automatique des couches corticales pour y réaliser une comparaison avec les vérités terrains établies dans la littérature et par nos soins via des études histologiques d'échantillons du cerveau Chenonceau, se basant sur de l'imagerie par lumière polarisée 3D. Figure 5 présente une mosaïque de tous les types d'images et de cartes qui ont pu être édités jusqu'à présent durant le projet Chenonceau.

**Résultats et conclusion** Les contrastes présents dans les cartes quantitatives ont permis l'identification d'une lamination du néocortex du cerveau Chenonceau. Cette lamination est observable aussi bien d'un point de vue cytoarchitectural que myéloarchitectural. La combinaison des informations cytoarchitecturales et myéloarchitecturales issues des cartes  $T_1$ ,  $T_2$ ,  $T_2^*$ , MWF et  $\kappa$  a permis une délimitation plus précise des deux régions corticales observées. La strie de Gennari présente dans le cortex visuel primaire a pu être délimitée. Les segmentations établies rendent bien compte de la non uniformité volumique des couches du néocortex, rendant ainsi bien compte de la complexité de la microstructure corticale.

La comparaison entre les données provenant de l'imagerie par résonance magnétique et celles issues de l'imagerie par lumière polarisée 3D qui se positionne comme vérité terrain durant ce projet, montre une grande similarité dans l'orientation et la densité des faisceaux de fibres blanches intracorticales. Ces résultats suggèrent une cohérence entre les données générées durant ces trois années de thèse et la réalité anatomique sous-jacente du cerveau Chenonceau.

En conclusion, les données uniques d'IRM de diffusion et quantitative acquises à une résolution mésoscopique sur le cerveau Chenonceau ouvrent la voie à une exploration du cortex cérébral avec un niveau de détails jamais atteint jusqu'à présent chez l'homme en IRM. Nous avons pu montrer que l'imagerie par résonance magnétique de diffusion et quantitative à très haut champ magnétique permet de mettre en lumière les couches corticales cellulaires et de myéline du sujet humain post-mortem. L'exploitation de ces données de nature diverse grâce à l'utilisation de méthodes de classification de données multivariées a ainsi permis d'étudier la structure laminaire de ce cortex cérébral au niveau du néocortex. L'utilisation conjointe de techniques de tractographies avancées a de même permis d'appréhender la connectivité structurelle. Ces données ont aussi permis de caractériser les tissus cérébraux, ainsi que de mettre en exergue les fibres intracorticales. Le travail mené présente une méthodologie précise pour la segmentation automatique des couches corticales du cerveau humain *ex vivo* à très haut champ magnétique. Il a nécessité deux années de campagnes d'acquisition pour établir les cartographies quantitatives ciblées à 7T et 11,7T pour cette thèse. L'application à très haut champ magnétique de l'IRM de diffusion et quantitative à une résolution spatiale mésoscopique fournit des informations en adéquation avec la réalité microscopique. Ces bases méthodologiques pourront être à nouveau explorées pour approfondir les connaissances du cerveau humain et les pathologies propres au cortex cérébral.

## Contributions et perspectives

**Le projet Neuro2Co** Il s'agit d'un projet français dirigé par Dr Elodie Chaillou (Unité de Physiologie de la Reproduction et des Comportements, INRAE, CNRS, IFCE, Université de Tours, Nouzilly, France) qui vise premièrement à étudier les circuits socio-émotionnels d'animaux d'élevage et de la faune sauvage. Les acquisitions IRM faites à très haut champ magnétique sur neuf espèces animales constituent un jeu de données unique pour mettre en relation la connectivité structurelle de ces animaux avec des propriétés cognitives et des observations éthologiques. Deuxièmement, ce projet vise à transmettre des connaissances neuroscientifiques à des collégiens volontaires pour découvrir les

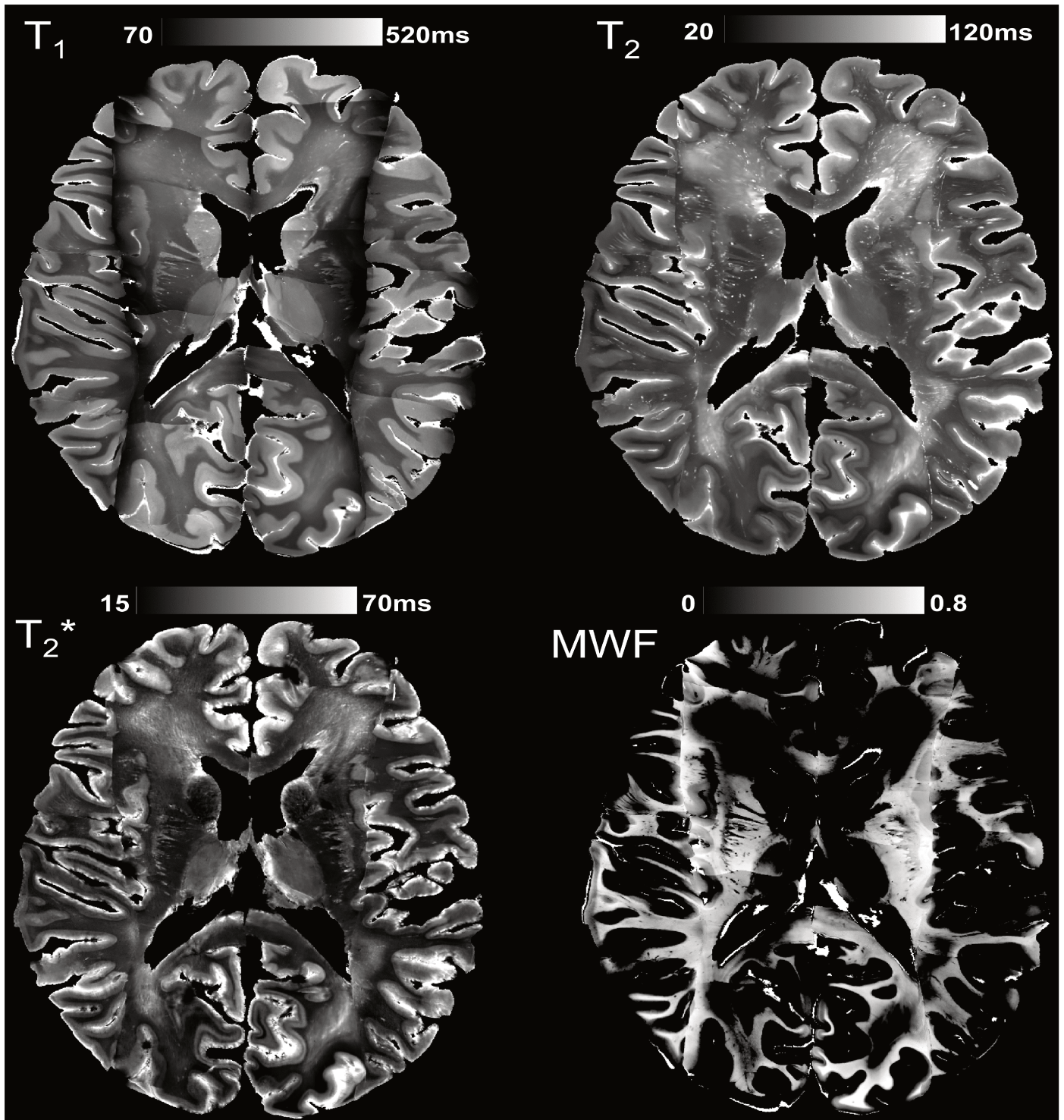


Figure 4: Cartes quantitatives des temps de relaxation  $T_1$ ,  $T_2$  et  $T_2^*$  et de la fraction de myéline locale (MWF) du cerveau Chenonceau en vue axiale.

neurosciences. Le projet a été financé par le conseil régional du Centre-Val de Loire. Des chercheurs, des doctorants et des enseignants collaborent pour faciliter l'apprentissage des logiciels utilisés par la communauté neuroscientifique par les collégiens qui analysent le jeu de données IRM. Ce projet de thèse a permis de démarrer la base de données



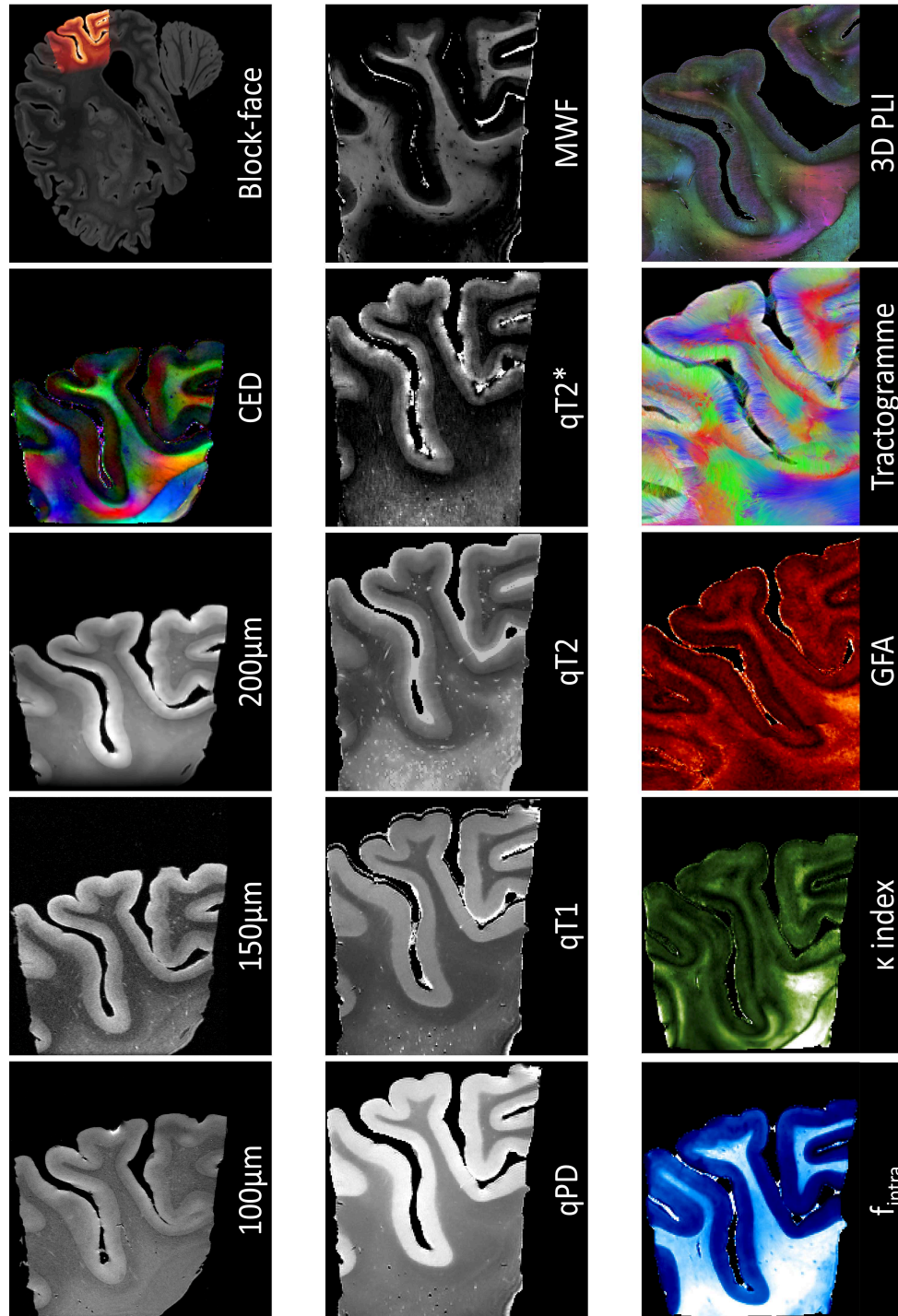


Figure 5: Mosaïque des différents types d'images et de cartes éditées pour le projet Chenonceau. La région servant d'exemple est celle du bloc F de l'hémisphère gauche, autour du sillon pariéto-occipital. En lisant de gauche à droite, la première ligne renvoie aux images IRM anatomiques, à la carte RGB des directions de diffusion (CED) issue du modèle DTI, et à l'image du champ de vue sur le block-face. La deuxième ligne esquisse les cartes relaxométriques (densité protonique relative  $qPD$ ,  $T_1$ ,  $T_2$  et  $T_2^*$ ), ainsi que la carte de fraction de myéline locale (MWF). La troisième ligne montre les cartes de  $f_{intra}$  et de  $\kappa$  index issues du modèle NODDI, la carte de GFA issue du modèle aQBI, le tractogramme issu de la tractographie par streamline déterministe, et l'image 3D réalisée grâce à de l'imagerie par lumière polarisée (PLI). Images de la première colonne adaptées de Beaujoin 2018. Image de PLI 3D, courtoisie de Axer, Amunts et al., Forschungszentrum, Jülich. Les images restantes sont issues des présents travaux de thèse.

IRM avec les neuf premières espèces animales scannées et à mettre en avant le potentiel d'exploration des circuits socio-émotionnels pour améliorer le bien-être animal.

**Le Human Brain Project (HBP)** Il s'agit d'une infrastructure de recherche créée en 2013 pour établir un atlas multi-échelle, du microscopique au macroscopique, du cerveau humain. Le projet est prévu une durée de dix ans et implique des centres de recherche européens afin d'étudier la singularité du cerveau humain, de faire progresser des solutions thérapeutiques pour les maladies du cerveau et de développer des ordinateurs neuromorphiques de pointe. Ce travail de thèse s'inscrit dans HBP et a contribué à enrichir l'atlas cérébral humain de HBP avec des données d'IRM anatomiques, quantitatives et de diffusion mésoscopiques post-mortem acquises tout au long du projet Chenonceau.

**Le projet FibrAtlasII-III** Il s'agit d'un projet français issue d'une ANR, mené par Pr Christophe Destrieux (unité INSERM iBrain U1253, CHU Bretonneau, Faculté de Médecine de Tours, France), qui vise à valider les méthodes de tractographie via une campagne d'acquisitions IRM sur une cohorte de volontaires seniors en bonne santé. Les participants ont accepté de donner leur corps à la science. De cette façon, leur cerveau a été scanné en utilisant l'imagerie par résonance magnétique, puis la dissection du cerveau suivant la méthode Klingler a été effectuée sur les mêmes cerveaux une fois les participants décédés. Ce travail de thèse s'inscrit dans le cadre du projet FibrAtlasII-III. L'ensemble des données d'IRM de diffusion résultant a conduit à la cartographie de la connectivité structurelle du cerveau de Chenonceau. Cette dernière fournit des informations permettant d'étudier avec précision la connectivité des cerveaux scannés et disséqués faisant partie du projet FibrAtlasII-III.

**Projets futurs** Les travaux à venir sur l'atlas de Chenonceau concernent trois thèses de doctorat déjà en cours au sein de l'équipe de recherche Ginkgo. D'une part, il y a le travail d'Alexandros Popov qui consiste à exploiter l'ensemble de données IRM anatomiques et de diffusion 11,7T du cerveau de Chenonceau afin d'y appliquer des méthodes de tractographie globale. D'autre part, il y a les travaux menés par Alexis Brullé et Anas Bachiri qui améliorent et exploitent un environnement de simulation de la microstructure cérébrale appelé MEDUSA pour recréer virtuellement et de manière réaliste la microstructure du cerveau humain. Enfin, un projet translationnel du CEA impliquant l'équipe de NeuroSpin/BAOBAB/Ginkgo, le Laboratoire des Maladies Neurodégénératives du CEA/MIRCen, l'unité INSERM U1253 iBrain du CHU de Tours, et le centre de calculs CEA/TGCC est sur le point d'être lancé pour accéder à la microstructure du cortex cérébral humain en combinant acquisitions IRM, histologie et intelligence artificielle.



# Chapter 1

## Introduction

### 1.1 Context and motivations

The brain is an organ that is distinguished by its complexity, both structurally and functionally. Its understanding is one of the main issues of the neuroimaging scientific community. The brain is the conductor of the body: it ensures the management and functioning of all the organs, it navigates between our conscious and our unconscious, and it creates our link with the surrounding world. The brain represents a gigantic network of neurons. The latter are specialized cells that stand for the fundamental, morphological, and functional unit of the nervous tissue. Almost 100 billion neurons communicate through synaptic connections. The human brain is made of the cerebral cortex, a continuous area of gray matter about three to four millimeters thick occupying the entire brain surface. It has a laminar structure, regarding both its cellular organization (cytoarchitecture) and its myelination (myeloarchitecture). Achieving automatic segmentation of cortical layers on a mesoscopic scale *in vivo* would allow to better understand the anatomical substrates of brain functions in the healthy subject, but also to better identify the abnormalities of these structures in brain pathologies, such as neurodegenerative pathologies (Alzheimer's, Parkinson's, Huntington's diseases) or psychiatric disorders (schizophrenia).

Histologists such as Santiago Ramón y Cajal who imaged neurons for the first time using Golgi's staining at the beginning of the 20<sup>th</sup> century, were the first neuroscientists and pioneers of modern neuroscience. Since the beginnings of neuroimaging, which used to be limited to postmortem dissections, modern techniques have multiplied from ionizing imaging methods including computed tomography (CT), positron emission tomography (PET) and single-photon emission computed tomography (SPECT), to non-ionizing techniques such as electroencephalography (EEG), ultrasound (US), magnetoencephalography (MEG), and magnetic resonance imaging (MRI). This last imaging modality, that appeared in the 1970s, revolutionized neuroscience by making it possible to image the brain of a living subject using the nuclear magnetic resonance (NMR) phenomenon, including that of the proton of the hydrogen atom. MRI does not generate ionizing radiation, it remains non-invasive and provides good soft tissue contrast. MRI can be subdivided into different modalities such as anatomical MRI that delivers 2D or 3D body images with relatively high spatial resolution and contrast, and functional magnetic resonance imaging (fMRI) which is based on the modulations of cerebral blood flow caused by brain activity and on the magnetization of red blood cell hemoglobin to know the location of functional regions. There is also diffusion-weighted magnetic resonance imaging (dMRI) which is based on changes in the NMR

signal induced by microscopic displacements of water molecules in the tissues, in order to trace back to the cerebral structural connectivity and probe its microstructural characteristics (axonal diameter, dendritic length). However, *in vivo* MRI has limited spatial resolution, in the range of 1-3mm, which does not allow for accurate imaging of structures such as cortical layers.

Technically, the combination of extreme magnetic fields ( $\geq 7\text{T}$ ) with powerful gradient sets ( $\geq 300\text{mT/m}$ ) is key to improve the signal-to-noise ratio, and the diffusion contrast mechanisms allowing to go beyond the millimeter scale and reach the mesoscale corresponding to a few hundreds of micrometers. Currently, clinical MRI systems cannot embed the two technologies due to various reasons: the use of strong gradient pulses of extreme fields that comes with major mechanical constraints or heat evacuation, the fast commutation of powerful gradients that can induce severe peripheral nerve stimulation if the gradient coil was not designed to prevent this physiological effect. To date, the ultra-high field (UHF) clinical MRI systems are often equipped with gradient sets that cannot deliver more than  $100\text{mT/m}$ . The strongest gradient sets, the Connectome gradient, is for now restricted to 3T. Technologists are working with MRI physicists to soon access 7T clinical MRI systems with Connectome gradient sets. But this approach remains out of the scope of this thesis which the chosen strategy will consist in pushing the limits of extreme field preclinical MRI systems equipped with powerful gradient sets to scan *ex vivo* animal and human brains at the mesoscale with anatomical, diffusion and quantitative imaging protocols.

Therefore, the work carried out during this thesis was performed in the frame of two complementary projects:

- the Neuro2Co project, in collaboration with INRAE (Dr Elodie Chaillou, Unité de Physiologie de la Reproduction et des Comportements, INRAE, CNRS, IFCE, Université de Tours, Nouzilly, France) and the ZooParc de Beauval (Dr Baptiste Mulo, Beauval zoo and Beauval nature, Saint-Aignan, France), aiming at studying *ex vivo* the brains of breeding and wildlife animals. The structural connectivity of their socio-emotional circuits were investigated. This project involved the contribution of French middle school students that volunteered in learning neuroscience and using scientific tools to explore the brains of the imaged animals.
- the Chenonceau project, in collaboration with the INSERM iBrain U1253 unit (Pr Christophe Destrieux, CHU Bretonneau, Faculté de Médecine de Tours, France) and the Institute of Neuroscience and Medicine 1 (Pr Katrin Amunts and Pr Markus Axer, Forschungszentrum, Jülich, Germany). The project was shared and funded in the frame of the French FibrAtlas II and III ANR project and the European flagship Human Brain Project (HBP) (FET-Open during SGA2 and SGA3 phases). The main purpose is here to acquire and provide an unprecedented MRI dataset at 7T and 11.7T on an *ex vivo* human brain sample at the mesoscopic scale. This thesis work significantly contributed to the acquisition campaigns and to the analysis of this unique dataset to investigate the laminar structure of the cortical ribbon using diffusion and quantitative MRI modalities, as well as the cortico-cortical connectivity.

## 1.2 Thesis organization

This thesis is made of three parts. The first one is the background part that reviews the general human brain organization (Chapter 2), as well as its cerebral cortex (Chapter 3). In Chapter 4, the basic principles of magnetic resonance imaging, diffusion-weighted magnetic resonance imaging and quantitative magnetic resonance imaging are addressed. The specificity of postmortem imaging is also detailed and the use of ultra-high and extreme magnetic fields is likewise

discussed in that chapter.

The second part dives into the structural connectivities of both breeding and wildlife animals in the frame of the Neuro2Co project and in two distinct studies. The latter were stepping stones in observing the structural intracortical connectivity made in the human cerebral cortex. They relied on in-house tools developed by the team and available in the Ginkgo toolbox (<https://framagit.org/coupon/gkg>).

The breeding species was the Japanese quail (*Coturnix japonica*), a bird which emotionality trait can be characterized through its specific response facing fearful situations called tonic immobility. A cohort of 21 subjects was formed to be scanned with anatomical and diffusion MRI sequences to validate if its propensity to express fearfulness is reflected in its connectome (Chapter 5). The eight scanned wildlife animals that lived in the ZooParc de Beauval are a Java mouse-deer, a ring-tailed lemur, a sitatunga, a baby jaguar, a puma, a bongo, a California sea lion and a baby Sumatran tiger. The goal was to create a structural connectivity map for each species based on high-resolution anatomical and dMRI data obtained at 7T and 11.7T in order to highlight and compare their socio-emotional circuits (Chapter 6).

The third part is focused on the Chenonceau project that is attached to the FibrAtlasII-III ANR project and the HBP. The aim of the Chenonceau project is to design a mesoscopic postmortem human brain MRI atlas using anatomical, diffusion and quantitative MRI at ultra-high and extreme magnetic fields. The diffusion MRI acquisition campaign was already engaged in Beaujoin 2018. Quantitative MRI was added in this thesis to specifically explore the cerebral cortex of the Chenonceau brain and was meant to automatically segment the cortical layers in order to investigate the cytoarchitecture and myeloarchitecture of the cortical ribbon as well as the intracortical connectivity. This study required both the development and the use of a quantitative imaging protocol at 7T, an advanced signal and biophysical model called NODDI [Zhang, Schneider, et al. 2012; Zhang, Mi, et al. 2019], streamline regularized tractography approaches, clustering methods [Guevara, Poupon, et al. 2011], 3D diffeomorphic registration of MR images, cerebral cortex masking, and delineation of the cortical layers using a non-linear programming Nelder-Mead-based algorithm. Histological analyses of parts of the Chenonceau brain were likewise performed in collaboration with Pr Markus Axer (INM-1, Forschungszentrum, Jülich) that conducted 3D polarized light imaging (PLI) on the samples. Chapter 7 introduces the Chenonceau project and the related 7T and 11.7T MRI protocols. Chapter 8 stresses the investigation on the Chenonceau cerebral cortex using the unique high-resolution dMRI and qMRI dataset.

The final chapter, Chapter 9, is the conclusion that recapitulates all the contributions of this thesis and presents the upcoming work related to the Chenonceau brain and the human cerebral cortex.



## **Part I**

# **Background**





## Chapter 2

# Human brain anatomy

This chapter presents the aspects of the human brain anatomy that are instrumental in understanding the articulation of this thesis. The brain can be apprehended on different scales. The sharpness of the scale comes from the technological feats that have been accomplished. Nowadays, the human brain can be observed from the macroscopic scale (over a millimeter) to the microscopic scale. Here, these distinct scales are described related to the cerebral features in tissue they reveal. Firstly, there is the presentation of the macroscopic anatomy of the human brain, including its neurodevelopment, and the main structures that compose it. Secondly, the gray matter and the white matter that are the two components of the brain tissue are defined. Then, the cerebral microscopic anatomy is detailed, distinguishing the neurons and their environment called the neuroglia.

### 2.1 Macroscopic anatomy

On a macroscopic scale, the human nervous system, as any other vertebrate, is divided into two parts: the central nervous system (CNS), which includes the brain (*encephalon*) and the spinal cord (*medulla spinalis*), and the peripheral nervous system (PNS) that is composed of the ganglia, nerves and plexuses. This section reviews the principal elements of the central nervous system, from their developments to their organizations and compositions.

#### 2.1.1 Global description

The brain is protected by the skull and surrounded by three membranes called meninges as depicted in Figure 2.1. The *pia mater* is the innermost layer, covers the surface of the CNS and enables the blood supply in the brain. The *arachnoid mater* is separated from the *pia mater* by the cerebrospinal fluid (CSF) located in the subarachnoid space. The CSF is a fluid constantly secreted by the choroid plexuses (about 500mL a day for an adult) which ensures the mechanical and immunological protections of the brain as a shock absorber and a brain waste cleaner, then is absorbed in the arachnoid granulations. Finally, the *dura mater* is the outermost meningeal layer, thicker and closer to the bony layer of the skull. On a global scale, the brain is subdivided into the cerebrum, the cerebellum and the brainstem as seen in Figure 2.2. The brainstem is the central axis of the brain and is composed of the medulla oblongata (myelencephalon), the midbrain

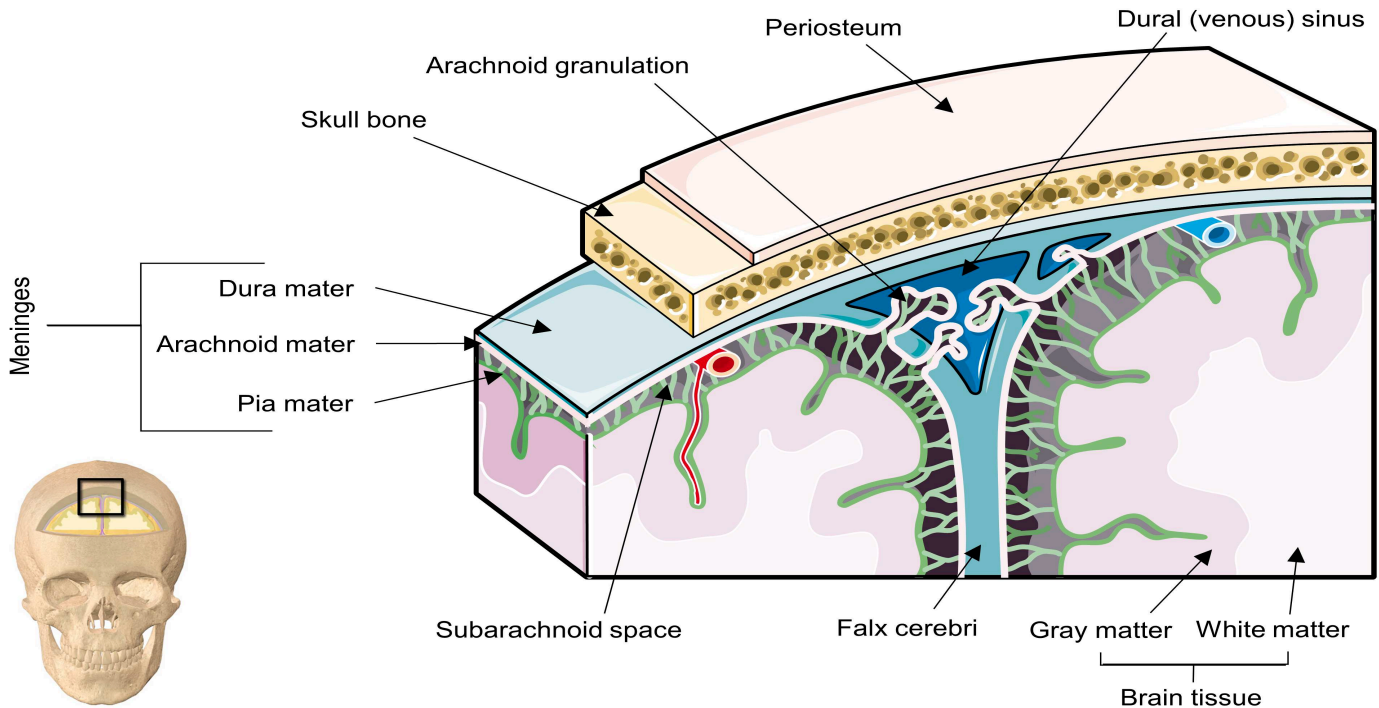


Figure 2.1: *Scheme of the brain skull and the meninges. Coronal section through the vertex of the skull showing the meninges and their direct surroundings. From the innermost to outermost: the pia mater, the arachnoid mater and the dura mater (adapted from <https://smart.servier.com/>).*

(mesencephalon) and the pons (metencephalon). It harbours the centers of origin and termination of ten out of twelve cranial nerves (III-XII). The brainstem coordinates movements and plays a key role in breathing control, heart rate and blood pressure. Moreover, it relays information from the cerebrum to the cerebellum or the spinal cord to the cerebellum. There are also fiber bundles within the brainstem that act as sensory and motor pathways in voluntary control of the muscles or the transmission of nerve impulses to the cerebrum.

The cerebellum is part of the hindbrain (rhombencephalon) and is located behind the medulla oblongata and pons. It comprised three parts: a median, two laterals as hemispheres and the cerebellum worm. It is linked to the medulla oblongata, pons and cerebral peduncles with the cerebellar peduncles. It is a terminal organ connected to voluntary and involuntary motor pathways. Thus, it controls equilibration, posture tone and all automatic movements. The morphogenesis and the macro-organization of the brain will be described next.

## 2.1.2 Neurodevelopment

The nervous system begins to develop in the human embryo at three weeks of age, with the formation of the neural plate. This is an elongated and thickened strip of the outer layer (ectoderm) of the embryo. As cells in the neural plate grow, the plate folds to form the neural groove. Finally, the latter deepens and closes off, forming the neural tube, which is located under the ectoderm. The entire central nervous system develops from the neural tube. Its cells proliferate within and grow unevenly, entailing the swelling and bending of its anterior part to form three distinct parts: the forebrain (prosencephalon), the hindbrain (rhombencephalon) and the midbrain (mesencephalon).

From both eye vesicles stemming from the forebrain, the telencephalic vesicle starts to grow. The lumen of the telen-

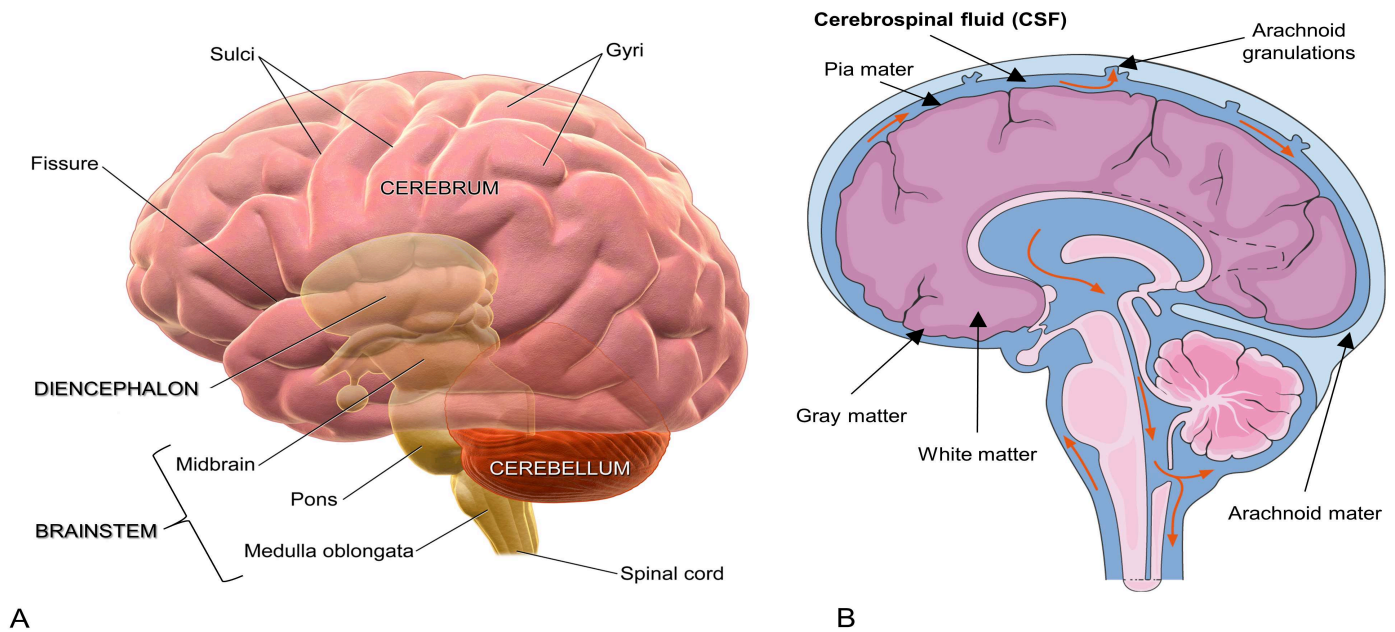


Figure 2.2: Illustrations of the principal regions of the human central nervous system (CNS) and locating the cerebrospinal fluid (CSF). A) Image of the main structures of the brain which can be divided into the cerebrum, the diencephalon, the cerebellum and the brainstem that includes the midbrain, the pons, and the medulla oblongata (adapted from [Blausen 2014]. B) Circulation of the intracranial CSF distribution within the brain (adapted from <https://smart.servier.com/>).

cephalic vesicles will become the lateral ventricles, and the brain hemispheres will develop out of these vesicles. The cells that multiply come from the innermost layers that line the lumen of the neural tube and gradually become differentiated into two types of cells: the neuroblasts that eventually become neurons, and those that develop into neuroglia. The cells of each brain region are created in the same order. First the large neurons, then the small neurons, and then the neuroglia are generated [Jacobson et al. 1978].

The thickness of the wall of the neural tube vastly increases. The migration of neuroblasts to the pial surface leads to the cerebral cortex. Each neuroblast settles, grows an axon and some dendrites to become a neuron. The deepest layers are the first ones to be developed. The cerebrum derives from the prosencephalon that comprises the telencephalon and diencephalon, an odd median part covered by the telencephalon. The telencephalon will become the cerebral hemispheres (neocortex or isocortex), the olfactory cortex (paleocortex), the hippocampus (archicortex) as well as the gray matter. The deep gray matter of the telencephalon will become the basal ganglia and the one at its surface will be the cerebral cortex. The diencephalon will lead to the hypothalamus, the thalamus, the optic vesicle, the epiphysis and the mammillary bodies. Therefore, the typical view on the human brain development can be epitomized as follows: 1) neural plate; 2) neural groove; 3) neural tube; 4) formation of three primary brain vesicles; 5) formation of five secondary brain vesicles. The evolution of the neural tube from the three-vesicle state to the five-vesicle state is shown in Figure 2.3.

### 2.1.3 Cerebral lobes

The cerebral cortex, *pallium* in Latin meaning "coat", is a highly folded sheet of neural cells that describes folds (gyri), grooves (sulci) and clefts (fissures) as the outer layer of the human cerebrum. This folding organization offers a larger

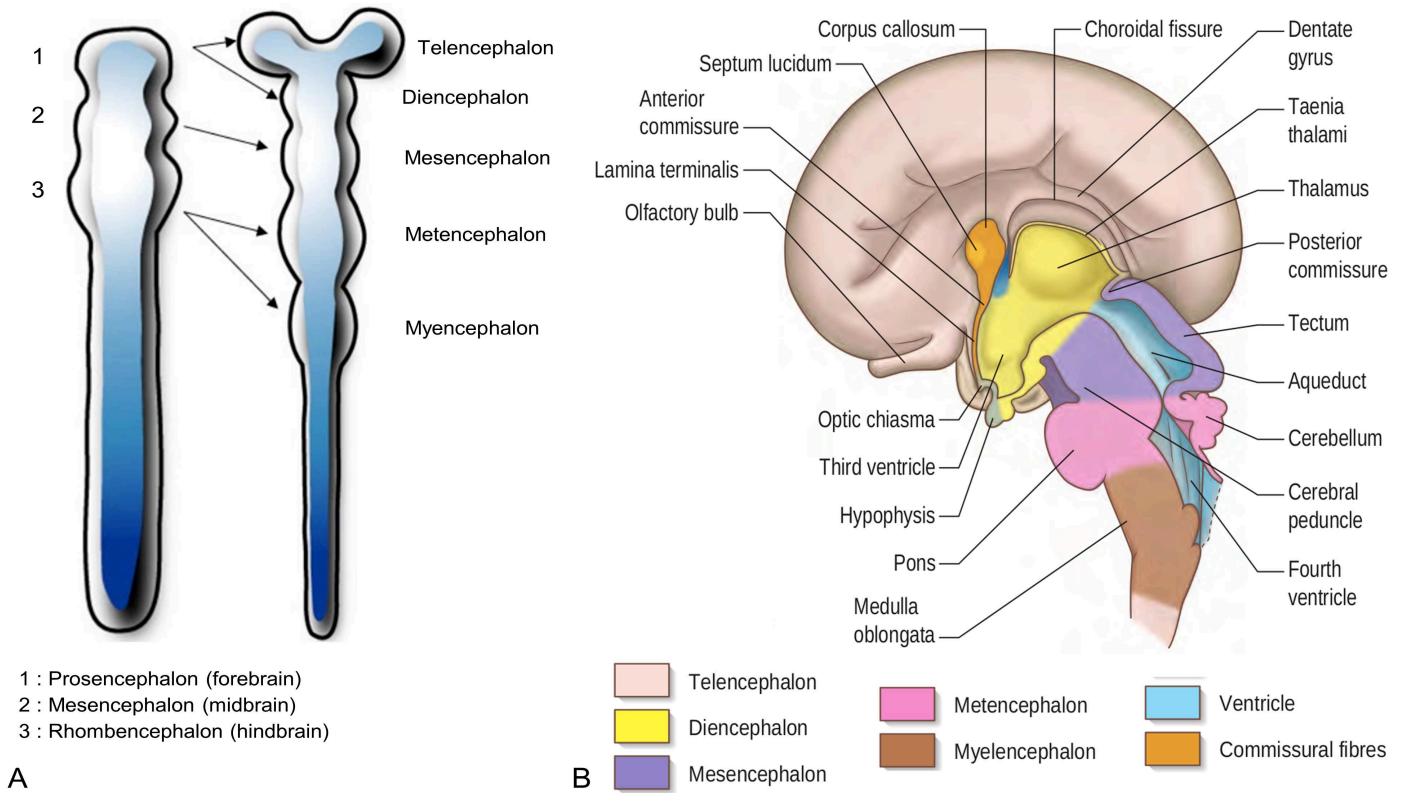


Figure 2.3: Scheme of the human neurodevelopment. A) Illustration of the three primary brain vesicles and the five secondary brain vesicles coming from the neural tube (courtesy of Pr D. Hasboun). B) Detailed image of a 16-week human fetus indicating the components of the five brain vesicles, the ventricle and the commissures (adapted from Standing 2015).

surface area in the confined volume of the cranium. The human cerebrum is divided into two hemispheres, the left and the right hemispheres. A hemisphere has a lateral (or external) face, a medial (or internal) face and an inferior (or ventral) face as shown in Figure 2.4. The hemispheres are connected by an interhemispherical commissure called the corpus callosum. Each hemisphere is divided into four external as well as two internal lobes with specific functions:

- The frontal lobe (*lobus frontalis*) reaches from the floor of the central sulcus (fissure of Rolando or Rolandic fissure) to the frontal pole, over and around it to the substantia perforata on the inferior hemispheric aspect, and to the limbic gyrus on the median aspect. It is functionally involved in speech and language production thanks to Broca's area, motor execution since it houses the premotor and primary motor cortices, cognition, behavior and planning.
- The parietal lobe (*lobus parietalis*) stretches behind the central sulcus on the median hemispheric faces to the limbic gyrus below, backwards until the interoccipital sulcus, and posteriorly to the parieto-occipital sulcus on the superolateral hemispheric faces (convexity); to the parietal lobe belongs from a cytoarchitectonic viewpoint the temporo-occipital transition zone on the lateral and ventral hemispheric aspects, all the way to the collateral sulcus. Functionally, it supports higher cognitive functions as mathematical cognition, semantic and pragmatic aspects of language, and abstract thinking.
- The occipital lobe (*lobus occipitalis*) is a direct caudal prolongation of the parietal lobe, from which it is separated cytoarchitectonically by the parieto-occipital and interoccipital sulci. It is the smallest of the four external lobes located near the posterior region of the cerebral cortex, next to the back of the skull. It contains the brain's visual

processing system including the primary visual cortex, as well as other functions like visual-spatial processing and movement and color recognition.

- The temporal lobe (*lobus temporalis*) spreads from the floor of the lateral sulcus (Sylvian fissure) to the collateral sulcus, in close proximity to the ears. The temporal lobe serves distinct functions. The auditory cortex is located on the upper banks of the temporal lobe and within the Sylvian fissure. There is also Wernicke's area for speech comprehension placed posterior to the auditory cortex. More inferior and posterior temporal lobe areas tuned for representing visual objects. The middle sections are essential for the memory and retrieval of the semantic knowledge of objects.
- The insular lobe (*lobus insulae*), or insula, is inserted in the form of a fan between the temporal, parietal, and frontal lobes, being separated from them by the posterior, superior, and anterior insular sulci. It lies deep within the lateral sulcus. The insula is implicated in a variety of functions from sensory processing to representing feelings and emotions, autonomic and motor control, decision-making, self-awareness, and complex social functions like empathy.
- The limbic lobe (*lobus limbicus*) is subdivided into two limbic lobes: the superior limbic lobe (*lobus limbicus superioris*) and the inferior limbic lobe (*lobus hippocampi* or *lobus limbicus inferioris*). The former represents the superior semicircular part of the fornicate gyrus (grand lobe limbique of Broca), which on the median aspect encircles the corpus callosum; it includes the cingulate gyrus and the retrosplenial region as far as the isthmus. The latter constitutes the inferior part of the fornicate gyrus that is accompanied by the fimbria; it includes the hippocampal and dentate gyri and the uncus. The limbic lobe is involved in processing learning, recent memory (hippocampal formation) and in the expression of emotion (amygdalar complex).

#### 2.1.4 Ventricles

The ventricles are one of the communicating cavities within the cerebrum, covered by an ependymal epithelium and numbered at four: two lateral ventricles, the third and the fourth ventricles (see Figure 2.5).

The lateral ventricles are the ependymal cavities of the cerebral hemispheres. They are wrapped around the thalamus and shaped as a triangular central body with four horns. The lateral ventricles communicate with the third ventricle through the left and right interventricular foramina (Monro foramina). The third ventricle is a median, symmetrical and uneven cavity grown from the diencephalic ependymal cavity, and bounded by the thalamus and hypothalamus on either side. Its back communicates with the fourth ventricle by the aqueduct of the midbrain (the aqueduct of Sylvius). The fourth ventricle is the most inferior one, and is a unique and median ependymal cavity near the brainstem area. Its back is covered by the cerebellum. It extends from the aqueduct of Sylvius to the central canal of the upper end of the spinal cord. The latter communicates with the fourth ventricle by the two foramina of Luschka and the foramen of Magendie. The four ventricles are filled with cerebrospinal fluid, which is secreted by choroid plexuses, that are located in the walls and roofs of the ventricles. The CSF follows a cycle of constant production and reabsorption. The plexus continues from the roof of the third ventricle into the plexus of the lateral ventricles. The choroid plexuses are found in the lateral ventricles amid the central part and the inferior horn of the ventricles.

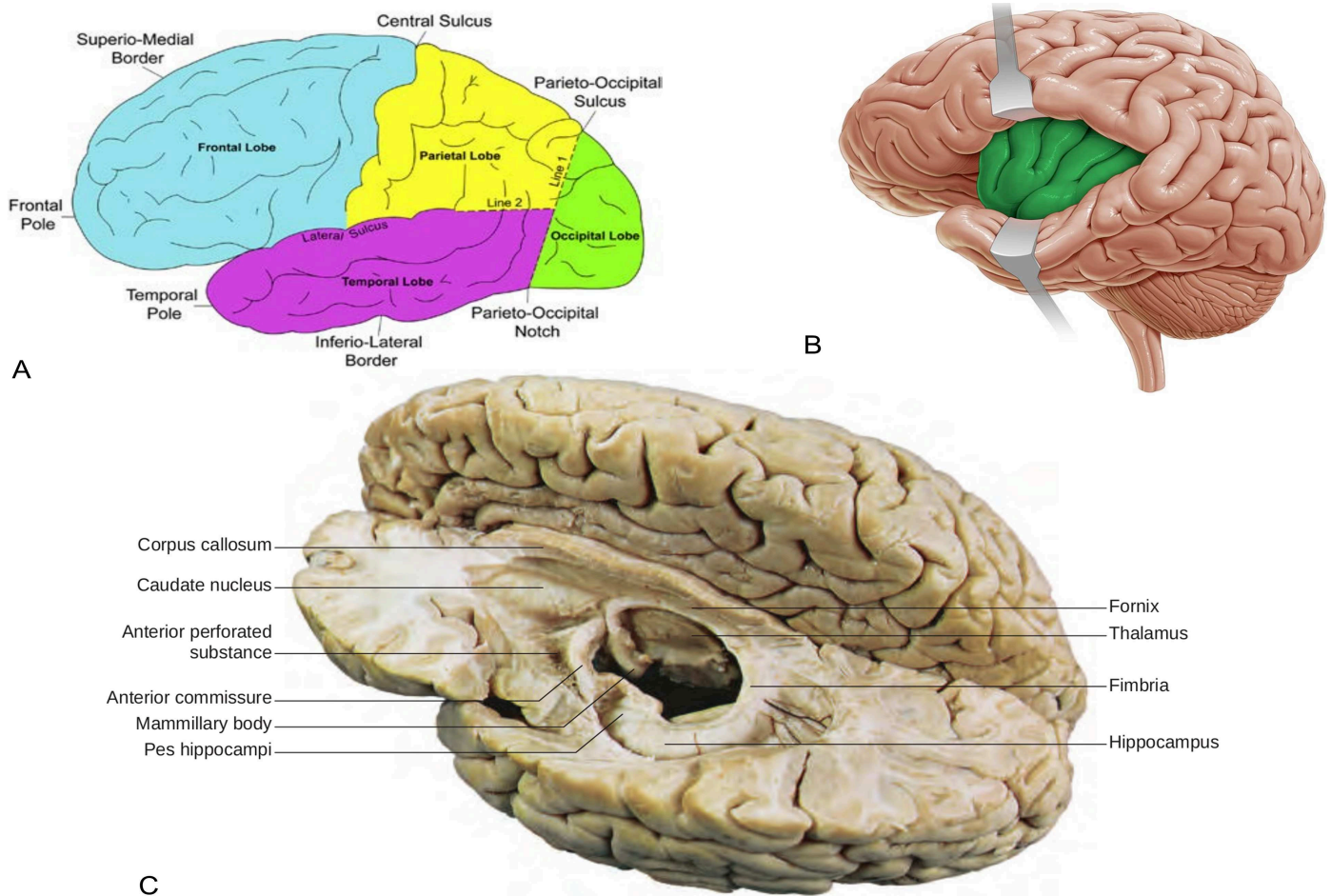


Figure 2.4: Images of the human brain lobes. A) Views from the left hemisphere of the four external lobes in a lateral aspect: frontal, parietal, occipital and temporal lobes. Line 1 = Lateral parietotemporal line; Line 2 = Temporooccipital line (adapted from Prabhakar 2017). B) Lateral view of the insular lobe from the left hemisphere colored in green (source <https://www.kennhub.com>). C) Dissection of the left hemisphere showing components of the limbic system only visible in the medial view (adapted from Standring 2015).

## 2.1.5 Brain vascular system

The brain vascular system presents a specific three-level organization to assure an optimal metabolism for nutriment and oxygen supplies. The system is schematized in Figure 2.6.

The first level are blood supply paths consisting of two of the greater vessels in the neck: the paired internal carotid (in front) and vertebral arteries (behind). The internal carotid arteries go through the skull by the petrosal bone in the carotid canal and loop through the cavernous sinuses. The vertebral arteries get through the skull by the foramen magnum. After their passage through the *dura mater*, the arteries go within connective tissue derived from the *pia mater* and *arachnoid mater*. They unite into the basilar artery at the ventral aspect of the medulla oblongata.

The second level is an anastomosis system between the vertebro-basilar arteries, which supply the brainstem and the cerebellum, and the carotid arteries, via the circle of Willis. Its terminal branches lead to the cerebral arteries.

The third level is therefore the cerebral arteries which have two different trajectories. The basal trajectory is horizontal to the base of the brain and creates perforating branches. These arteries vascularize the deep brain structures, the white

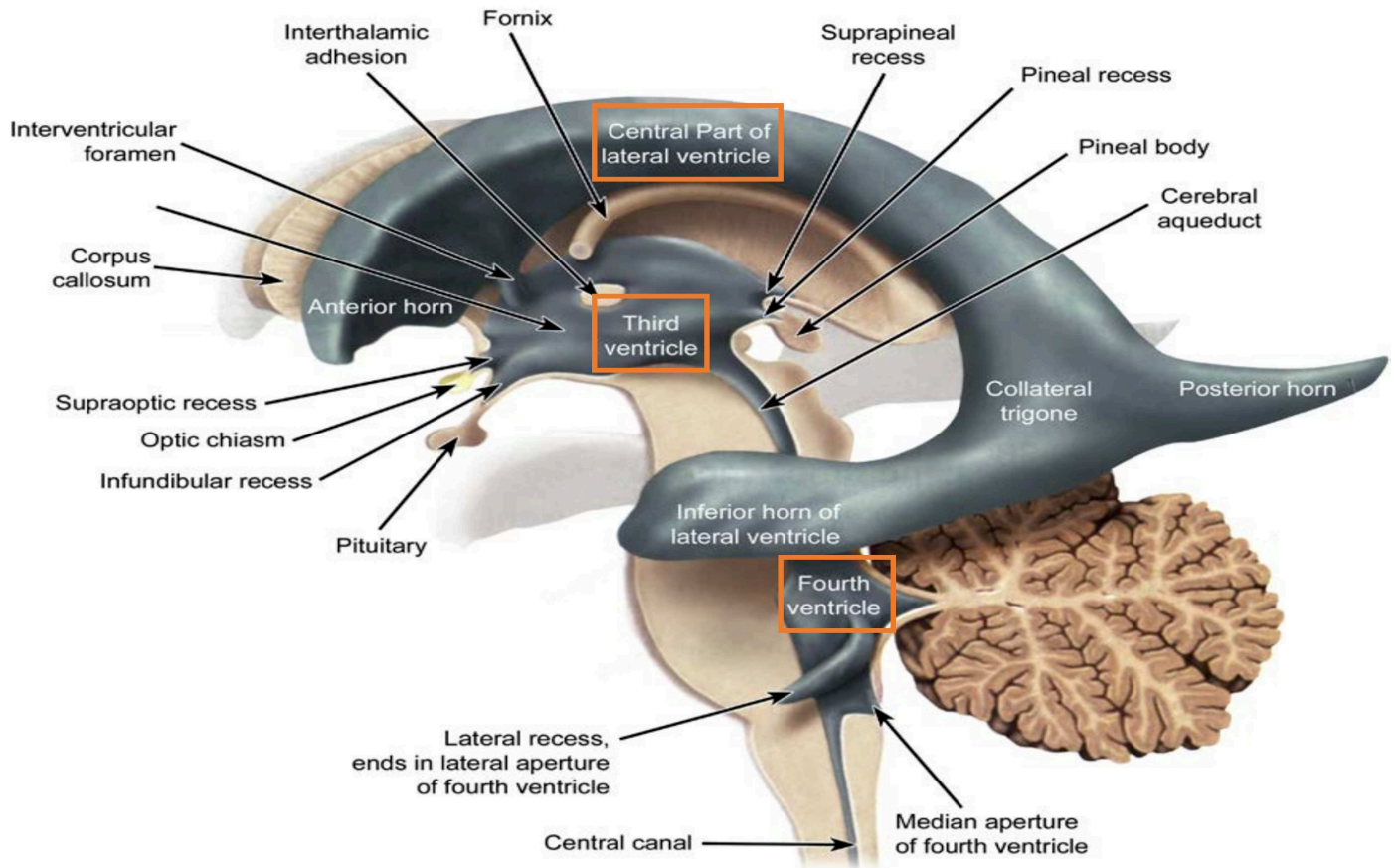


Figure 2.5: Images of the four ventricles in the human brain from the left lateral view, highlighted by the orange rectangles. Adapted from Prabhakar 2017.

matter and the nuclei, without any means of supplying. Cerebral arteries from the peripheral trajectory are in contrary anastomosed with each other. That way, the brain is partially preserved in case of a drop in the cerebral blood flow. Now that the macroscopic anatomy of the brain is presented, the two major types of brain tissues are depicted in the following sections, starting with the gray matter.

## 2.2 Gray matter

In the early twentieth century, Korbinian Brodmann subdivided the human cerebral cortex into 52 numbered areas based on histological observations of diverse mammalian brains where 44 areas actually exist in humans. He captured regional differences in the distribution, density, shape, and size of neural cell bodies also known as cytoarchitecture [Brodmann 1909]. The cerebral cortex is mainly composed of the gray matter which is made of neuronal cell bodies. The gray matter can be found in many regions of the central nervous system.



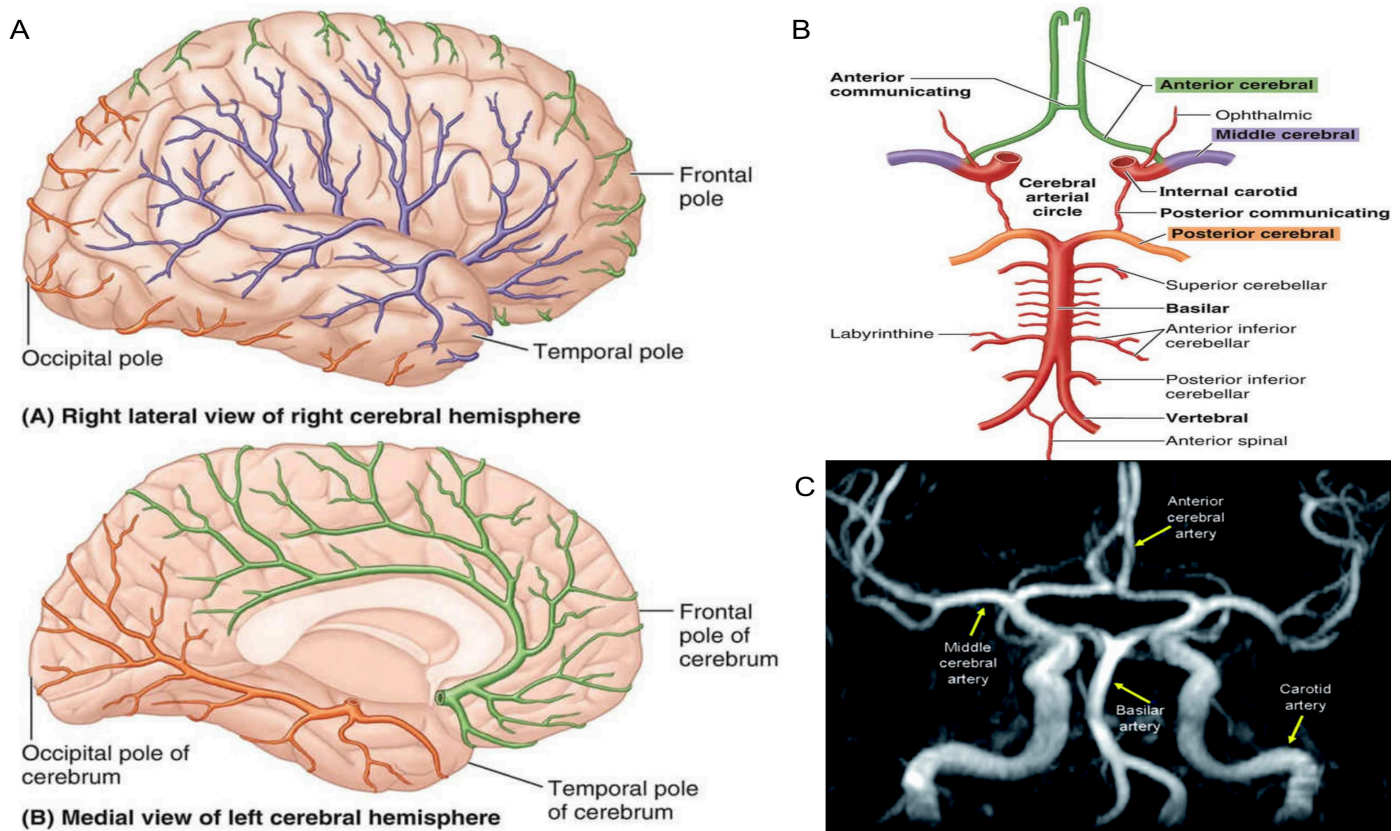


Figure 2.6: Schematic visualization of the brain vascular system including the circle of Willis. A) Color-coded arterial blood supply of the human cerebrum where: green = anterior cerebral arteries; purple = middle cerebral arteries; orange = posterior cerebral arteries. B) Inferior view of the cerebral arterial circle. Images A and B adapted from Moore et al. 2018. C) Angiogram of the circle of Willis (source <https://step1.medbullets.com>).

## 2.2.1 In the cerebellum and the brainstem

The cerebellum, meaning “little brain”, is placed in the posterior cranial fossa, at the back of the brainstem. It corresponds to 10% of the total brain volume and has over half of the total number of neurons in the central nervous system. The cerebellum has an outer mantle of three-layered gray matter, the cerebellar cortex, that uniformly covers an internal white matter where the four pairs of deep cerebellar nuclei are embedded. The cerebellar cortex is composed of an innermost monolayer of Purkinje cells, a layer of granule cells, and an outermost superficial cell-poor molecular layer. The different cortical cell types are discussed in Section 3.3.2.

The brainstem is connected to the cerebellum by three pairs of cerebellar peduncles. It contains as gray matter the nuclei of ten out of twelve pairs of cranial nerves that are distributed in the midbrain (III and IV), the pons (V-VIII), and the medulla oblongata (IX-XII). The reticular formation, the neuronal core of the brainstem, consists of a network of loosely packed multipolar neurons where other nuclei are embedded such as the substantia nigra or the red nucleus. Figure 2.7 describes the major structures in the cerebellum and the brainstem.

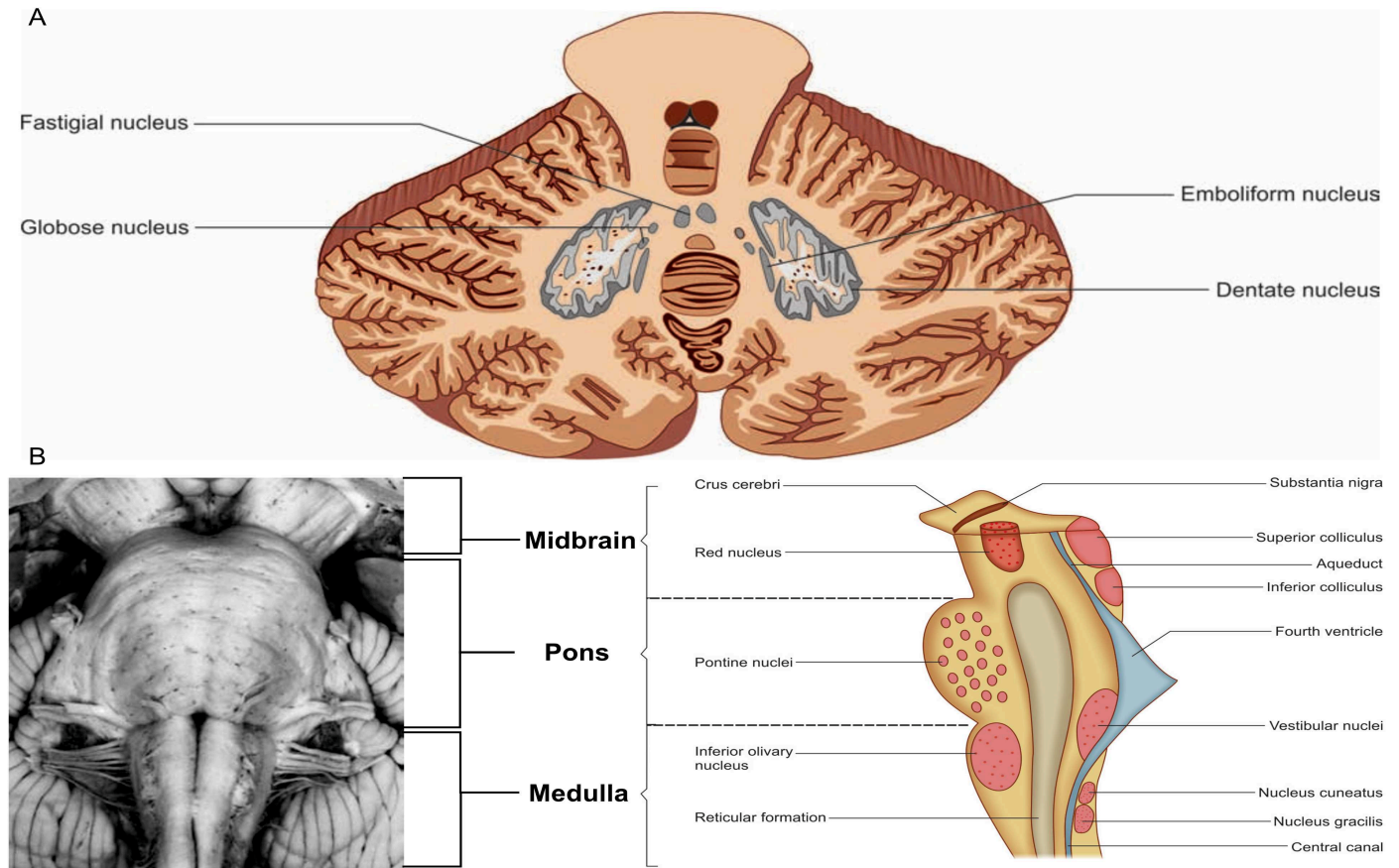


Figure 2.7: Illustrations of the cerebellar nuclei and the brainstem. A) Scheme of the cerebellum showing its numerous transversely curved fissures between narrow folds (folia), and the four pairs of deep nuclei: the dentate, fastigial, globose and emboliform nuclei (adapted from Bhuiyan et al. 2017). B) Ventral view of a human brainstem combined with a scheme of its median section (adapted from Naidich et al. 2009; Bhuiyan et al. 2017).

## 2.2.2 The diencephalon

The diencephalon is gray matter between the cerebrum and the brainstem, and encloses the third ventricle. The diencephalon can be divided into four longitudinal areas: the epithalamus, subthalamus, thalamus and hypothalamus. The epithalamus includes the habenular nuclei and their connections and the pineal gland. The subthalamus is between the thalamus and substantia nigra of the mesencephalon. The thalamus is made of numerous nuclei that correspond to the major part of the diencephalon (80%). The thalamus recognizes sensory stimuli and is the relay station for all output to the cerebral cortex coming from the cerebellum and basal ganglia. Finally, the hypothalamus is located below the cerebral cortex at the base of the diencephalon. It is the central regulation of homeostasis, since emotional, autonomic and endocrine dysfunctions are related to lesions in the hypothalamus.

## 2.2.3 In the cerebrum

In the cerebrum, the gray matter can be in the superficial layer of the brain, the cerebral cortex, or in deep structures called basal ganglia. The cerebral cortex is detailed in Chapter 3.

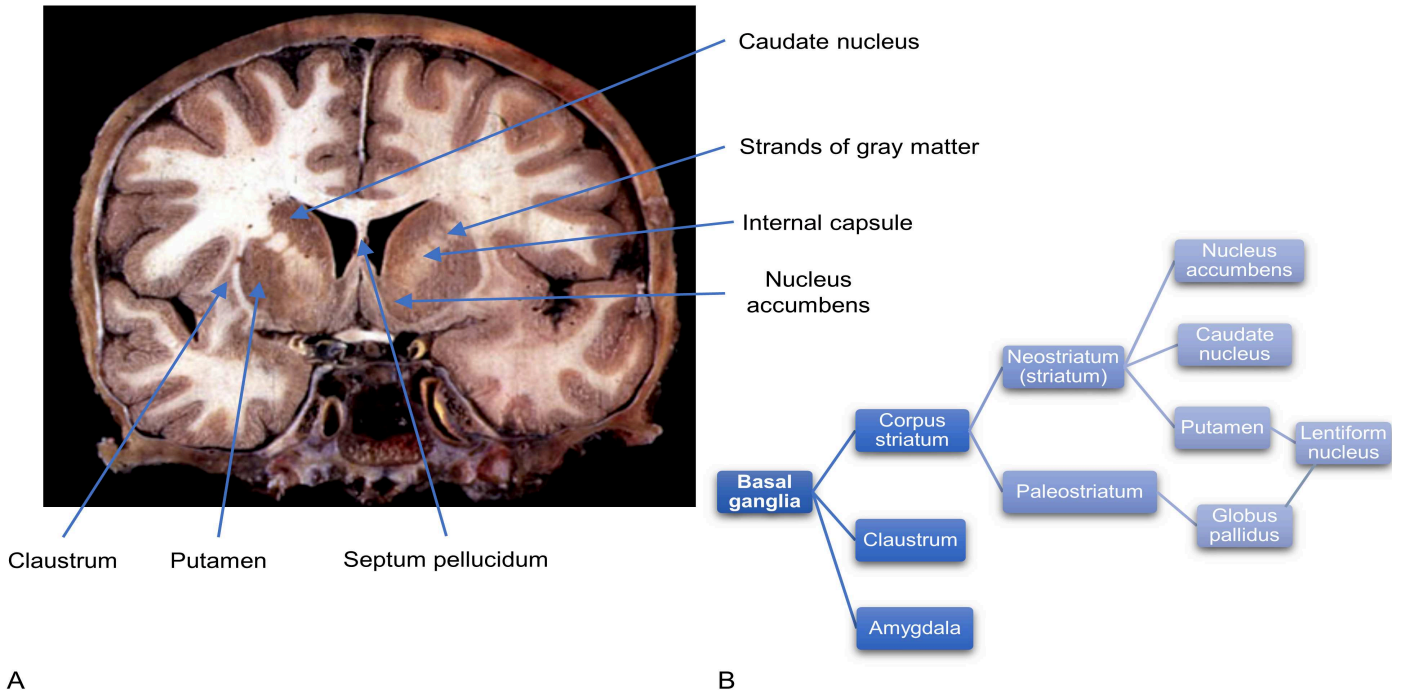


Figure 2.8: Images of the basal ganglia and the relationships between the structures forming them. A) Image of the basal ganglia (adapted from <http://www.chups.jussieu.fr/ext/neuranat>). B) Hierarchical scheme of the relationships between the structures composing the basal ganglia.

The basal ganglia is a set of deep nuclei that include the amygdala, the claustrum, and the corpus striatum which is itself a subset of three nuclei: the caudate nucleus, the nucleus accumbens and the lentiform nucleus that has an external part (the putamen) and an internal part (the globus pallidus). On a functional standpoint, the striatum is associated to the subthalamic nucleus located in the diencephalon and the substantia nigra located in the brainstem. The basal ganglia are represented in Figure 2.8.

The basal ganglia are responsible for programming, integration and termination of motor activity. They interact with the limbic system and with the frontal cortex. Basal ganglia pathologies such as Huntington's and Parkinson's diseases exhibit emotional and cognitive disturbances.

## 2.3 White matter

The white matter fills the space between the cerebral cortex, the subcortical nuclei and the ventricles. It states for about 40% of the CNS tissue. It is composed of unmyelinated and myelinated axons as well as glial cells. Most of the axons are surrounded by a lipid-rich myelin sheath that colors in white the white matter tracts. The axons usually lie parallel to one another, going either all in one direction or distinct populations may traverse the tract in opposite directions.

White matter fibers are divided into three types: projection, association and commissural fibers. The three types of fibers are described in this section.

### 2.3.1 Projection fibers

Projection fibers connect the cerebral cortex to internal structures (brainstem, cerebellum and deep nuclei), as well as the spinal cord. After decussation, these projections can be either ipsilateral or contralateral. Efferent projections mainly define motor tracts while the afferent projections mainly correspond to sensory tracts. All efferent and afferent projection fibers, conveying impulses from and to the cerebral cortex, converge toward the brainstem and constitute the corona radiata. The latter comes out of the internal capsule to the cortices of the frontal, occipital and parietal lobes.

The internal capsule is a compact band of white matter with a sharp 'knee-bend' or genu shape around the apex of the lentiform nucleus, that enters the cerebral peduncle in the upper brainstem, continues in the corticospinal tracts, and ends at the pyramid in the lower brainstem. The principal ascending and descending projection fibers are portrayed in Figure 2.9.

### 2.3.2 Association fibers

Association fibers connect different cortical regions within the same hemisphere. They can be sorted into short and long groups that are schematized in Figure 2.9. Short association fibers, also known as arcuate fibers or U-fibers, join adjacent gyri and have a transverse course to the long axis of the sulci. Long association fibers link distinct lobes in each hemisphere. Fasciculus, meaning "little bundle," is the kind of name given to some of these tracts that are important to language and speech.

Among long association fibers, important named bundles include:

- The uncinate fasciculus links the uncus, hippocampal gyrus, and amygdala in the rostral portion of the temporal lobe. It extends into the orbitofrontal cortex and prefrontal cortex. The connected areas are important for object, sound and memory recognition, as well as emotion, inhibition and self-regulation.
- The cingulum interconnects the cingulum gyrus to the parahippocampal gyrus in the temporal lobe.
- The arcuate fasciculus gathers the posterior temporal lobe to the motor association cortex in the frontal lobe. It is involved in language understanding and production.
- The superior longitudinal fasciculus (SLF) is nestled in the core of the hemisphere and joins frontal, parietal, and occipital cortices. It has three distinct parts: SLF I, II and III.
- The inferior longitudinal fasciculus connects the temporal lobe to the occipital one. It seems involved in object recognition as well as memory and visual discrimination.
- The external capsule runs between the putamen and the claustrum.
- The extreme capsule has bidirectional communication between the claustrum and the insular cortex, as well as the inferior frontal gyrus and the middle-posterior portion of the superior temporal gyrus.

### 2.3.3 Commissures

Hemispheres of the cerebrum are connected by white matter bundles called commissures. There are three types of commissures: the interhemispherical commissures which the four main ones are the anterior commissure, the posterior

commissure, the hippocampal commissure and the corpus callosum; the intrahemispherical commissures that are the associative fiber bundles; the inter and intrahemispherical commissures called the fornix. All types of commissural fibers are represented in Figure 2.9.

The anterior commissure is an arcuate tract connecting the olfactory regions of the cerebral hemispheres. In a later phase of development, fibers originating from the temporal neocortex join this commissure. They are placed near the anterior wall of the third ventricle and in front of the columns of the fornix. The posterior commissure is a pack of fibers gathering the left and right superior colliculus. It is located at the frontier between the mesencephalon and the diencephalon. The hippocampal (or fornical) commissure joins the most rostral part of the Ammon's horns and associated dentate gyri. The corpus callosum is the largest white matter bundle (about 300 millions of fibers) that interconnects reciprocally broad regions of the cortex in all lobes with corresponding regions of the opposite hemisphere. The fornix is a dense white matter bundle linking the hippocampus with the hypothalamus and various other structures. Its fibers form the alveus, a thin white layer on the ventricular surface of Ammon's horn, and then reunite as the fimbria along the medial aspect of the hippocampus.

The previous sections reviewed the macroscopic anatomy and the two tissue types of the human brain, the gray and the white matters. The following section details the microscopic constitution of the human brain. Understanding the cerebral organization at a cellular level is required to accurately analyze the cytoarchitecture of the cerebral cortex.

## 2.4 Microscopic anatomy

Observing the human brain at the microscopic scale reveals the variations in cellular distribution, size and morphology. Major developmental events such as proliferation, migration, differentiation, cell death, and formation of intercellular connections, which reflect an overall central nervous system organization. This section relates the existing cells in the CNS as well as their characteristics.

### 2.4.1 Neurons

Fundamental cellular units of the nerve tissue, neurons (or nerve cells) ensure the processing of information in the brain as electrical signals that are conducted over the cell membranes of neurons and transmitted from neuron to neuron through specific contact points called synapses. Neurons are complex, excitable, secretory and highly polarized cells that do not encounter cell division. A neuron size is very variable (from 4 to 130 $\mu$ m) likewise its shape that can be spherical, ovoid or polyhedral, which are both closely related to the functions it subserves. More than 100 billion neurons in the human brain create neuronal networks of processed environmental information (up to 15000 information per neuron) and eventually translate them into meaningful behaviors.

There are, on the one hand, a unique and constant process called the axon, and on the other hand inconstant protoplasmic processes at a variable number called the dendrites. Its cytoplasm is identical to the one of the cell body. The main elements constituting the neuron are schematized in Figure 2.10 and described as follows:

- The soma, also called the neural cell body or perikaryon, is the metabolic center of 45 to 100 $\mu$ m of diameter. Its nucleus contains the genetic materials (DNA, RNA) which control the cell functioning via proteins coming from a specific RNA. It is also the part of the nervous cell that includes a plasma membrane, a cytoplasm and

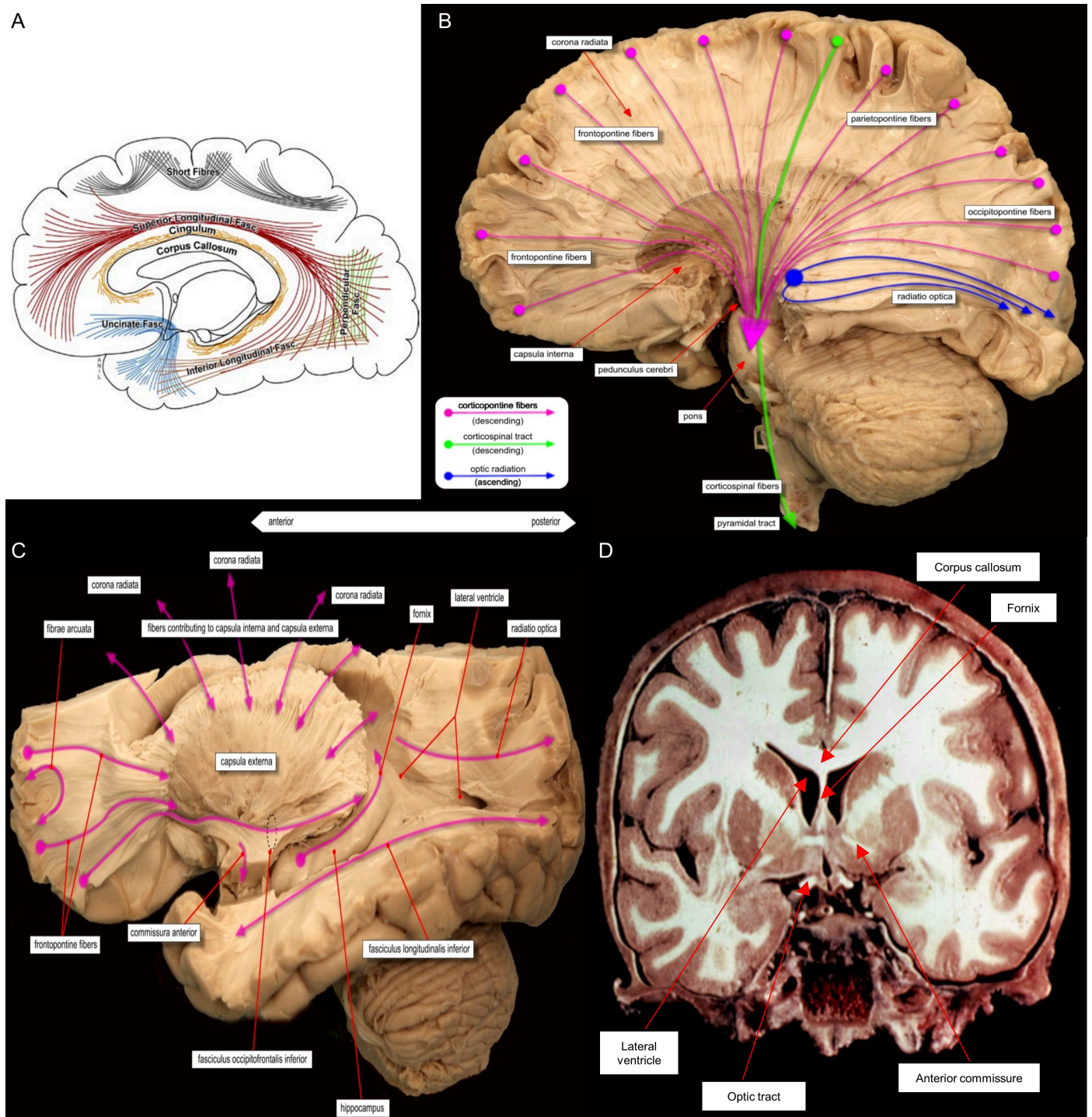


Figure 2.9: Schemes of the association, projection and commissural fibers of the white matter. A) Major association fibers in the cerebrum where each color refers to a different fiber bundle. Fasc = fasciculus. B) Ascending (or efferent) and descending (or afferent) tracts of the projection fibers observed in a sagittal slice of the human brain. C) Association fibers in a sagittal section showing the short ones (arcuate fibers) and the long ones. D) Coronal section of the human brain depicting the main commissural fibers. Images adapted from <http://www.anatomie-amsterdam.nl>, <http://www.chups.jussieu.fr/ext/neuranat> and Prabhakar 2017.

a nucleus. Inside the cytoplasm, there are Nissl bodies (granulations of chromophile substance), lipidic foamy grains, chondriochonts, a Golgi's apparatus and neurofibrils.

- The dendrites are fine tree-like arborizations around the cell body receiving information emitted by other neurons. They occupy a large surface area of a neuron, are about 2µm in length, five to seven in number, and they project directly from the soma and branch extensively. They receive many signals from other neurons and contain specialized proteins that receive, process, and transfer these signals to the cell body. Dendrites connect with the axons in the form of axodendritic synapses, which form an important mode of communication between neurons since about 75% of the dendritic membrane participate in synaptic transmission.
- The axon is the neuronal conductive unit of a large length range (a few millimeters to about a meter) [Braitenberg et al. 1998]. It conveys signals from one nerve cell to another nerve cell or to a muscle or gland. It also brings to its termination molecules created by the soma. The abusive term “nerve fiber” is used to designate the axon wrapped in a myelin sheath or not and in a Schwann sheath. The axon has its own surrounding cell membrane called the axolemma which is responsible for maintaining the membrane potential of the neuron, and it contains ion channels through which ions can flow rapidly.
- The myelin sheath is the coating surrounding axons in a spiral fashion. It acts to insulate the fibers and promotes efficient electrical conduction by reducing capacitance of the axolemma and allowing saltatory conduction through Ranvier nodes [Stämpfli 1954; Hodgkin 1964]. The myelin sheath is composed of lipids in a double slip and separated by protein layers. In unmyelinated axons, impulse conduction is propagated by local circuits of ion current that flows into the active region of the axolemma, through the axon, and out through adjacent sections of the membrane.
- The synapses are connection points between nerve cells, through which excitation is conveyed from one to the other. The secretory product of neurons called neurotransmitter is only released in synapses. The synaptic secretion is localized and directed on cell regions to which the neuron is connected. The synaptic secretion is thus different from hormonal and exocrine cells which respectively release their products into the general circulation (endocrine secretion) or the external environment (exocrine secretion).

## 2.4.2 Neuroglia

Neuroglia (or glia) gathers the other cell population that can be found in the white matter, besides the neurons. It can be divided into two broad classes, macroglia and microglia. Its cells represent the most numerous cell family in the CNS with five to ten glial cells per neuron. Glial cells retain their ability to divide. They provide metabolic and structural support for neurons, and maintain conditions that allow adequate functioning of neurons. They are less electrically excitable than neurons and do not form chemical synapses. Based upon their appearance, function, and origin, there are four types of glial cells that have been identified in the CNS: astrocytes, oligodendrocytes, ependymal cells, and microglia [Conn 2016]. The different types of non-neuronal cell in the CNS and their structural organization and interrelationships with each other and with neurons are represented in Figure 2.11.

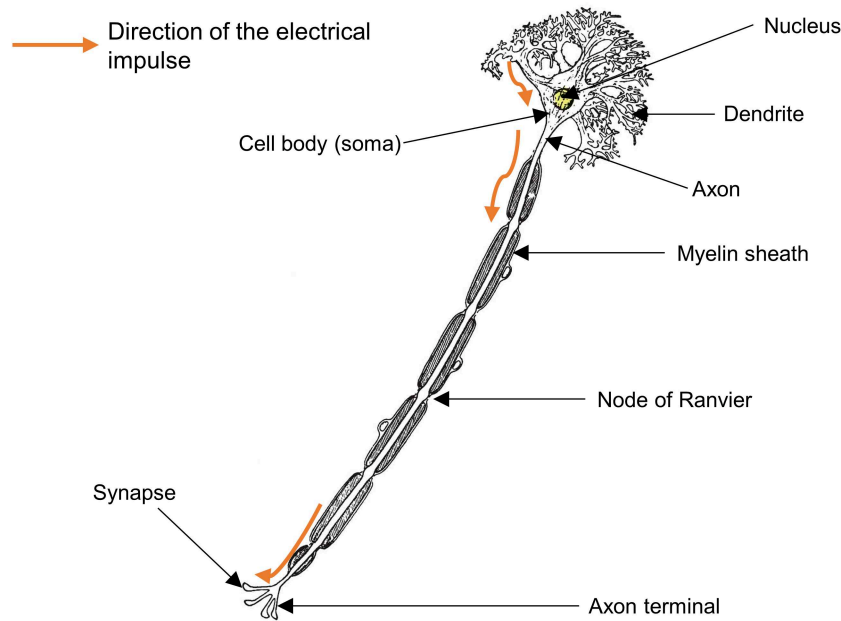


Figure 2.10: Drawing of a neuronal cell showing its major parts. There are the soma that is present in the gray matter, the dendrites surrounding the soma, the axon wrapped in a myelin sheath segmented by Ranvier nodes, then the synapses located at the axon terminals (adapted from [www.ninds.nih.gov](http://www.ninds.nih.gov)).

### 2.4.2.1 Macroglia

Macroglia is one of the two subpopulations of the glia existing in the white matter along with the neurons. There are three types of cell populations constituting the macroglia in the central nervous system that all arise from the ectoderm, the astrocytes, the oligodendrocytes and the ependymal cells.

**Astrocytes** play numerous support parts including maintaining the blood–brain barrier, adjusting extracellular ion concentration and providing structural and trophic support for neurons and oligodendrocytes. They regulate the formation, maturation, maintenance, and stability of synapses by secreting various vital molecules for synaptogenesis. They also have processes known as perivascular end feet that join to the capillary blood vessels.

**Oligodendrocytes** produce the myelin sheath. These relatively small glial cells have several processes that can flatten into sheet-like structures and wrap many times around portions of individual axons. Each oligodendrocyte can form several myelin sheaths covering different segments of a single axon, or they can provide myelin to several segments of different axons.

**Ependymal cells** line the ventricular system and the central canal in the spinal cord to form a mere cuboidal epithelium. They are instrumental in the homeostasis in the brain, especially for the CSF and the retinal extracellular space.



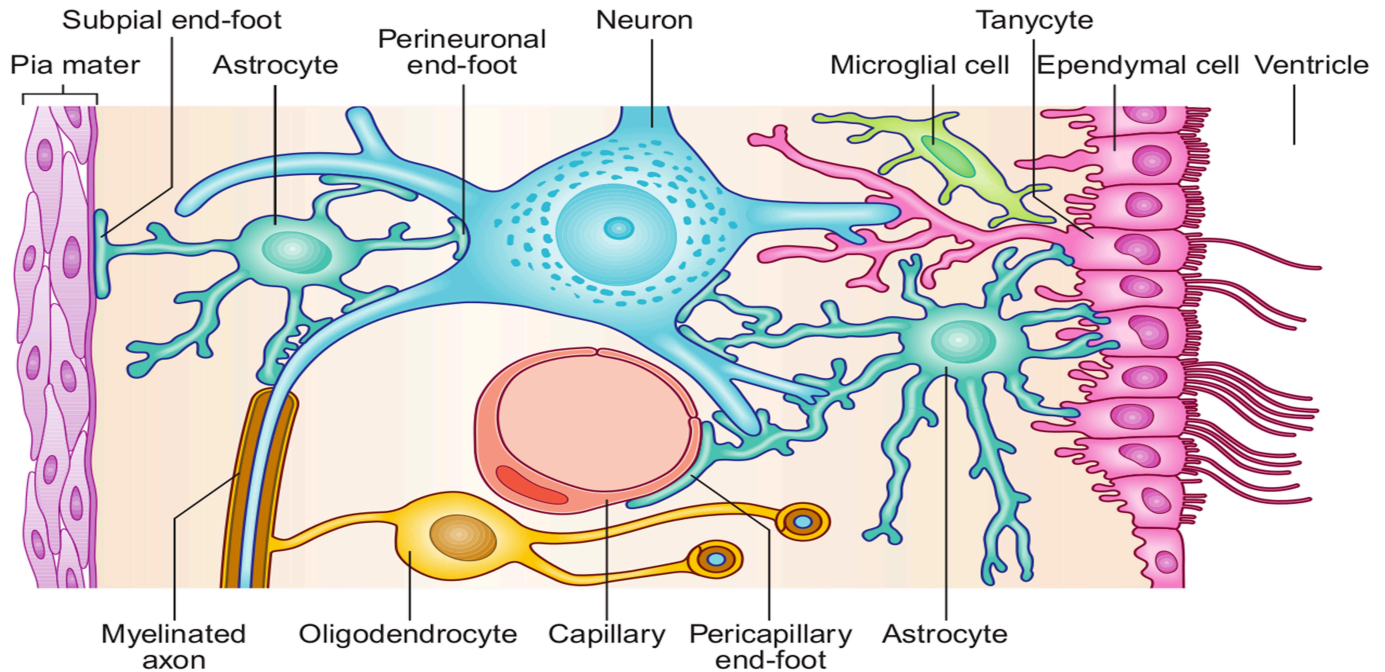


Figure 2.11: *Schematic visualization of the glia located in the central nervous system. Image adapted from Standing 2015.*

#### 2.4.2.2 Microglia

Microglia is the other one of the two subpopulations of the neuroglia. It corresponds to the immune cells of the CNS and are of mesodermal origin. As such, they are embryologically unrelated to the other cell types of the nervous system. They are macrophages within the CNS microenvironment. Microglia are highly dynamic cells that interact with neurons and non-neuronal cells, patrol the brain parenchyma via processes, and play a crucial role in the brain as regulators of synaptic function and adult neurogenesis.

## 2.5 Conclusion

This first background chapter reviews the essential aspects of the human brain anatomy, on the macroscopic and microscopic scales. From this global standpoint, the complexity of the human brain organization can be appreciated which offers an insight of the human cerebral cortex, the main interest of this thesis. Based on the knowledge given in this introductory chapter, the next one will develop the organization of the human cerebral cortex, according to its cellular, myelinated and vascular components.

# Chapter 3

## Human cerebral cortex

This chapter explores the constitution of the human cerebral cortex. The general aspect of the cerebral cortex is presented at diverse observation scales as well as its various layers and cells. The cellular, myelinated and vascular environments are likewise defined. Then, the pathologies related to the cerebral cortex are covered according to the type of disorders they are responsible for.

### 3.1 Global description

The cerebral cortex has been introduced in Chapter 2 as the superficial layer of the human brain mostly corresponding to gray matter and directly located under the *pia mater*, the innermost meningeal layer. This first section gives an overall description of the human cerebral cortex.

#### 3.1.1 Definition and embryogenesis

The cerebral cortex is a continuous zone of gray matter, 1.5mm to 4.5mm thick, with an overall average of approximately 2.5mm. It occupies the entire surface of the cerebral gyri (about 2500 cm<sup>2</sup>) and stands for 40% of the whole brain tissue. Interestingly, the distribution of the thickness is not uniform by layer, nor is the variation in the thickness of the cortical layers proportional to the variation in the total thickness [Fischl et al. 2000].

The human cerebrum derives from the prosencephalon that is composed of the telencephalon as well as the diencephalon. On a neurodevelopmental evolutionary basis, the telencephalic cortex can be divided into the archipallium, the paleopallium, and the neopallium, as shown in Figure 3.1:

- The archipallium (ancient cortex) and the paleopallium (primal cortex) make up the rhinencephalon, meaning the “small brain”. On an anatomical and functional standpoint, the rhinencephalon consists of an olfactory portion (paleopallium) and the limbic system (archipallium). The archipallium and paleopallium become respectively the archicortex and the paleocortex which compose the allocortex. The inner side of the allocortex is made of gray matter and its outer side is composed of white matter.

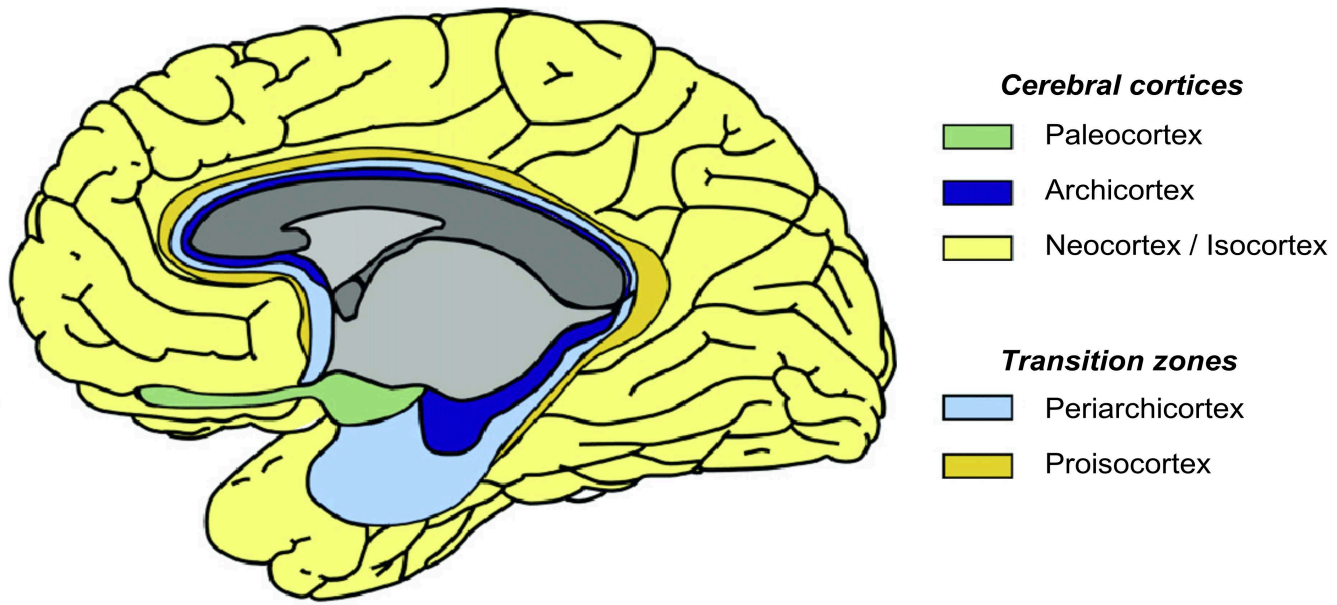


Figure 3.1: *Illustration of the phylogenetic types of the human cerebral cortex: the archicortex (archipallium), the paleocortex (paleopallium) and the neocortex/isocortex (neopallium). The proisocortex and the periarchicortex are parts of the transition zone from neocortex to allocortex called the mesocortex. Image adapted from Zilles 2004.*

- The neopallium (new cortex) has its territory entirely covered by the neocortex, also known as the isocortex. White matter is found on the inner side of the neocortex, and gray matter on the outer side. The neocortex accounts for over 90% of the cerebral cortex. A homotypical neocortex and a heterotypical neocortex are distinguished.

### 3.1.2 Cortex gyri and sulci

The surfaces of the cerebral hemispheres are highly folded and present a series of gyri delineated by sulci. Both are extensions of the meningeal subarachnoid space. When the sulci are deep and anatomically constant, they are called fissures. The cerebrum fits inside the skull thanks to the gyri. Without the latter, the cortical layers of the cerebrum would be one-third smaller and unable to process information as efficiently as they do. The spatial setting of the major gyri and sulci organizes the hemispherical division into frontal, parietal, occipital, temporal, insular and limbic lobes as portrayed in Figure 3.2. The main sulci are one to three centimeters depth, interrupted or continuous, and their walls nest transverse gyri connected to one another. Figure 3.2 illustrates the medial surface of the cerebral left hemisphere showing gyri and sulci.

Different types of sulci can be distinguished. Some separate two functionally distinct areas, such as the central sulcus that separates the frontal lobe from the parietal lobe. Others have one type of functional area on the surface and a concealed other one in its depth. For example, the posterior part of the calcarine sulcus is located in the primary visual area in its depth and in the secondary visual area on the surface. There are also sulci deep enough to produce an elevation on the ventricular wall, which does the collateral sulcus with the floor of the inferior horn of lateral ventricle.

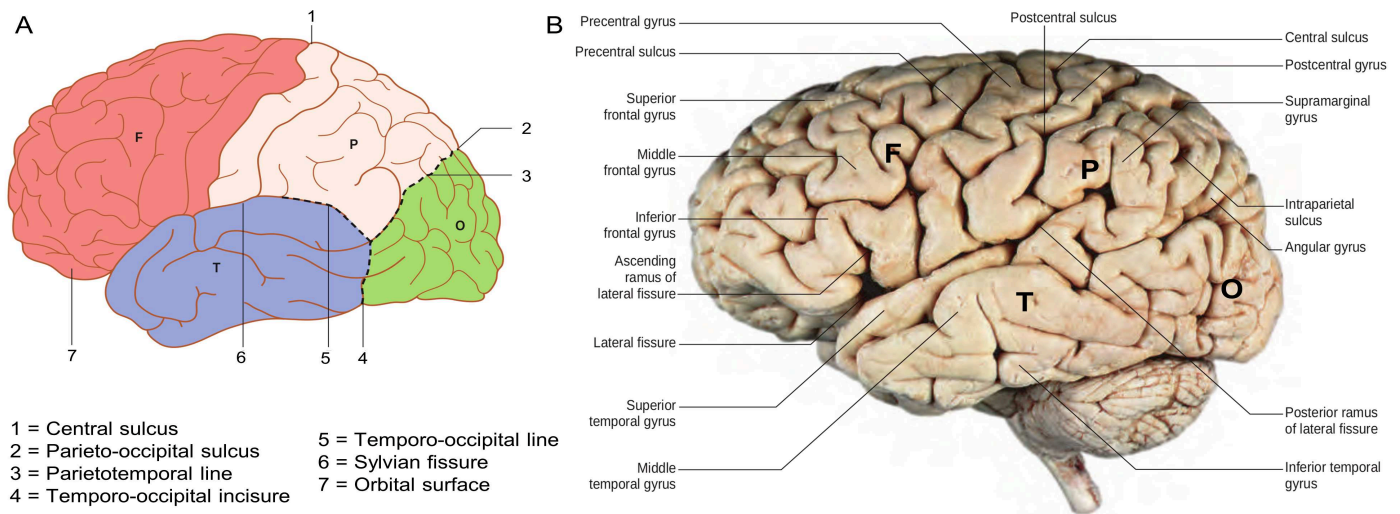


Figure 3.2: Schemes of the main lobes (A) gyri and sulci (B) of the cerebral left hemisphere. The limbic and insular lobes are not visible on the lateral face of the brain. F = frontal lobe; P = parietal lobe; T = temporal lobe; O = occipital lobe. Images adapted from Standing 2015.

### 3.1.3 Microstructure of the cerebral cortex

The microscopic structure of the cerebral cortex is an intricate arrangement of neuronal cells, fibers, neuroglia and blood vessels. The neurons are of various sizes and shapes. They establish elaborated connections with each other and with axons reaching the cortex from other masses of gray matter. The most noticeable microscopic feature of a thin section of the cerebral cortex stained to highlight cell bodies myelinated axons is its horizontal lamination. The structure of the cerebral cortex shows considerable variation from region to region, both in terms of thickness and the prominence of the laminae (layers of neuronal cell bodies) that vary from three layers to six layers according to the observed cortex. From this global description, an insight of the different cortices composing the human cerebral cortex is proposed in the next section.

## 3.2 The cerebral cortices

The cerebral cortex can be seen as two distinct cortices, the allocortex subdivided into the archicortex and the paleocortex, as well as the neocortex, as presented in Figure 3.1. Clear characteristics distinguish the neocortex from the allocortex. The neocortex has a single sheet of gray matter and covers the majority of the cerebral cortex, while the allocortex only covers the boundaries of the cerebral cortex. Furthermore, the conscious thoughts and actions are dictated by the neocortex, whilst the motivations, affective behaviors, and emotions are rooted in the allocortex. The transition zone between the allocortex and the neocortex is called the mesocortex [Schüz et al. 2002; Zilles, Palomero-Gallagher, and Amunts 2015]. The mesocortex includes major limbic regions involved in memory and emotion: the cingulate cortex, the entorhinal cortex, the parahippocampal gyrus, the orbitofrontal cortex, the insula and the temporal pole. The entire hierarchical organization of the cortex is schematized in Figure 3.3. Each subdivision of the human cerebral cortex is detailed in this section.

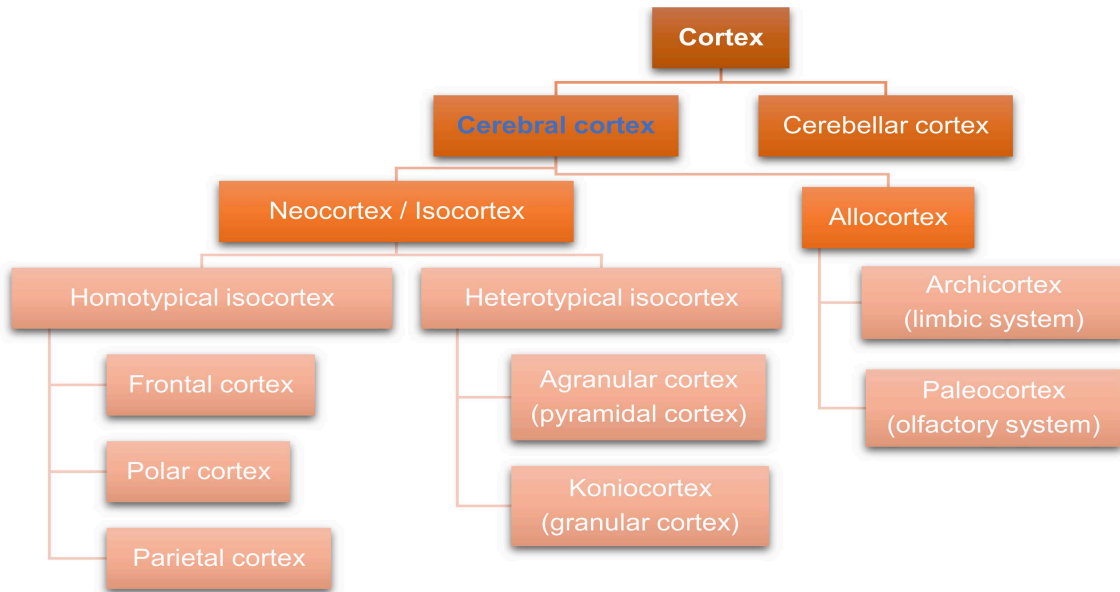


Figure 3.3: *Hierarchical graph of the cortices composing the human cortex.*

### 3.2.1 The allocortex

The allocortex consists of the archicortex and paleocortex that comprises the primary olfactory cortex and the hippocampus. It is composed of three to six layers of neurons and lies deep in the temporal lobe where olfactory input reaches the cortex. This part of the brain bark is characterized by its primitive and elementary structure.

The allocortex mainly comprises the cortical region that borders on the corpus callosum, the entire upper wall of the hippocampal gyrus with the dentate gyrus, the complete distended anterior part of the hippocampal gyrus, the uncus, lastly, the adjacent structures of the lateral olfactory gyrus at the base of the brain, the olfactory triangle, and the medial olfactory gyrus. In these various regions, the allocortex presents structural differences, sufficiently discernible to allow a delimitation into various areas based on their cellular organizations. A division into areas is more difficult at the level of the cortical margin, as the structure keeps changing there, with fields gradually attenuating and finally disappearing. But in the other regions of the allocortex, the cellular organization depicts more precise boundaries than in the neocortex [Economo and Triarhou 2009].

#### 3.2.1.1 The archicortex

The archicortex is the region of the cerebral bark that is phylogenetically the oldest, located at the dorsal part of the inner side of the hemispheres and corresponding to the olfactory system. Most of it is represented in the mankind by two primary areas: the dentate gyrus and the hippocampus. It consists of three laminae: a molecular surface layer, a receiving layer, and an effective layer.

### 3.2.1.2 The paleocortex

The paleocortex is a thin, primitive cortical region corresponding to the olfactory cortex, that consists of three to five cortical laminae. It is located in the parahippocampal gyrus, olfactory bulb, accessory olfactory bulb, olfactory tubercle, piriform cortex, periamygdalar area, anterior olfactory nucleus, anterior perforated substance, and prepyriform area. It does not develop through the cortical plate and constitutes less than 1% of the cerebral cortex's surface area.

## 3.2.2 The neocortex or isocortex

The neocortex covers the entire field of neopallium and is phylogenetically the most recent and the most elaborated cortex. It stands for 90% of the cerebral cortex, has up to 28 billions of neurons and glial cells, as well as  $10^{12}$  synapses that connect the neurons with each other and the other cerebral cells. This territory of the brain bark allows to individualize six functionally specialized structural layers represented in Figure 3.4. These are from the surface to the depth:

- The molecular or plexiform layer, *lamina molecularis / zonalis* (layer I).
- The external granular layer, *lamina granularis externa* (layer II).
- The external pyramidal layer, *lamina pyramidalis externa* (layer III).
- The internal granular layer, *lamina granularis interna* (layer IV).
- The internal pyramidal (ganglionic) layer, *lamina pyramidalis interna* (layer V).
- The multiform or fusiform layer, *lamina multiformi* (layer VI).

We can distinguish on the one hand the heterotypical isocortex at the level of which some structural layers (granular or pyramidal layers) take a preponderant development, which allows to differentiate the koniocortex (or granular cortex) from the agranular pyramidal isocortex. On the other hand, there is the homotypical isocortex with its three different types: the frontal, the parietal and the polar types [Economo and Triarhou 2009].

### 3.2.2.1 The heterotypical neocortex

The heterotypical isocortex corresponds to the projection zones. The agranular isocortex is a heterotypical isocortex for which the pyramidal layers predominate over all the others. The agranular pyramidal type, comprising large cells, and as a matter of fact robust pyramidal and spindle cells, and lacking granule cells. It corresponds to the place of origin of the cortifuge fibers or motor functions, but it is doubtful whether the same happens with the same structural type in other areas.

The koniocortex, also called granular cortex, exhibits small and numerous cells in all its layers with a predominant number of cells in layers II and IV compared to the others. The koniocortex predominates in primary sensory cortices. In layer V, there is an exogenous dense matrix of fibers, which may be considered as the cortical termination of sensory fibers. Moreover, the overall thickness is smaller than the adjacent areas, because the koniocortex is mainly found on the walls of gyri, where the thickness diminishes as illustrated in Figure 3.5.

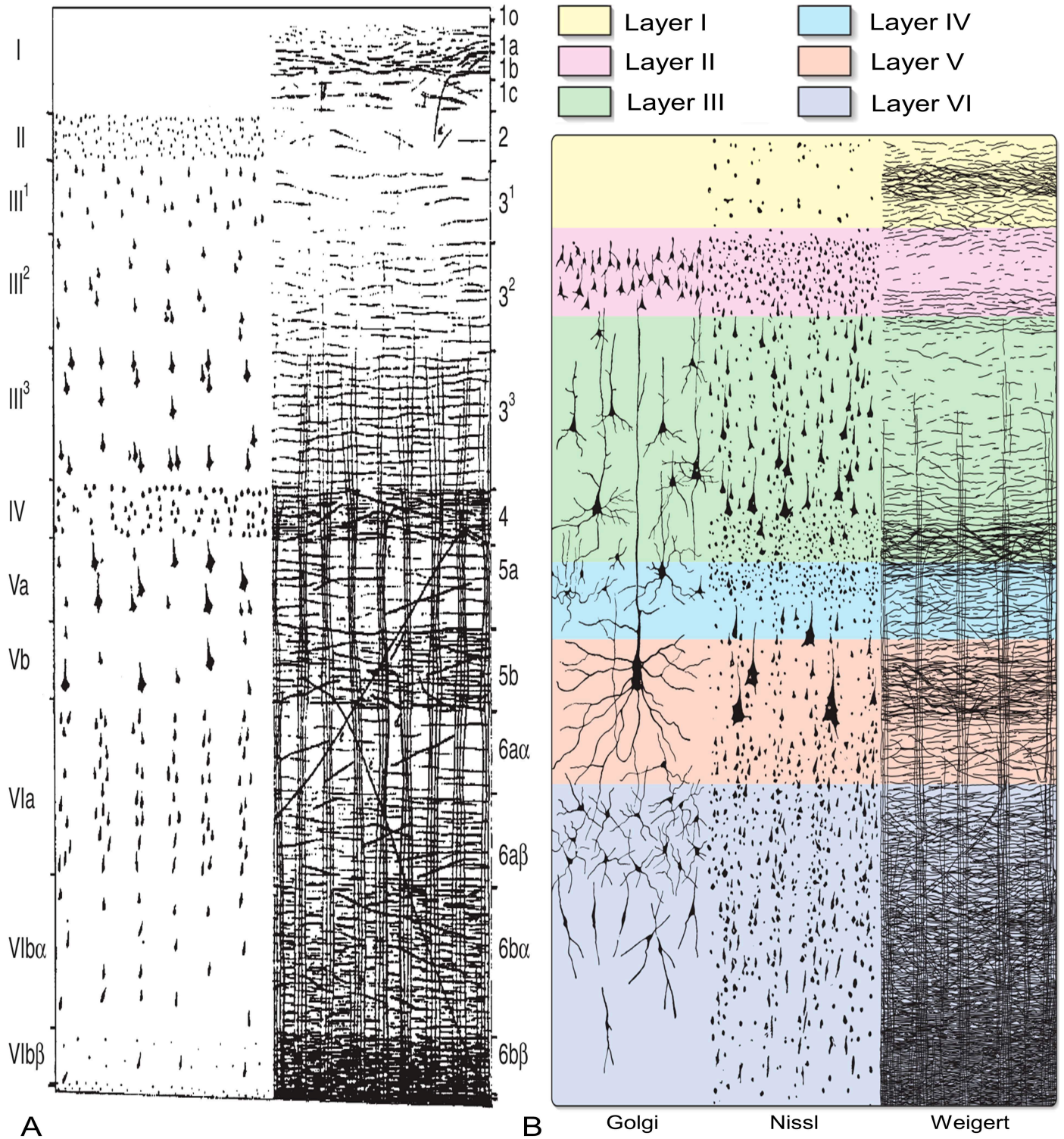


Figure 3.4: Representations of the laminar organization of the human cerebral cortex. A) Schematic drawing of a piece of association cortex: cytoarchitectonics (on the left, Roman numbers) and myeloarchitectonics (on the right, Arabic numbers). Image adapted from Vogt et al. 1919. B) Scheme of the layers of the cerebral cortex where the three vertical columns represent the disposition of cellular elements, as revealed by the staining techniques of Golgi (impregnating whole neurons), Nissl (staining perikarya) and Weigert (staining axons). Image adapted from Standring 2015.

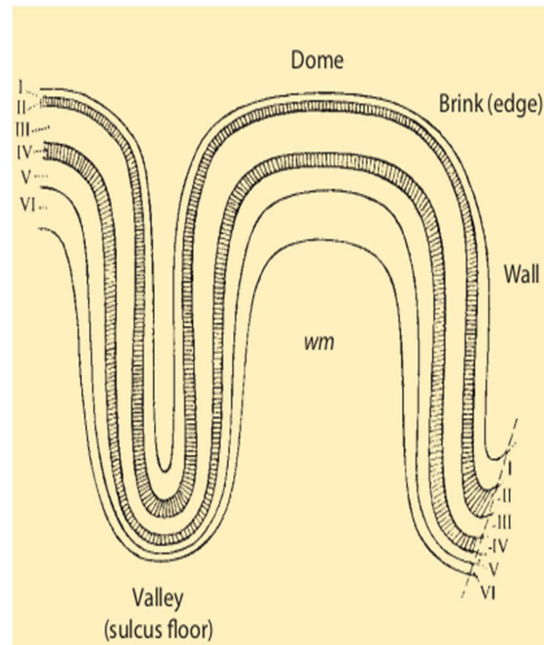


Figure 3.5: *Illustration of the cortical thickness variations at the dome, brink, wall, and valley of a gyrus. The Roman numbers refers to the numbering of the cellular cortical layers in the isocortex. wm = white matter. Image adapted from Economo and Triarhou 2009.*

### 3.2.2.2 The homotypical neocortex

The opposite homotypical isocortex is an isocortex at the level of which the six structural layers are distributed in harmonious proportions. It matches the areas of association of the cerebral cortex. It can be subdivided into three types [Economo and Triarhou 2009]).

**The frontal type** consists of large numbers of small and medium-sized pyramidal cells and the granular layers are less prominent. It is equally present in the middle frontal lobe, and in the upper parietal lobe.

**The parietal type** has the granular layers II and IV much more distinctly developed than the other layers. It contains more of the stellate cells than the other cell types that are much smaller. It is highly extended in the lower parietal, anterior occipital, and temporal lobes, which correspond to areas where lesions disturb sensory perception.

**The polar type** is the thinnest of the three types and composed of numerous granule cells. It is usually identified with small regions near the frontal and occipital lobes. Layer III is reduced in thickness and layer VI is better organized than for the other types.

This review of the cerebral cortices, which is summarized in Figure 3.3, evinces the variety of nomenclatures used to organize the cortex. It introduces the next section that explores the microstructure of the cerebral cortex to understand its laminar organizations as well as the cortical connections established by the cortical cells within.



## 3.3 Cortex histology

The development of staining techniques, from the early eighteenth century to the middle twentieth century, enabled to analyze histologically cell bodies and myelinated axons located in the cerebral cortex. These microscopic observations shed light on the laminar organizations of the human cerebral cortex which are defined in this section.

### 3.3.1 Cortical layers

The main focus on the cortex laminar organization is placed on the neocortex. There are six layers that are commonly present all over the isocortex and some are existing in exclusive cortical areas.

#### 3.3.1.1 The cortex laminar structure

The neocortex has a double organization according to the direction we observe it. Vertically, it is organized into different types of cells bounded by their synapses [Mountcastle 1957; Mountcastle 1997]. Horizontally, it is divided into six laminae going from the pial surface to ependymal cavity [Palomero-Gallagher and Zilles 2017], as shown in Figure 3.4.

**The molecular layer I** is cell-sparse and rich in glial cells. It mainly contains axons and dendrites such as the terminal ramifications of apical dendrites of pyramidal neurons that lie as a compacted horizontal mass. There is also a few scattered non-pyramidal neurons (Cajal-Retzius and spiny stellate cells). It is rich in glial cells that interconnect cortical areas. In histological sections stained to show myelin, layer I appears as a narrow horizontal band of fibers.

**The external granular layer II** contains a varying density of small, densely packed pyramidal cells and interneurons. The apical dendrites of the pyramids reach layer I and their axons extended into layer Vb. It receives input from other isocortical regions. Myelin fiber stains show mainly vertically arranged processes crossing the layer.

**The external pyramidal layer III** contains small and medium-sized pyramidal cells in layers IIIa-b as well as larger ones in layer IIIc together with scattered non-pyramidal neurons. It is the main source for cortico-cortical connections. The prevailing pyramidal neurons increase in size from superficial to deep layers. Myelin stains reveal a mostly vertical organization of fibers.

**The internal granular layer IV** contains densely packed, small, spiny and aspiny stellate and pyramidal cells. The dendrites and axon collaterals extend up to layer I. It receives multiple intra-hemispheric cortico-cortical afferents. Its axons go down to the thalamus. Within the lamina, in myelin-stained sections, a prominent band of horizontal fibers (the outer band of Baillarger) is visible.

**The internal pyramidal layer V** contains the largest pyramidal cells and can be sorted into layers Va and Vb according to the size and packing density of the neurons they contain. It projects into many subcortical regions including basal ganglia, thalamus, pons and brainstem nuclei. Scattered non-pyramidal cells are also present. In myelin stains, the lamina is traversed by ascending and descending vertical fibers, and also contains a prominent central band of horizontal fibers (the inner band of Baillarger).

**The multiform layer VI** consists of neurons with various shapes, small to medium in size. It can be divided into layer VIa which is densely populated and layer VIb that has low neuronal density. It is connected with the thalamus and sends efferent fibers to the other cortical areas. It blends gradually with the underlying white matter, and a clear demarcation of its deeper boundary is not always possible.

The mature human neocortex exhibits an internal functional organization called the minicolumns in Mountcastle 1997. It is defined as a narrow chain of neurons going vertically across layers II to VI and orthogonal to the pial surface. The term "column" refers to the observation that all cells encountered by a microelectrode penetrating and passing perpendicularly through the cortex respond to a single peripheral stimulus, a phenomenon identified in the somatosensory cortex. One minicolumn gathers from 80 to 100 neurons. A column, that has a diameter of 300-600 $\mu\text{m}$ , is composed of minicolumns and bounded by cell-autonomous and histogenetic influences. These columns are capable of memorizing relations and performing more complex operations than a single neuron. They have a supragranular part that projects to the other columns while receiving reciprocal connections from them, as well as an infragranular part that receives inputs from the supragranular portions of the adjacent columns and sends outputs to the thalamus.

### 3.3.1.2 Specific cortical layers

Some cortical layers received a proper name due to the cortical area they are attached to and the features linked to myelination they present. Here are three noticeable stripes usually referred in the literature and pictured in Figure 3.6:

**Gennari stripe** [Gennari 1782], is a band of myelinated fibers running parallel to the surface of the occipital lobe at the primary visual area V1 (Brodmann area 17). The stripe is about mid-thickness of the cortical gray matter, corresponding to the particularly well-developed outer line of Baillarger of that cortical area, and composed largely of tangentially disposed intracortical association fibers. Its presence, visible to the naked eye, is at the origin of the name of the striate cortex to designate the primary visual cortex.

**Baillarger stripes** [Baillarger 1840], are plexuses of horizontal myelinated fibers (striae) located in the internal granular layer (inner line) and the internal pyramidal layer (outer line) of the isocortex. They are between 100 and 300 $\mu\text{m}$  thick and appear in myelin-stained sections cut perpendicularly to the surface.

**Exner stripe** [Vogt et al. 1919], refers to the molecular layer I myelinated stripe. Its thickness is remarkably uniform across the entire cortical surface and much smaller than the Baillarger bands.

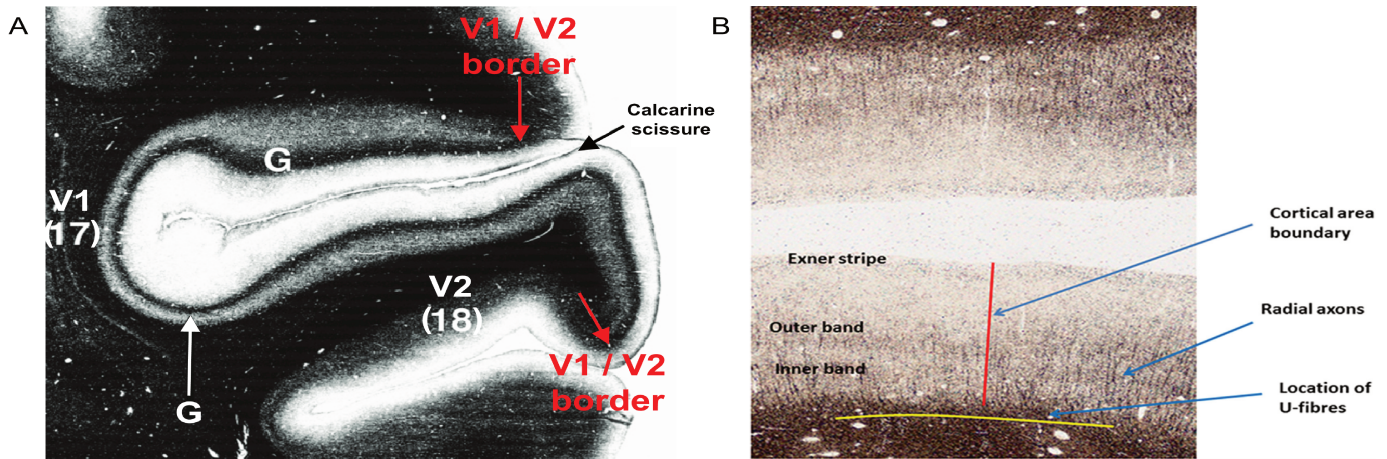


Figure 3.6: *Histological images of the Gennari (A), Baillarger and Exner (B) stripes. (A) The Gennari line (G on the image) appears here on a myelin-stained section of the visual cortex. V1 / (17) = primary visual area (Brodmann area 17); V2 / (18) = secondary visual area (Brodmann area 18) (adapted from Zilles 2004). (B) The histological section from the parietal cortex reveals the Exner stripe as well as the Baillarger inner and outer bands using Gallyas staining (adapted from Turner 2019).*

### 3.3.2 Cortical cell types

The cerebral cortex consists of billions of neurons. The latter are variations of three main morphological shapes: the pyramidal cells, the fusiform (or spindle-shaped) cells, and the granular (or stellate) cells. There are other types of cells existing in the cerebral cortex that are a modification of one of those three major shapes. All types of cells existing in the cerebral cortex are schematized in Figure 3.9 and detailed as follows:

#### 3.3.2.1 The pyramidal cells

They gather between 70 and 90% of the cellular component of the cerebral cortex and they are the principal output neurons of the cerebral cortex. They are referred to as (P) cells in Figure 3.9. Their sizes can vary from small (12/10 $\mu$ m) to gigantic (50–100/25–60 $\mu$ m), with a triangular shape being elongated in the vertical direction (see Figure 3.7). They emit a long dendrite from their upper pole, which reaches as far up as the molecular layer I. They are prominent in the layers III and V and are distinguished by their prominent apical dendrites and basal dendritic trees. Dendrites issued from the base of the cell body are oriented laterally and downwards. They stop within the immediate cortical vicinity at a short distance from the perikaryon. The axon comes also from the base of the soma, and usually invades the white matter of the gyrus. Hence, pyramidal cells make both short-range and long-range connections, forming almost all cortico-cortical connections as well as most subcortical connections. Moreover, pyramidal cells also release the excitatory neurotransmitter glutamate.

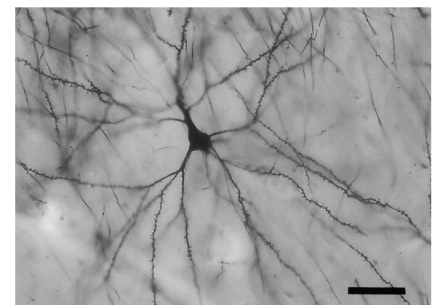


Figure 3.7: *Photomicrograph of a supragranular pyramidal cell. Scale bar = 50 $\mu$ m (adapted from Schüz et al. 2002).*

### 3.3.2.2 The fusiform cells

They are found in the multiform layer VI, directly lying on the white matter of gyri. They are referred to as (F) cells in Figure 3.9. The fusiform cells are characterized by their long axes arranged orthogonally to the cortical surface, while the axon can be commissural, association or projection oriented, with a higher possibility to project to the thalamus. Their sizes vary between 30/15 and 15/10 $\mu\text{m}$ , with an ovoid, vesicular and centrally placed nucleus.

### 3.3.2.3 The granular cells

They are round (see Figure 3.8) or polygonal, often triangular cells, with a very scanty cytoplasm since the nucleus occupies most of the cell. They are referred to as (S) cells in Figure 3.9. Their sizes vary from 4/4 $\mu\text{m}$  to 8/10 $\mu\text{m}$  (height-to-width ratio). They mainly populate layers II and IV. Dendrites are only visible with Cajal's silver impregnation to evince very short often bushy processes that project in all directions within the cortex, resembling to a star. The stellate cells are located all over the cortex, except for the molecular layer. Their processes modulate the activity of other cortical neurons. Based on whether their dendrites have dendritic spines, they are referred to as spiny cells or aspiny cells. Dendrites of spiny cells are mostly placed within layer IV where they release glutamate to excite interneurons, whilst aspiny cells secrete an inhibitory neurotransmitter.

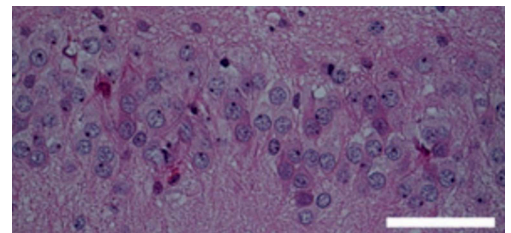


Figure 3.8: *Optical coherence tomography (OCT) image of granular cells in the hippocampus. Scale bar = 80 $\mu\text{m}$  (adapted from Assayag et al. 2013).*

### 3.3.2.4 Specific cortical cells

Cortical cell types present variations for some specific areas of the cerebral cortex. Some major non-pyramidal intrinsic cells are presented as follows.

**Basket cells** are neurons with mainly horizontally dispersed axons. They are referred to as (B) cells in Figure 3.9. They also possess a short, vertical axon, which rapidly divides into horizontal collaterals, which end in large terminal sprays synapsing with the cell bodies and proximal dendrites of pyramidal cells.

**Horizontal cells (of Cajal-Retzius)** are scarce and only visible in the molecular layer I. They are referred to as (H) cells in Figure 3.9. They are composed of a single pair of axon and dendrite that spreads within the layer I. Their long axons stretch over long distances parallel to the surface of the layer, where they also split into terminal branches. These cells are at the origin of the automation of the gastrointestinal smooth fibers. Gastrointestinal stromal tumors derive from Cajal-Retzius cells.

**Martinotti cells** have an ascending axon that is either short if the cells are in the middle layers of the cerebral cortex or long if their location is the deepest layers. They are referred to as (M) cells in Figure 3.9. The dendrites carry few

spine-like appendages that can be spherically confined around the cell body, or elongated either vertically or horizontally.

**Neurogliaform cells** are small spherical cells, of 10-12 $\mu$ m diameter, and also known as clewed, spiderweb or clutch cells. They are referred to as (N) cells in Figure 3.9. They are majorly located in the granular layers II and IV. They exhibit a spherical dendritic field of about 100-150 $\mu$ m diameter, as well as a slender axon growing from the soma or a proximal dendrite. Finally, they release an inhibitory neurotransmitter.

### 3.3.3 Cortical connections

The cortical connections are all mutual, being either afferent or efferent. The afferent connections made by cortical columns stem from the thalamus, brainstem, and hypothalamus and involve the circulation of neurotransmitters. As for the efferent connections, they usually correspond to the axons of pyramidal cells. Efferent fibers can be associative, originating from the cell bodies of the layers II and III. They can also be commissural, arising in the layers III and IV of a hemisphere and terminate in the corresponding cortical area of the opposite hemisphere. Aside from the radial fibers, there are three types of horizontal pathways previously defined: the Exner stripe, the Baillarger stripes, and the myelinated U-fibers, which lie just outside the cortical gray matter within the surface layer of the white matter [Turner 2019]. Therefore, these connections of the neocortex can be encapsulated as follows [Abeles 1991]:

- Connections between the two hemispheres.
- Connections between specific deep nuclei (mostly in the thalamus) and specific cortical areas.
- Diffuse connections between different areas of the brainstem and widespread areas of the cerebral cortex.
- Connections between cortical areas in one hemisphere, which stand for about 98% of the myelinated axons.

The microstructure of the cerebral cortex exhibits an organized laminar structure where multiple cells are involved to partake in the various connections made within the cortex and with other cerebral areas. The next section will review the advances and discoveries concerning the cellular organization of the cerebral cortex.

## 3.4 Cytoarchitectonics and myeloarchitectonics

Cytoarchitectonics refers to the neuroanatomical subdiscipline designed by the married couple Vogt in 1903, which aimed at the identification and delineation of areas with a different cytoarchitecture. The laminar pattern is recognizable throughout the isocortex while not being homogeneous. Differences in the relative thickness and cell density of the various layers, and in the size, shape and arrangement of the neuronal cell bodies, are present and have been used to divide the cortex into cytoarchitectural areas [Nieuwenhuys, Voogd, et al. 2007]. Myeloarchitectonics, in the same spirit as cytoarchitectonics, corresponds to the neuroanatomical subdiscipline, also devised in Vogt et al. 1903, aiming at the identification and delineation of areas with a different myeloarchitecture. The Vogts' groundwork was developed alongside Brodmann's who was a team-member of their laboratory. Substantial works were conducted before and after Brodmann's map to attempt to unveil cortical cytoarchitectonics and myeloarchitectonics.

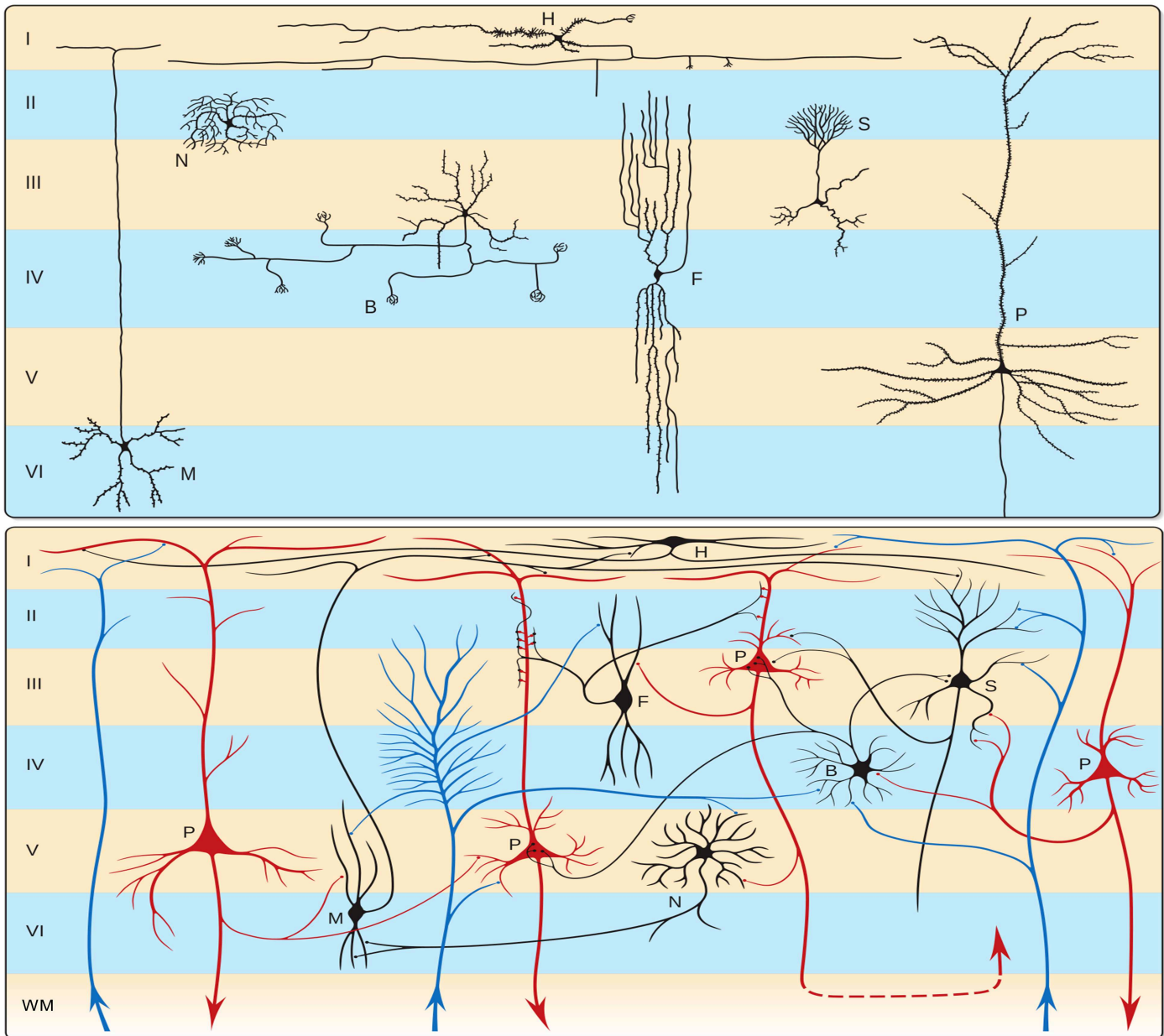


Figure 3.9: Major types of cells seen in the cerebral cortex. (At the top) Characteristic neocortical neurons. From left to right are shown Martinotti (M), neurogliaform (N), basket (B), horizontal (Cajal-Retzius) (H), fusiform (F), stellate (S) and pyramidal (P) types of neurons. (At the bottom) The most frequent types of neocortical neurons, showing typical connections with each other and with afferent fibers. The left and right afferent fibers are association or cortico-cortical connections; the central afferent is a specific sensory fiber. Neurons are shown in their characteristic laminae but many of them have cell bodies in more than one layer. Lines with arrowheads: blue = afferent connections; red = efferent connections; black = intracortical connections. Roman numbers I-VI = cellular neocortical layers; WM = white matter. Images adapted from Standring 2015.

### 3.4.1 Pre-Brodman cytoarchitectonic and myeloarchitectonic maps

Unraveling the functional properties of structural elements in the brain is one of the fundamental goals of neuroscientific research. Groundbreaking discoveries were made as soon as the late eighteenth century. In the early twentieth cen-

Author (discovery date)	Used methods	Cortical lamination	Analyzed species
Meynert (1867)	Histology, microscopy	1. Molecular layer 2. External granular layer 3. Pyramidal layer 4. Internal granular layer 5. Spindle cell layer	Human, ape, monkey, lion, bear, fox, cougar, wild cat, Viverrinae
Bevan Lewis (1878)	Macroscopy, optical microscopy	1. Plexiform layer 2. Small pyramids 3. Great pyramids 4. Inner small pyramids 5. Ganglion cell layer 6. Spindle cell layer	Human, pig, sheep, cat, calf, ocelot, Barbary macaque, rodents
Campbell (1905)	Cytoarchitectonics, myeloarchitectonics, topographical or provisional functional parcellation	1. Plexiform layer 2. Small pyramidal cells 3. Medium pyramidal cells 4. Large pyramidal cells 5. Stellate cells 6. Inner large pyramidal cells 7. Spindle cells	Human, chimpanzee, orangutan, gorilla, dog, cat, pig
Elliot Smith (1907)	Brain sections, magnifying lens	Baillarger stripes, density of intracortical white matter	Human, monotreme, marsupial

Table 3.1: *Timeline of major cytoarchitectonic discoveries made in the pre-Brodman era. Table adapted from Triarhou 2020.*

ture, the holding tenet amidst the neuroanatomist community was to define cortical cell architecture as a preamble to understand the mind. Table 3.1 encapsulates important discoveries regarding the cytoarchitecture of the human brain. During the previous centuries, essential contributions to cortical histology of the neocortex were achieved by:

- Félix Vicq d’Azyr (1748–1794)
- Francesco Gennari (1750–1797)
- Jules Baillarger (1809–1890)
- Theodor Meynert (1833–1892)
- Vladimir A. Betz (1834–1894)
- William Bevan Lewis (1847–1929)
- Santiago Ramón y Cajal (1852–1934)
- Theodor Kaes (1852–1913)
- Christfried Jakob (1866–1956)
- Alfred Walter Campbell (1868–1937)
- Korbinian Brodmann (1868–1918)
- Oskar Vogt (1870–1959)
- Sir Grafton Elliot Smith (1871–1937)
- Cécile Mugnier-Vogt (1875–1962)
- Baron Constantin von Economo (1876–1931)
- Georg N. Koskinas (1885–1975)

Major progress in myeloarchitectonics also occurred in that time frame. In 1782, Gennari first provided evidence of regional cortical differentiation by observing a white stria in the calcarine sulcus located in the primary and secondary visual cortices of frozen human brains. In 1786, Vicq d’Azyr described the same specific white band of myelinated axons in the occipital cortex. The French doctor Baillarger recognized in 1840 six cortical layers and identified the external stria of Gennari as forming the outer part of layer IV in all regions of the cerebral cortex and an internal stria in the layer V. The Vogt couple delivered the valuable groundwork on the laminar organization of the cortical myelinated content, and made detailed conjunctions between myeloarchitecture and cytoarchitecture in human and non-human primates

[Vogt et al. 1903; Vogt et al. 1919].

Campbell [Campbell 1905], and Elliot Smith [Elliot Smith 1907], were both pioneers who delivered detailed maps of cortical areas. The former presented a parcellation scheme of the most important cortical areas in humans and other mammals, simultaneously considering myeloarchitectonics. The latter rediscovered Baillarger's procedure for examining slices of the cerebral cortex, and he used the differences in the width and distinctness of the stripes of Baillarger for his parcellation scheme. The same year as Elliot Smith, Kaes was focused on myelinated fibers using Weigert method and produced measurements of cortical layer thickness from birth to the age of 97 years old. He separated the cerebral cortex into an 'outer main zone', corresponding to the current layers I–III, and an underlying 'inner main zone', consisting of the layers IV–VI [Triarhou 2020].

### 3.4.2 Brodmann areas and further works

In 1909, Brodmann published a far-reaching cytoarchitectonic map of the human cerebral cortex that he divided into 52 cortical areas, of which 44 are actually present in the human brain, and they belong to 11 regions. Each of the areas is characterized by a specific cytoarchitecture. He assumed that each cortical area was linked to functional purposes within a larger network. For Brodmann, cortical cytoarchitectonic localization could be sorted into three ways: elemental (based on histological elements observed with a microscope), laminar (based on cellular layers) and topographical (according to horizontally organized regions). Images of his original study are visible in Figure 3.10. Updates of his monograph were published up to 1914 to include a comprehensive treaty on the physiology of the human brain. Brodmann indicated through his numbering system similarities between the cortical areas of various mammalian species, based on his integrative concept mixing histology with phylogeny. Hence, cytoarchitecture and topography are considered important arguments in comparative neuroanatomy.

After the creation of Brodmann's map, neuroanatomists have continued to partake in the advancement of cortical architectonics. Therefore, all the predecessors of the tandem, von Economo and Koskinas, formed the basis upon which they produce their magnum opus on the adult human cerebral cortex [Economo and Koskinas 1925]. Both authors listed more cortical areas than Brodmann did. In the 1980's, Brodmann's founding-work got praised again, after years of being a bone of contention. For instance, it inspired the work of Galabruda and Sanides [1980] in the auditory cortex, and also Clarke [1990] in the occipital cortex.

In current neuroimaging studies, Brodmann's still-relevant schematic drawings of cortical maps are frequently used references to register functional activation to anatomical structures, although his map does not match more recent anatomical and functional data in many brain regions, and new approaches are mandatory [Amunts and Zilles 2015]. It is for instance possible to access cortical laminar distribution using multimodal receptor mapping, as it has been demonstrated by the works of Zilles and Amunts [Zilles, Palomero-Gallagher, Grefkes, et al. 2002; Zilles and Amunts 2009; Amunts, Lenzen, et al. 2010]. Recent research is focused on inter-subject variability and registering architectonic datasets in a common brain space, such as the Montreal Neurological Institute (MNI) space, or the Talairach space [Collins et al. 1994]. Developing reproducible and observer-independent descriptions of cortical areas and limits, as well as including structural connectivity, molecular and functional characteristics of the human cerebral cortex are likewise core issues that involve cutting-edge techniques and facilities that go beyond light-microscopical observations of brain's stained sections. A non-exhaustive list includes electron microscopy, immunohistochemistry, immunostaining, CLARITY, magnetic resonance imaging (MRI), polarized light imaging (PLI), optical coherence tomography (OCT) and tractography.

From this review of the cytoarchitectonics and the myeloarchitectonics of the human cerebral cortex, the organization of



the cortical vascular network will be synthesized in the next section to complete the description of the different elements located in the cerebral cortex of mankind.

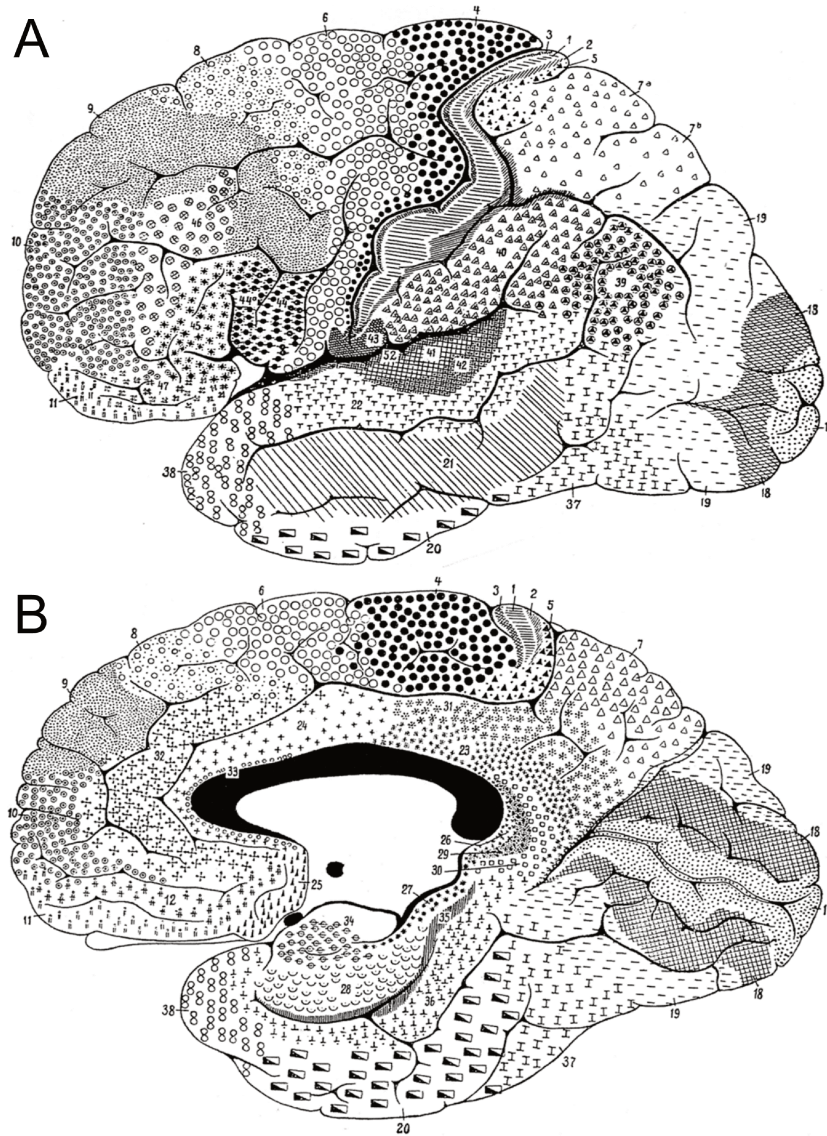


Figure 3.10: Brodmann's original maps (1914) in the lateral (A) and medial (B) views. The numbers refer to the identified Brodmann areas (adapted from Nieuwenhuys and Broere 2020).

### 3.5 Cortical vasculature

The arteries, veins and fine vascular network, which are the three categories responsible for cortical vascularization, can be described distinctly. The typical description of cortical veins and arteries concerns their degree of cortical penetration. In the literature, cortical vessels are generally sorted into three groups: short, intermediate and long.

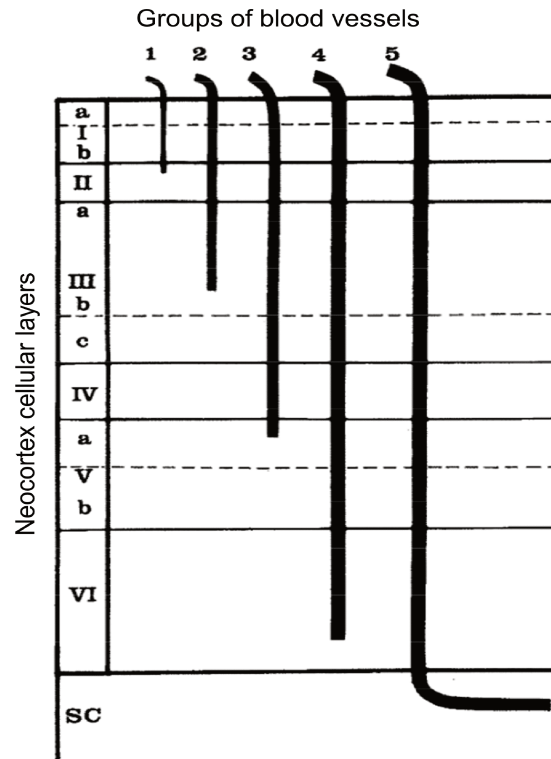


Figure 3.11: Groups of blood vessels of the cortical vascular system penetrating the six-layer neocortex. Arteries and veins are separated here into five groups, without illustrating the sixth group that only concerns arteries. The disposition of cortical cellular layers is shown on the left in Roman numbers from the pial surface inwards. SC = subcortical white matter (adapted from Duvernoy et al. 1981).

### 3.5.1 Cortex vascular network

In Duvernoy et al. 1981, cortical arteries (A) and veins (V) are divided into six groups that are illustrated in Figure 3.11. Each group has its own degree of vascularization ability, that goes from the the outermost layer of the cerebral cortex to the subcortical white matter:

- Vessels of group 1 (A1, V1) reach the layer I (molecular layer) and may extend into the layer II (external granular layer).
- Vessels of group 2 (A2, V2) reach the superficial part of the pyramidal layer (IIIa and IIIb).
- Vessels of group 3 (A3, V3) have the numerical dominance; they reach the middle region of the cerebral cortex which seems to be the most highly vascularized. This region is centered in the internal granular layer (IV) and overlaps the adjacent part of the pyramidal (IIIc) and ganglionic (Va) layers.
- Vessels of group 4 (A4, V4) reach the layer VI (multiform layer) and inner limit of the subcortical white matter.
- Vessels of group 5 (A5, V5) pass through and vascularize the cerebral cortex as well as the adjacent white matter.
- Arteries of special group 6 (A6) are wide, reach the gray matter without branching, and only vascularize the white matter.

### 3.5.2 Intracortical vessels

Duvernoy's observations indicated a laminar organization of the cortical vessels on par with the cells and the myelin content. There are four vascular layers in the cerebral cortex, as depicted in Figure 3.12:

- The first vascular layer is within the molecular layer I and partially overlaps the external granular layer II. The molecular layer is divided into two distinct vascular zones: the superficial zone (Ia), which is a clear band deprived of capillaries and crossed by the arterial and venous trunks; the deep zone (Ib), that comprises the aforementioned first vascular layer. The latter has its vessels mainly parallel to the surface, and with an orientation probably alike to the fibers coming from horizontal cells of Cajal-Retzius.
- The second vascular layer is within the most superficial part of the external pyramidal layer III. It is made of parallel vessels perpendicular to the surface.
- The third vascular layer is located in the middle part of the cerebral cortex, including the deep part of the external pyramidal layer III, the internal granular layer IV, and part of the internal pyramidal layer V. This layer stands for the largest vascular density of the cortex, with vessels oriented in all directions. It also contains particularly dense regions corresponding to bush-like venous branching.
- The fourth vascular layer is present in the deep cellular layers of the cortex, layers V and VI. The vascular network loses density until reaching the underlying white matter. At the top of the gyrus, layers V and VI are highly developed, and vascular layers are less distinct which leads to a structurally uniform vascular network.

The global distribution of the cortical vascular network is represented in Figure 3.13. Nevertheless, variations also occur among cortical areas. For instance, the frontal granular cortex has a homogeneous vascular network, whereas the parietal koniocortex sees its third vascular layer particularly dense. As for the striate cortex, it owns the densest vascular network of the CNS from its internal granular layer IV.

The cerebral cortex is organized in layers of cells, myelin and blood vessels, which are intertwined and specially oriented to serve diverse functions. However, the cortex as any other brain structure, can be dysfunctional and be plagued by pathologies. The following section goes over the different categories of diseases that are related to the cerebral cortex.

## 3.6 Cortex-related diseases

The human cerebral cortex is a complex structure that produces thoughts, emotions and perceptions. During cortical development, occurring at the fetal period of the pregnancy, the apparition of abnormalities may lead to disorders usually caused by aberrant cellular proliferation or migration. Consequently, three types of cortex-related disorders can be listed: neurodegenerative, neurodevelopmental and neuropsychiatric ones.

### 3.6.1 Neurodegenerative disorders

Neurodegenerative disorders are characterized by a progressive cell loss, entailing functional deficit and cognitive decline. Table 3.2 summarizes the pathologies that belong to this category.

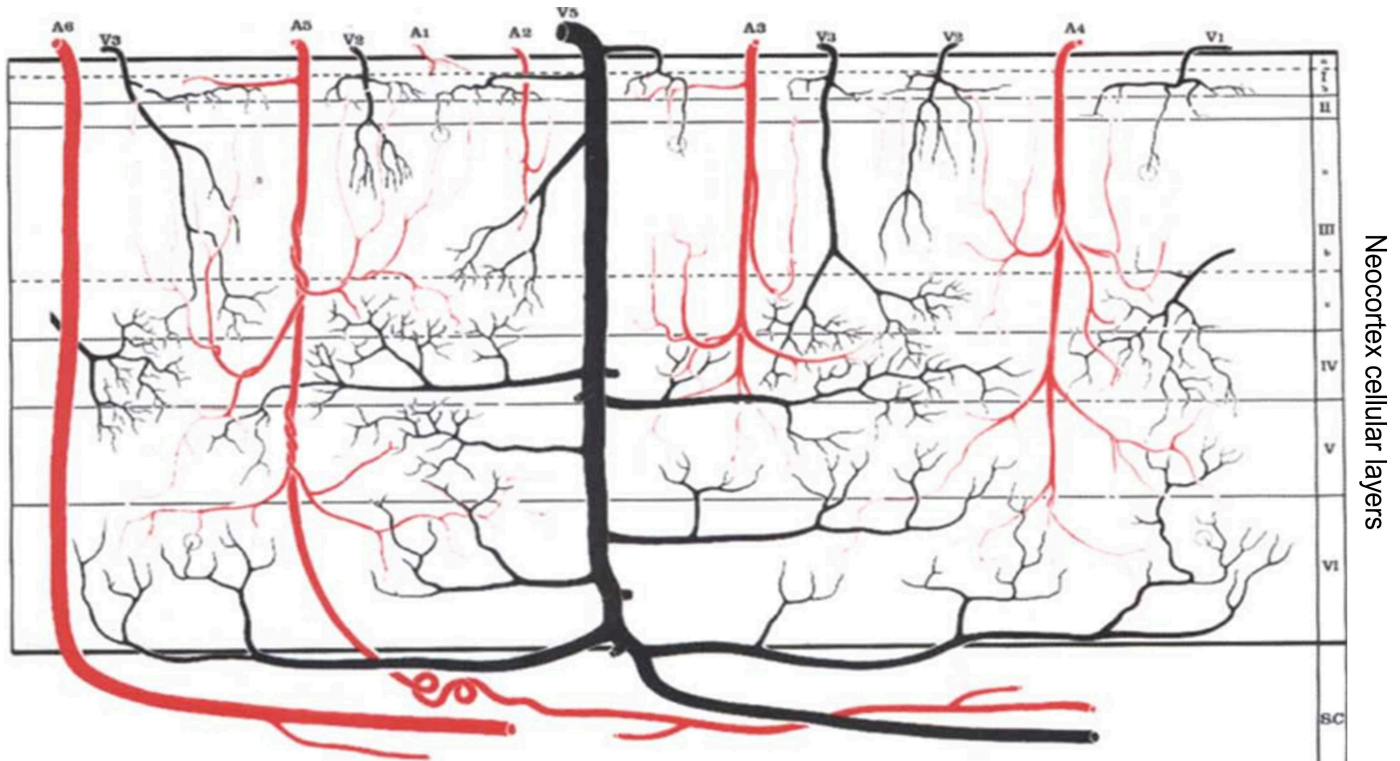


Figure 3.12: Drawing of the morphological features of intracortical arteries and veins. Arteries are divided into 6 groups (A1-A6), and veins into 5 groups (V1-V5). V5 is the main intracortical vein and V4 is not shown on this drawing. The disposition of cortical cellular layers is shown on the right in Roman numbers from the pial surface inwards. SC = subcortical white matter (adapted from Duvernoy et al. 1981).

The most broadly population-spread disorders are Alzheimer's, Parkinson's, Huntington's diseases, as well as corticobasal degeneration, frontotemporal degeneration, and amyotrophic lateral sclerosis (ALS). For all these diseases, the thickness of the cerebral cortex is of great interest since it is subject to changes in gray matter and cortical thinning. One should bear in mind that aging affects the brain at all levels, from molecules, vasculature, morphology to cognition. Most brain structures decline in volume, especially cortical gray matter with the greatest effects appearing on the frontal and prefrontal cortices [Prabhakar et al. 2019].

However, this volume loss is exacerbated for neurodegenerative diseases since the involved circuits are mostly located in the frontal neural circuits. Therefore, there is a necessity to reach submillimeter precision to characterize the location and progression of subtle cortical atrophy [Fischl et al. 2000]. It will enable to detect regional specific cortical atrophy related to the early stages of the previously cited neurodegenerative disorders. Thus, an accurately characterization of the degeneration early stages would offer a better understanding of the causative factors. In Tustison et al. 2019, the Alzheimer's disease sets the example by revealing that the external granular layer II of the entorhinal cortex is one of its earliest affected sites. The more advanced is the Alzheimer's dementia, the greater is the neuronal loss in the entorhinal cortex.

Disorder	Pathology and affected brain regions	Symptoms
Amyotrophic lateral sclerosis (ALS)	Motoneurons decline in the primary motor and premotor cortices (upper motoneurons), as well as in the brainstem and spinal cord (lower motoneurons)	Progressive weakness of voluntary muscles, muscular atrophy, spasticity and swift tendon reflexes. 25 months of life expectancy after symptoms' onset
Alzheimer's disease/dementia	Extracellular amygdaloid protein deposits and intracellular neurofibrillary tangles accumulation in entorhinal, temporo-parietal and frontal cortices. Progressive neuronal loss. Belongs to the tauopathy family alongside corticobasal degeneration, frontotemporal degeneration and Lewy's body dementia	Memory loss, mood disturbances, emotional lability, impulsivity. Progressive cognitive decline
Corticobasal degeneration (CBD)	Neuronal and glial pathological lesions containing abnormally hyper-phosphorylated microtubules associated tau protein. Initially affecting the basal ganglia circuits and the dorsolateral prefrontal cortex with marked neuronal loss and gliosis in layers II and III of the cerebral cortex	Apraxia, cortical sensory deficits, dystonia, prominent language disturbances and alien limb phenomenon
Frontotemporal degeneration	Circumscribed degeneration of the prefrontal and anterior temporal cortices. Asymmetric atrophy of the left hemisphere	Progressive changes in behavior, personality, and language. Cognitive impairments in executive function. Possible spasticity and non-fluent aphasia. 8 years of life expectancy after symptoms' onset
Huntington's disease	Hereditary autosomal dominant disorder affecting the central nervous system. Degeneration of projection neurons (pyramidal cells) from the layers III, V and VI leading to neuronal cell death. Affecting the basal ganglia, especially the putamen and caudate nucleus, as well as the frontal cortex due to a single defective gene	Abnormal movements (chorea-like), dementia, personality and behavioral changes. 20 years of life expectancy after symptoms' onset
Parkinson's disease	Neuronal loss targeting dopaminergic neurons from the mesencephalon (midbrain), especially in the substantia nigra. Formation of neuronal inclusions (Lewy bodies), composed of aggregated $\alpha$ -synuclein, in the cerebral cortex. Metabolic changes in cortical areas	Movement disorders such as tremor, bradykinesia, rigidity and postural instability

Table 3.2: Listing of the neurodegenerative disorders linked to their pathologies, affected brain regions, and noticed symptoms. Adapted from Yamauchi et al. 1998; Thompson et al. 2003; Neary et al. 2005; Rosas et al. 2008; Johansen-Berg et al. 2009; Constantinides et al. 2019 and <https://dictionnaire.academie-medecine.fr>.

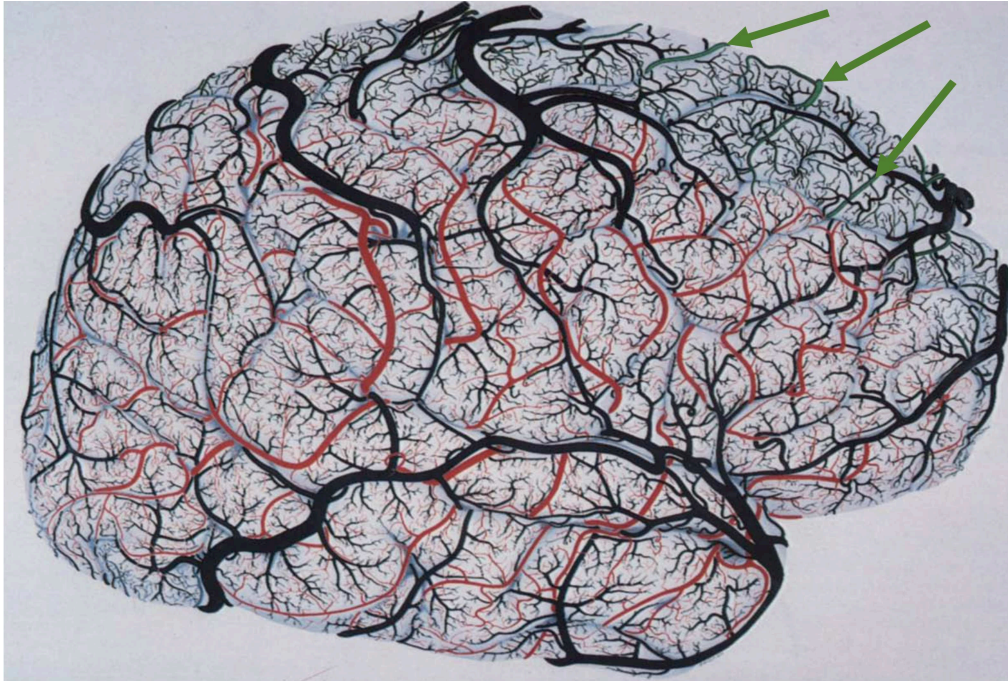


Figure 3.13: Drawing of the right-hemisphere cortical pial vessels. Veins are in black. Tributaries of the middle cerebral artery are in red. Tributaries of the posterior cerebral artery are in blue. Tributaries of the anterior cerebral artery are in green (see green arrows). Image adapted from Duvernoy et al. 1981.

### 3.6.2 Neurodevelopmental pathologies

Neurodevelopmental pathologies are related to failures in cellular migration, cortical maturation or synaptic pruning. These diseases include gray matter heterotopia and cortical malformations in general.

Gray matter heterotopia is a group of neurological disorders characterized by an abnormal neuronal migration in the cerebral cortex. It results from an *in utero* arrest of radial migration of neurons from the germinal matrix in the wall of the lateral ventricle to the developing cerebral cortex between 6 and 16 weeks of gestation. It is usually discovered during the evaluation of children or young adults with epilepsy, children with neurodevelopmental abnormalities [Barkovich et al. 2000]. Affected patients present as ectopic clusters of neurons along the ventricular walls (mainly comprising periventricular nodular heterotopia), or they form in the deep white matter a nodule (focal subcortical heterotopia), or a dense band of neurons (subcortical band heterotopia or double cortex) [Watrin et al. 2015].

In addition to abnormal proliferation or migration of neuronal cells during embryonic development, cortical malformations can also take the form of abnormal cortical folding, leading to lissencephaly (absent or decreased cerebral convolutions, producing cortical thickening and a smooth cerebral surface), or polymicrogyria (abnormal gestational development of the brain, which surface develops too many folds that are unusually small). The usual symptoms of these pathologies are mental retardation, motor and sensory impairment, developmental delay, as well as seizures.

### 3.6.3 Neuropsychiatric disorders

Schizophrenia is one of the cortex-related neuropsychiatric disorders. It is related to abnormal dopamine and serotonin transmission, and thinning of the cerebral cortex due to a gray matter loss in the particularly affected frontal and temporal

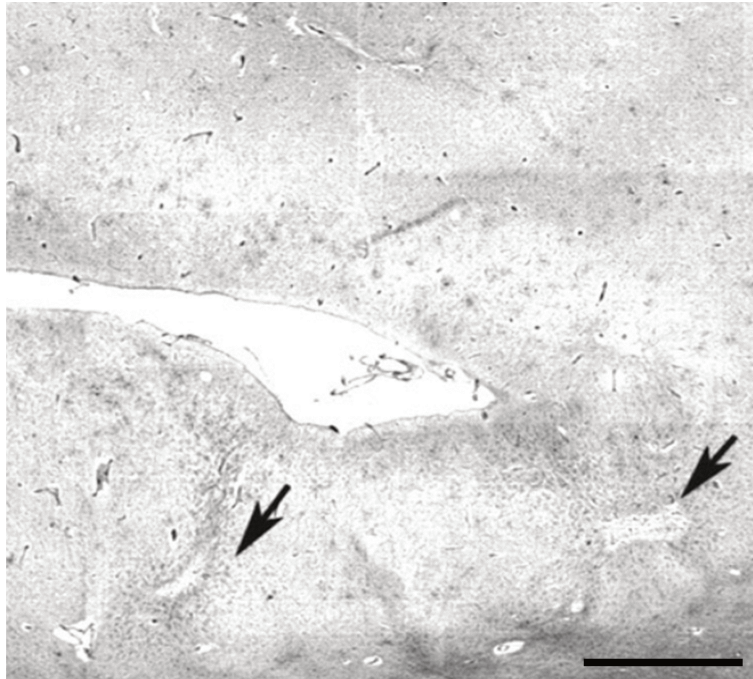


Figure 3.14: Image of multiple cortical microinfarcts indicated by black arrows in the frontal cortex of a human specimen. Section stained with Globus silver impregnation. Scale bar = 1 cm (adapted from Kövari Enikő et al. 2004).

cortices [Knöchel et al. 2016]. Gray matter abnormalities result in excessive pruning of synaptic contact during puberty, combined with aberrant organization of synaptic connections caused by the atypical migration of the neuron precursor cells during pregnancy [Zikidi et al. 2019]. The regular symptoms are psychosis, hallucinations, strange thoughts, delusions, sensory disturbances, depression, working memory impairment and asociality. In Ji et al. 2018, it has been highlighted that diffusion-weighted magnetic resonance imaging (dMRI) can indicate modifications in superficial white matter in the frontal cortex for schizophrenic patients.

Studies also point out that the prefrontal cortex is involved in addictive disorders. Indeed, the prefrontal cortex is a functional nexus point controlling subcortical neural reward and motivational pathways. The process of addiction involves the aberrant amplification of reward signals associated with drugs of abuse and the formation of powerful associative memories linked to the drug-taking experience [Cechetto et al. 2017]. The prefrontal cortex plays also a key role in bipolar disorder (cyclical pathological mood alternation between mania, hypomania, and depression). Sarrazin et al. 2019 study has revealed a higher neurite density in that region for patients treated with lithium, suggesting a possible improvement of their conditions.

### 3.6.4 Neurovascular disorders

This category of disorders encloses cortical microinfarcts, focal brain lesions, as well as cerebral small vessels diseases, that involve the cerebral cortex. Cortical microinfarcts correspond to cerebral infarcts, which their diameters are below  $15\mu\text{m}$  and they are located in the cerebral cortex. Microinfarcts in both cortical and subcortical structures have been evaluated as substrates of cognitive impairment. Their repetitions are associated with greater odds of dementia and with worsening semantic memory and perceptual speed [Kalaria 2018]. Figure 3.14 displays multiple cortical microinfarcts that occurred in a human frontal cortex.

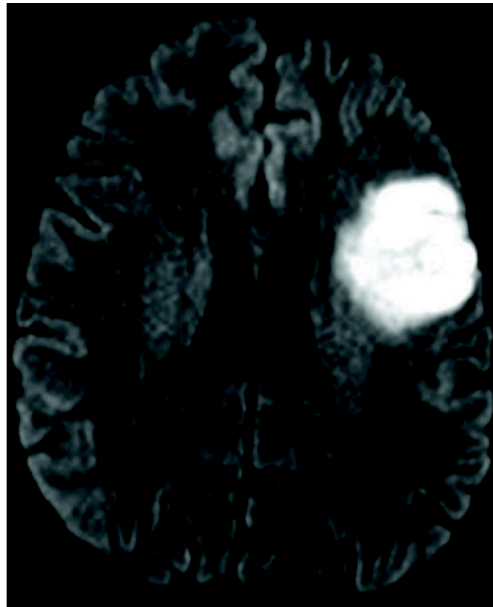


Figure 3.15: *Diffusion-weighted image of an acute patient presenting infarct/hypoperfusion involving Broca's area, appearing as a large white stain (adapted from Ochfeld et al. 2010).*

Focal brain lesions are synonyms of stroke which can damage various cortical areas and leave sequelae, as shown in Figure 3.15. Their consequences depend on the injured regions since there is a whole spectrum of motor, cognitive and sensory disorders that can emerge. For instance, lesions in the inferior frontal gyrus and its adjacent cortex, which correspond to Brodmann areas 44 and 45, could lead to Broca's aphasia. Thus, the patient would suffer from a deficit in the ability to speak and produce the proper words and sounds.

Cerebral small vessels diseases include pathologies of the small arteries, arterioles, capillaries, venules, and veins supplying the white matter and the deep gray matter structures of the brain. The diseases are associated with stroke, cognitive impairment, dementia and mortality [Shaaban et al. 2020]. An actively studied cerebral small vessel disease is cerebral autosomal dominant arteriopathy with subcortical infarcts and leukoencephalopathy (CADASIL) [Chabriat, Vahedi, et al. 1995; Chabriat, Joutel, et al. 2009; Di Donato et al. 2017] that showcases cortical alterations progressing parallel to clinical worsening [Jouvent, Mangin, Porcher, et al. 2008; Jouvent, Mangin, Duchesnay, et al. 2012; Guio et al. 2014].

## 3.7 Conclusion

This second background chapter looks over the primal characteristics of the human cerebral cortex, in order to prevent confusion with other brain parts made of gray matter such as the basal ganglia or the cerebellar cortex. The fundamental knowledge required to understand the human brain anatomy and more particularly the human cerebral cortex were presented. Few techniques are available to map the cyto- and myeloarchitecture of an entire human brain. Diffusion and quantitative MRI can be sensitized to tissue microstructure and are the core techniques used in this thesis. They will be applied to scan *ex vivo* brain samples of various species at very high spatial resolutions, combined with ultra-high and extreme field MRI scanners.





## Chapter 4

# Ultra-high and extreme fields postmortem MRI to probe cerebral microstructure

This chapter is made of four sections. The first one delivers theoretical background on physical principles magnetic resonance imaging (MRI). Secondly, emphasis is put on postmortem imaging at ultra-high and extreme magnetic fields, which concerns every specimen scanned during this thesis. The third and fourth sections present respectively diffusion-weighted and quantitative MRI, reviewing their basic concepts, specific MRI sequences and applications.

### 4.1 Physical principles of magnetic resonance imaging

Magnetic resonance imaging MRI originates from the nuclear magnetic resonance (NMR) phenomenon, which is exhibited by many atomic nuclei and relies on their magnetic properties. The historical discovery of MRI is as follows: in 1933, Otto Stern [Frisch et al. 1933] discovers the magnetic moment of the proton. Isidor Isaac Rabi [Rabi et al. 1938] describes in 1938 for the first time the NMR. Felix Bloch [Bloch 1946] and Edwards Mills Purcell [Purcell et al. 1946] detail the notion of resonance frequency in 1946. Finally, Paul Lauterbur [Lauterbur 1973] and Sir Peter Mansfield [Mansfield 1977] create methodology to generate images using NMR gradients. Each of them, except for Stern, was awarded a Nobel Prize for his work.

#### 4.1.1 Magnetic properties of hydrogen

The hydrogen atom,  ${}^1_1\text{H}$ , is composed of a single proton as a nucleon. The nucleus can be considered as a particle with a specific mass and an electrical charge spinning around its axis. The former is characterized by its angular momentum,  $\mathbf{L}$ . The latter is characterized by its magnetic moment  $\boldsymbol{\mu}$  (N.m.T<sup>-1</sup>) :  $\boldsymbol{\mu} = \gamma\mathbf{L}$ , where  $\gamma$  is the gyromagnetic ratio, proper to each nucleus. A spin is an intrinsic quantum parameter accounting for the rotational movement of a particle on itself. For the hydrogen, the resulting nuclear spin of its proton corresponds to the angular moment, which is non null ( $I = 1/2$ ), allowing the particle to self-rotate, and thus induces the nuclear magnetic resonance. Among all

the nuclei usually studied in NMR, the hydrogen has the highest gyromagnetic ratio (42.576 MHz/T), natural abundance (99.985/100) and relative sensibility (100/100). All these characteristics and the fact that the human brain is made of water (H<sub>2</sub>O) at 76% explain why hydrogen is a great candidate for MRI.

## 4.1.2 Magnetic resonance phenomenon

The magnetic resonance phenomenon is divided into three subsequent stages: polarization, excitation/resonance and relaxation. Those three stages are represented in Figure 4.1.

### 4.1.2.1 Polarization

In spite of having a resulting nuclear spin  $I$  non null, the magnetic moment  $\mu$  of the hydrogen nucleus cannot be directly measured. Indeed, it is randomly oriented in space and time, which causes on a group level a null global magnetization. It is then necessary to make hydrogen nuclei interact with an intense, static and external magnetic field,  $\mathbf{B}_0$  (T, the Tesla, is the derived unit of the magnetic field strength with  $1T = 1N.A^{-1}.m^{-1}$ ), in order to measure their magnetic properties. Therefore, the spins of hydrogen protons, H<sup>+</sup>, align either parallel or antiparallel to the  $\mathbf{B}_0$  field. A new equilibrium, order is created which is the polarization of the nuclei. The parallel spins slightly outnumber the antiparallel ones, due to their lower quantum energy levels, which is enough to generate a macroscopic net magnetization vector,  $\mathbf{M}$ .

### 4.1.2.2 Excitation or resonance

The polarized spins precess at a specific frequency called the Larmor frequency  $\nu_0$ :  $\nu_0 = \gamma B_0 / 2\pi$ . The resonance phenomenon occurs when an applied rotating electromagnetic field,  $\mathbf{B}_1$ , forms a radiofrequency (RF) wave with a pulsation equal to  $\omega_0 = \gamma B_0$ , that arrives orthogonally on the spins' rotational axis and disturbs the established equilibrium. The spins are now in their excitation phase that entails a magnetization switch: a transverse magnetization  $\mathbf{M}_{xy}$  appears, while the longitudinal magnetization  $\mathbf{M}_z$  disappears.  $\mathbf{M}_z$  fall corresponds to an energetic transfer from the parallel spins to the antiparallel spins. As for  $\mathbf{M}_{xy}$  appearance, it reflects the phasing of the two types of spins.

### 4.1.2.3 Relaxation

Eventually, the disturbing  $\mathbf{B}_1$  is no longer applied on the system and the spins enter the relaxation phase, which is a return to equilibrium of tissue magnetization. Spins progressively reorient along  $\mathbf{B}_0$  axis and in doing so, they transmit electromagnetic energy, making the NMR signal receivable by a reception coil or antenna located in the transverse plane. The longitudinal magnetization recovers at its initial value (longitudinal relaxation), whereas the transverse magnetization decays while helically spinning around the  $\mathbf{B}_0$  axis, at the Larmor frequency  $\nu_0$  (transverse relaxation).

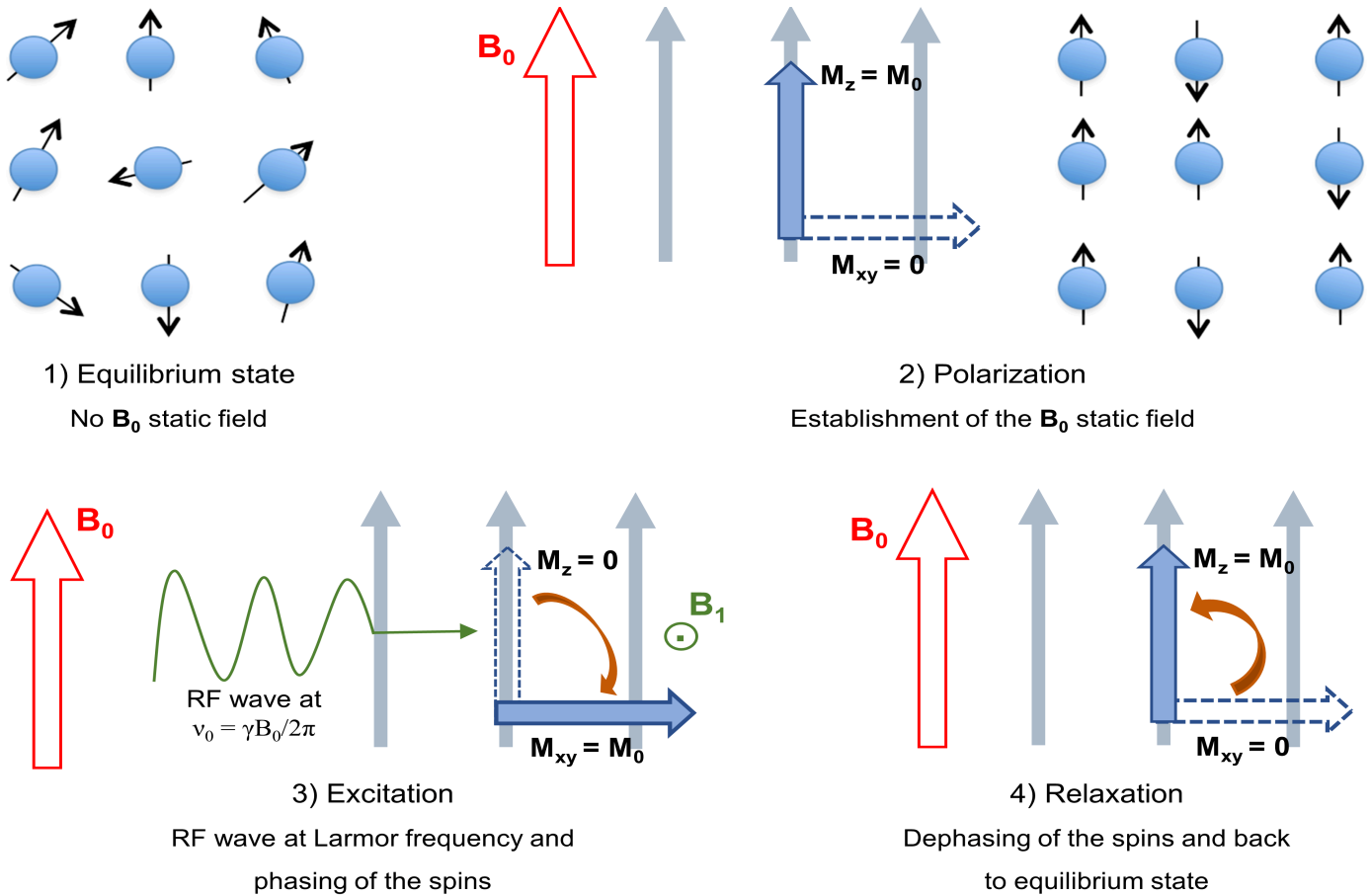


Figure 4.1: Illustration of the magnetic resonance phenomenon in four steps: equilibrium, polarization, excitation and relaxation.

### 4.1.3 Bloch equations, $T_1$ , $T_2$ and $T_2^*$ relaxation times

The recovery of the longitudinal magnetization  $M_z$  follows an exponential growth involving the time constant  $T_1$ . The spin-lattice relaxation time stands for the required time for longitudinal relaxation to reach 63% of its initial value. During the transverse relaxation phase, the emitted radiofrequency wave called Free Induction Decay (FID) follows an exponential attenuation involving the spin-spin time constant  $T_2$ . The latter represents the needed amount of time for transverse relaxation to hit 37% of its maximum value. A third implied relaxation time  $T_2^*$  expresses the molecular inhomogeneities stemming from  $T_2$  relaxation, as well as  $B_0$  magnetic field inhomogeneities ( $T_2'$ ). Figure 4.2 presents the three relaxation time constants,  $T_1$ ,  $T_2$  and  $T_2^*$ . Bloch equations [1946] address the time-dependent evolution of the net magnetization vector  $\mathbf{M}$ . When considering a  $90^\circ$  RF pulse applied in the transverse section, the spatial equations for  $\mathbf{M}$  are:

$$\begin{cases} M_x(t) = M_0 e^{-\frac{t}{T_2}} \sin(\omega t) \\ M_y(t) = M_0 e^{-\frac{t}{T_2}} \cos(\omega t) \\ M_z(t) = M_0 (1 - e^{-\frac{t}{T_1}}) \end{cases} \quad (4.1)$$

where  $M_0$  is the initial maximum value of  $M_z$  and  $\omega$  the angular velocity.

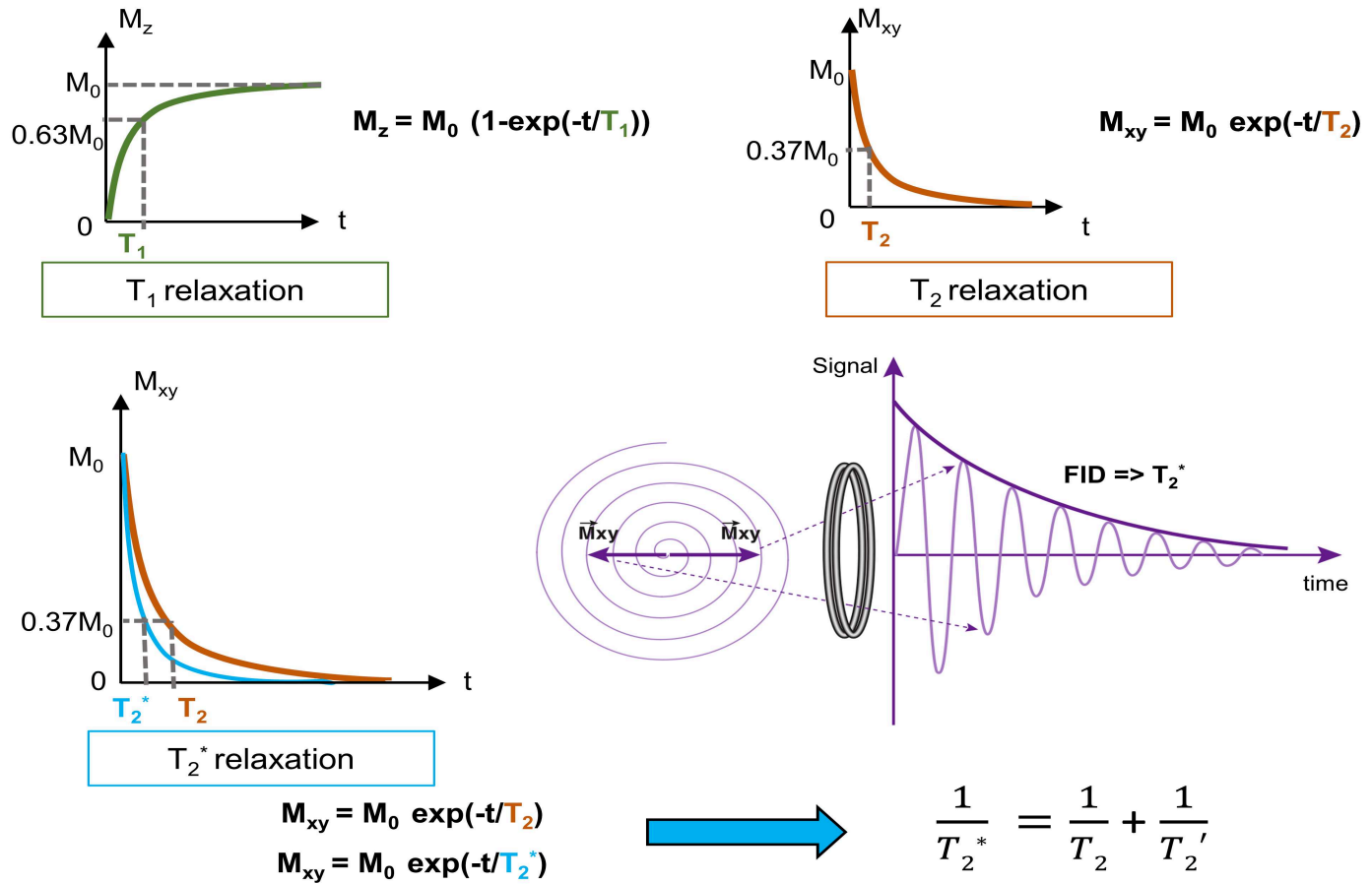


Figure 4.2: Description of the three relaxation times  $T_1$ ,  $T_2$  and  $T_2^*$  (adapted from Kastler et al. 2011).

The three time constants' values depend on the molecular structure of the substance and its physical state (liquid, solid or gas). MRI contrast originates from the relaxation time differences  $T_1$  and  $T_2$ .

### 4.1.4 2D image encoding

Obtaining images in MRI requires the accurate spatial localization of the NMR signal. This is another three-fold process which uses linear gradients of magnetic field ( $T.m^{-1}$ ): slice selection, phase encoding, then frequency encoding.

The gradient of slice selection  $G_{\text{slice}}$ , modifies the precession frequency of protons that will depend on their positions in the slice axis. Only the spins which precession frequency is equal to the applied RF pulse will be excited and tilted in the transverse plane. The stronger  $G_{\text{slice}}$  is, the thinner the selected slice is. An illustration of the slice selection process is shown in Figure 4.3.

Inside the selected slice, a double frequency and phase encoding is used to code information located within a voxel according to the two directions of the field of view (FOV). The phase encoding gradient ( $G_{\text{phase}}$ ) encodes the line, while the frequency encoding (or readout) gradient ( $G_{\text{read}}$ ) encodes the column.  $G_{\text{phase}}$  induces dephasing of same-column protons that keep precessing at the same pace. The procedure is repeated as many times as there are lines in the encoded image, changing the initial phase each time. Then,  $G_{\text{read}}$  is applied while collecting the NMR signal. It consists in acquiring the protons' signal of the selected slice in the presence of a magnetic field gradient along the second

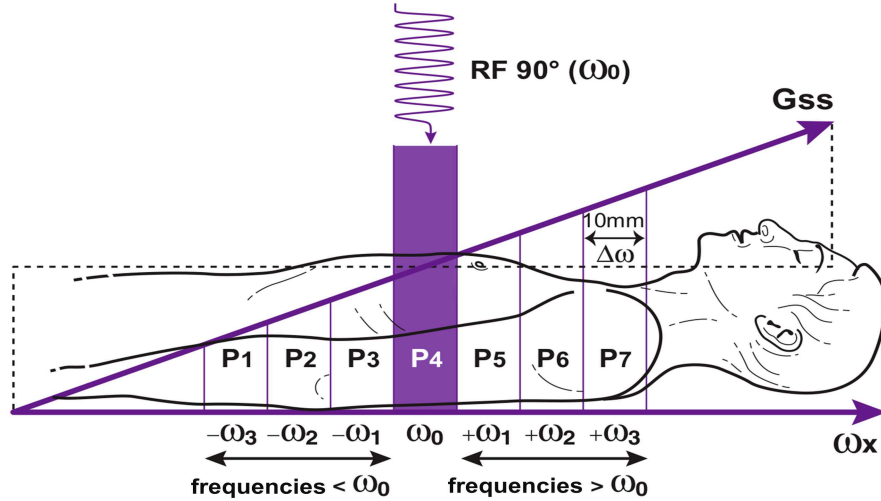


Figure 4.3: Illustration of a slice selection by applying the gradient of slice selection ( $G_{ss}$ ) along the axis  $z$ . The selected slice  $P4$  is the one with the angular frequency  $\omega_0$ , identical to  $\vec{B}_0$  frequency.  $P4$  protons will then contribute to the measured NMR signal (adapted from Kastler et al. 2011).

encoding direction. Figure 4.4 illustrates the output of frequency encoding.

Thereafter, the raw data are transferred in a Fourier plane called the  $k$ -space. Each line of the  $k$ -space contains information on the entire slice, as expressed in Equation (4.2). A double inverse Fourier transform of the  $k$ -space data leads to a 2D interpretable image. 3D imaging requires a second phase-encoding gradient along the slice selection direction.

$$k_i(t) = \gamma \int_0^t G_i(t) dt \tag{4.2}$$

with  $k_i(\text{m}^{-1})$  is the encoded spatial frequency in a specific 2D direction  $i = (x, y)$ , and  $G_i$  is the applied gradient in that direction during a certain amount of time  $t$ .

### 4.1.5 Conventional MRI sequences

#### 4.1.5.1 Image contrast

The contrast is one of the three major criteria to assess the image quality, along with the spatial resolution and the signal-to-noise ratio (SNR). The resulting image contrast is based on grayscale, where black refers to a low NMR signal and white a high level of signal. For the two basic MRI sequences (spin echo and gradient echo), the contrast can be modified by weighting the sequence through the operator-dependent parameters called the flip angle  $\theta$ , echo time (TE) and repetition time (TR). The flip angle is the angle to which the net magnetization vector  $\mathbf{M}$  is tipped or rotated relative to the static magnetic field  $\mathbf{B}_0$  direction. TE is the required time to measure the NMR signal. TR is both the recovery time for the longitudinal magnetization, and the cycle time between two consecutive excitations. The NMR signal for a spin echo sequence is proportional to  $\rho e^{-\frac{TE}{T_2}} (1 - e^{-\frac{TR}{T_1}})$  with  $\rho$  is the proton density. Hence the image contrast varies

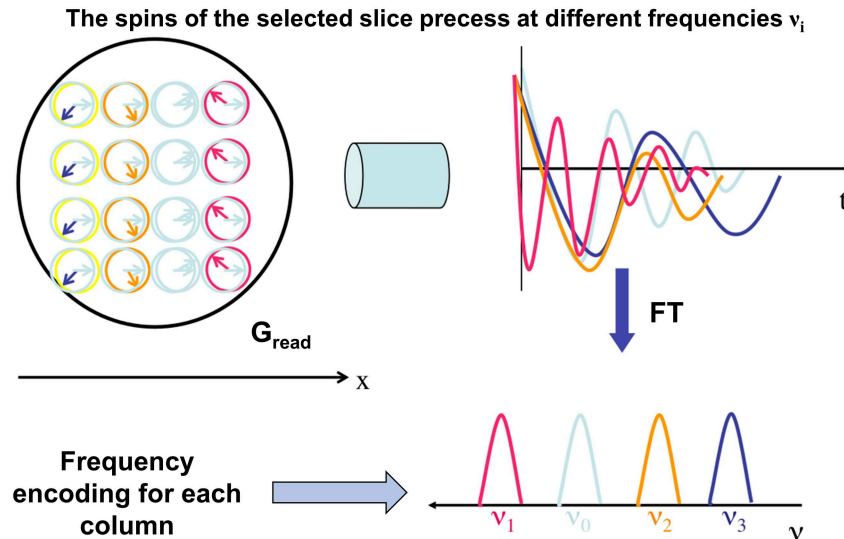


Figure 4.4: Image of the output of frequency encoding. After the Fourier transform (FT), each column signal produces a peak which area is prorated to the entire spins' magnetization of this column.

with TE and TR values, as presented in Figure 4.5:

- $T_1$ -weighting comes from a short TE and a short TR.
- $T_2$ -weighting comes from a long TE and a long TR.
- $\rho$ -weighting comes from a short TE and a long TR.

#### 4.1.5.2 Spin echo sequence

The major components of a MRI sequence are the RF excitations pulses,  $G_{\text{slice}}$ ,  $G_{\text{phase}}$ ,  $G_{\text{read}}$ , the signal sampling, and the delays based on TR and TE. Erwin Louis Hahn [Hahn 1950] detailed a method to suppress the external magnetic field  $\mathbf{B}_0$  inhomogeneities and get to the actual  $T_2$  with the spin echo (SE) sequence. It consists in a first  $90^\circ$  RF pulse to tilt the magnetization in the transverse plane. Then comes a second  $180^\circ$  RF pulse, applied at  $t = TE/2$ , to reestablish the phase coherence between the spins, and to alleviate  $\mathbf{B}_0$  inhomogeneities. Finally, the signal readout happens at  $t = TE$ . The sequential  $180^\circ$  RF pulses, which are the echoes, reveal the  $T_2$  signal decay, as seen in Figure 4.6. This pattern reiterates at every repetition time and as many times as there are lines in the image matrix.

#### 4.1.5.3 Gradient echo sequence

The gradient echo (GRE) sequence relies on the flip angle ( $\theta < 90^\circ$ ), a bipolar gradient, and does not involve any refocusing  $180^\circ$  RF pulse. A negative gradient (readout gradient) is first applied on the frequency encoding direction. A second positive gradient (rephasing gradient) comes right after, with the same amplitude but lasting twice as more, to compensate the dephasing made by the readout gradient. The GRE sequence diagram is displayed on Figure 4.7.

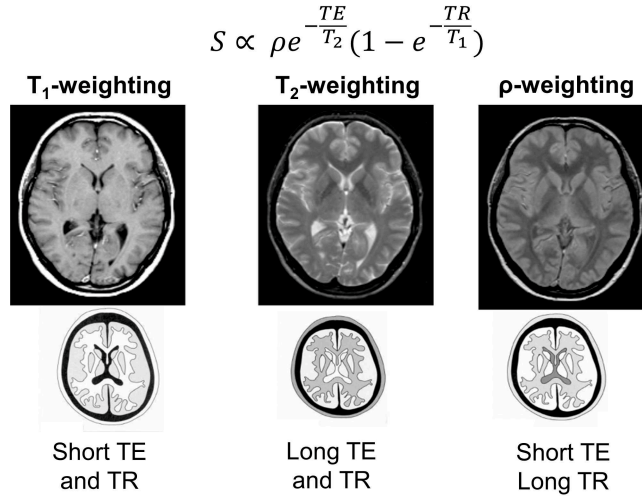


Figure 4.5: *Image weightings in MRI from a spin echo sequence. The  $T_1$ ,  $T_2$  and  $\rho$  weightings entail various contrasts in the brain tissue. At the top, there are actual clinical MRI images, and at the bottom there are schematic correspondences of the cerebral tissue contrast (adapted from Kastler et al. 2011).*

By reducing the flip angle, TR can be inferior to the tissue  $T_1$  value, without losing signal. This effect is linked to Ernst theory [Ernst et al. 1966], shown in Equation (4.3), where a maximum signal exists for an optimal flip angle  $\theta_{optimal}$ , as long as  $TR \gg T_2^*$ . Moreover, it offers a significantly shorter acquisition time than the SE sequence, which requires a long TR for a full longitudinal magnetization recovery.

$$\cos \theta_{optimal} = e^{-\frac{TR}{T_1}} \quad (4.3)$$

#### 4.1.6 Ultra-high and extreme magnetic fields

Ultra-high magnetic field refers to magnetic fields superior to 3 Tesla, which nowadays concerns preclinical and clinical MRI scanners. Extreme magnetic field refers to magnetic fields superior to 7 Tesla. This thesis only relied on these two kinds of magnetic fields. Many factors are influenced by the magnetic field strength. The chemical shift and magnetic susceptibility linearly increase with the magnetic field strength, while the SNR raises up such as  $SNR \propto (B_0)^{1.65}$  [Pohmann et al. 2016]. Likewise, acoustic noise and  $B_1^+$  inhomogeneities intensify with  $B_0$  value [Moser 2010].  $T_2$  relaxation time lowers and  $T_1$  relaxation time shoots up when  $B_0$  rises. Furthermore, the specific absorption rate (SAR) increases with the square of the magnetic field strength, which causes a lengthening of the scan duration for the subject. Nevertheless, higher spatial resolutions can be obtained at ultra-high field (UHF) and extreme field, thus offering a substantial amount of details to explore the MR images for brain research and clinical applications.

This section focused on the basis of magnetic resonance imaging which are instrumental in understanding diffusion and quantitative MRI that were used in this thesis. The next section details the specificity that brings *ex vivo* MR imaging.



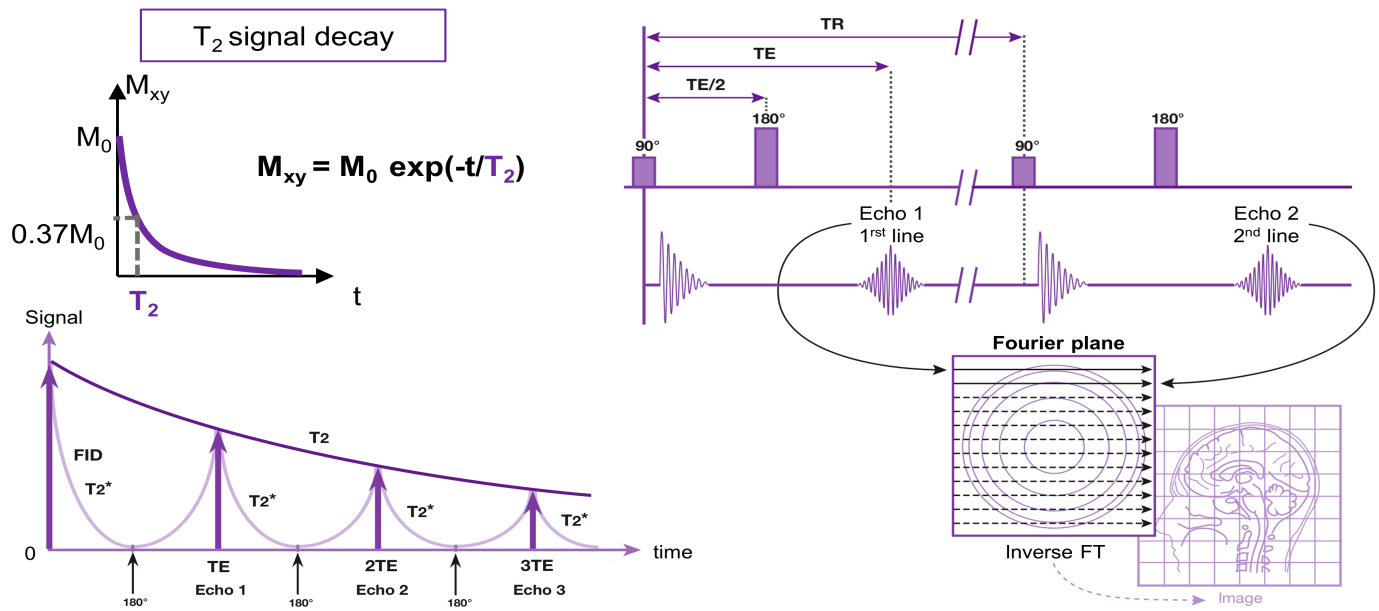


Figure 4.6:  $T_2$  signal decay (on the left) and the RF framework of the spin echo sequence (on the right). FT = Fourier transform. Image adapted from Kastler et al. 2011.

## 4.2 Postmortem imaging specificity

*Ex vivo* MRI aims at reaching a quality of the postmortem tissue as close as possible to the *in vivo* state but without the limitations of physiological noise or time constraints [Dyrby, Innocenti, et al. 2018]. It is even regarded as an indispensable tool to improve our understanding of relaxation mechanisms in normal and abnormal tissue on a microscopic level and to validate quantitative MRI methods [Birkel et al. 2016]. This configuration requires proper preparation of the tissue sample and setups for the MRI scanner that differ from living specimens. The *in vivo* tissue is intrinsically different from the *ex vivo* one, but the preparation and conservation conditions of the postmortem sample offers a wide scope of imaging resolutions. The images with the highest resolutions help to provide a sort of ground truth to the low-resolution images. Reviewing the characteristics concerning postmortem MRI enables the comparison between *ex vivo* and *in vivo* imaging.

### 4.2.1 Ex vivo brain tissue features

Once the brain dies, meaning there is cessation of all metabolic processes, cerebral tissue autolysis begins. If the latter is not stopped by fixation, the microstructural environment will deteriorate starting with the loosening of axonal myelin sheaths within six to twelve hours. Low temperatures (inferior to  $12^\circ\text{C}$ ) retard autolysis [Hukkanen et al. 1987], which allows a maximum 24-hour post mortem interval (PMI) for brain fixation, as part of a postmortem brain study. Therefore, the conducted postmortem study is not affected by bacterial decomposition, microbial contamination and damaging proteolytic enzymes, plus the structural properties existing *in vivo* are preserved.

Fixation can be accomplished by immersing the brain in a solution that contains a fixative agent such as formaldehyde (or formalin) or paraformaldehyde (PFA). Over time, the fixative agent diffuses inward from the surface of the brain, slowing or stopping tissue decomposition. Fixation can likewise be performed by perfusion of the fixative agent us-

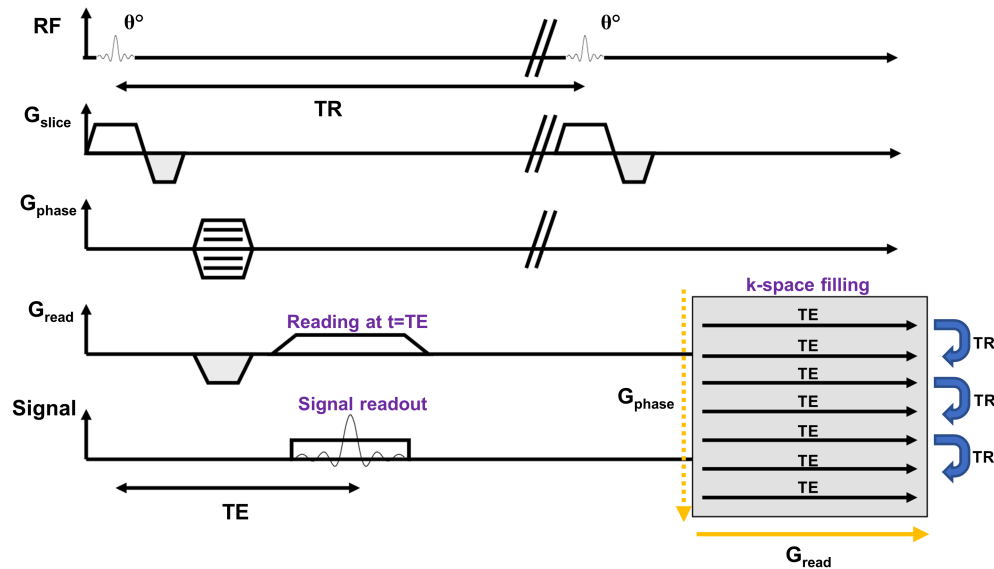


Figure 4.7: The principle of the gradient echo sequence. Each line of the  $k$ -space is read at  $t = TE$  with the readout gradient ( $G_{read}$ ). The switch to the next line occurs at  $t = TR$  with the increment of the phase gradient ( $G_{phase}$ ).

ing the vascular system to homogeneously fix each brain area, and thus leading to better results than the immersive technique. Indeed, postmortem tissue remains vulnerable to bacterial degradation and autolysis until complete fixation occurs. This issue can be tackled with perfusion-fixation, which is less time-consuming than immersion-fixation. Moreover, best-quality fixation is obtained by combining immersion and perfusion techniques [Beach et al. 1987]. Animal cerebral tissues are usually fixed pre-mortem by *in situ* perfusion or directly *ex vivo*, whilst the human brain is fixed after a certain PMI [D'Arceuil and Crespigny 2007].

Aldehyde fixatives alter the tissue water relaxation and diffusion properties significantly [Shepherd et al. 2009]. Physical changes caused by death and formalin fixation include modifications in water proton environment, collapse of CSF spaces, increased membrane permeability, lack of flowing blood and other fluids, reduced transmembrane water exchange, and drop of capillary volume [Pfefferbaum et al. 2004; Thelwall et al. 2006]. Formaldehyde fixation advocates water molecules immobilization and protein cross-linking, causing tissue rigidity and dehydration. On a clinical standpoint, since fixation stops all physiological functions of cells, acute cell swelling effects following brain disorders such as stroke or inflammation may manifest with a different contrast from *in vivo* MRI [Dyrby, Innocenti, et al. 2018]. The most blatant macroscopic effects of formaldehyde fixation are tissue shrinking and a changed gray-white matter contrast. The former can be assessed with the shrinkage factor that must be as little as possible to argue using *ex vivo* tissue as a paragon for *in vivo*.

Regarding postmortem imaging, diffusivity is known to decrease, thus impacting in the same way  $T_2$  relaxation time, proton density and apparent diffusion coefficient (ADC) [D'Arceuil and Crespigny 2007]. In addition, the  $b$ -value needs to be higher than for *in vivo* subjects (typically three to four times greater), requiring stronger gradient magnitudes and encouraging the use of UHF preclinical MRI systems to preserve a short TE, keep a reasonable SNR and satisfying contrast.

## 4.2.2 Considerations for MRI scanner setups

To set up the MRI scanner (preclinical or clinical) in the most optimal way, four endpoints must be considered:

- the fixative agent: formaldehyde ( $\text{CH}_2\text{O}$ ) or paraformaldehyde ( $\text{OH}(\text{CH}_2\text{O})_n\text{H}$ , with  $n=8-100$ ).
- the fixation technique: perfusion and/or immersion.
- the post mortem interval (PMI).
- the scan interval, which is the time separating the death to the MRI scanning.

Postmortem MRI must cope with  $T_1$  and  $T_2$  shortenings. The former is due to protein cross-linking that alters the macromolecular structure. The latter is greatly impacted by formalin-induced tissue dehydration, which can be toned down by the removal of excess fixative by washing in phosphate-buffered saline (PBS) [Thelwall et al. 2006], as well as rehydrating the sample in PBS [Duijn et al. 2011]. Conversely, decomposition of the tissue may lead to increased water content or increased water mobility which may increase  $T_2$  values. Thus,  $T_2$  relaxation time can potentially provide important information about the changes that occur in brain tissue during fixation [Dawe et al. 2009]. It also appears that the spin-lattice relaxation time is even shorter in the gray matter than in the white matter [Tovi et al. 1992]. Soaking the sample in a gadolinium-doped buffer solution reduces  $T_1$ , which is interesting in short TR sequences since the  $T_1$  saturation effect is weakened without significantly affecting spin-spin relaxation time [D'Arceuil and Crespigny 2007]. However, this procedure is defective in the incapacity of the buffer to fully impregnate the brain in the allocated time [Pfefferbaum et al. 2004; Miller, Stagg, et al. 2011].

There are also proton density [Yong-Hing et al. 2005] and  $T_2^*$  decays in *ex vivo* brain imaging. Indeed,  $T_2^*$  reflects spin dispersion due to microscopic field gradients, which is introduced by tissue components with different magnetic susceptibilities such as tissue water, proteins and iron. Its shortening is then probably induced by interstitial water partially replaced by formaldehyde, which has a different magnetic susceptibility than water (at 20 °C, 1atm:  $-18.6 * 10^{-6} \text{cm}^3 / \text{mol}$  for formalin versus  $-1.298 * 10^{-5} \text{cm}^3 / \text{mol}$  for pure water) [Birkl et al. 2016].

Temperature impacts as well diffusivity and relaxation times [Le Bihan, Delannoy, et al. 1989]. Hence it must be controlled and stabilized during scanning, along with remaining identical if multiple scans are scheduled over time. Transferring the specimen in the magnet room at least five hours before scanning should meekly warm up the brain to the regular 20-degree room temperature. It is also beneficial to store the fixed sample at low temperatures (typically about 5 °C) to sustain the life-like state of the cerebral tissues.

## 4.2.3 *Ex vivo* or *in vivo* imaging ?

The course of this thesis would have been different if *in vivo* imaging had been chosen over *ex vivo* imaging. A comparison between these two modalities must be here detailed.

On the one hand, *in vivo* MRI offers information on a living subject which can be combined with fMRI information, all the more as it probes the structure, function and connectivity of living human brain tissue, without any harmful side effects [Geyer and Turner 2013]. Nonetheless, there are drawbacks arising such as artifacts (motion, physiological noise, susceptibility), constrained acquisition time to respect the subject comfort, limited spatial resolution (mesoscopic scale hardly achievable with a homogeneous MR signal), partial volume effects from white matter and CSF due to low resolution, use of isoflurane (inhalation anesthetic) to sedate the subject, restricted SAR to prevent hazardous effects

on the living subject, infeasibility to conduct histological analyses once the MRI scan finished [Dawe et al. 2009]. On the other hand, *ex vivo* MRI profits by the same neuroanatomical complexity as the *in vivo* one, long scan times (from several hours to several days), increased SNR, no subject-related artifacts, high spatial resolutions, prolonged application of intense diffusion gradients, use of UHF MRI regardless of the SAR or any side effects. The selected MRI sequences in this thesis, which encapsulate all the aforementioned benefits of postmortem MRI, would not have been applicable on living subjects. However, postmortem imaging relies on the effective sample preparation, fixation and conservation to obtain high-quality dataset. Resorting to UHF MRI remains expensive and not mainstream. It is therefore high-end imaging. Considering the objectives of this thesis, the advantages of *ex vivo* MRI outweigh those of *in vivo* MRI, making UHF postmortem MRI the most suitable approach to probe cerebral microstructure. This section detailed the specificity of postmortem MRI, indicating the effects on the brain tissue, the altered environmental and MRI features, as well as the benefits and pitfalls of scanning *in vivo* or *ex vivo*. From here, we can now dive into diffusion-weighted MRI that is one of the two MRI modalities used in this thesis.

## 4.3 Diffusion-weighted MRI

Diffusion-weighted magnetic resonance imaging (dMRI) is currently the most suitable technique to probe *in vivo* the anatomical connectivity and the microstructure of the white matter [Mori and Zhang 2006]. Its physical process relies on the microscopic displacements of water molecules (Brownian motion) in tissues mostly embedding axonal connections, organized into tightly parallel bundles. Thus, the diffusion pattern measured using dMRI reveals not only the fibers' orientation, but it can also be used to probe more elaborated features characterizing the tissue cytoarchitecture, such as the cell density or dimension (e.g. the axonal diameter). dMRI protocols must be adapted according to the nature of the brain: *in vivo* or *ex vivo*.

### 4.3.1 The diffusion process

Diffusion highlights the microscopic displacements of molecules in a fluid (gas or liquid) due to thermal collisions. The molecules suspended in the fluid adopt a random motion called the Brownian motion, resulting from their collisions with the fluid particles. In brain tissues, the situation is different due to the presence of obstacles corresponding to the environment of the cell population. Water molecules depict as well random displacements linked to thermal collisions, but they also face the cell membranes of axonal fibers, neurons, glia and blood vessels. The molecules can bump into these membranes or cross them according to their permeability, which restricts their motion. Water molecules can likewise have interactions with macromolecules that entails a slow down of their movement leading to hindrance. Regarding white matter, the presence of myelinated fibers organized into parallel bundles leads to a macroscopic anisotropic restriction pattern, where water molecules present a bigger free average displacement in the direction parallel to the axons than along any other direction. The gray matter composed of somas, astrocytes, glial cells and dendrites randomly oriented in the space generally yields an isotropic diffusion pattern where no diffusion direction is favored. However, cellular organizations characterized by a macroscopically isotropic pattern can correspond to a diffusion process actually being microscopically anisotropic. Figure 4.8 illustrates the differences between unhindered and hindered diffusion.

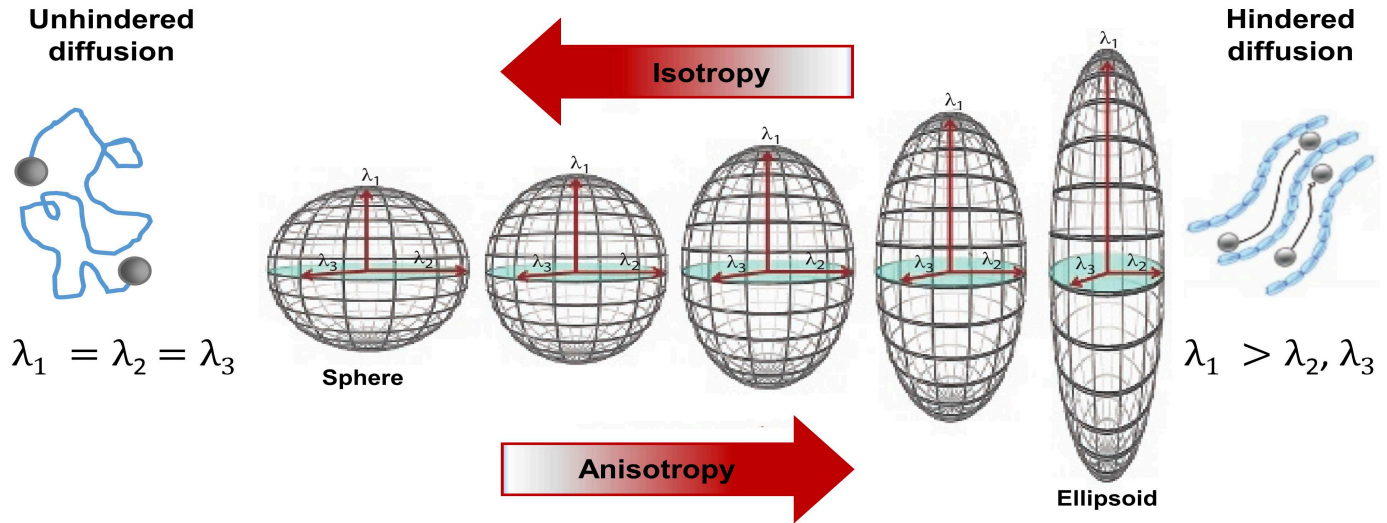


Figure 4.8: Comparison between unhindered and hindered diffusion. Hindered diffusion is based on anisotropy since diffusivity will be high in a preferential direction and limited in the others. Water motion will be restricted within an anisotropic medium such as the human brain (adapted from Tsougos 2017).

## 4.3.2 Diffusion NMR signal

### 4.3.2.1 Mathematical expression

Sensitization of the NMR signal to the diffusion process in tissues is achieved by the application of strong magnetic gradient pulses imposing a specific phase to the spins of protons, depending on their positions in space. The diffusion sensitization is corresponding to the integration of the phase evolution seen by all the spins contained in a voxel during their displacements. It causes a signal decay that directly depends on the apparent diffusion coefficient along a chosen direction of observation. The greater the diffusivity of water molecules is, the stronger the signal attenuation gets.

The groundwork on encoding the NMR signal for diffusion was made by Stejskal and Tanner [1965], who introduced the pulsed gradient spin echo (PGSE) sequence schematized in Figure 4.9. Its mathematical expression is indicated in Equation (4.4) obtained after resolving the Bloch-Torrey phenomenological NMR equations [Torrey 1956]. Diffusion gradients are applied on both sides of the 180° radiofrequency pulse of a spin echo sequence. Stationary protons' signal will not be lowered because the first dephasing gradient is entirely compensated by the second one. As for diffusion protons, the dephasing will not be completely compensated by the second gradient, leading to a signal decrease. The number of explored diffusion directions and diffusion gradient magnitudes varies on average between 30 to 150 for postmortem imaging, while it generally does not exceed 60 for living subjects in order to keep the acquisition time below a dozen of minutes on modern MRI systems.

$$S(\mathbf{b}, \mathbf{o}) = \rho(1 - e^{-\frac{TR}{T_1}})e^{-\frac{TE}{T_2}}e^{-bD(\mathbf{o})} \quad (4.4)$$

with  $S$  is the magnitude of the NMR signal from water in a specific orientation  $\mathbf{o}$ ,  $\rho$  is the proton density,  $b$  (s/mm<sup>2</sup>) is the diffusion-weighted factor  $b$ -value, and  $D$  (mm<sup>2</sup>/s) is the diffusion coefficient according to orientation  $\mathbf{o}$ .

$D$  reflects the diffusion in pure water but in practice it is the apparent diffusion coefficient (ADC) that is measured along

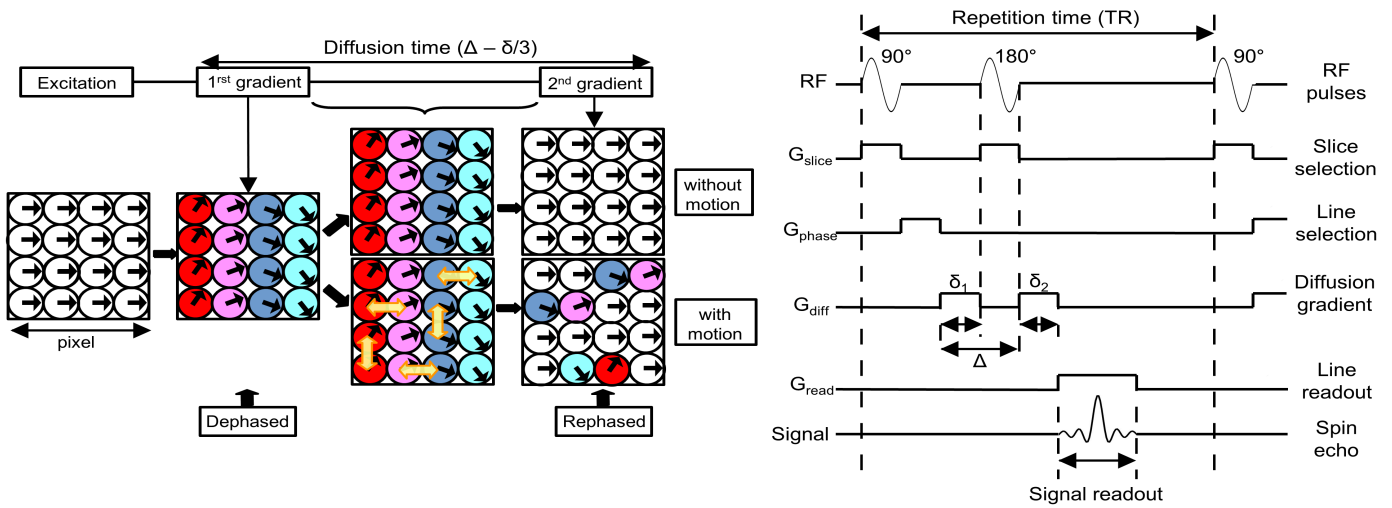


Figure 4.9: Scheme explaining the PGSE sequence and the effects of the application of diffusion gradients ( $\delta_1$  is the first diffusion gradient and  $\delta_2$  is the second one). Image adapted from Beaujoin 2018.

the direction  $\mathbf{o}$ . The ADC fluctuates with the medium viscosity and biological obstacle occurrence. The aforementioned signal decay depends likewise on the degree of diffusion weighting (DW) that corresponds to the b-value. The latter describes the strength and duration of the gradient pulses used to create diffusion-weighted images and is given for rectangular pulses in Equation (4.5):

$$b = (\gamma \|G\| \delta)^2 \left(\Delta - \frac{\delta}{3}\right) \tag{4.5}$$

with  $\gamma$  is the gyromagnetic ratio of protons ( $=42.58$  MHz/T),  $G$  is the gradient amplitude,  $\delta$  is the gradient duration application, and  $\Delta$  is the temporal separation of gradient pulses. The diffusion time  $\tau$  is referred to as  $\tau = \left(\Delta - \frac{\delta}{3}\right)$  and the b-value implies that we can increase sensitization by increasing either gradient timing ( $\delta$  or  $\Delta$ ), or gradient amplitude  $G$ . The spatial distribution of diffusion displacement can hence be mapped in the q-space [Callaghan 1993]. Q-space imaging is a non-parametric method to access the diffusion distribution, which estimates the ensemble average propagator. The latter refers to a 3D probability density function of diffusion displacement. The related  $q$  value to q-space imaging is as follows:  $q = \gamma \|G\| \delta / 2\pi$ .

### 4.3.2.2 Noise and artifacts

Noise is corruption of the signal that originates from physiological sources as well as imperfections in the transmission and reception electronic chains that need to be corrected. Major sources of physiological noise are patient breathing and movements. The SNR of dMRI dataset is relying on multiple sequence parameters (voxel size, receiver bandwidth, number of excitations or averages). It assesses the image quality and corresponds to the mean signal intensity divided by the standard deviation of the noise, as defined in Equation (4.6) that differentiates 2D imaging from 3D imaging :

$$(2D) \quad SNR \propto \frac{e^{-\frac{T}{T_2}} e^{-bD} (\Delta_x \Delta_y \Delta_z) \sqrt{N_y} \sqrt{N_{rep}} B_0}{\sqrt{RBW}} \tag{4.6}$$

$$(3D) \quad SNR \propto \frac{e^{-\frac{T}{T_2}} e^{-bD} (\Delta_x \Delta_y \Delta_z) \sqrt{N_y N_z} \sqrt{N_{rep}} B_0}{\sqrt{RBW}}$$

with  $\Delta_x \Delta_y \Delta_z$  the spatial resolutions,  $N_y$  the number of phase-encoding steps in the y-axis,  $N_z$  the number of phase-encoding steps in the z-axis,  $N_{rep}$  the number of excitations (or averages),  $B_0$  the static magnetic field and  $RBW$  the readout bandwidth.

Artifacts can cause real anatomical image distortion or simulate pathologies. Knowing their origin prevents interpretation errors and improves image quality (e.g. SNR, contrast). The existing artifacts are categorized into two types: artifacts related to MRI scanner hardware and those patient-related. From the first category, there are:

- eddy current artifacts, specific to dMRI. They stem from loops of electrical current caused within conductors by a modified magnetic field in the conductor. They produce unwanted additional magnetic field gradients that may interfere with the actual shape of diffusion and encoding spatial gradient pulses and distort the resulting image.
- truncation artifacts, also known as ringing artifacts or Gibbs' artifacts, induced by an abrupt signal transition at the biological interfaces (e.g. fat/muscle interface). They arise as low and high-intensity periodical stripes remaining parallel to the transition area.
- aliasing artifacts appearing in phase-encoding and frequency-encoding directions when the scanned element is bigger than the field of view (FOV). The elements out of the FOV fold back in the contralateral side.
- chemical shift artifacts coming from variations of the protons' Larmor frequency in distinct chemical environments (for example, fat/water). A bright line appears where two signals overlap and a dark line stands out where they cancel each other.
- magnetic susceptibility artifacts due to an overlay of two structures with really different magnetic susceptibilities which causes an intrinsic magnetic gradient at their interface. Thus the MR signal is hypointense at the transition area with a broaden cavity.
- cross-talk (or slice-overlap) artifacts occurring when surrounding slices of the selected slice are excited by a RF pulse. It leads to a contrast modification and/or a signal loss through partial saturation in the slice or zone of intersection.

From the second category, that was not encountered during this thesis thanks to *ex vivo* MRI, there are:

- metal artifacts, where ferromagnetic structures provoke local distortions of the magnetic field and so no-signal area which leads to a distorted image. They are emphasized in high-field devices.
- motion artifacts, where the image is blurred due to signal dispersion and ghosting is possible (alternating between hypointense and hyperintense signal stripes). They are exacerbated by high-field and long TR sequences.

### 4.3.3 Diffusion MRI sequences

Plenty sequence schemes exist to acquire diffusion-weighted dataset: schemes based on single SE or multi SE sequences, schemes based on STEAM sequences, schemes based on balanced SSFP sequences. In addition to these common schemes, it is also possible to use various diffusion pulse shapes: trapezoidal PGSE, sine and cosine PGSE, oscillating profiles such as sine and cosine OGSE, sine and cosine trapezoid-OGSE [Parsons et al. 2003; İlanuş et al. 2013; Baron et al. 2014; Drobnjak, Zhang, İlanuş, et al. 2016], simple or double diffusion encoding.

Free diffusion gradient profiles were introduced by Callaghan 1993 to optimize the profile according to the target microstructural feature using a matrix formalism based on the decomposition of the profile into a series of narrow pulses [Drobnjak, Zhang, Hall, et al. 2011]. More recently, the b-tensor formalism was presented to allow complex trajectories in the diffusion space [Westin et al. 2002; Jespersen et al. 2007; Nilsson et al. 2013]. It enables the computation of advanced features characterizing the diffusion process locally and relying on complex diffusion pulse shapes.

Last, the signal acquisition can rely on many readout schemes, from 2D/3D EPI readout to advanced readout schemes taking into account the signal parsimony to fasten the acquisition. Here are presented two sequences that were employed in the course of this thesis: 3D multi-shot echo planar imaging (EPI) and steady state free precession (SSFP) sequences.

The EPI acquisition technique was introduced by Peter Mansfield [Mansfield 1977]. It is part of the fast imaging MRI sequence family and it is also insensitive to small motion, making EPI widespread in clinical DW imaging. The original single-shot sequence swiftly acquires adjacent lines one after another, covering up to the entire k-space with only one RF excitation pulse. The multi-shot version uses multiple RF pulses, hence reducing the echo train duration and the fraction of k-space captured per shot. Therefore, the SNR is increased in exchange of a longer scan time than single-shot EPI, which is usually not a downfall in postmortem imaging, as well as a substantial reduction of the sensitivity of the sequence to magnetic susceptibility effects. To gain in efficacy, multi-shot EPI sequences require the use of powerful gradient sets to rapidly commute that are usually only available on UHF preclinical MRI scanners. Unfortunately, human connectome gradients do not allow to commute gradients *in vivo* without preventing the induction of peripheral nerve stimulation.

The alternative SSFP sequence was introduced by Herman Y. Carr [Carr 1958]. It corresponds to a GRE sequence where a non-null steady state exists for the longitudinal and transverse components of magnetization, plus the TR is shorter than the  $T_1$  and  $T_2$  relaxation times of the tissue. The NMR signal never fully decays, provided that the RF excitation pulses are close enough one to another. Consequently, the proton spins in the transverse plane never fully dephase. The steady state is maintained by the TR and the flip angle that must be as short as possible in order to allow the NMR signal to propagate through many TRs and accumulate from multiple echoes in a highly efficient manner [Buxton 1993; McNab, Jbabdi, et al. 2009]. This sequence was proven to be highly efficient in the case of postmortem DW imaging in large-bore clinical MRI scanners [McNab, Jbabdi, et al. 2009; Miller, Stagg, et al. 2011; Miller, McNab, et al. 2012; Foxley et al. 2014], compared to diffusion weighting SE that seems to be more suited for *in vivo* diffusion weighting imaging. Foxley et al. 2014 points out that DW SSFP achieves greater performances at higher magnetic fields (7T versus 3T). Nevertheless, modeling the actual diffusion sensitization remains a complex task due to mitigation between diffusion attenuation and  $T_1$  relaxation effects.



### 4.3.4 Local modeling of the diffusion process

#### 4.3.4.1 Diffusion tensor imaging (DTI)

The diffusion tensor imaging (DTI) model developed by Basser et al. 1994, is one of the most broadly used modeling for the primary orientation of white matter axonal pathways in the brain. DTI derives fiber tract directional information from the diffusion-weighted data using three-dimensional or multidimensional vector algorithms, based on a theoretical minimum of 6, but of 30 in practice, diffusion-sensitized gradient directions, to obtain robust diffusion tensor estimation. The target diffusion tensor corresponds to a 3x3 matrix  $\mathbf{D}$  that is symmetrical and positive-definite. It can be achieved using simple log-multilinear regression, advanced Riemannian, or log-euclidean estimators that ensure its positiveness [Fillard et al. 2009]. The tensor model assumes the existence of a single homogeneous population of fibers within each voxel, but this assumption is seldom correct. The model is defined as a Gaussian diffusion propagator which isosurfaces can be geometrically represented by ellipsoid. The  $\mathbf{D}$  matrix can be diagonalized, giving 3 eigenvalues ( $\lambda_1 > \lambda_2 > \lambda_3$ ) and 3 eigenvectors ( $\mathbf{e}_1, \mathbf{e}_2, \mathbf{e}_3$ ), corresponding to the axes of the ellipsoid (see Figure 4.10).  $\mathbf{e}_1$  points to the principal orientation of the axon. The corresponding  $\lambda_1$  eigenvalue is called the longitudinal, axial, or parallel diffusivity ( $D_{\text{parallel}}$ ). The two other eigenvectors are the two small axes tensors, corresponding  $\lambda_2$  and  $\lambda_3$  eigenvalues, that are usually averaged to produce a measure called the perpendicular, radial or transverse diffusivity ( $D_{\text{transverse}}$ ). From the diffusion tensor  $\mathbf{D}$ , diffusion anisotropy measures, such as the fractional anisotropy (FA) (Equation (4.7)) or the mean diffusivity (MD) (Equation (4.8)) can be computed. FA describes the degree of anisotropy of the diffusion process, going from 0 (isotropic diffusion) to 1 (fully hindered diffusion in one direction). MD expresses the average mobility of water molecules by being the mean of the three eigenvalues of  $\mathbf{D}$ .

$$FA = \sqrt{\frac{3}{2}} \sqrt{\frac{(\lambda_1 - \bar{\lambda})^2 + (\lambda_2 - \bar{\lambda})^2 + (\lambda_3 - \bar{\lambda})^2}{\lambda_1 + \lambda_2 + \lambda_3}} \quad (4.7)$$

$$MD = \bar{\lambda} = \frac{\lambda_1 + \lambda_2 + \lambda_3}{3} \quad (4.8)$$

Limitation of the DTI model is due to its Gaussian assumption that makes it unable to model the existence of several fiber populations. DTI can indicate the direction of only one fiber population per voxel, which pushed the MRI community to develop high angular resolution diffusion models.

#### 4.3.4.2 High angular resolution diffusion imaging (HARDI)

**Model-based and model-free reconstruction techniques** To tackle the limitations of the DTI model, a plurality of local models of the diffusion process has emerged. They can be partitioned as model-based techniques, which make assumptions on the biological diffusion properties, and model-free techniques that are assumption-free. Table 4.1 reviews the main models stemming from the high angular resolution diffusion imaging (HARDI) techniques.

HARDI was first introduced by Weeden with diffusion spectrum imaging (DSI) [Wedeen et al. 2000]. An alternative approach presented by David S. Tuch [Tuch 2002] aimed at solving the crossing-fiber issue raised by DTI using a decomposition of the diffusion propagator as a weighted mixture of multiple Gaussian tensors. Tuch's method requires to sample the signal along a greater number of diffusion directions than DTI, as well as a higher b-value in order to

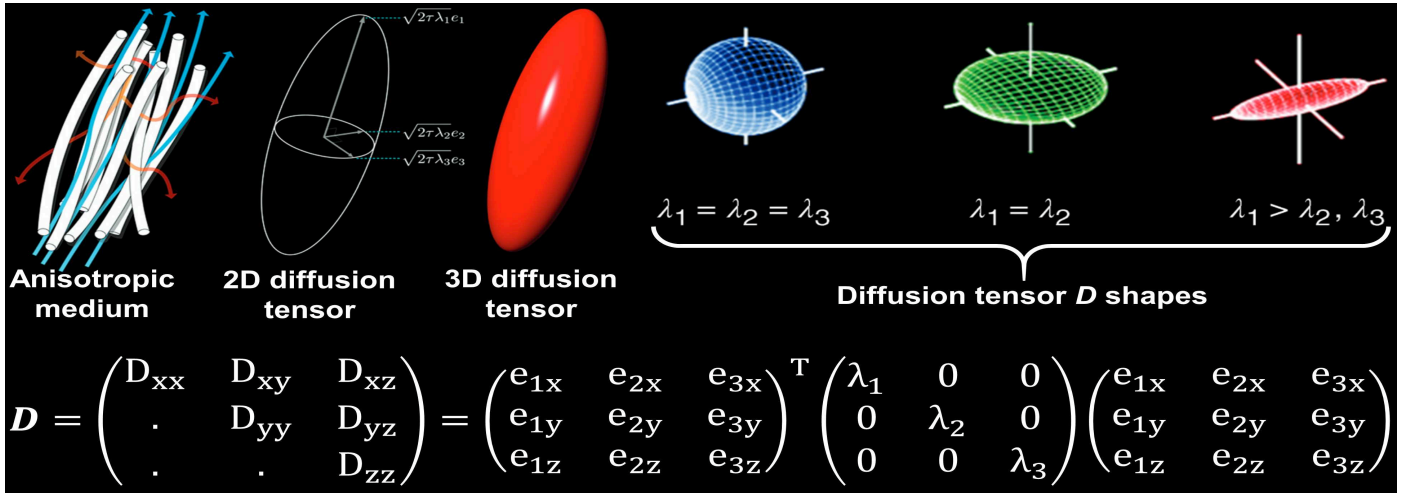


Figure 4.10: Illustration of the DTI diffusion tensor and its matrix  $\mathbf{D}$ .  $\tau = \Delta - (\delta/3)$  is the diffusion time (adapted from Descoteaux 2015).

improve the angular contrast and resolution. From there, three commonly used types of approaches can provide the q-space sampling (space gathering the dynamic spin displacements, distinguished to the k-space that collects static spin displacements):

1. Dense 3D Cartesian grid sampling of the q-space based on the Fourier relationship between q-space and the propagator space introduced by Callaghan 1993. That sampling led to diffusion spectrum imaging (DSI) [Wedeen et al. 2000].
2. Spherical sampling of the q-space for a single (single-shell) or multiple (multiple-shell) b-values [Tuch 2002].
3. Hybrid sampling of the q-space using several shells (corresponding to distinct b-values), with distinct number of orientations for each shell, or other more elaborate distributions. This q-space sampling led to hybrid diffusion imaging (HYDI) [Wu and Alexander 2007].

The diffusion orientation distribution function (dODF) and the fiber orientation distribution function (FOD), illustrated in Figure 4.11, are the two major depictions produced by the HARDI approaches cited in Table 4.1. The dODF is the probability distribution of the diffusion spins on a sphere, while the FOD is the probability distribution of the fiber orientation in a sphere. They are now must-have tools to reconstruct dODF and FOD maps for the established HARDI techniques. Similar to the FA related to DTI, rotationally-invariant scalar features can also be computed from HARDI-based ODFs, like the generalized fractional anisotropy (GFA) defined in Equation (4.9) as the ratio of the root mean square of the standard deviation of the ODF values over the mean sphere.

$$GFA = \frac{std(ODF)}{rms(ODF)} = \sqrt{\frac{n \sum_{i=1}^n (ODF(\mathbf{o}_i) - \langle ODF(\mathbf{o}) \rangle)^2}{(n-1) \sum_{i=1}^n ODF(\mathbf{o}_i)^2}} \quad (4.9)$$

where  $ODF(\mathbf{o})$  is the ODF value in direction  $\mathbf{o}$ ,  $n$  is the number of considered ODF directions and  $\langle ODF(\mathbf{o}) \rangle$  is the mean ODF intensity.

Today, Q-ball and CSD models are the most commonly used models because of their simplicity and computational

Model-based approach			Model-free approach		
Model name	Publications	Guiding principle	Model name	Publications	Guiding principle
Ball and Stick	Behrens, Woolrich, et al. 2003	Multi tensor based	aQBI	Descoteaux, Angelino, et al. 2007	SH decomposition, FHT
CHAR-MED	Assaf and Basser 2005	Hindered compartment separation	DSI	Wedeen et al. 2000	Cartesian sampling, FFT 3D
CSD	Tournier, Calamante, et al. 2007	Spherical deconvolution with	QBI	Tuch 2002	Spherical sampling, FRT
SDT	Descoteaux, Deriche, et al. 2008	a Gaussian fiber response	DOT	Özarslan, Shepherd, et al. 2006	Pointwise convergent expansion of the plane wave
Wisharts mixtures	Jian et al. 2007	Functions of sphere	GDTI / HOT	Liu, Bammer, et al. 2003; Ghosh et al. 2008	Generalization of Fick's Law, high-order diffusion tensors
			K <sub>D</sub> T	Jensen et al. 2005	Kurtosis analysis
			PAS-MRI	Jansons et al. 2003	Dirac radial propagator shape
			SHORE	Özarslan, Koay, et al. 2013	MAP per voxel from dMRI data

Table 4.1: Review of the major HARDI techniques, distinguishing model-dependent from model-free reconstruction techniques. FFT = fast Fourier transform. FRT = Funk Radon transform. SH = spherical harmonics. FHT = Funk-Hecke transform. MAP = mean apparent propagator.

efficiency to produce complete ODF/FOD maps over the entire brain.

**Multi-compartment models** Microstructure modeling of the brain tissue aims at detailing the diffusion-weighted signal not only by one mono-exponential component, but also by combining the signals arising from distinct compartments of the cerebral tissue within the voxel. The multi-compartment models are part of biophysical models that consist in a geometrical representation of the brain tissue, associated with multiple components. The models existing in the literature (see Figure 4.12) rely on natural compartmentalization of the brain tissue. These models infer the measured diffusion-weighted signal attenuation as the integration of individual contributions stemming from each compartment, weighted by their given volume fractions. Then, the solving of the inverse problem gives brain tissue features from the measured diffusion-weighted data. The compartments in the white matter are the axons, the glial cells and the extracellular space, while they correspond to the cell bodies, the astrocytes, the dendrites and the extracellular space in the gray matter. The CSF is likewise considered in order to reflect any partial volume effect due to the limited spatial resolution of dMRI data. A variety of models has emerged during the last decade and Figure 4.12 summarizes the major ones. A special emphasis is next put on the neurite orientation dispersion and density imaging (NODDI) model [Zhang, Schneider, et al. 2012] that was used in this thesis.

Zhang, Schneider, et al. 2012 present the neurite orientation dispersion and density imaging (NODDI) model as a simplified version of ActiveAx with clinical purposes [Colgan et al. 2016; Kodiweera et al. 2016; Kamiya et al. 2020; Nazeri et al. 2020]. NODDI operates with two to three shells, agreeing then with clinical routine expectations. This three-compartment model, shown on Figure 4.12, represents the intracellular compartment as sticks mathematically following a Watson distribution. Hindered Gaussian distribution accounts for the extracellular space. As for the CSF compartment, it is modeled by unhindered isotropic diffusion. The Watson distribution is however symmetrical around

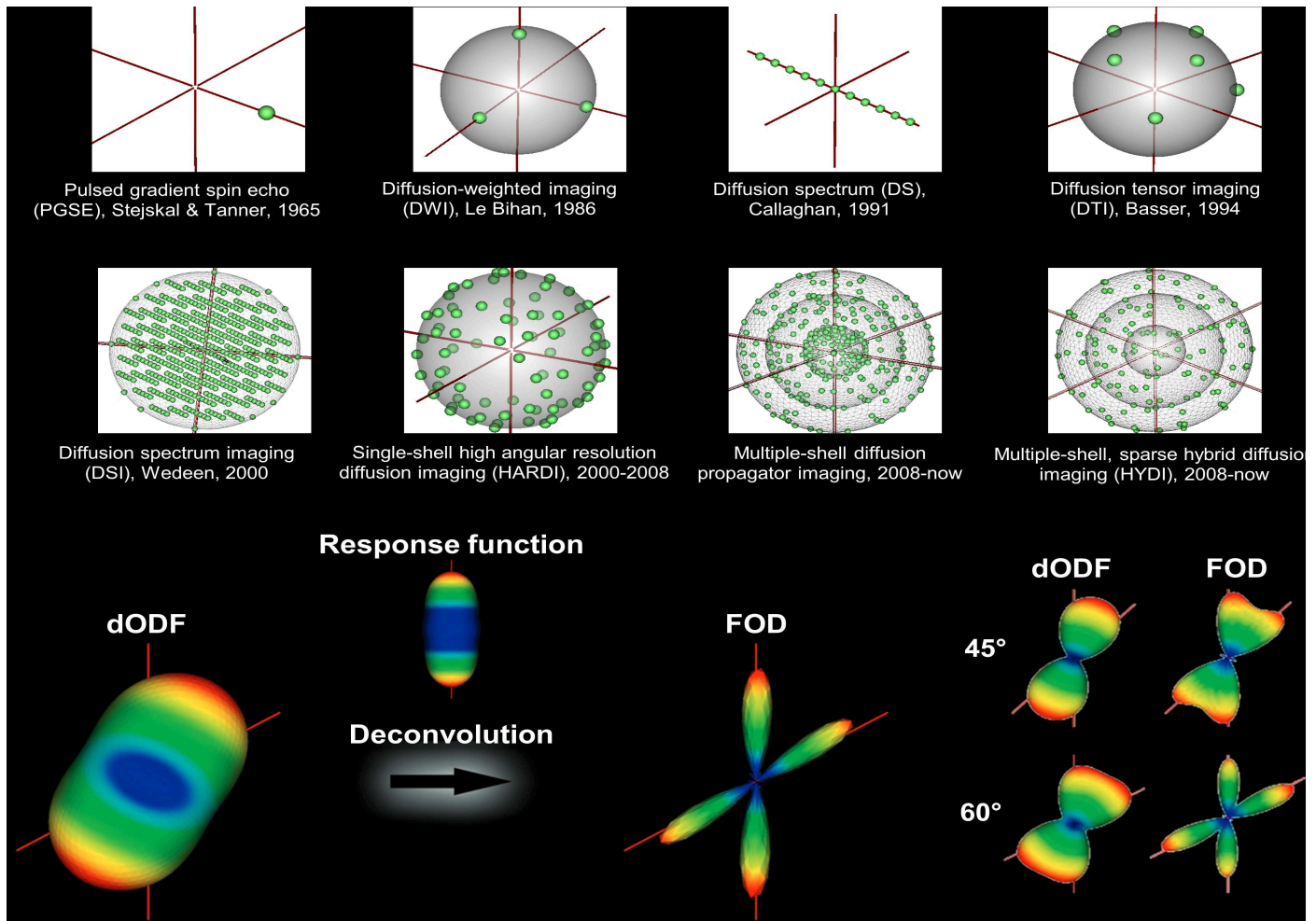


Figure 4.11: Representation of the evolution of the q-space sampling (at the top), the diffusion orientation distribution function (dODF) and the fiber orientation distribution function (FOD) (at the bottom). Courtesy of Dr C. Poupon and adaptation from Descoteaux 2015.

the principal fiber orientation, making crossing-fiber situations uncovered. That is why Bingham-NODDI [Tariq et al. 2016], NODDI-SH [Zucchelli et al. 2017] and MTE-NODDI [Gong et al. 2020] were developed to increase the robustness of the NODDI model.

### 4.3.5 Applications of diffusion-weighted imaging

#### 4.3.5.1 Tractography to access the structural connectivity

The directional information stemming from the diffusion local models can be exploited to reconstruct fiber tracts through the brain. This process is called tractography. Tractography algorithms are typically classified into three groups: deterministic methods, probabilistic methods and global methods. The streamline deterministic approach [Pierpaoli and Basser 1996; Poupon et al. 1998; Mori, Crain, et al. 1999] computes streamlines following the best diffusion path (e.g. systematically following the most likely direction of the underlying dODF or FOD) [Conturo et al. 1999]. The streamline












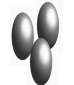


	Compartments				Major models			
	Intra-cellular	Extra-cellular	Isotropic	Stationary (fixed tissue)				
A.	 Parallel sticks	+	 Sphere (ball)		<b>Ball &amp; Stick</b> [Behrens et al., 2003]			
B.	 Parallel cylinders with : 1. fixed diameter 2. diameters following a gamma distribution 3. mean diameter	+	 Gaussian anisotropic diffusion	+	 Sphere (ball)	+	 Dot	1. <b>CHARMED</b> [Assaf and Basser, 2005] 2. <b>AxCaliber</b> [Assaf et al., 2008] 3. <b>ActiveAx</b> [Alexandre et al., 2008, 2010]
C.	 Cylinders with orientation dispersion	+	 Gaussian anisotropic diffusion	+	 Sphere (ball)	+	 Dot	<b>ActiveAx with orientation dispersion</b> [Zhang et al., 2011]
D.	 Sticks with orientation dispersion	+	 Gaussian anisotropic diffusion	+	 Sphere (ball)	+	 Dot	<b>NODDI</b> [Zhang et al., 2012]

Figure 4.12: *Compilation of the major multi-compartment models with the corresponding compartments. The Ball & Stick model [Behrens, Woolrich, et al. 2003] is the only two-compartment one, whereas CHARMED [Assaf and Basser 2005], AxCaliber [Assaf, Blumenfeld-Katzir, et al. 2008], ActiveAx [Alexander 2008; Alexander et al. 2010; Zhang, Hubbard, et al. 2011] and NODDI [Zhang, Schneider, et al. 2012] models differentiate the extracellular space from the CSF. The stationary compartment corresponds to the water trapped in glial cells after tissue fixation and is consequently used only for ex vivo studies. Image adapted from Beaujoin 2018.*

probabilistic approach [Behrens, Woolrich, et al. 2003; Parker et al. 2003; Perrin, Poupon, Rieul, et al. 2005; Chao et al. 2007] allows to moderate deviations from the most likely direction, which enables to increase the robustness of the tractography algorithm to the noise corrupting the dMRI dataset and thereby the ODF field. Global approaches [Poupon 1999; Jbabdi et al. 2011; Reisert et al. 2011; Neher et al. 2012; Mangin, Fillard, et al. 2013] go a step further by computing simultaneously all the trajectories in a competitive manner to avoid the creation of fiber configurations that would not correspond to plausible anatomical connections, depending on the level of anatomical and microstructural priors taken into account. Figure 4.13 shows an example of a human tractogram, obtained using a regularized streamline deterministic tractography approach.

Tractograms reconstructed at the individual scale on a cohort stand for inputs of two core applications. Firstly, there is the inference of the human connectome [Sporns et al. 2005] aiming at providing a joint representation of the structural and functional networks. It relies on the computation of individual connectivity matrices between regions of interest (cortical areas provided by cortex parcellations and deep gray structures). The connectivity matrix generates for each pair of regions a feature indicating the connectivity strength, whether it is structural or functional. That is why the American Human Connectome Project (HCP) was launched in 2010 to scan 1200 twin subjects from whom high-resolution diffusion, functional and anatomical MRI data were collected on advanced 3T Connectome MRI scanners. It allowed new parcellations of the cortical surface [Van Essen and Glasser 2016]. The construction of an average structural connectivity matrix for the HCP cohort is still an ongoing task since the community realized that the available diffusion

processing pipelines stemming from the main diffusion groups over the world could provide highly variable results between groups. This major variability is not only due to the ill-posed nature of the fiber reconstruction from dMRI data, but also to the numerous pre-processing steps inducing poor accuracy of the diffusion-based tractography methods to reconstruct the fiber terminations entering the cortical ribbon. The harmonization of pre- and post-processing pipelines is currently undertaken by the diffusion community to reduce the variability across pipelines.

Secondly, there is the inference of high-resolution atlas of the structural connectivity which led to *in vivo* structural connectivity. dMRI has revolutionized the study of white matter fiber bundles. Before its introduction in the 1990s, only postmortem Klinger's dissection approaches were available to map fiber bundles. The pitfall of this technique is the possibility to investigate a few bundles from a single brain sample, whereas dMRI offers a complete *in vivo* investigation at the scale of each subject. Using diffusion-based tractograms and advanced clustering methods allowed to establish new atlases of the larger white matter bundles and to study their morphometric changes across subjects [Guevara, Poupon, et al. 2011; Garyfallidis et al. 2012]. More recently, thanks to high-resolution dMRI datasets, an emphasis was put on the creation of new atlases of superficial connectivity, which has never been described by neuroanatomists before due to missing imaging techniques [Guevara, Perrin, et al. 2008; Avila et al. 2019; Guevara, Guevara, et al. 2020]. Such atlases are a unique opportunity to investigate the inter-subject variability of functional networks and to investigate these new information to establish novel imaging markers in brain pathologies that could be related to abnormal structural connectivity patterns.

Aside these two core applications of dMRI, tractography is also instrumental in deciphering the tissue microstructure and to estimate proxies to the cytoarchitecture. The proxies provide new contrast mechanisms that are worth being investigated to better delineate the anatomical structures and characterize them from a microscopic standpoint. Changes of gross anatomical structures can be related to microstructural changes that can be efficiently probed with dMRI.

#### 4.3.5.2 Clinical applications

dMRI has become a routine modality for the diagnosis of stroke in emergency cases. Unlike conventional  $T_1$ -weighted,  $T_2$ -weighted, or FLAIR imaging, dMRI reveals infarcted brain regions as soon as the occlusion of the arteries occurs. It is arising by a decreased diffusivity in impaired tissues or increased diffusivity in case of hemorrhagic strokes [Le Bihan, Turner, et al. 1992; Ebisu et al. 1997; Lansberg et al. 2000; Fink et al. 2002].

Nevertheless, applications of dMRI goes far beyond neurovascular diseases. A non-exhaustive list includes cerebral development and aging, neurodegenerative diseases, neuropsychiatric disorders, stroke, inflammatory pathologies (i.e. multiple sclerosis (MS)), drug-resistant epilepsy, infarct and tumors [Schellinger et al. 2001; Sullivan et al. 2006; Li et al. 2012; James et al. 2015; Bergamino et al. 2021; Cimflova et al. 2021; Rahmzadeh et al. 2021]. Diffusion-derived parameters can account for the white matter healthy state. For instance, longitudinal or radial diffusivity can reflect pathological processes, as in the evaluation of white matter infarct. Radial diffusivity is considered to be related to membrane integrity. Furthermore, diffusion-weighted imaging may also have a significant role in therapeutic follow-up and prognosis establishment in various brain lesions, and thus be an integral part of diagnostic brain imaging protocols [Tsougos 2017]. By enabling the evaluation of the brain parenchyma on a submillimeter scale, very small cerebrovascular lesions, such as cortical microinfarcts, have come within the detection limit of 7T and to a lesser degree 3T MRI [De Cocker et al. 2018].

This section integrated the many aspects of diffusion-weighted magnetic resonance imaging (dMRI), considering its physical process, the applied dMRI sequences, its specificity regarding postmortem imaging, the local models revealing structural connectivity, as well as the applications. The next section reflects on quantitative magnetic resonance imaging

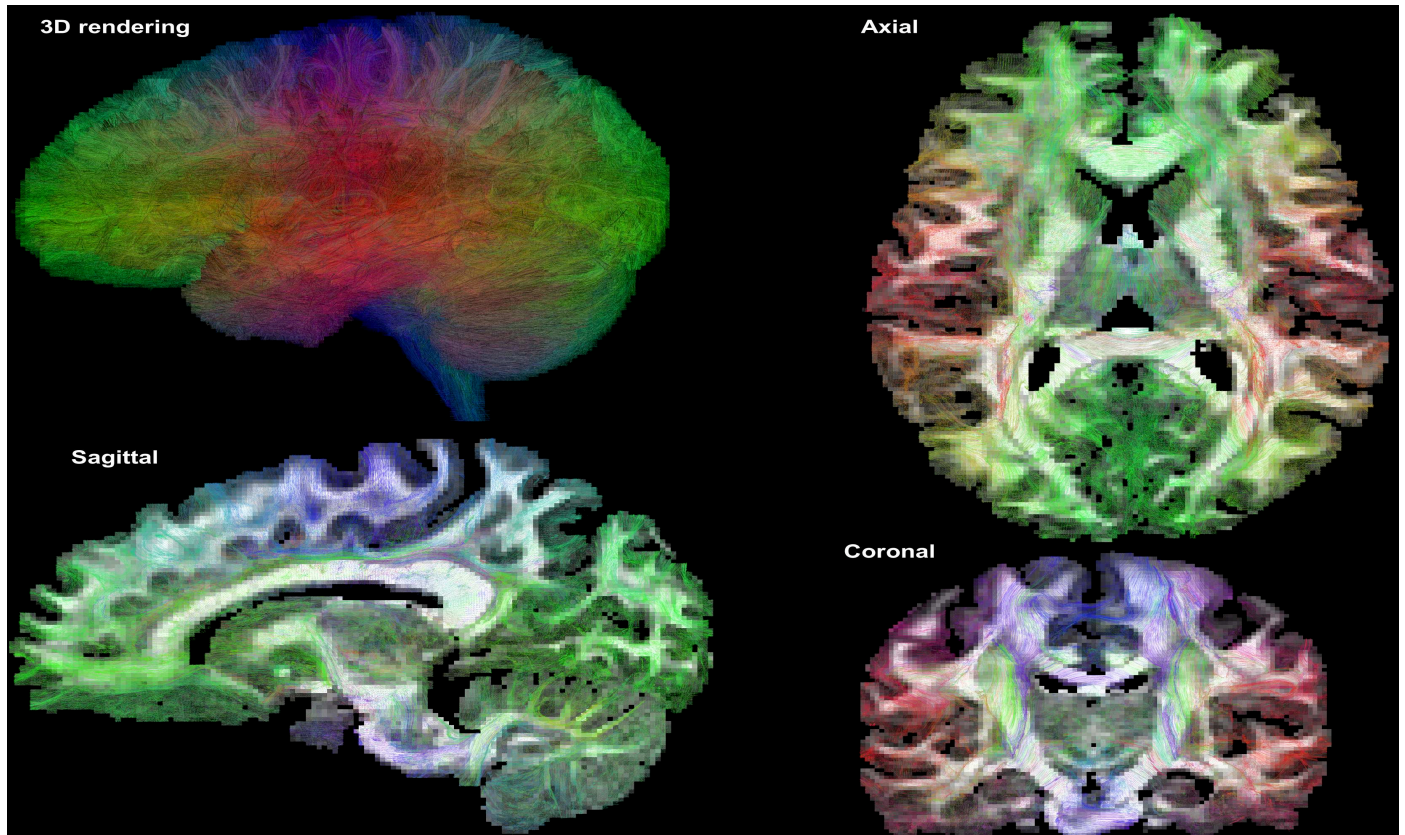


Figure 4.13: Human tractogram from the HCP database computed using a streamline regularized deterministic approach. The tractogram is superimposed on its GFA map. Courtesy of Dr I. Uszynski and Dr B. Herlin.

(qMRI), to understand the process, the related qMRI sequences, and eventually its applications that can be coupled with dMRI.

## 4.4 Quantitative MRI

In contrast to conventional MRI ( $T_1$ -weighted,  $T_2$ -weighted,  $T_2^*$ -weighted), quantitative magnetic resonance imaging (qMRI) or relaxometry aims at measuring the absolute  $T_1$ ,  $T_2$  and  $T_2^*$  relaxation times. The parameters are corrected for instrumental biases [Lutti, Hutton, et al. 2010], making qMRI suited for standardization. Furthermore, the direct relation of qMRI parameter maps to single physical properties of the tissue increases its sensitivity to microscopic tissue properties as compared to standard anatomical images [Cercignani et al. 2018]. Various MRI methods have been developed in the literature (see Cercignani et al. 2018 for an overview of them). The current section will focus on the ones that have been investigated in the frame of this thesis.

### 4.4.1 Quantitative $T_1$ mapping

The gold standard for  $T_1$  quantification is the inversion recovery (IR) technique. Several measurements are performed, each of which comprises spin inversion made by a  $180^\circ$  RF pulse, a subsequent delay called the inversion time (TI) (time interval between spin inversion and measurement), spin excitation using a  $90^\circ$  RF pulse, and then signal readout. The signal equation referring to the inversion recovery curve is given by:  $S(TI_i) = S_0(1 - 2e^{-TI_i/T_1})$ , where  $TI_i$  is the  $i$ -th inversion time and  $S_0$  corresponds to the signal at  $TI = 0$ ms. By changing the TI, the IR curve is sampled, that way  $T_1$  value in the scanned tissue is inferred to by exponential data fitting. The major downfall of IR method is its time-consuming aspect, since it requires a full spin relaxation before each spin inversion. The need for fast  $T_1$  mapping techniques, especially in high-resolution postmortem imaging, was self-evident.

The variable flip angle (VFA) technique enables likewise  $T_1$  mapping [Wang et al. 1987; Trzasko et al. 2013; Heule et al. 2017]. In contrast to the resembling Look-Locker technique that also quantifies spin-lattice relaxation time [Look et al. 1970], acquisition times are noticeably longer than  $T_1$ , due to the use of relatively long TR. The principle is to acquire multiple datasets with different flip angles  $\alpha$  to assess the signal amplitude for each voxel (see Equation (4.10)), while assuming perfect RF spoiling. It requires then spoiled gradient echo (SPGR) imaging, which relies on short TR, making this method clinically feasible [Stikov et al. 2012]. Nonetheless, a common pitfall of the Look-Locker and the VFA techniques is inaccurate knowledge of the flip angles due to transmit field  $B_1^+$  inhomogeneity [Cheng et al. 2006]. Consequently, VFA method implies additional  $B_1$  mapping, as well as calculation of the actual flip angle for each voxel, and usage of this angle in Equation (4.10). Various  $B_1^+$  mapping methods are available, such as the dual angle method [Insko et al. 1993; Stollberger et al. 1996; Cunningham et al. 2006; Boudreau et al. 2017] or the 3D EPI method [Lutti, Hutton, et al. 2010].

$$S(\alpha) = S_0 \sin(\alpha) \frac{1 - \exp(-TR/T_1)}{1 - \cos(\alpha) \exp(-TR/T_1)} \quad (4.10)$$

### 4.4.2 Quantitative $T_2$ mapping

$T_2$  quantification can be undertaken with a spin echo sequence. Variations of the basic sequence led to MRI sequences offering a robust estimation of  $T_2$ , such as the multi slice multi echo (MSME) sequence. After the  $90^\circ$  RF pulse, a series of  $180^\circ$  refocusing pulses are applied to create a train of  $n$  echoes. Each echo amplitude decreases due to  $T_2$  decay. The output image integrates the  $n$  acquired echoes:  $S(t) = S_0 e^{-t/T_2}$ , with  $t = TE_i, i \in n$ . The multi-slice dimension comes from the acquisition of the same line in different slices of the sample, using distinct frequencies to navigate amid the acquired slices. This is all happening during the repetition time that is relatively long ( $TR \gg T_1$ ). The SE sequence has other  $T_2$ -quantifying variations including the multi-echo  $T_2$  (MET<sub>2</sub>) approach [Carr and Purcell 1954], the Carr–Purcell–Meiboom–Gill (CPMG) sequence [Meiboom et al. 1958], and the gradient and spin echo (GRASE) acquisition [Schachter et al. 2000]. They are all commonly employed in the MRI community.

The steady state free precession (SSFP) sequence can also lead to  $T_2$  mapping. For instance, driven equilibrium single-pulse observation of  $T_2$  (DESPOT2) [Deoni et al. 2003] relies on balanced SSFP (bSSFP) sequence by exhibiting a  $T_2/T_1$  contrast and measures  $T_2$  value. This method has been criticized for its difficult fitting with standard non-linear fitting algorithms [Bouhrara et al. 2016].



### 4.4.3 Quantitative $T_2^*$ mapping

The conventional technique for  $T_2^*$  quantification is gradient echo (GRE) imaging. The corresponding equation is shown in Equation (4.11), where  $\theta$  is the applied flip angle that tips the longitudinal magnetization [Bernstein et al. 2004]. One can also resort to fast-low-angle shot (FLASH) MRI sequence. The latter is a fast GRE imaging sequence with complete spoiling of transverse coherences, which provides a MR contrast largely independent of the spin-spin relaxation time. This is achieved by cycling adequately the phase of the RF excitation pulse, which has the effect of spoiling the transverse magnetization. It appears that  $T_2^*$  relaxation time is higher for *ex vivo* than *in vivo* subjects [Sengupta et al. 2018], leading to different values and contrasts in postmortem imaging.

$$S(\theta) = \rho_0 \sin(\theta) \frac{[1 - \exp(-TR/T_1)]}{[1 - \cos(\theta)\exp(-TR/T_1)]} \exp(-TE/T_2^*) \quad (4.11)$$

with  $\rho_0$ , the initial proton density of the imaged tissue.

### 4.4.4 Applications of quantitative MRI

Conventional MRI techniques show mixed contrasts but qMRI provides quantitative values for each voxel image, which can be compared between follow-up scans of the same patient. Relaxometry alone has multiple clinical applications, especially in neuroimaging studies.  $T_1$  mapping enables, for instance, the differentiation of different types of dementia, the detection of hemorrhagic transformation in patients with stroke, the evaluation of cerebral tissue abnormalities in patients with human immunodeficiency virus infection, or the detection of tissue changes in patients with temporal lobe epilepsy ([Cercignani et al. 2018].  $T_1$  mapping is also greatly considered for brain tumor, multiple sclerosis and movement disorder diagnoses. The myelin water fraction (MWF) mapping is the most common use of quantitative  $T_2$ . It corresponds to the fraction of the myelin water NMR signal relative to the total signal, knowing that the myelin water NMR signal is the fraction of the signal from water trapped in myelin bilayers [Liu, Rubino, et al. 2019]. This highly hindered environment reduces the amount of possible motion for the water molecules and thus it shortens the  $T_2$  values. Mapping myelin water fraction must take into account the temperature surrounding the sample, which can modify the the resulting map [Prevost et al. 2021].  $T_2$  mapping as a single component is otherwise a mere quantitative indicator of biological change in the tissues.  $T_2^*$  is inversely proportional to the concentration of iron content [Gelman et al. 1999; Dyrby, Innocenti, et al. 2018], and this sensitivity to iron content is enhanced at high magnetic field [Peters et al. 2007]. The  $T_2^*$  contrast comes from the magnetic susceptibility of lipid molecules and iron-containing molecules, particularly ferritin, which differs from the magnetic susceptibility of water [Duyn 2012].

Beyond relaxometry, qMRI has seen its field of quantitative features expand, thanks to the development of advanced biological models of tissue structure and function. A non-exhaustive list of features would include quantitative magnetic susceptibility (QSM), magnetization transfer (MT), myelin volume fraction (MVF), and water content (WC). However, their estimations were out of the scope of this thesis.

## 4.5 Conclusion

This third and last background chapter reviewed the principles linked to ultra-high field imaging of *ex vivo* specimens to enable the investigation of the cerebral microstructure. The physical bases of conventional MRI, dMRI and qMRI were presented due to their contributions to the thesis. Postmortem imaging was also detailed to understand its specificity on the scanned sample and the choice of MRI scanners and sequences.

The next part of this manuscript presents the investigation of the structural connectivities conducted on a distinctive breeding animal, the Japanese quail, as well as on wildlife animals raised in the ZooParc de Beauval (Beauval zoo, Saint-Aignan, France), based on *ex vivo* ultra-high field MRI. This second part takes an interest in the benefits of connectomics on a behavioral standpoint. In addition, the applied tractography approach of this second part has set a precedent for mapping the intra-cortical connectivity of the human cerebral cortex, as discussed in the third part of this manuscript.



## **Part II**

# **Postmortem investigation of the structural connectivity in breeding and wildlife animals**



## Chapter 5

# Structural connectivity atlas of the Japanese quail, a breeding bird to explore emotivity

This chapter presents the study conducted on a cohort of Japanese quails separated into two lineages based on their emotionality trait. The tested hypothesis was to verify if the two lines present the same connectome, especially concerning the connections involved in their emotivities. Our work led to the creation of the very first structural connectivity atlas of the Japanese quail using diffusion anatomical MRI at 11.7T that exhibited hemispherical differences, as well as a lineage effect for the identified white matter bundles.

### 5.1 Introduction

Connectomics research, which was initiated for humans, has also aroused the interest of the animal neuroscience community, due to its contribution to study animal cognition. The latter includes adaptation coping and environmental perception. In this context, more and more studies focused their interest on the animal cognitive abilities [Boissy et al. 2007; Destrez et al. 2013; Perez et al. 2020] and the animal brain mapping [Guesdon et al. 2015; Menant et al. 2018]. For instance, non-human primates studies were conducted to understand the commonalities and singularities of the human brain [Savage-Rumbaugh et al. 1986; Phillips, Bales, et al. 2014]. Livestock animals have been little exploited in connectomics studies, even though they offer many advantages. These benefits comprise improving animal well-being and breeding conditions, all the more so as their breeding is often accompanied by selection processes aiming at creating different lines. The lines are mostly selected for their productive traits, but the selection can also target the modification of some of their morphological characteristics or behavioral traits. Therefore, lineages can be created to pinpoint specific behaviors, and explicitly induce some variabilities in the associated functional networks. Such animal models could be used to investigate how the variability of a functional network correlates with the variability of the underlying anatomical structures. In addition, they offer to readily cross-validate the applied methods since they enable to combine different imaging modalities from *in vivo* methods such as MRI to *ex vivo* methods including histology and

microscopy. The murine model is probably the most widely used since rodents can be genetically modified to create lines of particular phenotypes of interest. Their anatomic-functional MRI acquisitions made *in vivo* can also be complemented with postmortem MRI acquisitions as well as histology and microscopy, thus providing access to ultra-high resolution data that are close to ground truth [Aoki et al. 2004; Sun et al. 2006; Barrière et al. 2019].

The Japanese quail (*Coturnix japonica*) is a proper farm animal to study cognitive functions and emotivity [Wilson et al. 1961; Huss et al. 2008; Calandreau, Favreau-Peigné, et al. 2011; Calandreau, Bertin, et al. 2013; Baer et al. 2015; Lormant et al. 2018, 2020]. Indeed, this bird presents an easily inducible and quantifiable response to fear called tonic immobility that has been described in the literature on animal behavior [Mills and Faure 1991; Jones, Mills, Faure, and Williams 1994; Mills, Crawford, et al. 1997]. This innate behavior has been used to successfully produce two lines of Japanese quails: the short tonic immobility (STI) line and the long tonic immobility (LTI) line. One line has been selected for its long tonic immobility duration (the LTI line), the other one for its short tonic immobility duration (the STI line). Previous studies have demonstrated that Japanese quails genetically selected for their long tonic immobility duration, in comparison with quails selected for their short tonic immobility duration, exhibit a decreased activity when exploring a novel environment, longer latencies to enter into a new environment, and to approach novel food [Jones, Mills, and Faure 1991; Faure et al. 2006; Calandreau, Favreau-Peigné, et al. 2011; Favreau-Peigné et al. 2014]. Quails with a long tonic immobility duration are more frightened than quails with a short tonic immobility duration when introducing a novel object into their home cage [Calandreau, Bertin, et al. 2013]. Physiological studies have likewise revealed differences in plasmatic corticosterone responses to restraint between the two lines [Hazard, Couty, and Guémené 2007; Hazard, Couty, Richard, et al. 2008; Hazard, Leclaire, et al. 2008]. More recently, it has been showed that an anxiolytic treatment with diazepam alleviates behavioral differences between the two lines when birds are exposed to a new environment [Boulay et al. 2013]. Altogether, these findings have led to the assumption that the LTI and STI lines of Japanese quails are generally highly divergent on their emotionality trait, respectively displaying a high (LTI quails) or a low (STI quails) emotionality trait [Lormant et al. 2018]. There are currently no consensual information on the main structures controlling the Japanese quail's emotivity, especially regarding fearfulness, and little is known about its structural connectivity. Beyond this specific emotivity network, few studies have been performed to map the structural connectivity in birds, and the Japanese quail might be the adequate species to establish a first atlas of the structural connectivity in birds.

The volume of the Japanese quail's brain is similar to the rodents' one, thus advocating for the use of a small bore preclinical ultra-high field (UHF) MRI system to scan the birds' brains postmortem. The combination of the ultra-high magnetic field and strong gradient magnitudes available in preclinical UHF MRI systems would allow not only to reach very high spatial resolutions for both anatomical and diffusion-weighted magnetic resonance imaging (dMRI) datasets, but also a high angular resolution for diffusion MRI, thus allowing to better disentangle the local orientation of white matter fibers. The basic principle of diffusion-weighted magnetic resonance imaging to probe the local orientation of axons embedded in white matter and organized into tightly parallel bundles of fibers is based on a phase encoding of the positions of water molecules through the application of strong gradient pulses. The net phase accumulated over the molecules during their Brownian displacements using magnetic gradient pulses induces a strong decay of the NMR signal along the direction of the axons, thus allowing to identify this mean direction. Diffusion MRI has become an established tool to probe the structural brain connectivity both *in vivo* and *ex vivo* [Basser et al. 1994; Parker et al. 2003; Mori and Zhang 2006; Behrens, Berg, et al. 2007; Reisert et al. 2011; Teillac et al. 2017], as well as its microstructure.

Post mortem dMRI enables longer scan times (from several hours to several days). Hence it offers greater spatial resolution, better signal-to-noise ratio (SNR) and higher achievable b-values than with living subjects that cannot practically

be scanned more than a couple of hours. In addition, *ex vivo* dMRI is free from artifacts of motion and physiological noise. Nevertheless, *ex vivo* imaging protocols have to be revisited compared to *in vivo* protocols. Since the *ex vivo* apparent diffusion coefficient (ADC) is significantly reduced [D'Arceuil and Crespigny 2007], the b-value has to be significantly increased to preserve the diffusion contrast. The  $T_2$  relaxation time is also drastically reduced [Pfefferbaum et al. 2004; Shepherd et al. 2009] and narrows the window width available to acquire the data, reinforcing the need for stronger gradient magnitudes to keep echo times short and preserve the SNR.

dMRI on *ex vivo* animal and human brains has been the subject of many studies [D'Arceuil, Westmoreland, et al. 2007; McNab, Jbabdi, et al. 2009; Dyrby, Baaré, et al. 2011; Miller, Stagg, et al. 2011; Sébille et al. 2019], mostly focused on primates and rodents but few on birds. As an example, previous studies mapped the vocal pathways and functional vocal networks of song birds using manganese-enhanced MRI [Van Der Linden et al. 2004] and diffusion tensor imaging (DTI) [De Groof, Verhoye, et al. 2006; De Groof and Linden 2010; Hamaide et al. 2018]. To date, no study involving MRI has been done to map the anatomy and the structural connectivity of Japanese quails. However, a fine mapping of both the anatomy and connectivity in birds divergent on their emotivity would allow to better capture the anatomical substrates underlying the behavioral traits in Japanese quails.

To unveil the link between behavior and neuroanatomy, this work is focused on the inference of the first structural connectome of the Japanese quail. To this aim, *ex vivo* UHF MRI datasets were acquired on two cohorts of STI and LTI Japanese quails from which the first structural connectivity atlas of the Japanese quail was established. Then, to investigate the research hypothesis claiming that these two breeding lines do not show the same connectome, we studied the morphometric variability of all the white matter bundles available in the established connectivity atlas between the two lines. We also statistically analyzed microstructural features along the same bundles to find differences that could be related to their distinct emotivities. Specific analyses of the structures and connections involved in the emotional circuits were undertaken at the subject/lineage/species levels.

## 5.2 Material and methods

### 5.2.1 The Japanese quail cohort

21 male Japanese quails (*Coturnix japonica*) were scanned during the study and provided by the Pôle d'Expérimentation Avicole de Tours 103 (UEPEAT, INRAE 2018, Experimental Poultry Facility, doi: 10.15454/1.5572326250887292E12), where they were bred and maintained. All the animals were sacrificed at 10 weeks of age in order to be considered as sexually mature. The population included 11 LTI and 10 STI Japanese quails obtained after 65 generations of Japanese quails which represents 33 years of breeding. The two lineages were created on the base of two selective tests, the treadmill test and the tonic immobility test. The former measures social reinstatement behavior to ensure the absence of divergence for both lines on this trait, and thus their uniform social motivation stability. The latter is a robust test of fearfulness in birds [Gallup 1977]. The Japanese quails were euthanized with an intraperitoneal injection of pentobarbital (36mg/100g). After death, the quails were fixated using an intracardiac perfusion process with 400mL of ice-cold 4% paraformaldehyde (PFA) solution in 0.1M phosphate buffer for ten to twenty minutes. Afterwards, their heads were removed and preserved in PFA 4% at a temperature of 4°C for a duration of 8 weeks in order to continue the fixation process by immersion until scanning. The *ex vivo* brains were kept in their skulls to avoid any mechanical deformation during the fixation process, the skull being the most adequate container to reach this goal. Animal care



and experimental treatments complied with the French Ministry of Agriculture guidelines for animal experimentation and European regulations on animal experimentation (86/609/EEC). They were performed in conjunction with the local animal regulation (authorized C37-175-1) of the French Ministry of Agriculture under the EEC directive and the ethics committee approval (Val de Loire, agreement N°1789 and 1848).

Nevertheless, Japanese quails' heads were plucked to avoid corruption of the MR images by susceptibility artifacts. The latter can be induced by air bubbles trapped within the plumage and by the presence of oil in the plumage secreted by the uropygial gland [Jacob et al. 1982]. The oil entails a fat peak on the NMR signal that needs to be canceled using a fat saturation preparation and thus increasing the scan duration. At least two days before scanning, the sample was placed in 0.1M phosphate-buffered saline (PBS) to achieve an optimal rehydration favorable to enhance the diffusion contrast [Thickman et al. 1983]. Before scanning, each quail sample was put in a hermetically sealed Falcon® tube containing Fluorinert® (Fluorinert, 3M), an inert fluid that does not exhibit any NMR signal and conserves the hydration of the tissues. Finally, the Falcon® tube was soundly fixed on a MRI bed originally built for rats during the scanning.

## 5.2.2 MRI protocol

All MR acquisitions were performed on a preclinical Bruker BioSpec MRI scanner at 11.7 Tesla. This imaging system is equipped with a powerful gradient set capable of delivering up to 780mT/m with a slew-rate of 9500T/m/s allowing to reach very short echo times (less than 25ms) in order to obtain images with a large SNR, and offering the possibility to scan the *ex vivo* samples with large diffusion sensitizations (b-value of 4500s/mm<sup>2</sup> for the current scans). The Bruker <sup>1</sup>H transmit-receive volume coil originally built for rats (40mm inner diameter) was preferred to surface coils in order to preserve the homogeneity of the diffusion-weighted NMR signal over the entire FOV of the quail's head. The imaging protocol includes an anatomical MRI scan to provide a high-resolution dataset to be used to create the cohort's brain template and a diffusion-weighted MRI scan to infer the structural connectivity at the individual scale and then at the population scale.

The anatomical MRI scans were performed using a conventional 2D T<sub>2</sub>-weighted spin echo (SE) sequence with the following parameters: isotropic spatial resolution of 150μm, flip angle FA=90°, echo time TE=16ms, repetition time TR=9s, 8 averages, 1 repetition, read bandwidth RBW=65789.5Hz, total scan duration of 2h45min. The SE MRI dataset offered an enhanced contrast, facilitating the delineation of the deepest regions of interest (ROIs) by two independent biologists.

The diffusion-weighted MRI scans were implemented using a 3D segmented echo planar imaging (EPI) pulsed gradient spin echo (PGSE) pulse sequence. A single-shell high angular resolution diffusion imaging (HARDI) scheme was chosen to sample the diffusion Q-space along 75 diffusion-encoding directions uniformly distributed over the sphere of magnitude  $q = \gamma \delta G = 42.57 \text{ MHz/T} \times 500 \text{ mT/m} \times 5 \text{ ms} = 106425 \text{ m}^{-1}$ , thus being sensitive to displacements of water molecules on the order of 10μm. The isotropic spatial resolution of the images was set at 200μm and the b-value was fixed at 4500s/mm<sup>2</sup>. The other imaging parameters for this protocol corresponded to: echo time TE=23.88ms, repetition time TR=250ms, flip angle FA=90°, read bandwidth RBW=300kHz, 18 EPI segments, pulse duration δ=5ms, pulse separation time Δ=12.3ms, leading to a diffusion time of 10.6μs and to a total scan duration of 13h04min. In addition, 5 T<sub>2</sub>-weighted volumes were also collected at b=0s/mm<sup>2</sup> to obtain a mean reference image for each individual.

### 5.2.3 Image processing and analysis

#### 5.2.3.1 Pre-processing

dMRI data usually need to be corrected from several artifacts such as susceptibility-induced geometrical and signal intensity distortions, eddy currents-induced geometrical distortions caused by the commutation of the strong diffusion gradients in single-shot EPI schemes, or even subject motion when they are acquired *in vivo*. These artifacts are mainly related to the integration of phase errors during the echo train readout of fast single-shot EPI technique. The latter is generally used *in vivo* and is extremely sensitive to any field inhomogeneity or motion. *Ex vivo* dMRI allows to perform much longer scans and to use alternative sequences such as multishot 3D diffusion-weighted EPI sequences. The combination of UHF (11.7T) increasing the SNR, of very strong gradients (up to 780mT/m at 9500T/m/s) reducing the echo time and the echo train length, and of a large number of segments allows to compensate for most of the artifacts, and thus avoid the use of many pre-processing steps. In this *ex vivo* study, we used 18 segments and measured a SNR level above 11 for all the 75 diffusion-weighted volumes that were deprived of any visual geometrical distortion. A non-local means filter was applied to the raw dMRI data to suppress Rician noise [Buades et al. 2011]. Even though a Rician model was applied to correct for the noise present in the data, it should be noted that a Gaussian noise model would have given approximately the same result, given the SNR level is significantly greater than 8 in all diffusion-weighted images.

#### 5.2.3.2 Local modeling of the diffusion process

Beyond the historical diffusion tensor model [Basser et al. 1994; Pierpaoli, Jezzard, et al. 1996], a plethora of existing HARDI reconstruction models enables the computing of the local orientation distribution function (ODF) from model-free to model-based approaches (see [Tournier, Mori, et al. 2011] for a more exhaustive review of diffusion models). The impulse response function is usually established using the diffusion-weighted NMR signal stemming from the most anisotropic voxels, typically the corpus callosum in primates. However, the Japanese quail is deprived of a corpus callosum ([Diekamp et al. 2005]) making the construction of an impulse response more difficult than for animals featuring a corpus callosum. Therefore, we chose to apply the analytical Q-ball reconstruction model that combines the efficiency of the decomposition of the signal onto a modified spherical harmonics basis with the robustness of the L-curve regularization factor to compute the local ODFs within a mask corresponding to the quail's brain. To this aim and for each quail, a robust brain mask was segmented manually by two independent neurobiologists from the average  $T_2$ -weighted MRI scan acquired at  $b=0s/mm^2$ . The latter was superimposed to the color-encoded diffusion direction (CED) map stemming from the Q-ball model to enhance the delineation of brain structures using the boundaries of surrounding white matter bundles when available.

The analytical Q-ball reconstruction was performed using a spherical harmonics order of 8 with a regularization L-curve factor of 0.006, providing, in addition to the ODFs, maps of generalized fractional anisotropy (GFA) for all the quails. A further DTI reconstruction was performed using a Log-Euclidean estimator to preserve the positiveness of the tensor eigenvalues and to compute rotationally-invariant maps including the fractional anisotropy (FA), the apparent diffusion coefficient (ADC), the longitudinal and transverse diffusivities ( $D_{parallel}$  and  $D_{transverse}$ ).

### 5.2.3.3 Fiber tracking

Various tractography methods exist to infer the trajectories of axonal white matter fibers from dMRI-based ODF maps. Fiber tracking algorithms are typically classified into three groups: deterministic methods, probabilistic methods and global methods. Despite their greater immunity to the presence of false positives than the deterministic and probabilistic approaches, the global ones require an intricate computational effort that appeared to be unnecessary in the context of this exploratory study. Therefore, whole brain tractography was performed at first glance from the Q-ball ODF field using both streamline regularized deterministic (SRD) and streamline regularized probabilistic (SRP) methods [Perrin, Poupon, Cointepas, et al. 2005] with the following parameters: creation of 8 seeds per voxel of the brain mask, aperture angle of 30°, fiber length range of [0.1-100]mm, forward and backward integration step of 50 $\mu$ m, anisotropy-based regularization factor of 0.12. All streamlines were stopped when they reached the boundaries of the previously mentioned brain mask, without any stopping criteria related to FA (or GFA) in order to avoid the definition of any empirical threshold. The fiber length range was tuned to discard fibers smaller than half the voxel size and to prevent the existence of infinite loops.

### 5.2.3.4 Template creation and normalization

To our knowledge, no MRI template has been published for the Japanese quail. Avian templates exist for the canary and the pigeon [Vellema et al. 2011; Güntürkün, Verhoye, et al. 2013; Behroozi et al. 2020], but the brain of these species remains different from the Japanese quail's on an anatomical point of view. This situation advocated for the creation of a specific quail template, available online as "Quail (*Coturnix japonica*) brain MRI template and whole-brain atlas" (<https://doi.org/10.5281/zenodo.4700523>). Some references in the literature [Karten et al. 1967; Güntürkün, Verhoye, et al. 2013] suggest to reorient the bird's head based on the midline of its beak. But this strategy does not really take into consideration the anatomy of the brain itself. We propose an alternative strategy that more specifically integrates the brain anatomy. To this aim, all T<sub>2</sub>-weighted MRI scans were first masked at the individual scale with their corresponding brain masks previously manually delineated to discard the NMR signal coming from outside the brain. After being reoriented such that the anterior commissure (AC) and the posterior commissure (PC) lie in the same transverse plane, as seen in Figure 5.1, the template image was eventually computed.

The manual segmentation of the Japanese quail's anatomical substrates was realized on the template image, available on the online content entitled "Quail (*Coturnix japonica*) brain MRI template and whole-brain atlas" (<https://doi.org/10.5281/zenodo.4700523>). The structures were identified from the chick atlas [Kuenzel and Masson 1988; Puelles et al. 2018], but also lots of similarities with other avians (pigeon, canary, starling and zebra finch) were noticed and helped in the segmentation process [Poirier et al. 2008; Vellema et al. 2011; Güntürkün, Verhoye, et al. 2013; De Groof, George, et al. 2016; Güntürkün, Stacho, et al. 2017]. Finally, diffusion MRI scans were registered to the template image using Advanced Neuroimaging Tools (ANTs) [Avants et al. 2011], for diffeomorphic and affine registrations in order to register the resulting tractograms in the template space.

### 5.2.3.5 From fibers to bundle segmentation

One of the main purposes of this work is to establish an atlas of the Japanese quail structural connectivity that consists of grouping the fibers obtained from diffusion-based tractography into bundles corresponding to the significant connection

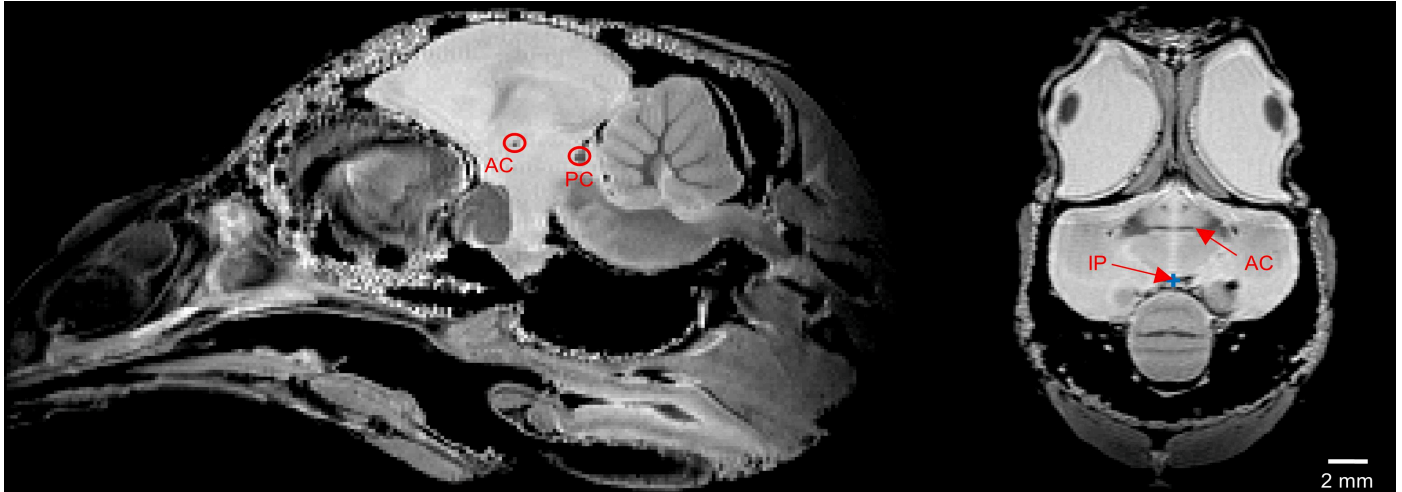


Figure 5.1: Anatomical images of subject 7133 LTI in the sagittal (on the left) and axial (on the right) views with an isotropic  $150\mu\text{m}$  resolution showing three typical reference points used to define the AC-PC frame for each Japanese quail. AC = anterior commissure. PC = posterior commissure. IP = interhemispheric point.

hubs of the Japanese quail's brain. Two different approaches exist to achieve this goal divided into supervised and unsupervised methods. The supervised approach assumes that the target white matter bundles are already known and well described in the literature. Hence these methods lead to extracting the fibers composing each bundle from a set of ROIs and a set of intersection/exclusion rules defining whether the target bundle should cross or avoid the predefined ROIs. Since the pathways of long white matter bundles were finely described by neuroanatomists from postmortem studies at the beginning of the 20<sup>th</sup> century [Cajal 1911; Klingler 1935; Klingler and Gloor 1960], supervised approaches were the first ones to be applied by clinicians to design atlases of human long fiber bundles [Mori, Wakana, et al. 2005; Oishi et al. 2010; Catani et al. 2012]. The latest refinements proposed to improve supervised methods consist in defining prior distributions of the neighboring anatomical structures of each pathway to further constrain the segmentation of white matter bundles such as TRACULA (TRActs Constrained by UnderLying Anatomy) [Yendiki et al. 2011].

However, it should be noticed that supervised approaches do not take into account the specific geometry of white matter bundles that consist of a set of closely arranged parallel axonal fibers having a low curvature. This observation paves the way to the second class of unsupervised algorithms aiming at grouping fibers according to their distance [Corouge et al. 2004], which does not necessitate the definition of region-based anatomical priors. This second approach is suitable to investigate the structural connectivity without any knowledge of the existing fiber tracts. A good example of it is the human sub-cortical superficial connectivity that was poorly described by neuroanatomists, due to the difficulty its dissection represents. Defining a metric to measure the distance between fibers allows the application of clustering methods partitioning the fibers into clusters based on the computation of connectivity matrices that provide for any couple of fibers a measure of the affinity between them. Choosing the adequate distance is not trivial as the quality of the resulting fiber clusters strongly depends on it.

Tractography can generate up to several millions of streamlines at the individual scale. Computing a connectivity matrix with such a sizable number of streamlines is not realistic from a computational standpoint. It is even worse when considering the plethora of streamlines available at the population level. In order to alleviate these computational bottlenecks, developing strategies to reduce the dimension of the problem becomes mandatory. It is the case in this study by relying on a three-fold dimension reduction involving two consecutive clustering steps [Guevara, Poupon, et al.

2011]. Similar approaches were also devised in Garyfallidis et al. 2012 and Siless et al. 2018.

The structural connectivity of the Japanese quail has never been investigated broadly in the literature using MRI, even though some anatomical atlases published for the canary [Vellema et al. 2011] and the starling [De Groof, George, et al. 2016] provide some insights about the expected connectivity of quails. This lack of preliminary data tipped the balance in favor of unsupervised techniques, and we propose here to extend the approach of Guevara, Poupon, et al. 2011 originally designed for humans to infer the structural connectivity of Japanese quails. As mentioned previously, the fiber clustering method relies on a three-fold process: 1) a first clustering step operated at the individual scale to partition the fibers of a subject into small fascicles; 2) a second step performed at the population level to match inter-individual fascicles and create inter-individual clusters; 3) a third step to label inter-individual clusters and build the target structural connectivity atlas. It remains out of the scope of this study to detail the clustering approach proposed by Guevara, Poupon, et al. 2011. But for the sake of clarity, the three steps are summarized hereafter, highlighting the main parameters that need to be tuned accurately.

**Clustering of fibers at the individual scale** To reduce the scale of the problem, fibers are first separated according to the gross anatomical region they belong to: left hemisphere, right hemisphere or cerebellum. Fibers are then divided into groups corresponding to their length ranges. In order to define the adequate ranges able to cover the entire set of fibers, group level histograms of fiber length were preliminary computed from the SRD and SRP tractograms and analyzed to define the minimum and maximum length thresholds corresponding to 2% and 98% of the cumulative histograms of fiber lengths observed over the entire population. The SRD and SRP tractograms were then explored based on the division of these length ranges into ten sub-classes to simplify the problem complexity by processing independently each of the sub-classes.

For each fiber subclass, a density map was computed at the resolution of the diffusion scan ( $200\mu\text{m}$ ) and thresholded to define a binary mask composed of the voxels crossed by at least 5 fibers. A k-means algorithm was then used to create a set of random parcels (including 27 voxels on average) within each binary mask, from which a connectivity matrix specific to the fiber length range of interest could be established simply by computing an affinity metric between parcels resulting from the integration of the contribution of each fiber connecting them. In the end, a hierarchical clustering algorithm was applied to the connectivity matrix to extract clusters of connected parcels (with a minimum cluster size set to 300 voxels representing  $2.4\text{mm}^3$  and with an average cluster size set to 6000 voxels representing  $48\text{mm}^3$ ). The brain volume of the reconstructed template being close to  $1.85\text{cm}^3$ , these cluster minimum and average sizes represent 0.013% and 0.26% of the total brain volume respectively.

The resulting clusters were used to select the underlying fibers, assuming that a fiber belongs to a cluster if at least 31% of its trajectory intersects the cluster area. Finally, the obtained fiber clusters were subdivided into smaller components based on a watershed analysis of the density image of their fiber extremities to ensure that the ends of the final fascicles are spatially coherent. Clusters containing less than 5 fibers were discarded. Every cluster was associated with a unique centroid defined as the fiber belonging to the cluster which depicts the smallest (symmetric mean of mean closest point) distance to the other fibers and representing a skeleton of the corresponding fascicle. Each individual fiber cluster map was associated to a centroid map providing a sparse representation of the individual fiber cluster map. Table 5.1 summarizes the parameters applied for this individual clustering step.

**Clustering of fibers at the population scale** The second clustering step, occurring at the population level, consisted in creating a second level of clusters of the centroids stemming from all the individuals. This sparse representation of clusters allows to keep the issue dimension reasonable, whatever the population size is. All the individual centroid maps

parameter name	value
parcellation resolution	200 $\mu$ m
average cluster size	6000 voxels
minimum cluster size	300 voxels
min. percentage of fiber length intersecting a cluster	31%
length range of the fibers	0.64-49.06mm (SRD) 0.63-28.71 mm (SRP)
minimum fiber count in a cluster	5

Table 5.1: Set of intra-subject fiber clustering parameters used for the Japanese quail cohort

were first of all registered to the template Japanese quail space previously established in order to enable their merging. An affinity matrix between all merged centroids was then computed and followed by a hierarchical clustering based on a DBSCAN (density-based spatial clustering of applications with noise) algorithm [Ester et al. 1996]. The affinity was defined using a Gaussian kernel and a normalized pairwise centroid distance integrating a correction to release the distance constraint when the minimum centroid length increases (Equation (5.1)).  $nf$ ,  $l_{min}$  and  $l_{max}$  respectively correspond to a normalization factor, two lower and upper length thresholds used to correct the actual distance between centroids. Table 5.2 synthesizes the chosen parameters for the inter-subject clustering step.

$$affinity(C_1, C_2) = e^{-\frac{d(C_1, C_2)}{\sigma^2}}$$

*with*

$$d(C_1, C_2) = \min \left( \max_{p_{1,i} \in C_1, p_{2,i} \in C_2} \|p_{1,i} - p_{2,i}\|, \max_{p_{1,i} \in C_1, p_{2,i} \in C_2} \|p_{1,i} - p_{2,N-i}\| \right) - nf$$

$$\times \frac{\min(l(C_1), l(C_2)) - l_{min}}{l_{max} - l_{min}} \quad (5.1)$$

where  $C_1$  and  $C_2$  are the two analyzed centroids,  $d$  is the normalized pairwise distance between the centroids,  $\sigma^2$  is the variance of the centroid affinity,  $p_{1,i}$  and  $p_{2,i}$  are the points respectively belonging to the centroids  $C_1$  and  $C_2$ ,  $l$  is a centroid length.

**Bundle atlas construction: labeling of the inter-subject centroids** A final stage performed in close collaboration with neuroanatomists involves regrouping inter-subject clusters to reconstruct white matter bundles plausible from an anatomical point of view. The latter task is carried out semi-automatically. When the bundles pass through anatomical constituent regions that are well identified using the anatomical template of the Japanese quail, these regions are then used to select candidate centroids. Exclusion anatomical regions can also be used to remove some of the candidates selected in the previous step that do not belong to the targeted fiber bundle. At the end of this semi-automatic step, each bundle of interest is then made up of centroids representing fibers from all individuals matched to the template space, which are then re-aggregated to form a new anatomical connectivity atlas of the Japanese quail.

parameter name	value
type of centroid distance	normalized pairwise
normalization factor $nf$	4.0 (SRD) 2.0 (SRP)
minimum centroid length $l_{min}$	0.64mm (SRD) 0.63mm (SRP)
maximum centroid length $l_{max}$	49.06mm (SRD) 28.71mm (SRP)
default normalized distance	0.01
maximum distance for the centroid affinity	2.0 (SRD) 1.8 (SRP)
max. distance for the centroid affinity after exclusion	0.4
variance of the centroid affinity $\sigma^2$	1600
number of point to compute the centroid affinity	21
minimum population percentage	40%

Table 5.2: Set of inter-subject fiber clustering parameters for the Japanese quail cohort

### 5.2.3.6 Statistical analyses along the white matter fibers

A paramount objective of this study is to explore the microstructural differences in anatomical connectivity that could explain the behavioral differences between the two studied quail lines, the emotional lineage (LTI) and the non-emotional lineage (STI) resulting from a long genetic selection process. In this perspective, a statistical analysis of the microstructural markers of the cerebral white matter quantifiable from the acquired dMRI data is set up. The diffusion tensor and analytical Q-ball models provide access in particular to measurements of mean diffusivity (MD), fractional anisotropy (FA) and generalized fractional anisotropy (GFA), parallel diffusivity ( $D_{parallel}$ ), and transverse diffusivity ( $D_{transverse}$ ).

All of the 34 white matter bundles listed in the established Japanese quail connectivity atlas were segmented on an individual scale from their respective SRD and SRP tractograms. For each bundle, the mean values of the aforementioned microstructural imaging markers were evaluated and compared between the two populations. Primal verification on the two distributions (STI and LTI quails) was realized using the Shapiro-Wilk test for the verification of the normality of the distributions, and the Levene test for the verification of the homogeneity of the variances in the distributions. The two distributions had to pass both Levene and Shapiro-Wilk tests (p-value superior to 0.05) in order to perform the Student test afterwards. Non-parametric Wilcoxon-Mann-Whitney tests were employed if the Student tests could not be performed due to a non-normality of the distributions. The Student and Wilcoxon-Mann-Whitney tests were considered relevant if their p-values were at most inferior to 0.05.

Multiple tests corrections were then applied to determine the false discovery rate. The null hypothesis was that the connectomes of the LTI quails and the STI quails are not significantly different. Each hemisphere was considered as an independent system, meaning that there were 15 tests that had to be corrected per hemisphere. Both Bonferroni and Benjamini-Hochberg corrections were applied on the distributions of diffusion-based features.

All the analyses were conducted with the Python seaborn statistical data visualization module. The white matter bundles, known to connect more specifically regions involved in the control of emotivity, are analyzed in more detail in order to better understand the microstructural changes induced at the level of this functional network during the selection process that led to the creation of the STI and LTI lines. The entire pipeline was carried out using the Ginkgo toolbox developed by the CEA/NeuroSpin team and available at <https://framagit.org/coupon/gkg>.

## 5.3 Results

### 5.3.1 Diffusion MRI and inference of the structural connectivity

The data collected using the dMRI acquisitions performed at 11.7 Tesla provided for each individual a set of 5 null b-value volumes and 75 volumes at  $b=4500\text{s/mm}^2$  allowing to explore its structural connectivity at both the individual and group levels.

#### 5.3.1.1 Noise correction in the pre-processing step

Raw diffusion-weighted images were filtered using the non-local means filter described in Section 5.2.3.1, using a noise standard deviation computed from the quail background image (yielding a mean  $\sigma = 105.75 \pm 10.92$ ), a half search block distance of 8, a 26-neighborhood, and a degree of filtering set to 0.3 to avoid an excessive smoothing of the diffusion-weighted dataset. The resulting filtered images depicted in Figure 5.2 showed an efficient removal of the Rician noise with no obvious smoothing effect, thus preserving the fine structures present in the diffusion-weighted dataset.

#### 5.3.1.2 Local modeling at the individual scale

The analytical Q-ball imaging (aQBI) and DTI local models of the diffusion process enabled to obtain the maps in Figure 5.3 that offer information on the microstructure of the quail's brain. Figure 5.4 stresses the diffusion ODF map depicting various orientation profiles of the diffusion process, from configurations corresponding to the presence of a single fiber population represented by sharp single-lobe ODFs, to more complex configurations corresponding to the crossing of different fiber populations represented by multiple-lobe ODFs. A zoomed area over the cerebellum clearly shows its various lobules and the branching occurring at their basis, hence assessing the efficacy of the analytical Q-ball model to represent the underlying axon directions.

#### 5.3.1.3 Tractography of quails at the individual scale

In order to adjust the regularization factor of the tractography algorithms, an analysis of the GFA histogram provided in Figure 5.5 is performed for each individual in order to compute a threshold value corresponding to 98% of its cumulative GFA histogram, yielding an average threshold of 0.12 across the population. This value allows to regularize the streamline construction as described in Perrin, Poupon, Cointepas, et al. 2005 and needs to be carefully chosen to avoid excessive regularization that would erase the actual curvature of streamlines.

Figure 5.6 depicts the tractograms obtained from the analytical Q-ball ODF maps using the SRD and SRP fiber tracking methods. The number of resulting streamlines was quite comparable between the two approaches, leading to a mean number of streamlines equal to 879036 with a standard deviation of 60039 for the former approach, and a mean number of streamlines equal to 879267 with a standard deviation of 60011 for the latter approach.

In order to adequately choose the fiber length ranges to be considered in the next clustering steps, histograms of the



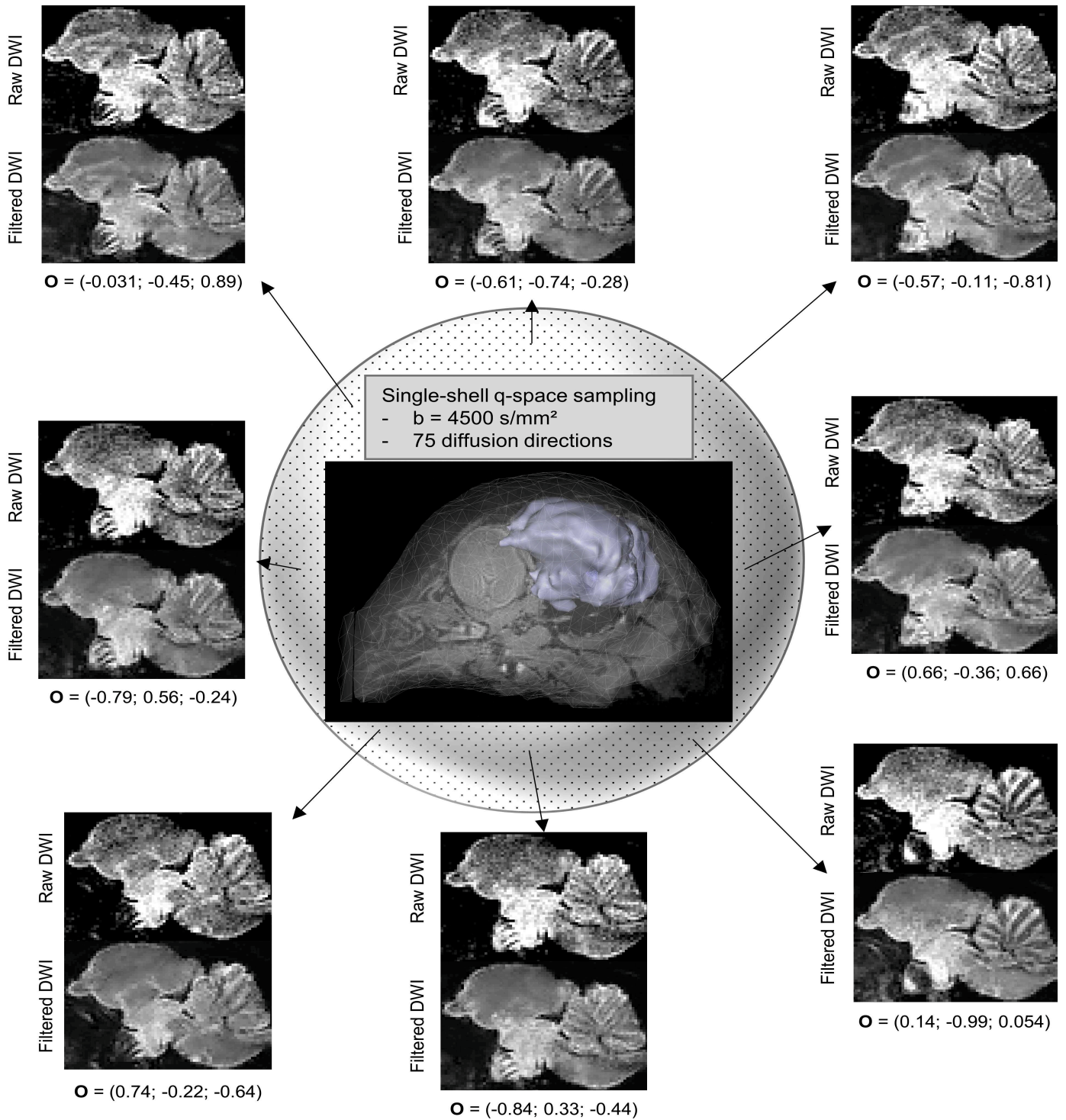


Figure 5.2: 3D mesh image of quail 7426 STI brain and skull (in the middle) and eight pairs of raw diffusion-weighted and filtered diffusion-weighted images using a non-local means filter of that Japanese quail in eight different diffusion directions. DWI = diffusion-weighted image.

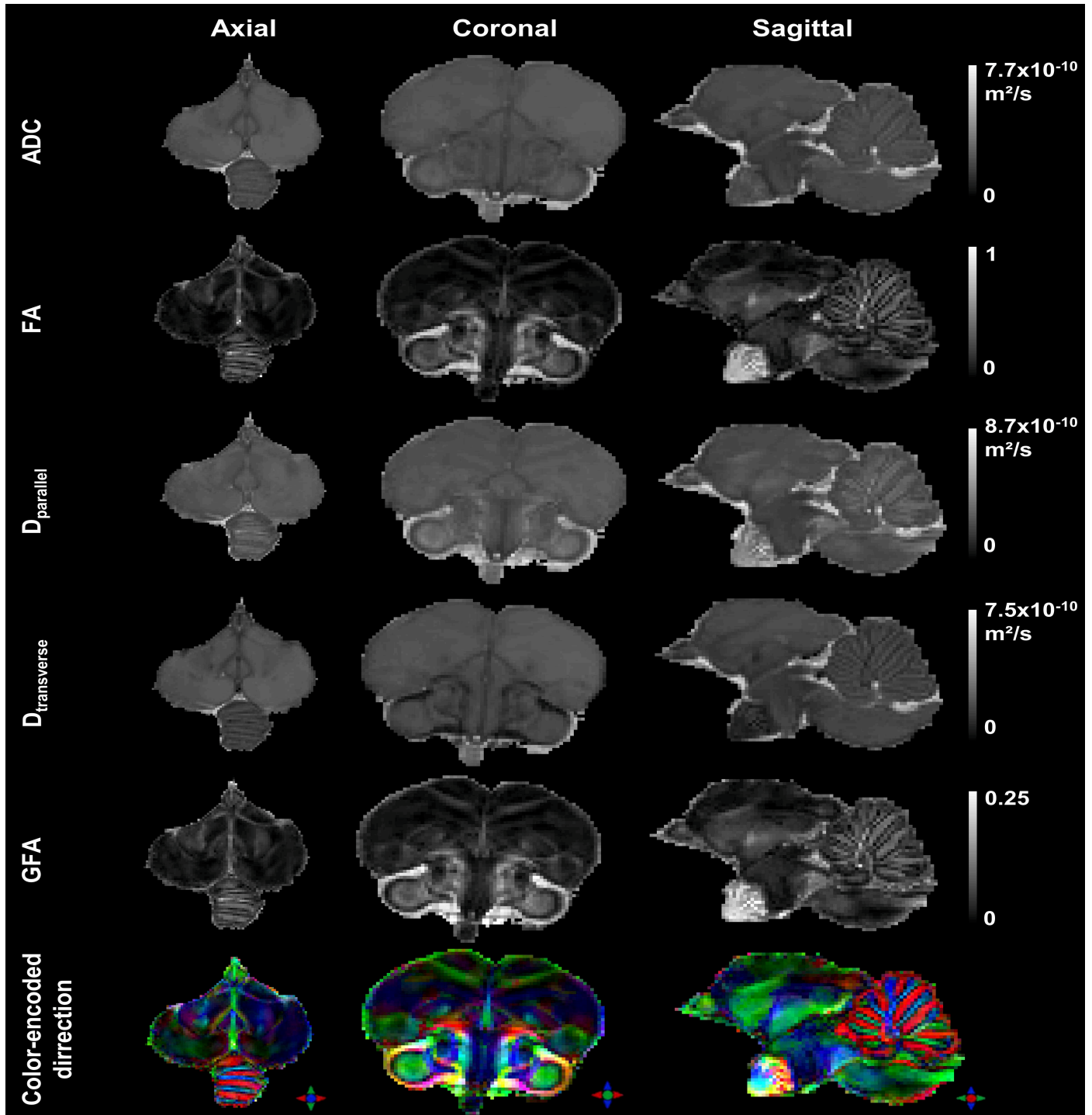


Figure 5.3: Maps of subject 7426 STI showing its apparent diffusion coefficient (ADC), fractional anisotropy (FA), axial diffusivity ( $D_{\text{parallel}}$ ), radial diffusivity ( $D_{\text{transverse}}$ ), generalized fractional anisotropy (GFA) and color-encoded diffusion direction in the three spatial views, based on the aQBI (at spherical harmonics order 8) and DTI local models.

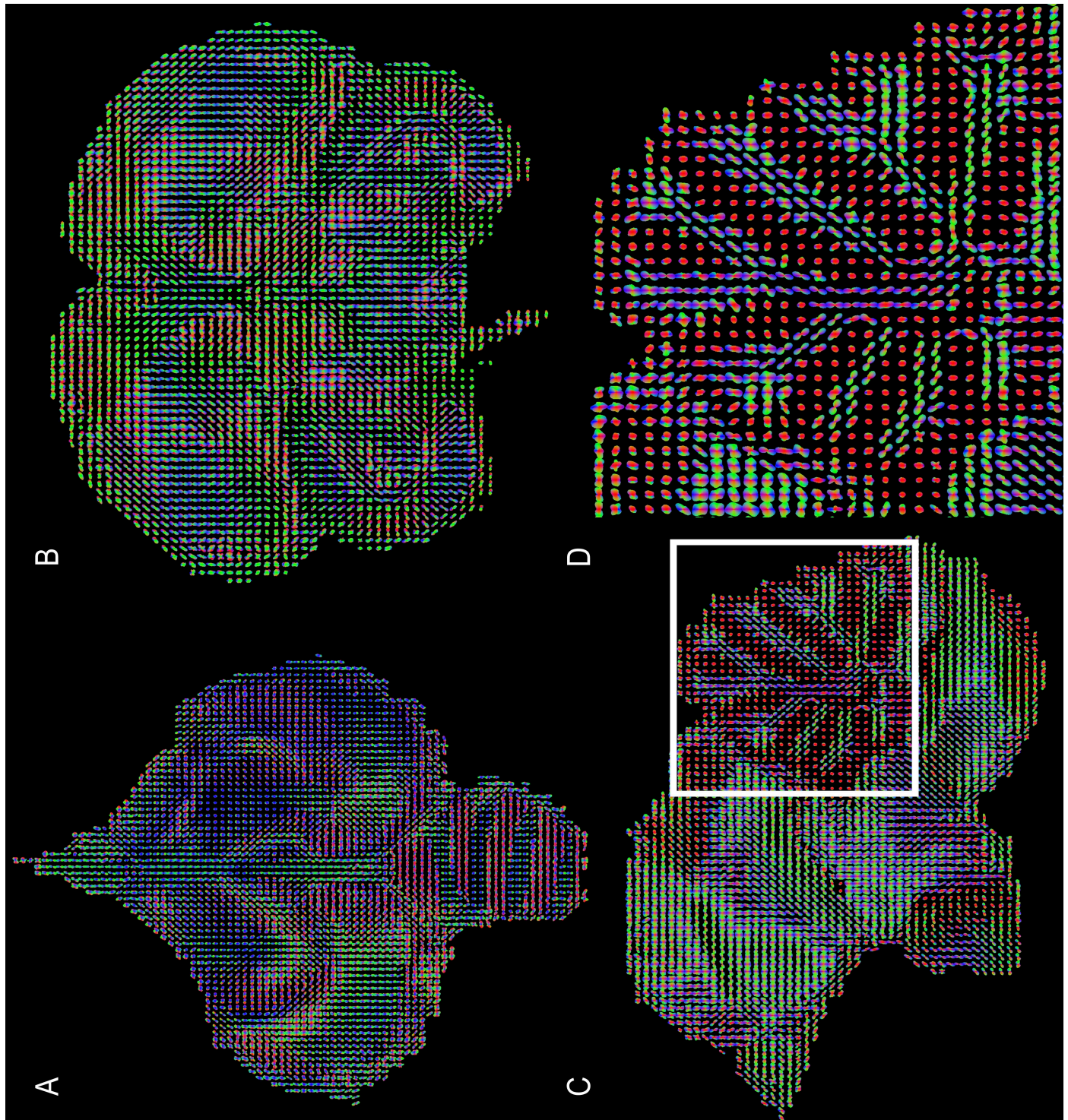


Figure 5.4: Orientation distribution function (ODF) maps of subject 7426 STI stemming from the analytical Q-ball model at spherical harmonics order 8. A) In the axial view. B) In the coronal view. C) In the sagittal view. D) A zoom in ODFs located in the cerebellum.

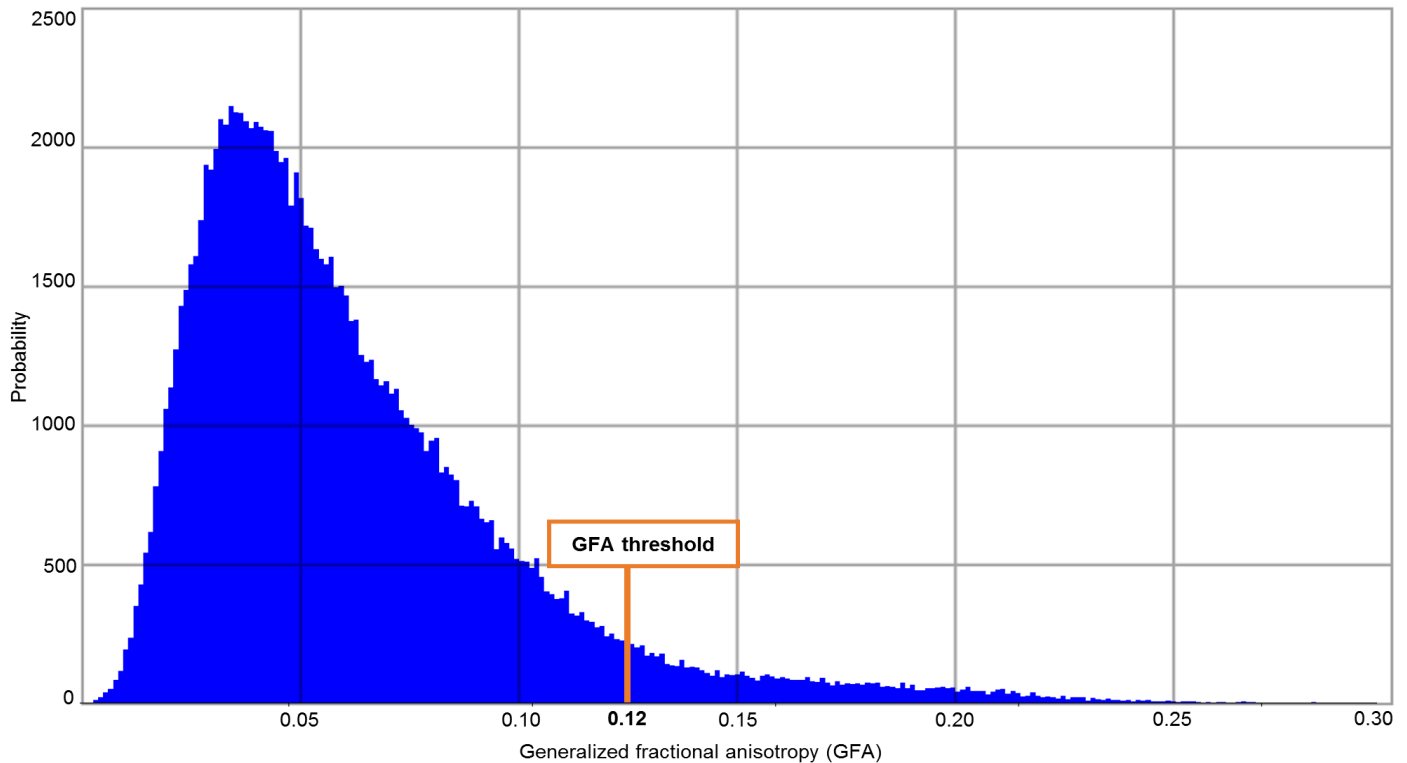


Figure 5.5: Histogram of generalized fractional anisotropy (GFA) for quail 7412 STI indicating the GFA threshold used for the entire cohort.

obtained fiber length across the 21 quails was computed for the two SRD and SRP approaches as depicted in Figure 5.7. Lower and upper length thresholds were defined corresponding to 2% and 98% of the cumulative histograms respectively, yielding a 0.64mm-49.06mm and 0.63mm-28.71mm ranges for the SRD and SRP approaches respectively.

#### 5.3.1.4 The anatomical template and its labeled structures

The  $T_2$ -weighted Japanese quail template was performed in this study by the INRAE team in the frame of a study carried out separately, and is shown at the top of Figure 5.8. This template then allowed two independent neurobiologists to manually segment and identify 195 anatomical structures, also available at <https://doi.org/10.5281/zenodo.4700523>, based on the  $T_2$ -weighted contrast mechanisms observed at 11.7 Tesla. A specific pair of label and color was assigned to each structure, as shown at the bottom part of Figure 5.8. As we will see next, the set of labeled structures facilitated the naming of the identified white matter bundles in the final structural connectivity atlas.

### 5.3.2 Fiber clustering on an individual scale

The outcome of the fiber clustering step performed on an individual scale provides a set of fascicles, each of which is populated by a reduced set of fibers sharing similar trajectories and being close to each other. Figure 5.9 displays an example of cluster set computed for a LTI quail from the two SRD and SRP tractography approaches. All the fibers belonging to a cluster are represented using a unique color assigned to the whole fascicle, with distinct colors assigned

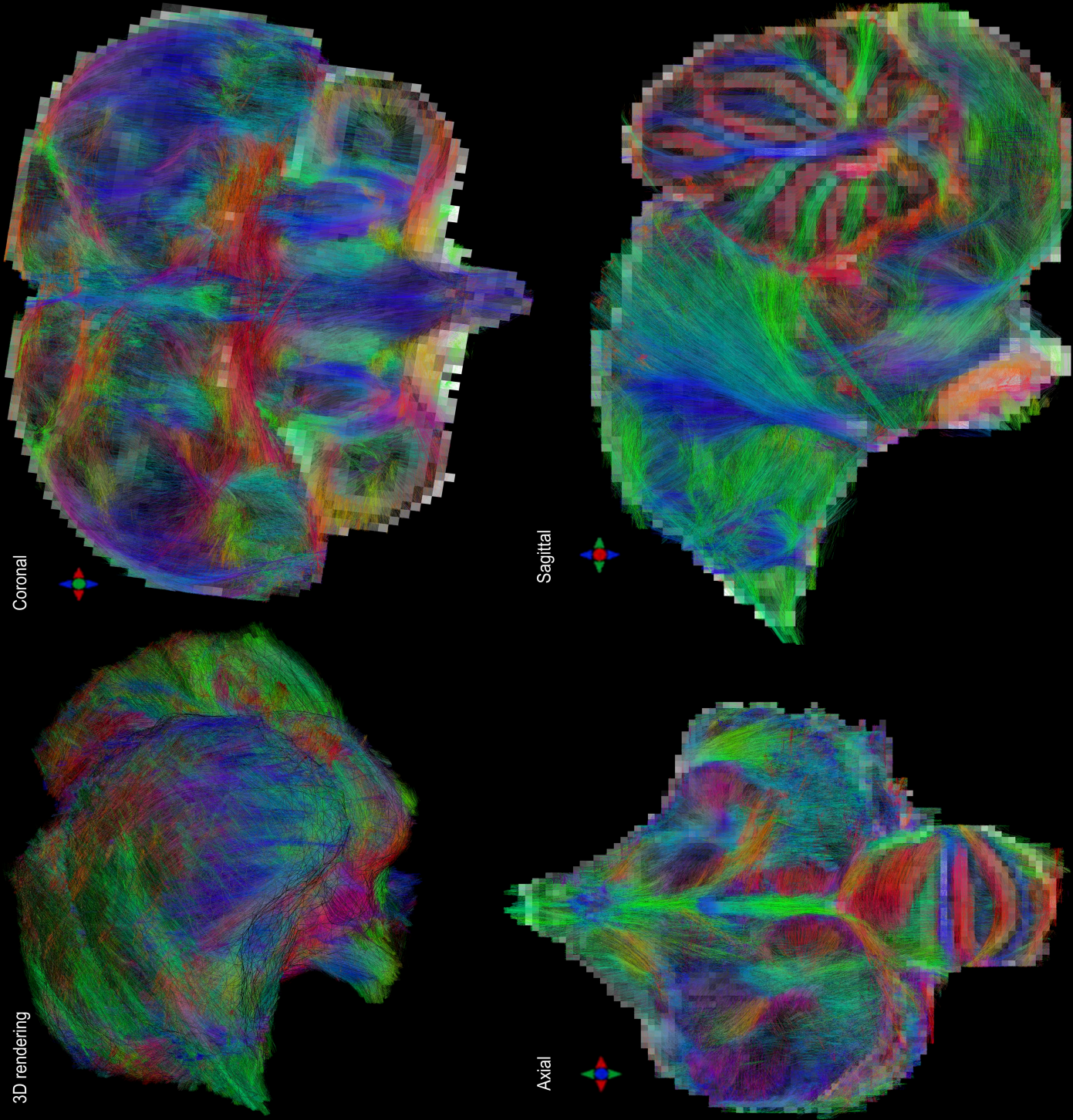


Figure 5.6a: Images of subject 7167 LTI showing 50% of its tractograms' streamlines obtained from streamline regularized deterministic (SRD) tractography superimposed on its generalized fractional anisotropy (GFA) map in the three spatial views and a 3D rendering of 50% of the final streamlines.

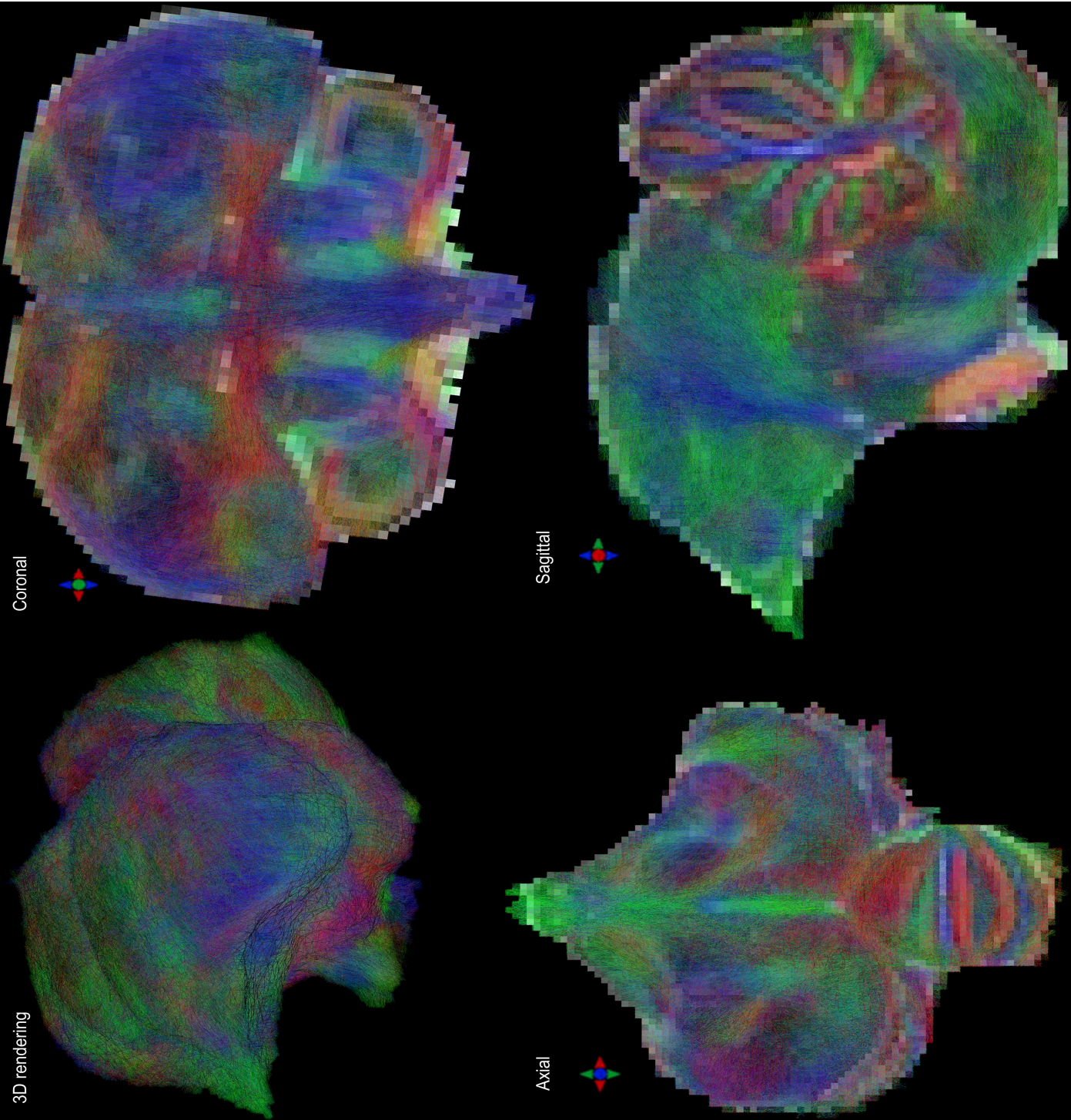


Figure 5.6b: Images of subject 7167 LTI showing 50% of its tractograms' streamlines obtained from streamline regularized probabilistic (SRP) tractography superimposed on its generalized fractional anisotropy (GFA) map in the three spatial views and a 3D rendering of 50% of the final streamlines.

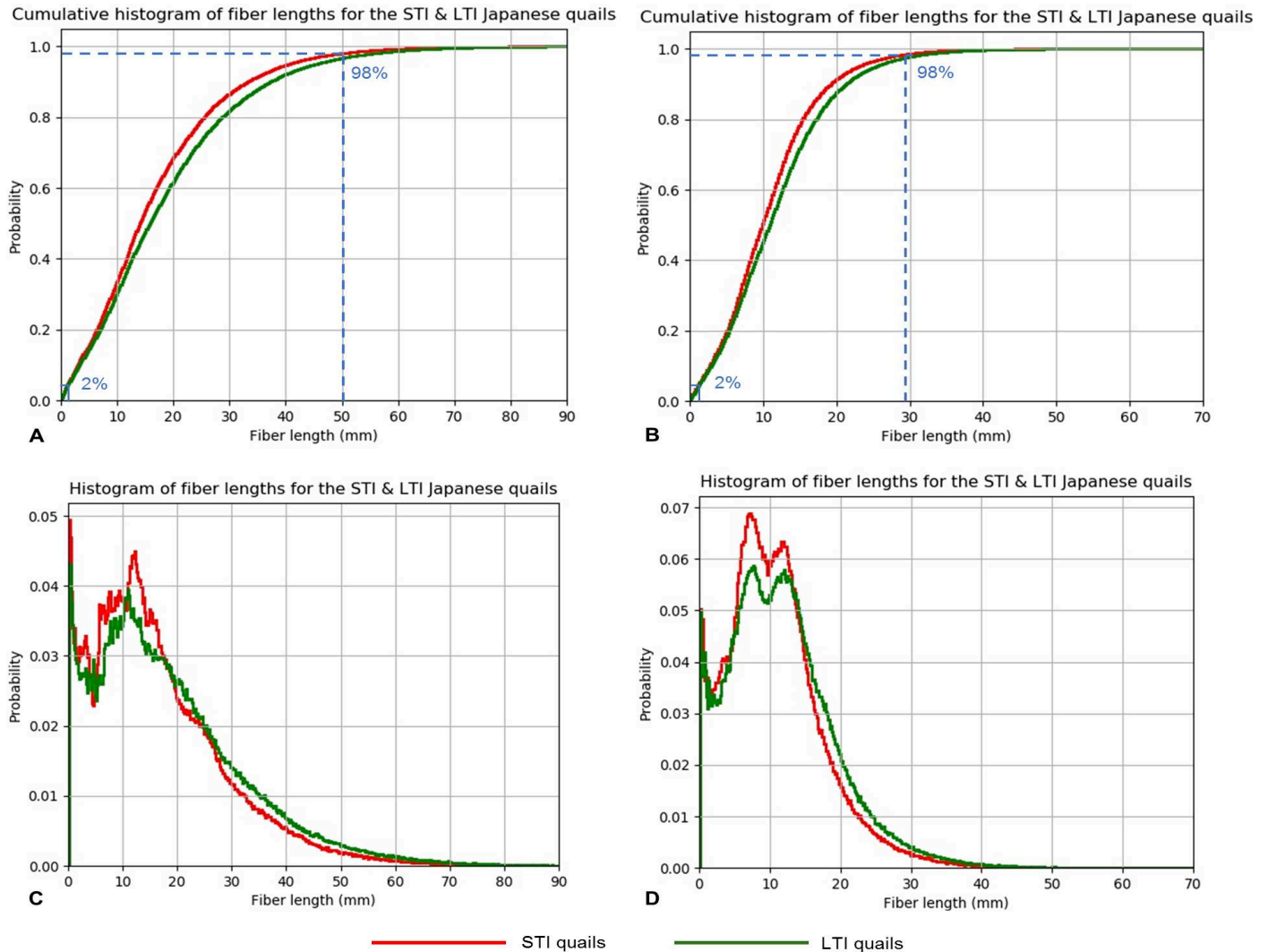


Figure 5.7: Histograms of the fiber lengths from the Japanese quails' cohort. The red plot refers to the STI line and the green one to the LTI line. The blue plain and dotted lines refer respectively to the 2% and 98% thresholds of the cumulative histograms. A) Cumulative histogram based on the streamline regularized deterministic (SRD) tractograms. B) Cumulative histogram based on the streamline regularized probabilistic (SRP) tractograms. C) Non-cumulative histogram based on the SRD tractograms. D) Non-cumulative histogram based on the SRP tractograms.

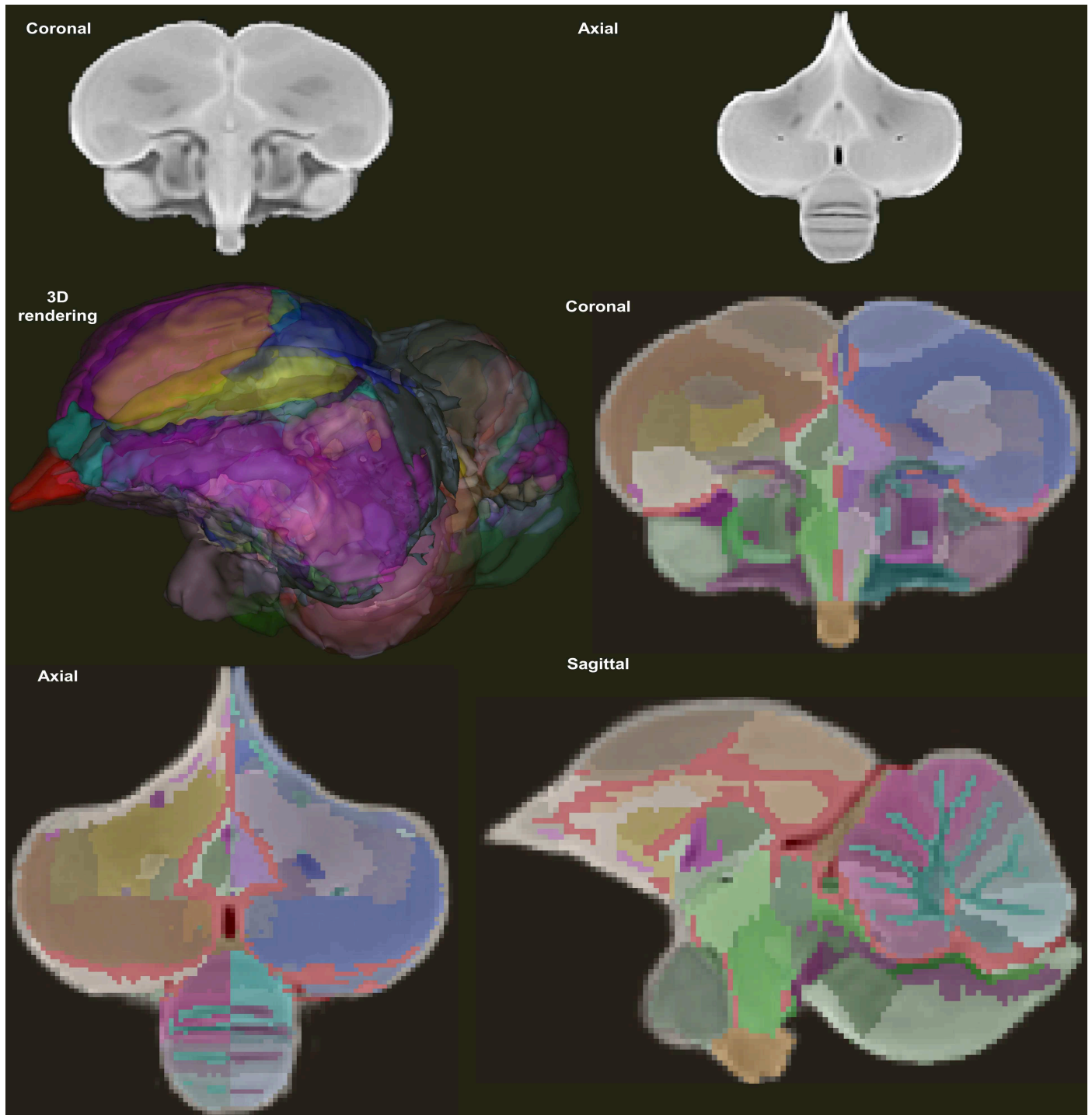


Figure 5.8: Template images obtained from the Japanese quail cohort. A) The template image in the coronal and axial views. B) The template image superimposed on the 195 delineated structures labeled and represented with distinct colors in the three spatial views as well as a 3D rendering of the template labels. These images are available at <https://doi.org/10.5281/zenodo.4700523>.



brain location	number of clusters (SRD)	number of clusters (SRP)
left hemisphere	7247	5936
right hemisphere	7206	6020
cerebellum	4321	3173
interhemisphere	3105	1568

Table 5.3: Table showing the number of clusters generated by the inter-subject fiber clustering steps from both tractography methods for the entire cohort depending on the located region of the brain. SRD = streamline regularized deterministic. SRP = streamline regularized probabilistic.

to the different clusters. A visual comparison reveals the existence of similar fascicles between two individuals, and also reveals the possibility to establish larger white matter fiber bundles coherent between subjects by aggregating subsets of clusters for an individual, noting that the number of clusters to be aggregated may differ from one individual to another. Regardless of its belonging lineage, this first clustering step provided 79207 fiber clusters on average with a standard deviation of 26713 fiber clusters between subjects for the SRD tractography approach, and 64567 fiber clusters on average with a standard deviation of 22597 fiber clusters between subjects with the SRP tractography approach.

### 5.3.3 Fiber clustering at group level

All the cluster centroids obtained from the fiber clustering step performed at the individual scale were registered to the template space using the non-linear transformation computed from the ANTs toolbox, before proceeding to the fiber clustering step at the group level. To properly tune the normalization factor  $nf$  and the maximum distance for the centroid affinity  $CAMD$  in order to maximize the number of inter-subject fiber clusters, a preliminary study was conducted using a subset of four individuals, including two STI quails and two LTI quails, in order to evaluate the obtained cluster number for a discrete  $10 \times 10$  grid of  $(nf, CAMD)$  values covering two  $[1.0; 100.0]$  and  $[0.1; 4.0]$  ranges of values for  $nf$  and  $CAMD$  respectively. Figure 5.10 shows the corresponding 3D surface plots for the SRD and SRP approaches, depicting a convex landscape of the cluster count with respect to the  $nf$  and  $CAMD$  parameters. It allowed to get the optimal settings  $(nf, CAMD) = (4.0, 2.0)$  and  $(nf, CAMD) = (2.0, 1.8)$  respectively for the SRD and SRP approaches.

Using these optimal parameters, the inter-subject clustering step yielded a higher number of centroid clusters using the SRD approach in comparison to the SRP approach. Table 5.3 summarizes the results for the left and right hemispheres, the interhemispheric region and the cerebellum, and for the two SRD and SRP approaches. These results highlight the fact that SRD tractography led to a more balanced cluster and fiber distribution in the quail's brain. The SRD method was believed to eventually induce a better defined structural connectivity atlas with less anatomically implausible white matter fibers and bundles than the SRP method. Consequently, the SRD approach is here the selected one to create the structural connectivity atlas. The obtained centroid clusters can be now investigated in order to design the target Japanese quail connectivity atlas.

### 5.3.4 Atlas building

This last semi-manual step consists in a consolidation of these individual clusters to point out the anatomically relevant white matter bundles. The final structural connectivity atlas shown in Figure 5.11 illustrates 34 major fiber tracts which labeling was realized in collaboration with neurobiologists to ensure a coherence with the 195 neuroanatomical struc-

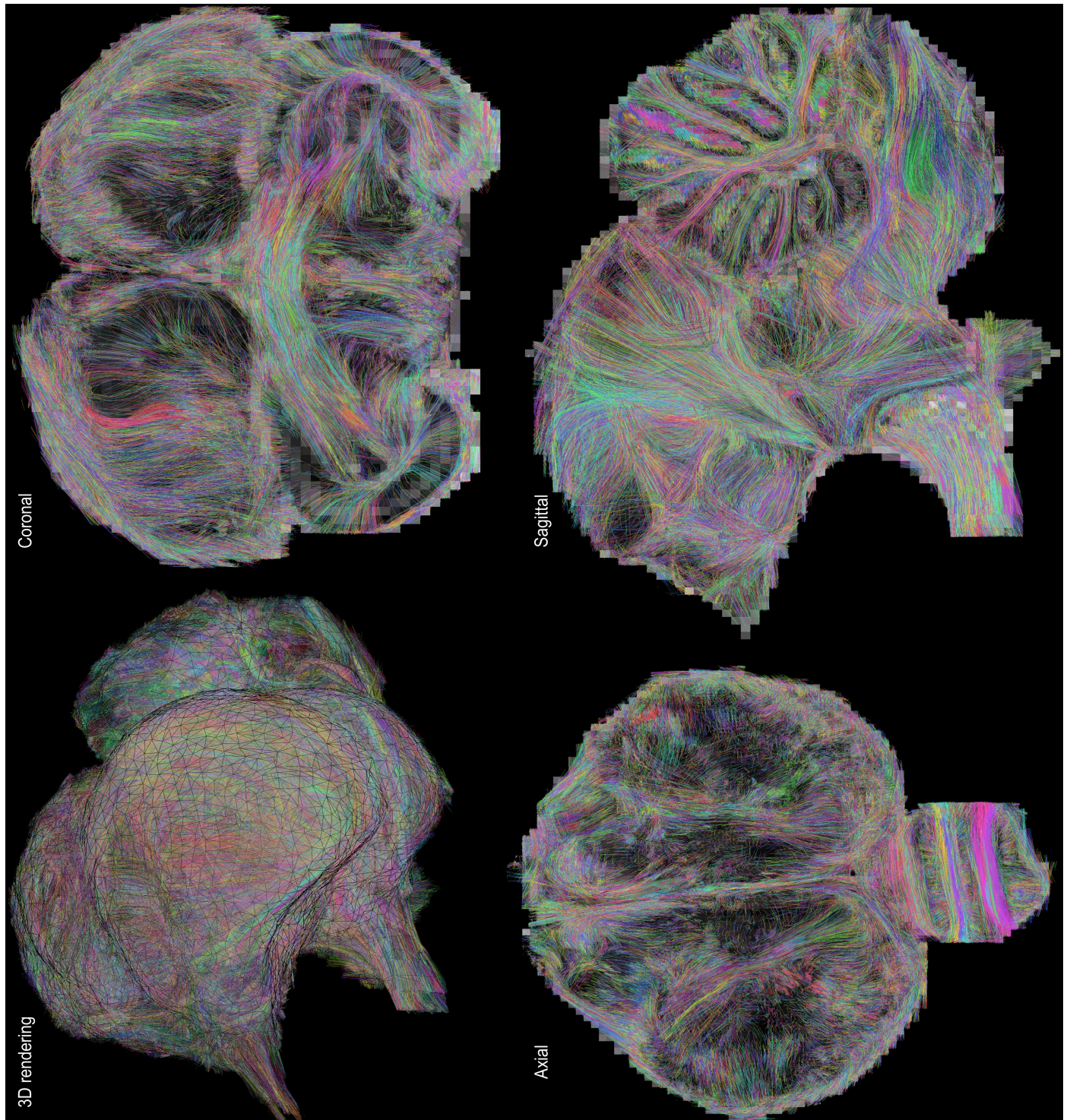


Figure 5.9a: Results of the intra-subject fiber clustering step based on streamline regularized deterministic (SRD) tractography for 7147 LTI quail superimposed on its generalized fractional anisotropy (GFA) map in the three spatial views and a 3D rendering of the generated fibers.

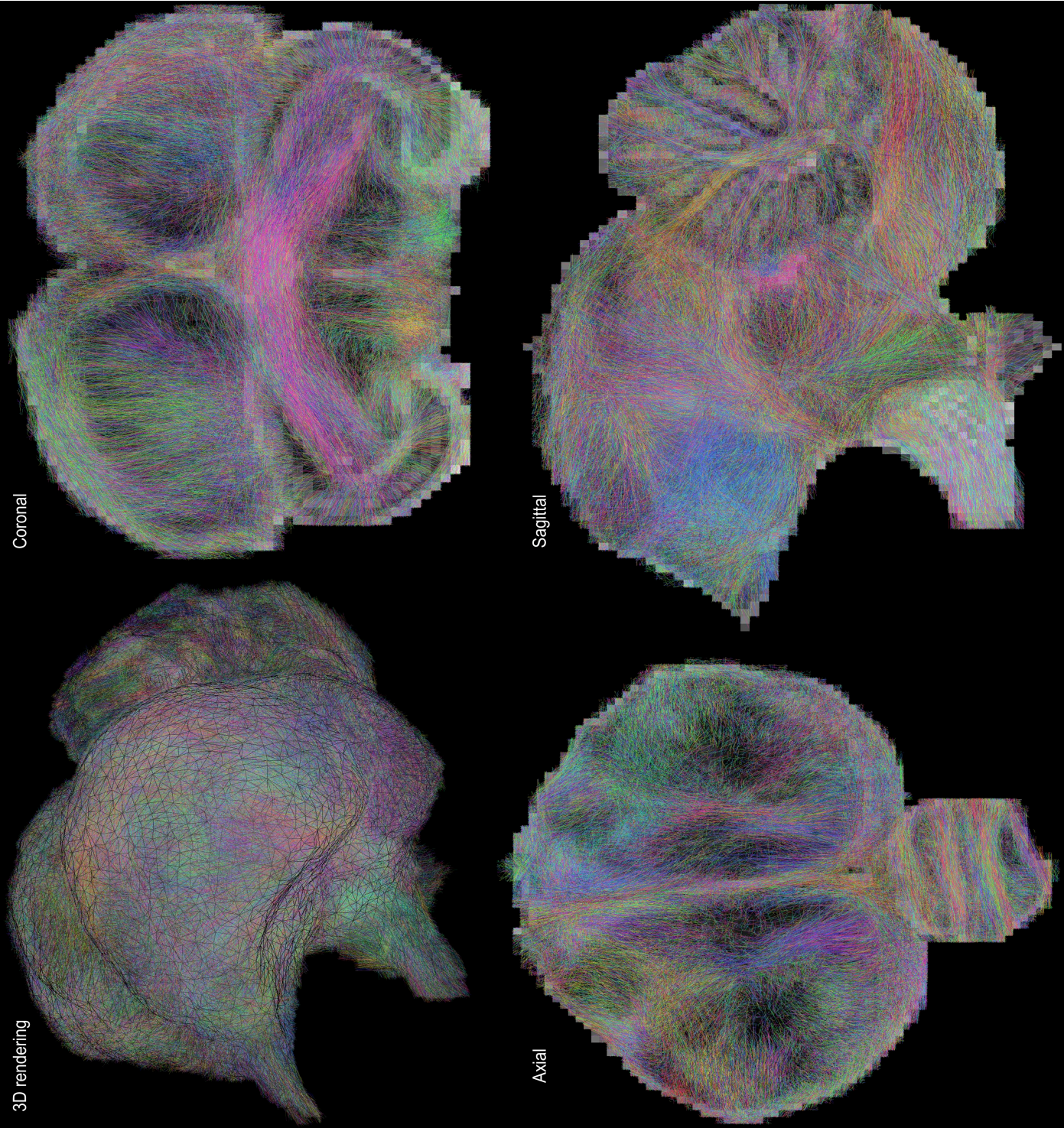


Figure 5.9b: Results of the intra-subject fiber clustering step based on streamline regularized probabilistic (SRP) tractography for 7147 LTI quail superimposed on its generalized fractional anisotropy (GFA) map in the three spatial views and a 3D rendering of the generated fibers.

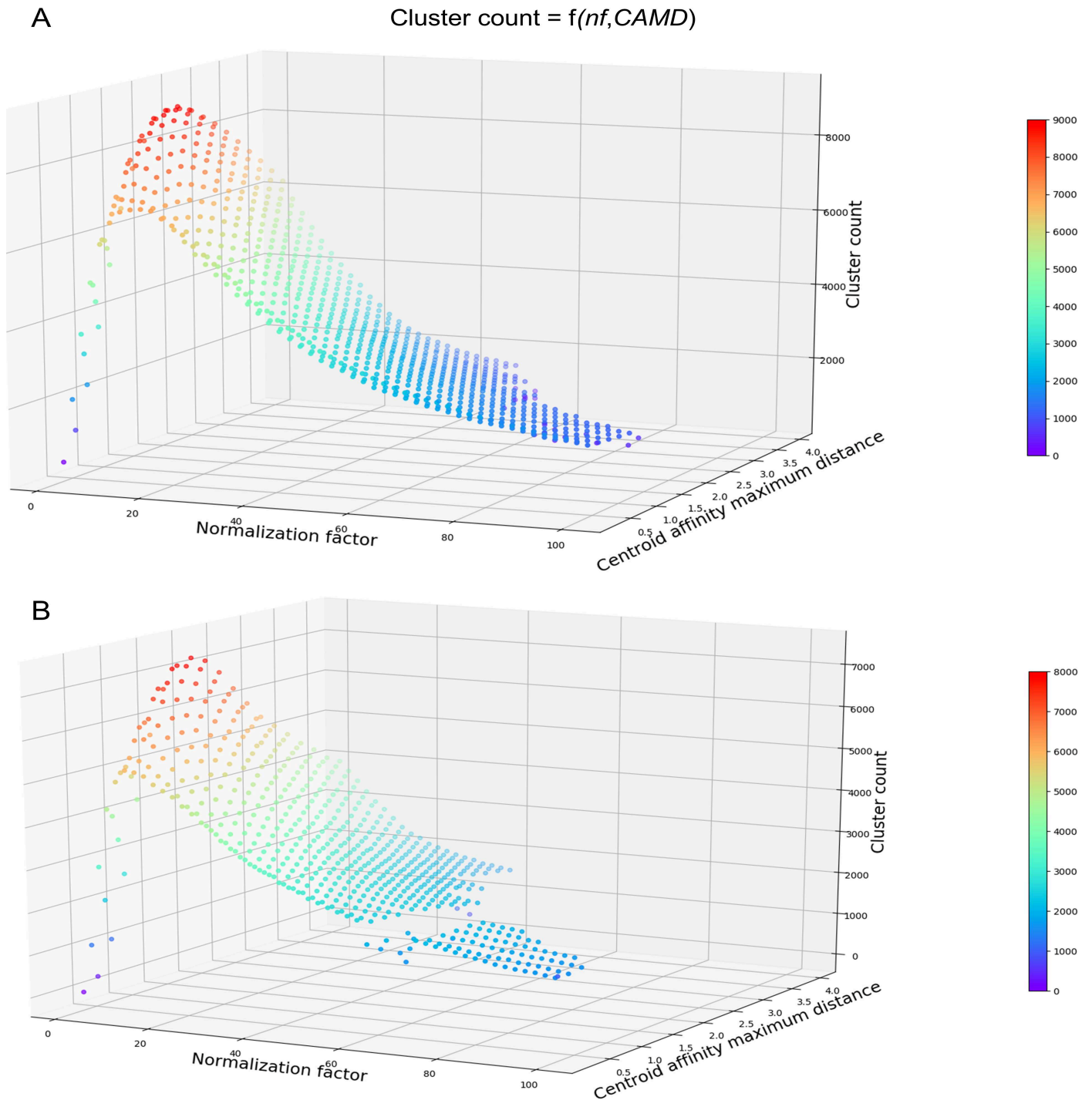


Figure 5.10: 3D surface plots of the number of clusters obtained at the inter-subject fiber clustering step stemming from the streamline regularized deterministic (SRD) (A) and streamline regularized probabilistic (SRP) (B) tractographies for four quails according to the normalization factor  $nf$  and the maximum distance for the centroid affinity  $CAMD$ . The variance of the centroid affinity was set at 1600 for the optimization process.

tures identified from the template previously presented. Some of the identified structures were used to both select and group inter-subject fiber clusters, and to name the 34 resulting white matter bundles listed below. We can partition the fiber tracts into three groups alike humans: commissural, projection and association fiber tracts.

The commissural fiber tracts refer to the anterior commissure (only direct intertelencephalic pathway [Ehrlich et al. 1985]), the posterior commissure (serves auxiliary visual functions [Stanic et al. 2010]), the vestibular commissure (part of the flight control system [Bilo 1978]), and the optic chiasm (initiates visual pathways).

The projection fiber tracts gather the corticoseptomesencephalic tract (descending pathway that innervates thalamic and brainstem nuclei [Güntürkün, Verhoye, et al. 2013]), the medial longitudinal fasciculus (part of the motor system), the nigrostriatal tract (major dopaminergic pathway involved in expectation and delivery of food rewards [Ogura et al. 2015]), and the quinfrofrontal tract (afferent component in the control of mandibulation [Kuenzel 1982]).

The association fiber tracts correspond to the cerebellar peduncles (part of the motor system), the cerebellum fibers (part of the motor system), the frontoamygdaloid tract (part of the reward-circuit [Kalenscher et al. 2005]), the olfactory tract (part of the olfactory system), the optic tract (part of the visual system), the oculomotor nerve (part of the visual system), the rostroventrolateral band (part of the visual system), the tectothalamic tract (part of the tectofugal system and thus motion detection [Wu, Russell, et al. 2000]), the amygdalo-nidopallial tract which connects the amygdaloid taenial nucleus, amygdala, parataenial area, nidopallium and arcopallium amygdaloid complex (AAC), the ventral amygdalofugal tract which connects the AAC, bed nucleus of stria terminalis, striatum, nidopallium, mesopallium and ventral hyperpallium, the left-hemisphere (lh) dorsal amygdalofugal tract which connects the AAC, nidopallium and apical hyperpallium (only existing in the left hemisphere), and the right-hemisphere (rh) dorsal amygdalofugal tract which connects the AAC, mesopallium, nidopallium and ventral hyperpallium (only existing in the right hemisphere).

Table 5.4 distinguishes the structural connectivity atlas fiber tracts according to the part of the brain they belong to. Among the 34 white matter bundles of the structural connectivity atlas, 28 of them have their names based on literature [Puelles et al. 2018]. As for the 6 fiber tracts that may reflect the emotivity of the Japanese quail (amygdalo-nidopallial tracts, ventral amygdalofugal tracts, lh and rh dorsal amygdalofugal tracts), their names were based on the main neuroanatomical structures they connect. Despite their slightly different pathways, we chose to assign the same name for lh and rh dorsal amygdalofugal tracts, considering that the avian brain lateralization (namely left/right asymmetry) may be the reason for this disparity.

### 5.3.5 Statistical analyses of the diffusion features along each quail tractogram streamline

The output of the statistical analyses are presented in Table 5.5, where all the atlas bundles are compared statistically to show a potential line effect. The relevant p-values are in bold type. 14 out of 34 white matter bundles appeared to be statistically relevant, evincing a line effect on the considered diffusion features from aQBI and DTI local models:

- the ventral amygdalofugal tract, left hemisphere: AD ( $p = 0.049$ ), ADC ( $p = 0.031$ ), RD ( $p = 0.031$ ).
- the lh dorsal amygdalofugal tract, left hemisphere: AD ( $p = 0.026$ ), ADC ( $p = 0.026$ ), RD ( $p = 0.019$ ).
- the rh dorsal amygdalofugal tract, right hemisphere: AD ( $p = 0.022$ ), FA ( $p = 0.0022$ ), GFA ( $p = 0.00114$ ), RD ( $p = 0.0133$ ).
- the cerebellar peduncles, left hemisphere: GFA ( $p = 0.0408$ ).
- the cerebellum fibers, right hemisphere: FA ( $p = 0.031$ ).

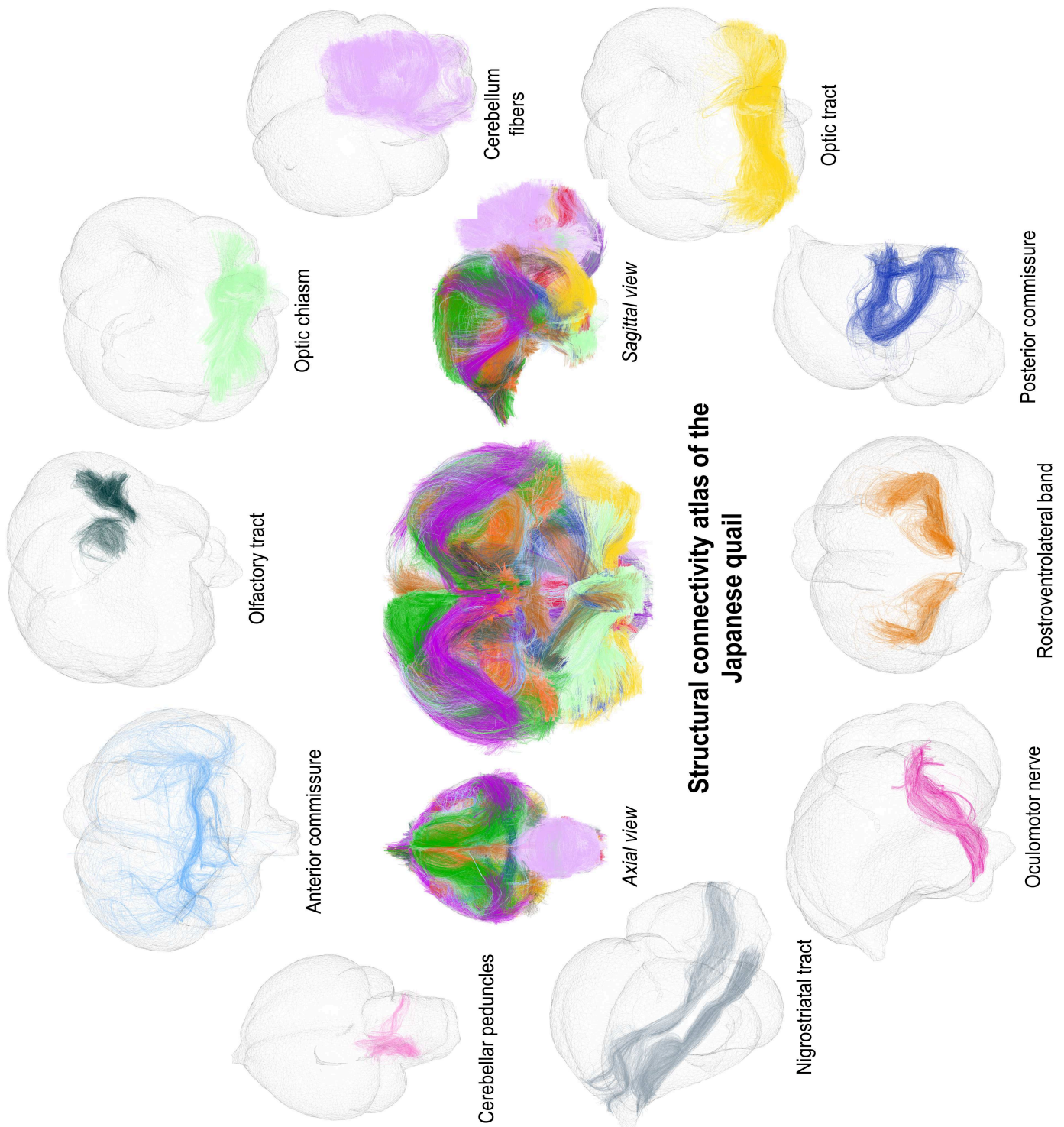


Figure 5.11a: The structural connectivity atlas of the Japanese quail based on streamline regularized deterministic (SRD) tractography and represented on a 3D mesh image of the template. The 34 identified white matter bundles are shown here in different colors as fibers of the clusters they belong to. The first set of white matter bundles shown here includes the olfactory tract, optic chiasm, cerebellum fibers, optic tract, posterior commissure, rostromentrolateral band, oculomotor nerve, nigrostriatal tract, cerebellar peduncles and anterior commissure.

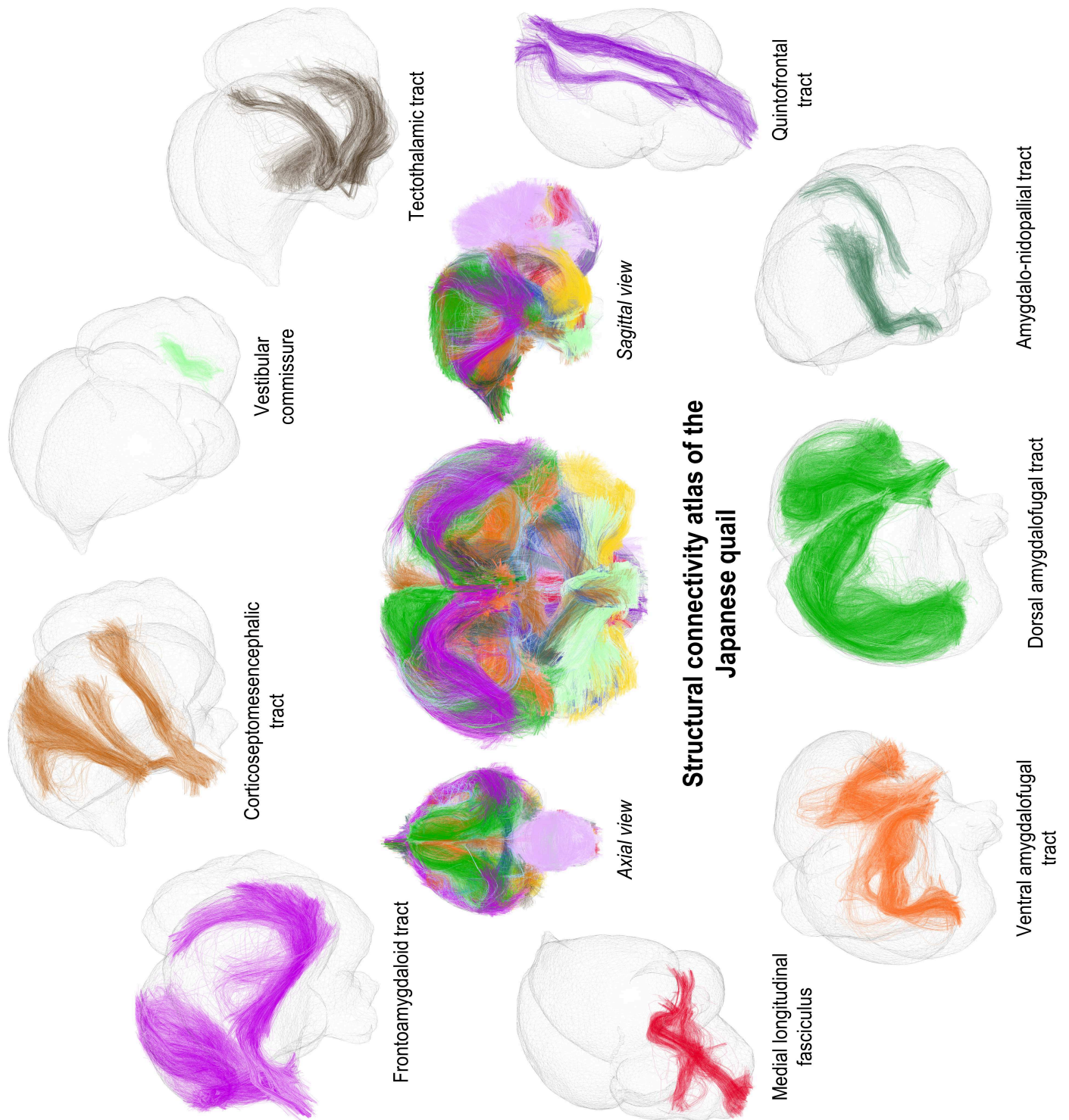


Figure 5.11b: The structural connectivity atlas of the Japanese quail. The second set of white matter bundles shown here includes the vestibular commissure, tectothalamic tract, quintofrontal tract, amygdalo-nidopallial tract, dorsal amygdalofugal tract, ventral amygdalofugal tract, medial longitudinal fasciculus, frontoamygdaloid tract and corticoseptomesencephalic tract.



































connectivity atlas bundle name	LH	RH	Int
anterior commissure			
posterior commissure			
optic chiasm			
vestibular commissure			
ventral amygdalofugal tract			
lh dorsal amygdalofugal tract			
rh dorsal amygdalofugal tract			
cerebellar peduncles			
cerebellum fibers			
corticoseptomesencephalic tract			
frontoamygdaloid tract			
medial longitudinal fasciculus			
nigrostriatal tract			
oculomotor nerve			
olfactory tract			
optic tract			
quintofrontal tract			
rostromedial longitudinal tract			
tectothalamic tract			
amygdalo-nidopallial tract			

Table 5.4: Table sorting the structural connectivity atlas fiber bundles according to the part of the brain they belong to. The colored squares have the same color as the corresponding bundles in the presented connectivity atlas of the Japanese quail in Figure 5.11. Int = interhemisphere. LH = left hemisphere. RH = right hemisphere.

- the corticoseptomesencephalic tract, left hemisphere: FA ( $p = 0.00455$ ), GFA ( $p = 0.00479$ ).
- the frontoamygdaloid tract, left hemisphere: FA ( $p = 0.0189$ ).
- the medial longitudinal fasciculus, left hemisphere: AD ( $p = 0.0363$ ), ADC ( $p = 0.031$ ), RD ( $p = 0.0224$ ).
- the nigrostriatal tract, left hemisphere: FA ( $p = 0.0305$ ), RD ( $p = 0.0189$ ); right hemisphere: GFA ( $p = 0.0264$ ), RD ( $p = 0.00217$ ).
- the optic chiasm: FA ( $p = 0.0239$ ), GFA ( $p = 0.0338$ ).
- the optic tract, left hemisphere: FA ( $p = 0.00189$ ), GFA ( $p = 0.0264$ ); right hemisphere: FA ( $p = 0.0189$ ).
- the posterior commissure: ADC ( $p = 0.042$ ), RD ( $p = 0.026$ ).
- the quintofrontal tract, left hemisphere: FA ( $p = 0.0111$ ), GFA ( $p = 0.0271$ ); right hemisphere: RD ( $p = 0.0490$ ).
- the rostromedial longitudinal tract, left hemisphere: RD ( $p = 0.0490$ ); right hemisphere: FA ( $p = 0.0377$ ), GFA ( $p = 0.0331$ ), RD ( $p = 0.0363$ ).

The Bonferroni correction validated the right-hemisphere dorsal amygdalofugal tract for the GFA and FA distributions considering the T-test, and the right-hemisphere nigrostriatal tract for the FA distribution considering the U-test. The Benjamini-Hochberg correction validated as well the right-hemisphere dorsal amygdalofugal tract for the GFA distribution considering the T-test, and for the FA distribution considering the U-test.



connectivity atlas bundle name	$p_{T-test}(GFA)$	$p_{T-test}(ADC)$	$p_{T-test}(FA)$	$p_{T-test}(AD)$	$p_{T-test}(RD)$	$p_{U-test}(GFA)$	$p_{U-test}(ADC)$	$p_{U-test}(FA)$	$p_{U-test}(AD)$	$p_{U-test}(RD)$
cc AC	0.579	0.586	0.738	0.545	0.654	0.486	0.376	0.486	0.458	0.376
cc OpticChiasm	<b>0.034</b>	0.200	<b>0.024</b>	0.080	0.491	0.065	0.230	0.057	0.138	0.324
cc PC	0.466	0.517	0.405	0.856	0.364	0.171	<b>0.042</b>	0.252	0.096	<b>0.026</b>
cc VC	0.160	0.712	0.116	0.367	0.930	0.252	0.123	0.299	0.252	0.123
lh ANT	0.439	0.448	0.296	0.426	0.507	0.486	0.376	0.458	0.403	0.324
rh ANT	0.798	0.385	0.686	0.676	0.452	0.065	0.123	0.057	0.096	0.109
lh CerebellarPeduncles	<b>0.041</b>	0.785	0.078	0.422	0.963	0.138	0.299	0.123	0.275	0.230
rh CerebellarPeduncles	0.180	0.708	0.234	0.980	0.576	0.376	0.123	0.430	0.189	0.065
lh CerebellarFibers	0.841	0.654	0.338	0.729	0.627	0.299	0.486	0.230	0.430	0.458
rh CerebellarFibers	0.429	0.912	0.174	0.928	0.817	0.109	0.486	<b>0.031</b>	0.324	0.403
lh CST	<b>0.005</b>	0.894	<b>0.005</b>	0.091	0.286	<b>0.011</b>	0.486	<b>0.019</b>	0.096	0.138
rh CST	0.256	0.830	0.120	0.637	0.379	0.138	0.486	0.057	0.171	0.299
lh DAT	0.674	0.057	0.192	0.060	0.056	0.230	<b>0.026</b>	0.109	<b>0.026</b>	<b>0.019</b>
rh DAT	<b>0.001</b>	0.299	<b>0.002</b>	0.618	0.184	0.430	<b>0.022</b>	0.376	0.138	<b>0.013</b>
lh FAT	0.146	0.862	<b>0.028</b>	0.600	0.947	0.085	0.458	<b>0.019</b>	0.324	0.486
rh FAT	0.753	0.512	0.254	0.683	0.414	0.430	0.376	0.096	0.430	0.349
lh MLF	0.152	0.060	0.609	0.074	0.054	0.096	<b>0.031</b>	0.154	<b>0.036</b>	<b>0.022</b>
rh MLF	0.801	0.267	0.351	0.367	0.224	0.349	0.096	0.209	0.138	0.138
lh NigrostriatalTract	0.075	0.533	<b>0.031</b>	0.983	0.321	0.057	0.403	<b>0.019</b>	0.458	0.275
rh NigrostriatalTract	0.354	0.228	0.095	0.377	0.177	<b>0.026</b>	0.275	<b>0.002</b>	0.376	0.275
lh OculomotorNerve	0.614	0.726	0.208	0.882	0.646	0.252	0.189	0.458	0.171	0.171
rh OculomotorNerve	0.998	0.631	0.377	0.643	0.637	0.275	0.085	0.299	0.189	0.189
lh OlfactoryTract	0.206	0.420	0.134	0.373	0.457	0.171	0.252	0.096	0.171	0.299
rh OlfactoryTract	0.466	0.666	0.322	0.602	0.713	0.376	0.430	0.275	0.430	0.458
lh OpticTract	<b>0.028</b>	0.190	<b>0.021</b>	0.083	0.414	<b>0.026</b>	0.209	<b>0.0189</b>	0.074	0.252
rh OpticTract	0.272	0.895	0.082	0.565	0.741	0.074	0.189	<b>0.019</b>	0.171	0.403
lh QuintofrontalTract	<b>0.028</b>	0.760	<b>0.019</b>	0.394	0.970	<b>0.049</b>	0.275	<b>0.011</b>	0.189	0.275
rh QuintofrontalTract	0.082	0.468	0.182	0.719	0.359	0.065	0.065	0.109	0.074	<b>0.049</b>
lh RVB	0.098	0.528	0.088	0.963	0.317	0.349	0.057	0.430	0.085	<b>0.049</b>
rh RVB	<b>0.033</b>	0.483	<b>0.038</b>	0.928	0.292	0.430	0.057	0.299	0.189	<b>0.036</b>
lh TectothalamicTract	0.168	0.405	0.160	0.204	0.917	0.349	0.230	0.299	0.252	0.096
rh TectothalamicTract	0.411	0.633	0.461	0.490	0.956	0.096	0.154	0.138	0.123	0.171
lh VAT	0.099	0.621	0.359	0.768	0.553	0.209	<b>0.031</b>	0.123	<b>0.049</b>	<b>0.031</b>
rh VAT	0.912	0.497	0.303	0.520	0.494	0.171	0.109	0.349	0.123	0.209

Table 5.5: Table of the diffusion features from the aQBI and DTI local models (the apparent diffusion coefficient (ADC), axial diffusivity (AD), fractional anisotropy (FA), generalized fractional anisotropy (GFA) and radial diffusivity (RD)), regarding the fiber tracts from the connectivity atlas and the resulting p-values of the statistical tests (unpaired Student T-test or Wilcoxon-Mann-Whitney U-test). The relevant p-values are in bold type. AC = anterior commissure. ANT = amygdalo-nidopallial tract. CST = corticoseptomesencephalic tract. DAT = dorsal amygdalofugal tract. FAT = frontoamygdaloid tract. Int = interhemisphere. LH = left hemisphere. MLF = medial longitudinal fasciculus. RH = right hemisphere. RVB = rostroventrolateral band. PC = posterior commissure. VAT = ventral amygdalofugal tract. VC = vestibular commissure.

## 5.4 Discussion

### 5.4.1 Connectivity-based comparisons between the two lineages

No variance in the brain volume among the cohort was observed, with similar volumes found for the STI and the LTI quails. Therefore, analyses of variance were conducted on the 21 intra-subject fiber clusterings, based on the SRD tractograms at the root of the connectivity atlas, and presented in Figure 5.12. We observed a lineage effect in favor of the STI line with a higher fiber average than the LTI line. There were slightly more fibers in the left hemisphere considering the whole cohort as well as each lineage. This left/right effect was even more accentuated for the STI quails than the LTI ones. The cerebellums of the LTI quails appeared to have a few more fibers than the STI quails, while the two lineages were equivalent regarding the interhemispheric fibers. Therefore, the LTI line has a less dense connectivity in both hemispheres than the STI line, which could reflect poorer connections related to its emotivity.

### 5.4.2 The brain lateralization of the Japanese quail

The functional brain lateralization is a common trait for all birds [Rogers 2008; Jonckers et al. 2015]. The final structural connectivity atlas presented in Figure 5.11 seems to mirror the brain lateralization of the Japanese quail on a structural connectivity level. We indeed counted 708 fiber clusters in the left hemisphere, 577 fiber clusters in the right hemisphere, 521 fiber clusters in the cerebellum and 145 interhemispheric fiber clusters. It has been defined that there is a domestic chick (*Gallus domesticus*) brain lateralization caused by the exposure to natural light *in ovo* [Wichman et al. 2009]. Our findings suggest the brain lateralization may persist even for the studied Japanese quails that come from years of dark-incubated breeding. They are in fact in conjunction with Costalunga et al. 2021 study that addresses the presence of multiple light-independent lateralization effects in the visual Wulst of the domestic chick, based on neural responses. These light-independent lateralization effects could then involve an asymmetrical distribution of fibers in the Japanese quail's brain.

Furthermore, this tendency reappears on a volumetric level. Chick's left eye is specialized in responding to small changes in any of a variety of stimulus properties [Vallortigara et al. 1991] and is preferentially used in dangerous situations [Rogers 1995]. As mentioned in Richard 2000, a higher volume of the right-hemisphere arcopallium amygdaloid complex (AAC) was noticed in this study, plus a larger number of fibers crossing the right optic tract and the right-hemisphere AAC compared to their left counterparts. From there, observations were conducted on the potential motor fiber connections triggered in those dangerous situations. However, no fiber connection in the structural connectivity atlas and on the individual scale was found between the AAC and the periaqueductal gray (PAG), the mesencephalic reticular formation (MRF) or the lateral pontine nucleus (LPN), as hypothesized in Saint-Dizier 2008, which could have reflected the motor pathway controlling fear-related behaviors of the Japanese quail. The 200 $\mu$ m isotropic resolution of the dMRI dataset may have been not enough to confirm the existence of such fiber connections. Only volumetric differences stood out, where the MRF and PAG (dorsolateral and medio ventral parts) are significantly bigger for the STI quails than the LTI quails. Considering the entire cohort, the left-hemisphere LPN and medio ventral parts of the PAG are wider than on the right-hemisphere side. The opposite effect is observed for the MRF and the dorsolateral parts of the PAG. Consequently, a direct link on the one hand between connections of the right optic tract and AAC, and on the other hand between the aforementioned anatomical structures and their brain volumes must be confirmed with further functional and neurochemical studies.

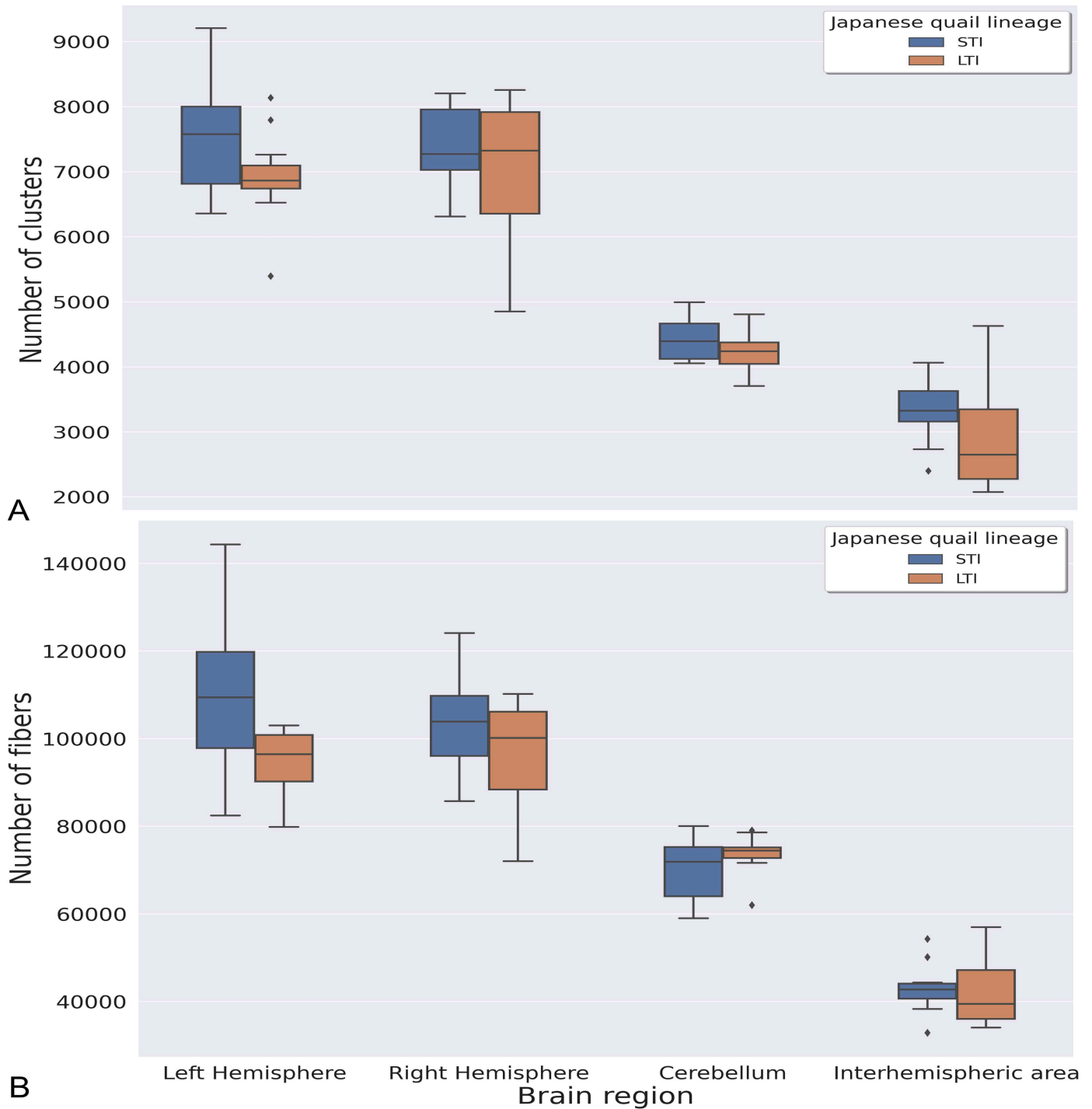


Figure 5.12: Box-plot diagrams realized on the 21 intra-subject fiber clusterings issued from the streamline regularized deterministic tractograms, covering the lineage effect for the different brain regions. A-B) Number of clusters (A) and number of fibers (B) counted for the STI and LTI lines regarding the left-hemisphere, right-hemisphere, cerebellar and interhemispheric tracts.

### 5.4.3 The fear-related circuit of the Japanese quail

Creating divergent lineages of Japanese quails based on tonic immobility duration offers a substantial advantage to explore the emotivity of that breeding animal. Indeed, this selection results in the development of different coping strategies in response to restraint stress between the two lines. The LTI quails, characterized by long tonic immobility durations, are more likely to adopt a passive behavior coping strategy upon exposure to fearful situations, while the STI quails, which exhibit short tonic immobility durations, behave more actively [Hazard, Leclaire, et al. 2008; Calandreau, Favreau-Peigné, et al. 2011]. These distinct coping mechanisms must be associated with the fear-related circuit that is likely to exist for every Japanese quail. The circuit must involve this bird's forebrain and thereby its equivalent of the human amygdala, which is known to participate in the control of fear-conditioned responses [LeDoux 2007; Martinez-Garcia et al. 2009]. The avian amygdala, which is referred to as the amygdaloid complex (formerly called the archistriatum), is comparable to the mammalian amygdala [Orosz et al. 2007]. It has been addressed that the avian amygdala does not correspond to the mammalian motor cortex [Medina et al. 2000]. But Xin et al. 2017 suggests that the lateral amygdaloid complex of the domestic chick is analog to the anterior cingulate cortex, as well as the basolateral amygdala of mammals. That is why bird's amygdaloid complex is namely involved in high-level functions such as decision-making and emotivity [Phillips 1964; Phillips and Youngren 1986; Bertin et al. 2018]. The avian amygdala is divided into the posterior pallial amygdala, the anterior arcopallium, the intermediate arcopallium, the dorsal arcopallium, the median arcopallium and the amygdaloid taenial nucleus (nucleus taeniae amygdalae, TnA) [Reiner et al. 2004].

The arcopallium amygdaloid complex (AAC), which is known to be a structure involved in fear-related behaviors for the Japanese quail according to functional data presented in Saint-Dizier 2008, refers to a broad heterogeneous structure that seems to have a dense connectivity. We indeed noticed connections with many brain structures including the mesopallium, the nidopallium, the apical hyperpallium, the ventral hyperpallium, and the TnA. In addition, the TnA, the lateral part of the bed nucleus of stria terminalis (BST), and the anterior amygdala area could be connected and involved in the expression of fear-related behaviors for the Japanese quail [Richard et al. 2000; Saint-Dizier 2008; Saint-Dizier et al. 2009]. According to LeDoux 2000, the primal structures that integrate input from the amygdala are cortical somatosensorial structures. They relay information from environmental stimuli to specifically involved brain regions in the control of fear-related behaviors. In Saint-Dizier 2008, it is hypothesized that telencephalic areas such as the hyperpallium, mesopallium and nidopallium could be involved in that somatosensorial integration.

Figure 5.13 depicts the resulting connections that may reflect the Japanese quail's emotivity in terms of fearfulness. Six tracts that were included in the final connectivity atlas stood out: the amygdalo-nidopallial tract (in both hemispheres), the ventral amygdalofugal tract (in both hemispheres), the lh dorsal amygdalofugal tract (only in the left hemisphere); the rh dorsal amygdalofugal tract (only in the right hemisphere). The functional role of these connections remains unknown and these connections are unlabeled, even though their existences were suggested in Saint-Dizier 2008. Nonetheless, in Hanics et al. 2017 fiber connections were exhibited between the AAC and the lateral part of the BST using anterograde tracing on domestic chicken's brains. This finding sets a precedent to confirm the existence of the ventral amygdalofugal tract obtained in this study.

As hypothesized in some previous studies [Martinez-Garcia et al. 2009; Saint-Dizier et al. 2009], we found a strong connectivity between the AAC and telencephalic regions (nidopallium, mesopallium, ventral hyperpallium and apical hyperpallium), which may convey their implications in somatosensorial integration of fear-related behaviors. Considering fiber architecture in the Japanese quail's brain, our findings correlate with the results presented in Stacho et al. 2020. The latter reported a fiber organization resembling the mammalian isocortex in the Wulst (also called the hyperpallium) and the sensory dorsal ventricular ridge (DVR) of the pigeon (*Columba livia*), using 3D polarized light imaging (3D-PLI).

From the output of the SRD inter-subject fiber clustering, we observed as well radial fibers located in the left-hemisphere apical hyperpallium, tangential fibers crossing the apical hyperpallium and ventral hyperpallium, on both sides of the septum. Since the sensory DVR of the Japanese quail seems to include the nidopallium, mesopallium and auditory parts of the nidopallium, all parts of the 3D anatomical atlas, tangential fibers were also located in that area. Therefore, the presented SRD inter-subject fiber clustering suggests the observation at the mesoscopic scale of a cortex-like fiber architecture of the Japanese quail's sensory pallium.

Our statistical results presented in Table 5.5 revealed that the right-hemisphere dorsal amygdalofugal tract differs significantly from its hemispherical opposite, the left-hemisphere dorsal amygdalofugal tract, regarding their FA and GFA values (unpaired T-test,  $p < 0.01$ ). In addition, the STI line has greater FA and GFA values than the LTI line for rh dorsal amygdalofugal tract. These results may point out a stronger coherence for this tract as well as more fibers composing it. As for the left-hemisphere ventral amygdalofugal tract connecting the AAC, BST, striatum, nidopallium, mesopallium and ventral hyperpallium, its radial diffusivity showed a significantly lower value for the STI line compared to the LTI line (Mann-Whitney,  $p < 0.05$ ). This value may indicate a stronger myelination for this bundle by improving the efficiency of the bundle conductivity, which we may assume to act in favor of fearfulness inhibition. The AAC input to the lateral part of the BST and to the nucleus accumbens (a component of the striatum) is, in fact, likely to transmit fear and aggression related signals to ventrobasal forebrain regions in domestic chicken [Hanics et al. 2017], which may be in conjunction with the radial diffusivity value of the ventral amygdalofugal tract.

If we consider the multiple tests corrections that have been conducted, it appears that two white matter bundles out of 34 passed either or both Bonferroni and Benjamini-Hochberg corrections. The dorsal amygdalofugal tract belongs to the fear-related circuit of the Japanese quail, while the nigrostriatal tract is known to be a major dopaminergic pathway involved in expectation, delivery of food rewards, and critical in the production of movement. They may be both inhibited when the bird experiences fearfulness, which could be the trigger for tonic immobility. Moreover, the two considered white matter bundles are located in the right hemisphere, suggesting that the fear-related behaviors strongly involve that part of the brain. Therefore, these results indicate that the STI and LTI quails present different structural connectomes that specifically concern fiber tracts involved in fear-related behaviors.

We may thus suggest that the discovered differences are diffusion-based markers reflecting the exacerbation of the fear-related behaviors for the LTI subjects, and they require further functional and ethological investigations to be confirmed as such.

#### 5.4.4 Methodological optimization

The designed Japanese quail's structural connectivity atlas ushers the deep investigation of its various functional circuits, as it has been proven in this study with the investigation of the fear-related circuit. The established postmortem imaging protocol assesses the added value of preclinical MRI systems, benefiting from both ultra-high magnetic fields and powerful gradients to map the anatomical substrates of avian brains. The proposed post-processing pipeline also showcases its robustness to map *ex vivo* the anatomical circuits of the Japanese quail. The imaging protocol and the post-processing pipeline still has room for improvement. The use of higher magnetic fields (15.4T or 17.2T) and higher gradient magnitudes (1000mT/m) could improve the spatio-angular resolution of individual anatomical and diffusion MRI dataset. This would allow the imaging of finer fascicles that are not accessible with the current protocol, such as the connections between the AAC and the PAG, the MRF and the LPN, as hypothesized by Saint-Dizier 2008. Further analyses need to be performed to better understand why the deterministic tractography approach provided better results than the probabilistic algorithm. This implies to significantly increase the seed count to widen the propagation domain.

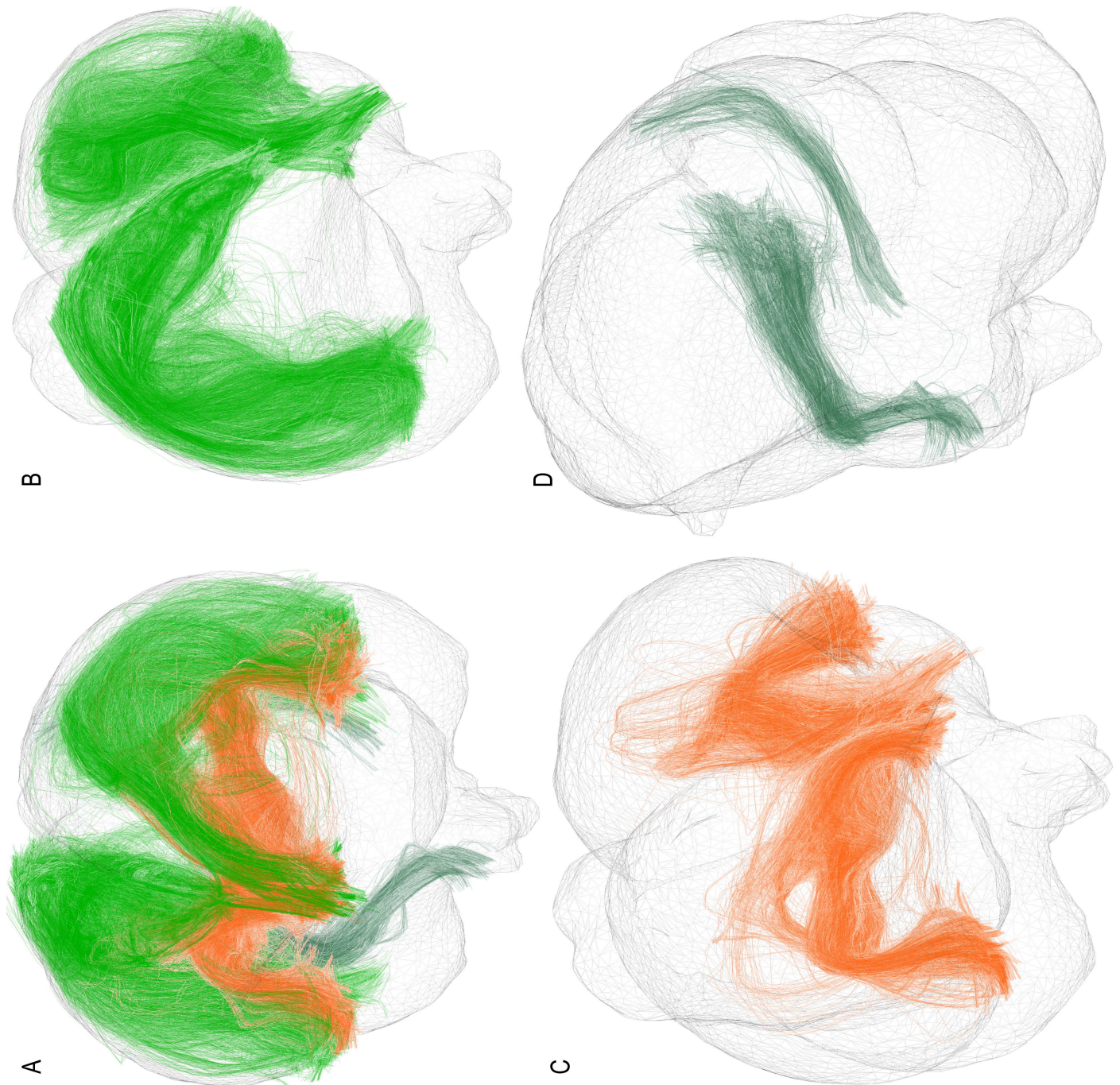


Figure 5.13: *The probable circuit of fear-related behaviors of the Japanese quail, based on streamline regularized deterministic and superimposed on a 3D mesh image of the template. A) Global view of the six fiber tracts. B) The lh dorsal amygdalofugal tract (only in the left hemisphere) and the rh dorsal amygdalofugal tract (only in the right hemisphere). C) The ventral amygdalofugal tract (in both hemispheres). D) The amygdalo-nidopallial tract (in both hemispheres).*

Future studies will include the validation of the obtained results in the frame of this work with histology. There are ongoing discussions with PLI experts [Axer et al. 2011] to scan two STI and LTI specimens at the microscopic scale in order to realize ultra-high resolution connectivity map of these individuals. Therefore, their reconstructed connections could

be compared to those in the created atlas.

Last, it could be interesting to evaluate the feasibility of scanning Japanese quails *in vivo* at 11.7T to generate functional MRI data, using a suitable functional paradigm involving the fear-related circuit.

## 5.5 Conclusion

This study provides the first structural connectivity atlas of the Japanese quail (*Coturnix japonica*) established using ultra-high field diffusion-weighted magnetic resonance imaging at 11.7 Tesla with advanced tractography and fiber clustering methods. It is composed of 34 white matter bundles reproducible between individuals, that correspond to connections. Similar to what has already been done for the human brain, this novel atlas allows to explore the diversity of the structural connectivity of the Japanese quail. Moreover, it enables to automatically segment the white matter bundles of any new quail individual, in order to better explore the functional networks of the Japanese quail. This study focused notably on the relationship between the emotivity of Japanese quail and its structural connectivity, showing significant differences between the short tonic immobility (STI) and the long tonic immobility (LTI) lines, in terms of morphometry of their neuroanatomical structures, and connectivity between the involved structures. The analyses of the dMRI data based on the scans of 21 Japanese quails highlighted 6 fiber tracts that are likely to reflect the emotivity of the Japanese quail in fearful situations. Hemispherical differences were noticed for these bundles, suggesting different connectivities related to emotivity, and especially fearfulness, between the two lineages. This work paves the way to comprehend how the anatomical structures of the Japanese quail communicate and how this communication regulates its emotivity. It is likewise a milestone to design the structural connectivities of wildlife animals from the ZooParc de Beauval (Beauval zoo, Saint-Aignan, France), as discussed in the next chapter.

## Chapter 6

# Structural connectivities of wildlife specimens from ZooParc de Beauval

As part of the Neuro2Co project, in the frame of which we investigated the structural connectivity of the Japanese quail (*Coturnix japonica*), we also conducted the investigation of the structural connectivities of eight wildlife animals bred in the ZooParc de Beauval (Beauval zoo, Saint-Aignan, France). The main objective is here to perform a comparative study of their structural connectomes at the mesoscopic scale using ultra-high field anatomical and diffusion MRI to get further insight about the potential cortical white matter bundles that are shared between these mammals. All the brain specimens provided by Dr Baptiste Mulot, head of the veterinary service of the ZooParc de Beauval, were scanned. However, the COVID-19 pandemic drastically reduced the interactions between the INRAE team, the ZooParc de Beauval team and the NeuroSpin team, hence not all of the brain samples could be explored. This chapter is therefore limited to the presentation of the acquired dataset and puts the emphasis on the preliminary investigations done on the California sea lion as an example of what will be done in all specimens.

### 6.1 Introduction

The brain of all the mammals exhibits two common features: the neocortex and the cerebellum. Placed in the dorso-lateral part of the telencephalon in mammals, the neocortex is a complex laminar structure, as discussed in Chapter 3. Moreover, the neocortex contains specific sensory, associative, and motor areas that allow mammals to obtain a detailed map of their surroundings and to adapt their behaviors according to their environments [Martinez-Garcia et al. 2009]. Therefore, accessing the connectomes of mammals enables a better understanding of their brain functionality, as well as their socio-emotional circuits that dictate their behaviors. For instance, preys and predators among the mammalian class do not operate the same way according to the emotions they are feeling (e.g. pain, fear, joy, anger or sadness). Comparative neuroanatomy of these two types of mammals could clarify the involved white matter bundles in the regulation of their behaviors and thus offering a better understanding of their conducts.

The printed socio-emotional circuits of mammals can be probed using diffusion-weighted magnetic resonance imaging



(dMRI) [Parker et al. 2003; Perrin, Poupon, Rieul, et al. 2005; Mori and Zhang 2006; Behrens, Berg, et al. 2007; Reisert et al. 2011; Teillac et al. 2017]. By exploiting dMRI datasets, the structural connectivity can be inferred using a two-fold process: first, modeling the local diffusion process and second, applying a fiber tracking (or tractography) method to infer virtual connections using a local model-informed streamlining technique. Previous studies were conducted using dMRI and tractography approaches to establish the structural connectivity of a single non-human species [Calabrese, Badea, Coe, et al. 2015; Calabrese, Badea, Cofer, et al. 2015; Gao et al. 2016; Uszynski 2018; Barrière et al. 2019; Bryant et al. 2020; Girard et al. 2020] or an extended cohort [Assaf, Bouznach, et al. 2020] at various spatial resolutions. None of them address the socio-emotional circuits of multiple mammals at the mesoscopic scale. This work focused on the inference of the structural connectomes at the mesoscopic scale of wildlife animals that used to live at the ZooParc de Beauval (Beauval zoo, Saint-Aignan, France) using *ex vivo* UHF dMRI. The purpose is to investigate the singularities of the anatomical connectivity for eight animal species, five preys (ring-tailed lemur, sitatunga, bongo, Java mouse-deer and California sea lion), and three predators (jaguar, Sumatran tiger and puma), to understand the specific patterns between observed neuroanatomical variability and animals' behavior.

The study will be divided into several steps, similar to those made for the Japanese quails (see Chapter 5) that consist in acquiring the MRI datasets for each individual including anatomical and diffusion MRI, computing an ODF map and performing fiber tracking to infer a dense set of virtual connections at the individual scale. The obtained tractogram thus allows to investigate the structural connectivity of specific functional networks, the socio-emotional circuit, in the frame of this study.

## 6.2 Material and methods

### 6.2.1 The wildlife species

Eight wildlife animal brain samples were provided by the ZooParc de Beauval (Beauval zoo, Saint-Aignan, France) and were collected from animals that died from a natural cause of death in the zoo before the extraction of their brains. The brains were perfused with paraformaldehyde (PFA) 4% and conserved in the same solution at 5 °C for immersion fixation until rehydration. Table 6.1 summarizes the main information gathered for each scanned species. The recovered brains were globally in a good state, with no or little visible damage.

### 6.2.2 MRI protocol

The acquisitions were performed over two years, depending on the point in time the samples were delivered for scanning. Due to the significant number of brain specimens to be scanned, the chosen scanning strategy was to perform only whole-brain acquisition without prior cutting. Consequently, the MRI instrument chosen to collect the anatomical and diffusion MRI data depended on the size of the target brain specimen.

The Java mouse-deer, ring-tailed lemur, sitatunga, baby jaguar, puma and baby Sumatran tiger were scanned on a preclinical Bruker BioSpec MRI scanner at 11.7 Tesla ( $G_{\max}=780\text{mT/m}$ ,  $\text{slew-rate}=9500\text{T/m/s}$ ) using a Bruker  $^1\text{H}$  transmit-receive volume coil preferred to surface coils in order to preserve the homogeneity of the NMR signal over the entire FOV. The bongo and the California sea lion were scanned on a clinical Siemens system at 7T ( $G_{\max}=150\text{mT/m}$ ,

species	category	age of death	brain volume (cm <sup>3</sup> )
Bongo ( <i>Tragelaphus eurycerus</i> ) female	prey	2 years old	611.5
California sea lion ( <i>Zalophus californianus</i> ) male	prey	unknown	630
Java mouse-deer ( <i>Tragulid javanicus</i> ) male	prey	1 year old	21.82
Ring-tailed lemur ( <i>Lemur catta</i> )	prey	unknown	116.16
Sitatunga ( <i>Tragelaphus spekii</i> ) female	prey	2.75 years old	224.4
Baby Sumatran tiger ( <i>Panthera tigris sumatrae</i> )	predator	unknown	190.03
Baby jaguar ( <i>Panthera onca</i> ) female	predator	1 month old	92.12
Puma ( <i>Puma concolor</i> ) male	predator	15 years old	269.5

Table 6.1: Table presenting the major information on the eight Beauval specimens.

slew-rate=333T/m/s) with a 1Tx/32Rx Nova Medical coil. Full brains were scanned at once, except for the sitatunga for which the cerebrum and the cerebellum were set apart and acquired in two distinct sessions with the same parameters and spatial resolutions. The best isotropic spatial resolutions were applied for all the performed sequences.

The imaging protocol includes an anatomical MRI scan to provide a high-resolution reference image, as well as a diffusion-weighted MRI scan to infer the structural connectivity of every wildlife animal. At least two days before scanning, the sample is placed in phosphate-buffered saline (PBS) to rehydrate the brain tissue. Then, the scanned sample is placed either in a well-sealed plastic bag or in a tailor-made hermetic container, and immersed in Fluorinert (FC-40, 3M, USA), an inert fluid that does not exhibit any NMR signal and preserves the hydration of the tissues.

The Bruker 11.7T MRI protocol included:

- an anatomical MRI scan performed using a conventional 2D T<sub>2</sub>-weighted spin echo (SE) sequence. The isotropic spatial resolution was set at 150µm for the Java mouse-deer and the ring-tailed lemur, 200µm for the baby jaguar, the sitatunga and the baby Sumatran tiger and 250µm for the puma. The other sequence parameters were TE/TR = 16/9000ms, flip angle = 90°, 9-10 excitations, 1 repetition, scan time of about five hours.
- a diffusion-weighted MRI scan using a 3D segmented echo planar imaging (EPI) pulsed gradient spin echo (PGSE) sequence with a single-shell high angular resolution diffusion imaging (HARDI) sampling of the Q-space at  $b=4500\text{s/mm}^2$  along 75 uniformly distributed diffusion directions, plus 5 volumes at  $b=0\text{s/mm}^2$ . The isotropic spatial resolution was set at 200µm for the ring-tailed lemur, 250µm for the Java mouse-deer, 300µm for the the baby jaguar and the baby Sumatran tiger, and 350µm for the sitatunga and and the puma. The other sequence parameters were TE/TR = 23/250ms,  $\delta = 5\text{ms}$ ,  $\Delta = 12.3\text{ms}$ , 21-25 segments, flip angle = 90°, scan time ranged from 22h to 25h.

The Siemens 7T MRI protocol included:

- an anatomical MRI scan performed using a 3D T<sub>2</sub>-weighted SPACE sequence. The isotropic spatial resolution was set at 500µm for the bongo and the California sea lion. The other sequence parameters were TE/TR = 193/3200ms, 1 excitation, 1 echo, flip angle = 120°, scan time = 54min38s.

- a diffusion-weighted MRI scan using a 3D diffusion-weighted True Fast Imaging with Steady Precession (TrueFISP, also known as balanced Steady State Free Precession [Miller, Stagg, et al. 2011]) sequence with a single-shell high angular resolution diffusion imaging (HARDI) sampling of the q-space at  $b=10000\text{s/mm}^2$  along 50 uniformly distributed diffusion directions, plus 2 volumes at  $b=0\text{s/mm}^2$ . The isotropic spatial resolution was set at  $600\mu\text{m}$  for the bongo and the California sea lion. The other sequence parameters were TE/TR = 18.37/26.74ms, 1 excitation, 1 echo, flip angle =  $35^\circ$ , scan time = 16h26min.

Table 6.2 indicates the isotropic spatial resolutions used for the anatomical and diffusion MRI data for each wildlife animal.

species	Anatomical data resolution	Diffusion data resolution
Bongo	500 $\mu\text{m}$	600 $\mu\text{m}$
California sea lion	500 $\mu\text{m}$	600 $\mu\text{m}$
Java mouse-deer	150 $\mu\text{m}$	250 $\mu\text{m}$
Ring-tailed lemur	150 $\mu\text{m}$	200 $\mu\text{m}$
Sitatunga	200 $\mu\text{m}$	350 $\mu\text{m}$
Baby Sumatran tiger	200 $\mu\text{m}$	300 $\mu\text{m}$
Baby jaguar	200 $\mu\text{m}$	300 $\mu\text{m}$
Puma	250 $\mu\text{m}$	350 $\mu\text{m}$

Table 6.2: Table indicating the spatial resolutions of the MRI data (anatomical and diffusion-weighted).

### 6.2.3 Image processing and analysis

A similar pipeline to the one used for the Japanese quail cohort was applied for each animal brain (see Chapter 5 for details). It is based on the Ginkgo toolbox (<https://framagit.org/cpoupon/gkg>) developed in the NeuroSpin/BAOBAB/Ginkgo team. Some pre-processing steps were needed to correct artifacts stemming from the diffusion MRI sequences. A non-local means filter was applied to the raw dMRI data to suppress Rician noise [Buades et al. 2011], followed by a correction of eddy currents-induced geometrical distortions. The used diffusion-weighted sequences (balanced SSFP on the clinical 7T MRI system and segmented 3D EPI PGSE on the preclinical 11.7T MRI scanner) were insensitive to eddy currents and susceptibility-induced geometric distortions, and produced diffusion-weighted MRI dataset free of such artifacts. Therefore, no specific eddy-current and susceptibility artifact correction methods were applied to the resulting dataset.

The measured SNR level was above 10 for all the dMRI data. Brain masks were computed from each averaged  $T_2$ -weighted volume for each animal brain. The local modeling of the diffusion process was realized using diffusion tensor imaging (DTI) and analytical Q-ball imaging (aQBI). The analytical Q-ball reconstruction was performed using a spherical harmonics order of 8 with a regularization L-curve factor of 0.006, providing ODFs and generalized fractional anisotropy (GFA) maps. The DTI reconstruction was performed using a Log-Euclidean estimator to preserve the positiveness of the tensor eigenvalues and to compute rotationally-invariant maps including the fractional anisotropy (FA), the apparent diffusion coefficient (ADC), the longitudinal and transverse diffusivities ( $D_{\text{parallel}}$  and  $D_{\text{transverse}}$ ). Both streamline regularized deterministic (SRD) and streamline regularized probabilistic (SRP) tractography approaches were used from the computed Q-ball ODF field [Perrin, Poupon, Cointepas, et al. 2005] using 8 seeds per voxel of the brain mask, an aperture angle of  $30^\circ$ , a forward step corresponding to a fourth of the spatial resolution. The explored fiber length range and the selected anisotropy-based regularization factor vary significantly from one species to another, considering their

distinct brain volumes listed in Table 6.1.

To build the target structural connectivity maps of the wildlife specimens, the chosen clustering approach is the one proposed by Guevara, Poupon, et al. 2011 and previously detailed in Chapter 5. It was used to process the individual tractograms and obtain a set of fascicles (or clusters) facilitating the identification of white matter bundles. Its parameters were fixed as follows for each animal brain:

- the fiber length range was set from the histogram of fiber length computed from the tractogram and corresponding to 2% and 98% of the cumulative histogram;
- the minimum percentage of fiber length intersecting a cluster was set at 31%;
- a minimum fiber count in a cluster and a minimum cluster size were respectively fixed at 5 and 3000.

Table 6.3 recapitulates the parameters applied for the intra-subject fiber clusterings, from SRD and SRP tractograms, exhibiting the structural connectivity of each scanned brain.

species	parcellation resolution	average cluster size	fiber length range
Bongo	600 $\mu$ m	9000	7.16-405.7mm (SRD) 7.09-388.5mm (SRP)
California sea lion	600 $\mu$ m	9000	7.17-356.4mm (SRD) 7.11-326.3mm (SRP)
Java mouse-deer	250 $\mu$ m	9000	1.85-129.9mm (SRD) 1.84-93.4mm (SRP)
Ring-tailed lemur	200 $\mu$ m	6000	3-140.0mm (SRD) 1-105.0mm (SRP)
Sitatunga (cerebrum and cerebellum)	350 $\mu$ m	9000	3.89-206.8mm (SRD) 3.79-177.7mm (SRP)
Baby Sumatran tiger	300 $\mu$ m	6000	1-138.8mm (SRD) 2.80-157.2mm (SRP)
Baby jaguar	300 $\mu$ m	9000	1.69-174.9mm (SRD) 1.67-146.5mm (SRP)
Puma	350 $\mu$ m	9000	6.39-218.2mm (SRD) 5.48-190.7mm (SRP)

Table 6.3: *Distinct sets of intra-subject fiber clustering parameters used for each Beauval animal for both SRD and SRP tractograms.*

## 6.3 Results and discussion

As mentioned in the introduction, the COVID-19 pandemic did not allow us to exploit the extent of the acquisition work carried out during this thesis, as we were unable to devote sufficient time to interact with the INRAE and the ZooParc de Beauval teams on that matter. Therefore, this section will only present preliminary results on all the scanned anatomical parts, with a particular focus on the California sea lion to illustrate the richness of the acquired data that can be exploited in the future.

### 6.3.1 General overview

The  $T_2$ -weighted anatomical images for all the animals offer a suitable contrast between gray and white matter structures. This contrast can be appreciated in Figure 6.1, which presents the anatomical MRI scans for the Java mouse-deer and the ring-tailed lemur reoriented in their anterior commissure-posterior commissure frames (AC-PC frames).

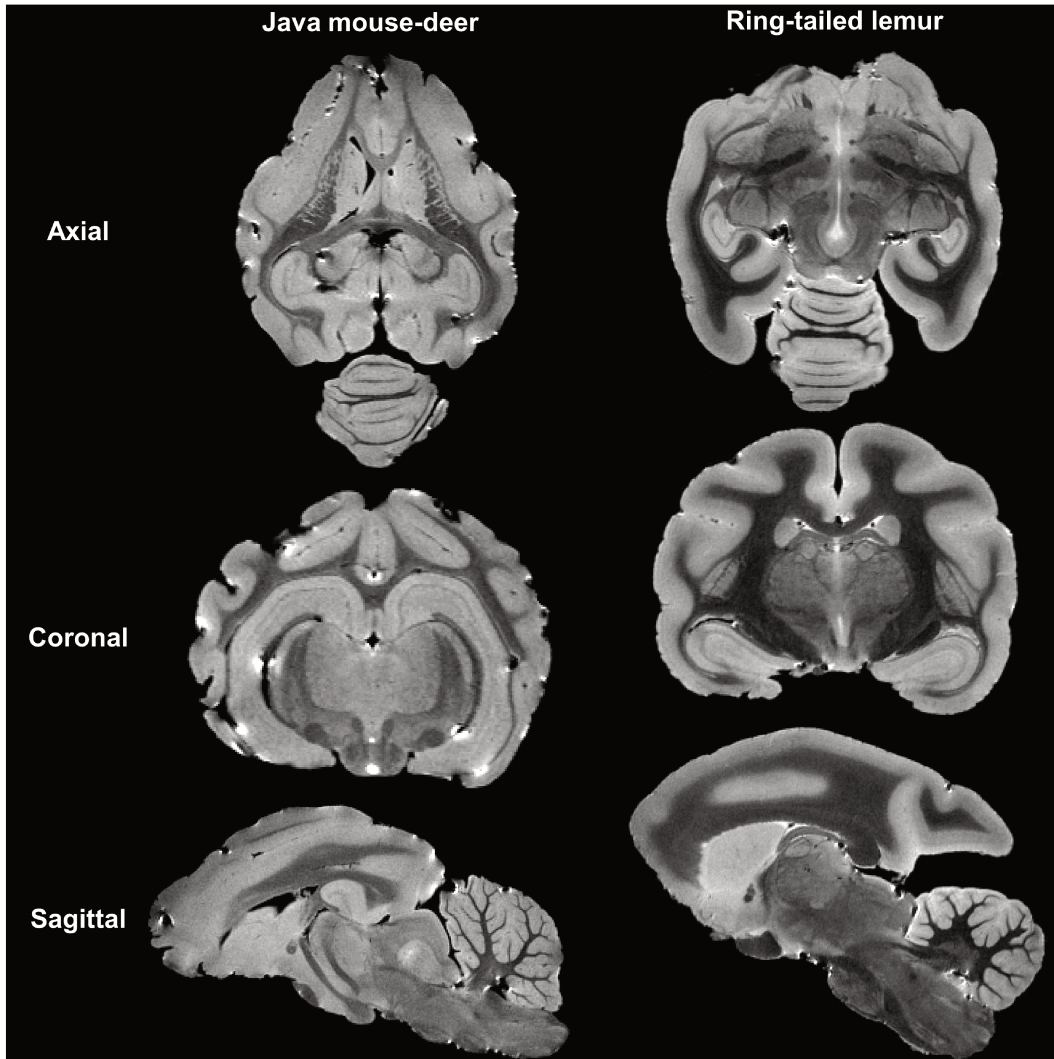


Figure 6.1:  $T_2$ -weighted anatomical images of the Java mouse-deer and the ring-tailed lemur in their AC-PC frames. The isotropic spatial resolution of the images is  $150\mu\text{m}$ . AC = anterior commissure. PC = posterior commissure.

The DTI and aQBI local models rendered diffusion-based feature maps characterizing the microstructure of the scanned brains: FA, GFA, ADC,  $D_{\text{parallel}}$  and  $D_{\text{transverse}}$  maps. Tractograms were then obtained from the analytical Q-ball ODF maps using the SRD and SRP tractography approaches and are shown on Figure 6.2. The latter exhibits the output of SRD tractography methods with only 10% of the computed streamlines due to the large number of generated streamlines for each animal. The number of produced streamlines are presented in Table 6.4, regarding the species and the fiber tracking technique. They depict a primal level of connectivity for the eight animals, revealing the plausible white matter bundles structuring their connectivities. Major white matter bundles that are common for all these mammals can be recognized, such as the corticospinal tract, the optic tract, the anterior and posterior commissures. The anterior and

species	number of streamlines (SRD)	number of streamlines (SRP)	number of fibers (SRD)	number of fibers (SRP)
Bongo	13545537	13604082	5064297	2849370
California sea lion	14416133	14480871	5855829	3462564
Java mouse-deer	5611281	5767408	1755679	973315
Ring-tailed lemur	24268920	24271078	9776278	4174524
Sitatunga	17267950 (cerebrum) 3241431 (cerebellum)	17267252 (cerebrum) 3241129 (cerebellum)	8720872 (cerebrum) 1423497 (cerebellum)	4316276 (cerebrum) 990797 (cerebellum)
Baby Sumatran tiger	14227867	14235372	7570548	3894952
Baby jaguar	14102356	14119143	8749192	4308791
Puma	22196262	22878549	9216527	4522724

Table 6.4: Table showing the number of streamlines and clusters respectively generated by the two tractography methods and intra-subject fiber clustering steps. SRD = streamline regularized deterministic. SRP = streamline regularized probabilistic.

posterior commissures were instrumental in the reorientation of the anatomical images, as those exhibited in Figure 6.1, following the same procedure as the one applied on the Japanese quail's population (see Chapter 5). A close examination of the intracortical connectivity was undertaken for every wildlife specimen.

Resembling fiber architectures for the bongo and the sitatunga were noticed. This observation does not come as a surprise since these two ruminants display an identical phylogeny (Mammalia; Theria; Eutheria; Boreoeutheria; Laurasiatheria; Artiodactyla; Ruminantia; Pecora; Bovidae; Bovinae; Tragelaphus). The actual disparity lies in the brain volume of the two female specimens that died at a similar age, as presented in Table 6.1. This result advocates for a conservation of the fiber architecture across mammals phylogenetically close.

As for cortico-cortical connectivity, we chose to focus on the Java mouse-deer and the ring-tailed lemur connectivity maps since their dMRI data have spatial resolutions similar to the one used for the Chenonceau project (see Table 6.2). The major limit of the acquisition scheme lies in the inability to illustrate the structural laminar connectivity, notably for the ring-tailed lemur which is a primate (Mammalia; Theria; Eutheria; Boreoeutheria; Euarchontoglires; Primates; Strepsirrhini; Lemuriformes; Lemuridae; Lemur). It was indeed suggested in Beul et al. 2019 that the primate cerebral cortex has a structural connectivity that can be assessed with neuron density. Vertically oriented cortical connections, such as the ones in Figure 6.3, are a moot point among the MRI community [Shamir et al. 2021], where only the extrinsic connections are observed with fiber tracking methods.

The imaging protocol did not include multiple MR contrasts (e.g.  $T_1$ -weighted,  $T_2$ -weighted or  $T_2^*$ -weighted sequences) that may have unveiled the distinct cortical layers and help to define the real pathways of the cortico-cortical connections. False-positive streamlines and bottlenecks are major issues emerging from postmortem dMRI data [Girard et al. 2020], that need to be tackled with anatomical priors or ground-truth validation, namely histology. Goulas et al. 2018 hypothesized that the graded laminar origin of intrahemispheric cortico-cortical connectivity in mammals is associated with the cytoarchitectonic gradients of the cerebral cortex, especially with the gradual changes in the soma size of the pyramidal neurons located in lower and upper cortical layers. Therefore, the quantification of cytoarchitectural proxies should be in line with the results of an advanced intracortical tractography approach. Such proxies can be obtained with the NODDI model [Zhang, Schneider, et al. 2012] or SANDI model [Palombo et al. 2020]. The latter could not be implemented for the study of these wildlife animals due to a single-shell diffusion MRI acquisition scheme, but that

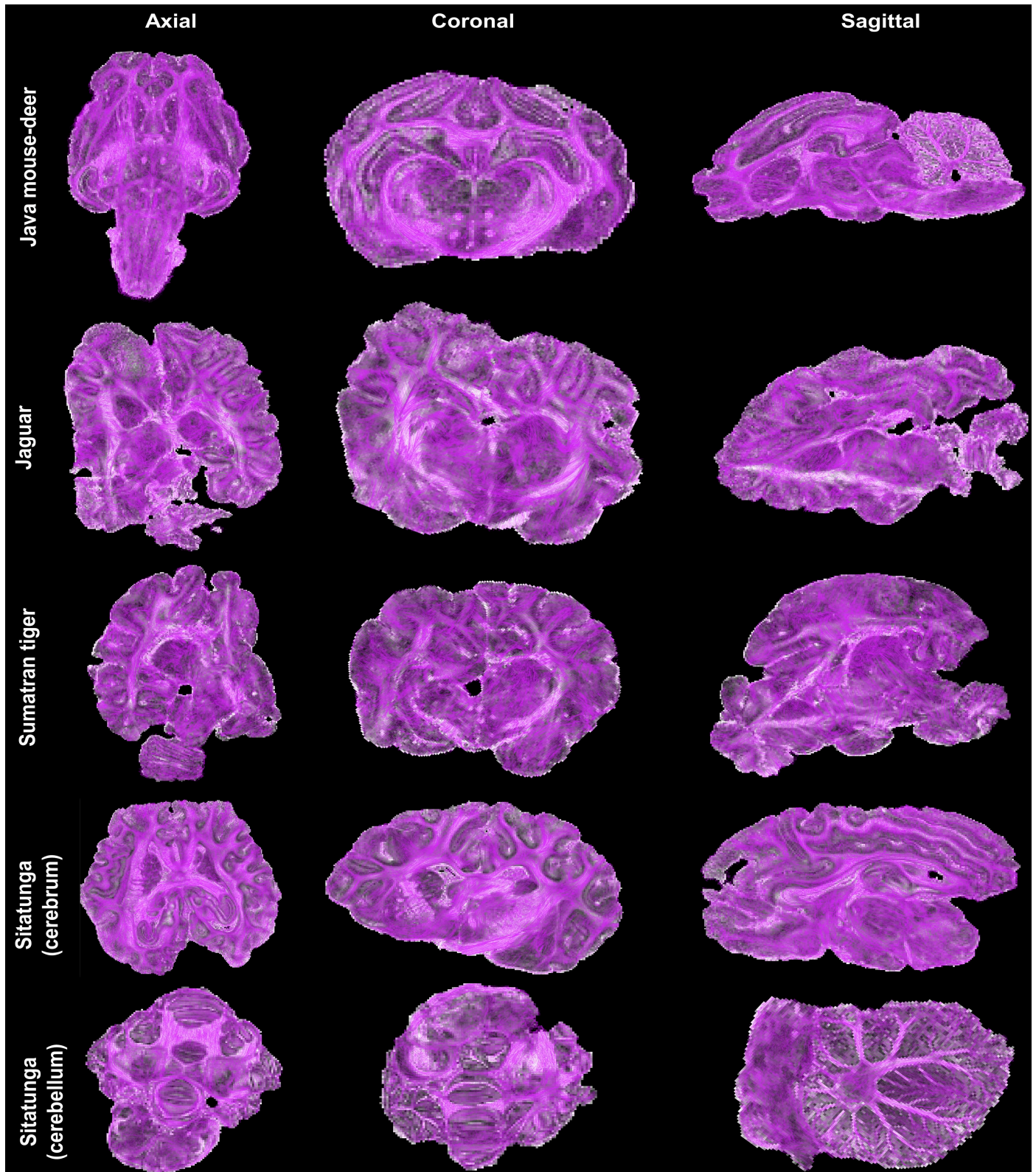


Figure 6.2a: Cerebral tractograms of Beauval animals based on streamline regularized deterministic (SRD) tractography, superimposed on their generalized fractional anisotropy (GFA) maps in the three spatial views. Only 10% of the streamlines are shown. The first set of images presents the Java mouse-deer, the baby jaguar, the baby Sumatran tiger, the sitatunga (cerebrum and cerebellum).

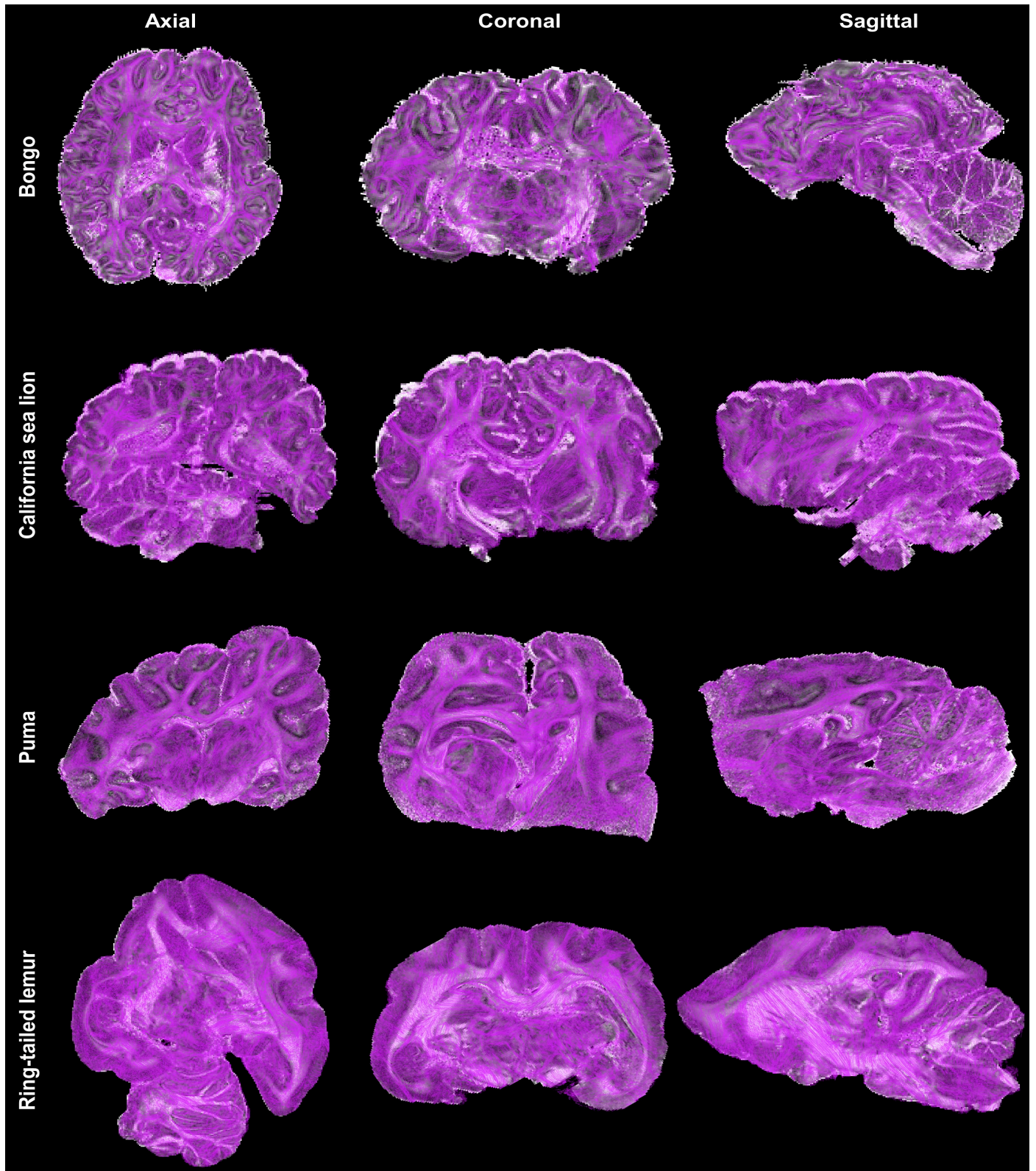


Figure 6.2b: Cerebral tractograms of Beauval animals based on streamline regularized deterministic (SRD) tractography, superimposed on their generalized fractional anisotropy (GFA) maps in the three spatial views. Only 10% of the streamlines are shown. The second set of images presents the bongo, the California sea lion, the puma and the ring-tailed lemur.



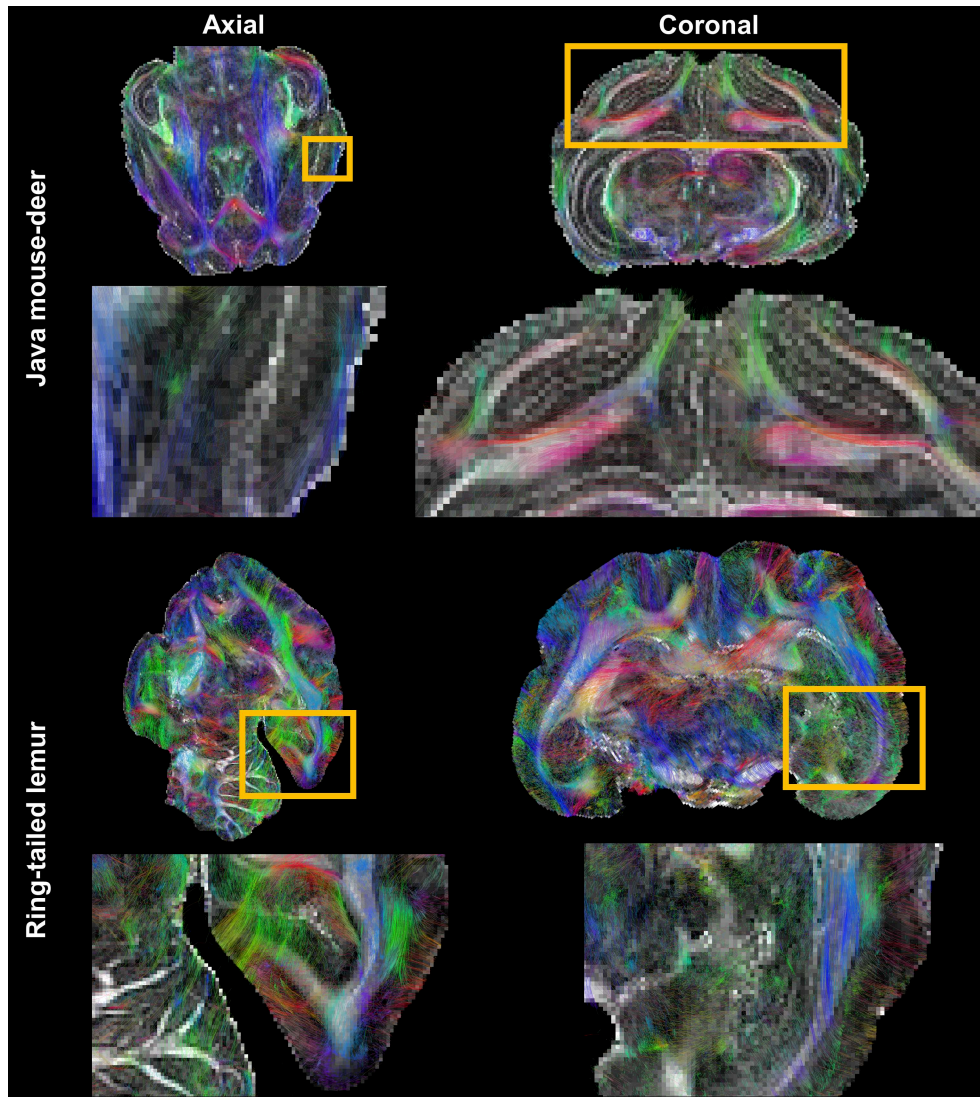


Figure 6.3: Zoom in the intracortical connectivity of the Java mouse-deer and the ring-tailed lemur, based on streamline regularized deterministic (SRD) intra-subject fiber clusterings. Radial and tangential fibers (yellow squares) appear at the cortical surface of both specimens.

conjunction is discussed in Chapter 7 where a multiple-shell scheme was utilized to establish the *ex vivo* dMRI dataset of the human brain.

The fact there are five preys and three predators offer the ability to explore the connectivity located in the amygdala and the periaqueductal gray of each animal. The investigation could pinpoint the differences between these two categories of animals regarding their fear-related circuits. For instance, the bongo emits a bleat in a frightening situation, while the sitatunga either performs feinting or stays still. The Java mouse-deer makes a high-pitched cry or a drum-roll sound with its hooves. As for the three scanned predators, the jaguar and the puma adopts a stalk-and-ambush game plan, whereas the Sumatran tiger chases its prey even though it is fruitlessly 90% of the time. It is all that diversity of fleeing/hunting strategies that may be reflected in the structural connectivities of these mammals.

On a greater scale, a comparison can be made between these wildlife animals and the breeding animal that is the Japanese quail. We may hypothesize differences along the white matter bundles related to the amygdala and the peri-

aqueductal gray. An accurate delineation of the amygdala and the periaqueductal gray from the  $T_2$ -weighted anatomical MRI data for all the studied animals is currently under consideration to validate or not the aforementioned hypotheses. Limitations to the analyses could arise from the unequal quality of the samples. Despite the preparation effort to hermetically seal the sample, air bubbles were sometimes trapped in the extracted brains, leading to chemical shift artifacts such as those visible on the coronal slice of the Java mouse-deer in Figure 6.1. Some brains were slightly damaged before or during the brain extraction process. The baby jaguar had its cerebellum partially ripped and the forebrain of the puma was somewhat squashed. The affected brain regions will be further examined to assess to what extent the observed damage hamper the validation of the hypotheses.

### 6.3.2 Focus on the California sea lion

The ratio of brain size to body size has long been considered as an allometric measure reflecting the cognitive abilities of a species. It was used as a specific marker of evolutionary theory, with the assumption that this measure was stable for a single vertebrate species and was guided by a linear law with a coefficient varying between two-third and three-quarter. The ratio remained relatively stable between vertebrate species, and that any gradient over time in this allometric ratio indicated a period of brain evolution (Figure 6.4). A recent study challenged this assumption, tending to show that the evolution of the body of the species under consideration to adapt to its environment was also an important factor that could be responsible for a change in the allometric ratio characteristic of that species [Smaers et al. 2021].

A second fundamental hypothesis is that the brain-body allometric ratio reflects the maintenance of basic autonomic functions (breathing, heart rate, vasomotor activity, autonomic reflexes such as swallowing, coughing or sneezing) and that any deviation would be related to cognitive development [Jerison 1955]. However, although their body sizes are comparable and they live in similar environments, the polar bear and the sea lion have a brain size that goes from simple to double in favor of the polar bear. But from a cognitive standpoint, the sea lion has a ratio between brain regions dedicated to higher order cognitive functions and brain regions dedicated to autonomic functions 3.6 times higher than the polar bear. This difference would be due to the fact that the sea lion has a much more developed vocalization and memorization capacity than the polar bear [Schachter et al. 2000].

One of the particularities of the sea lion is its ability to manage two types of sleep [Lyamin et al. 2002]. It does not need rapid eye movement (REM) sleep at sea for long periods of time, which can extend to several weeks. The California sea lion practices a unilateral sleep: one of the two hemispheres stays awake to maintain a sufficient body temperature and to keep an active vigilance in front of the potential dangers of the marine environment. When it returns to land, the sleep becomes bilateral again and the sea lion finds REM sleep phases similar to most terrestrial mammals, which contribute to maintaining its body balance. This ability to adapt its sleep to marine or terrestrial conditions is unique and illustrates its great capacity to adapt to the environment in which it evolves, giving up REM sleep at sea to maintain its body temperature at 39°C. Figure 6.5 shows a three-dimensional rendering of the pial surface of the California sea lion brain bred in ZooParc de Beauval, as well as its  $T_2$ -weighted anatomical MR images.

The size of the California sea lion brain is about 10cm in the antero-posterior direction, about 9cm in the right-left direction, about 5cm in the superior-inferior direction excluding the trunk and the cerebellum, and 7cm including the trunk and the cerebellum. The pial surface is the result of a gyrification process that presents numerous relatively deep grooves, with a central groove that is easily identifiable by being more pronounced than the others.

Axial/coronal/sagittal sections extracted from  $T_2$ -weighted anatomical SPACE MRI show a relatively developed cortical ribbon with a thickness similar to that of humans, ranging from two to four millimeters. The cerebellum also exhibits

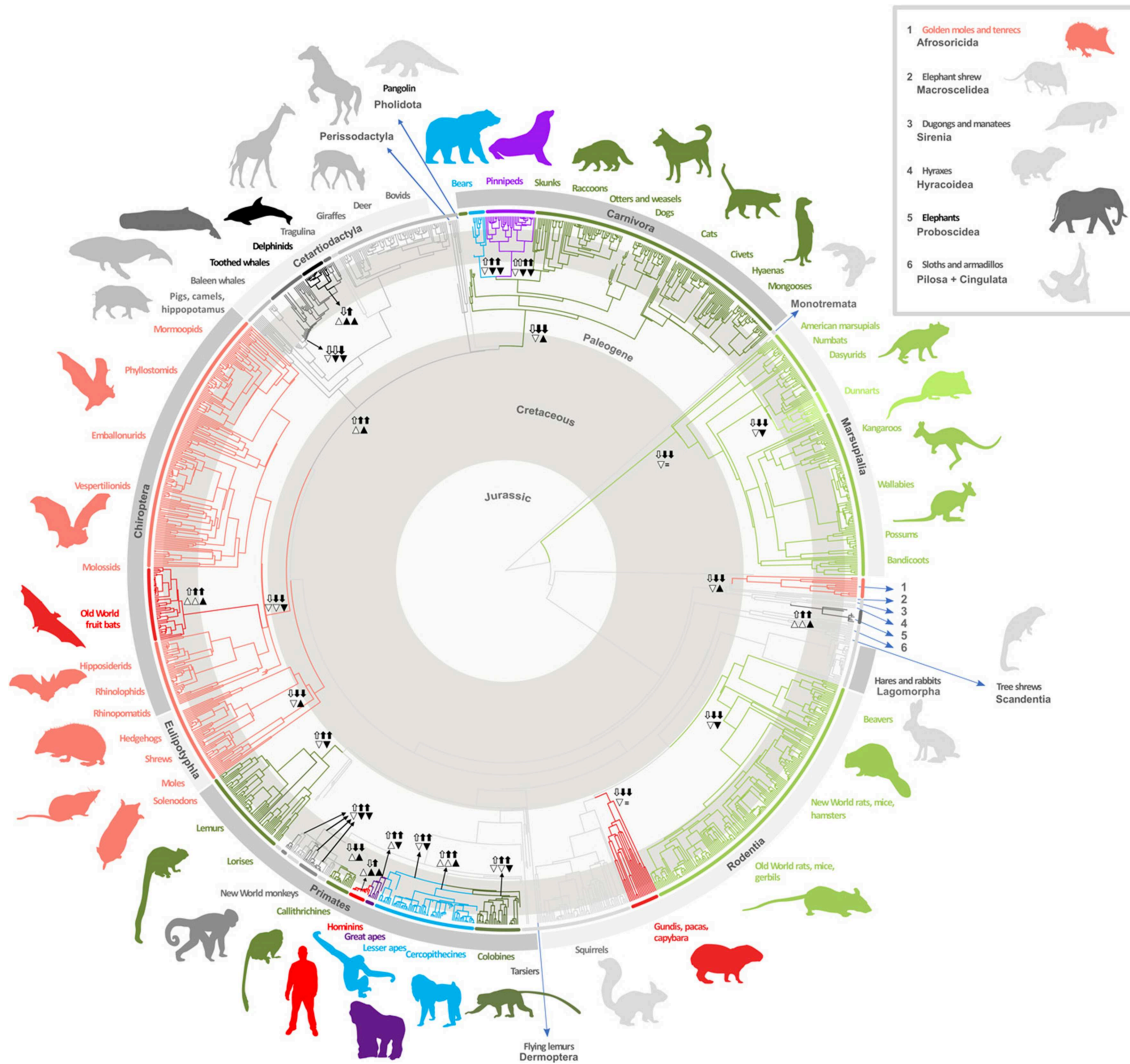


Figure 6.4: Time-calibrated phylogeny of mammals with branch colors corresponding to the 30 significantly different allometric grades identified in Smaers et al. 2021.

a strong folding and asymmetry of positioning with respect to the sagittal median plane. The origin of which is to be confirmed and may be related to the fixation process of the brain sample.

The basal ganglia (caudate nucleus, putamen, nucleus accumbens, globus pallidus) are readily identifiable. The thalami occupy a large volume. The anterior and posterior commissures are also easily recognizable, allowing the definition of a reference frame equivalent to Talairach’s reference frame, namely the AC-PC frame, and the reorientation of the brain to facilitate its study.

Figure 6.6 gives a two-slice sagittal and coronal overview of the ODFs reconstruction obtained from the analytical Q-ball model at spherical harmonics order 8 using a Laplace-Beltrami regularization factor of 0.006. The lobes of the ODFs have a high angular resolution which, coupled with the high spatial resolution, gives accurate and consistent information on the local orientation of axonal fibers.

Figure 6.7 illustrates the quantitative mappings resulting from the analysis of the ODFs map: the generalized fractional anisotropy (GFA) map and the color-encoded diffusion direction (CED) map providing the ODFs main peak orientations. The red color corresponds to the right-left direction, the green color to the anterior-posterior direction, and the blue color

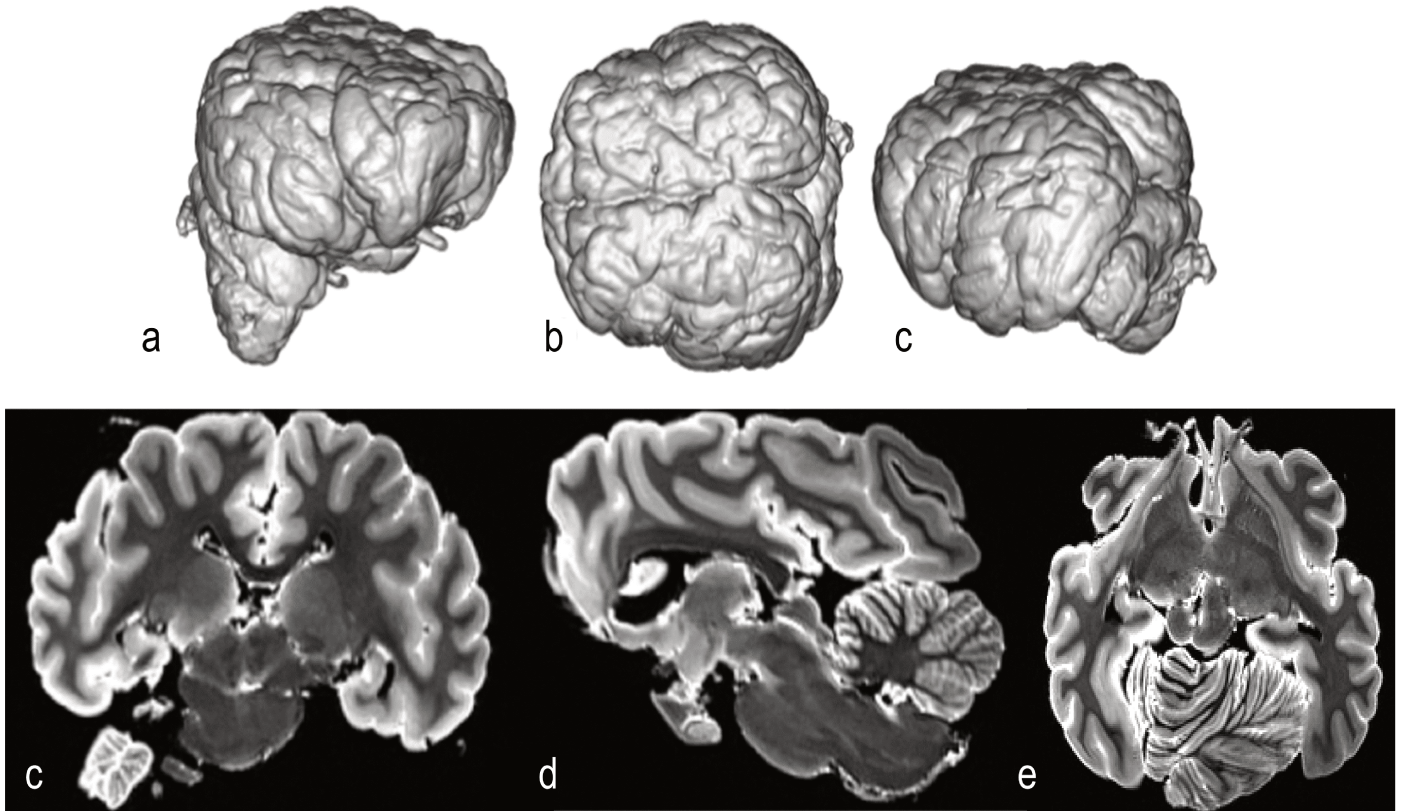


Figure 6.5: 3D rendering and anatomical MR images of the California sea lion brain. (a-c) 3D rendering of the cortical surface in three different spatial orientations. The 500 $\mu$ m anatomical images in the coronal (d), sagittal (e) and axial (f) views present a noticeable gray/white matter contrast.

to the superior-inferior direction. The CED map allows the identification of multiple major white matter bundles such as the corpus callosum, anterior and posterior commissures, corticospinal tract, cingulate bundles, optic radiations, and cerebellar peduncles.

Figure 6.8 gives an overview of the reconstructed brain connections using the streamline regularized deterministic (SRD) tractography algorithm proposed by Perrin, Poupon, Cointepas, et al. 2005 with: a forward step of 50 $\mu$ m, an aperture angle of 30°, a regularization factor of 0.15 corresponding to the GFA threshold obtained at 98% of the GFA cumulative histogram, generating 20 random starting seeds within each voxel of the tractography mask computed from T<sub>2</sub>-weighted anatomical imaging and realigned to diffusion MRI data, and with discrete sampling of the unit direction space along 50 directions uniformly distributed on the unit radius sphere and endowed with antipodal symmetry of directions as proposed by Koay et al. 2011. Figure 6.8a presents a three-dimensional representation of 5% of the 35 millions of reconstructed fibers, the pial surface made transparent for visualization purposes, as well as the representations of the fibers around orthogonal slice planes. Limitations of the graphics processor on which the 3D renderings are performed explain the illustration of just 5% of the reconstructed fibers. In a similar way to what has been observed from the CED maps, several of the large white matter bundles are identifiable: corpus callosum, corticospinal tract, cingulate bundles, cerebellar peduncles. As shown in Figure 6.8e, lots of fine anatomical details can be found at the level of the brainstem and the cerebellum that is worth being investigated in the future.

The high spatial resolution obtained from *ex vivo* diffusion MRI performed at ultra-high field is also an asset to better

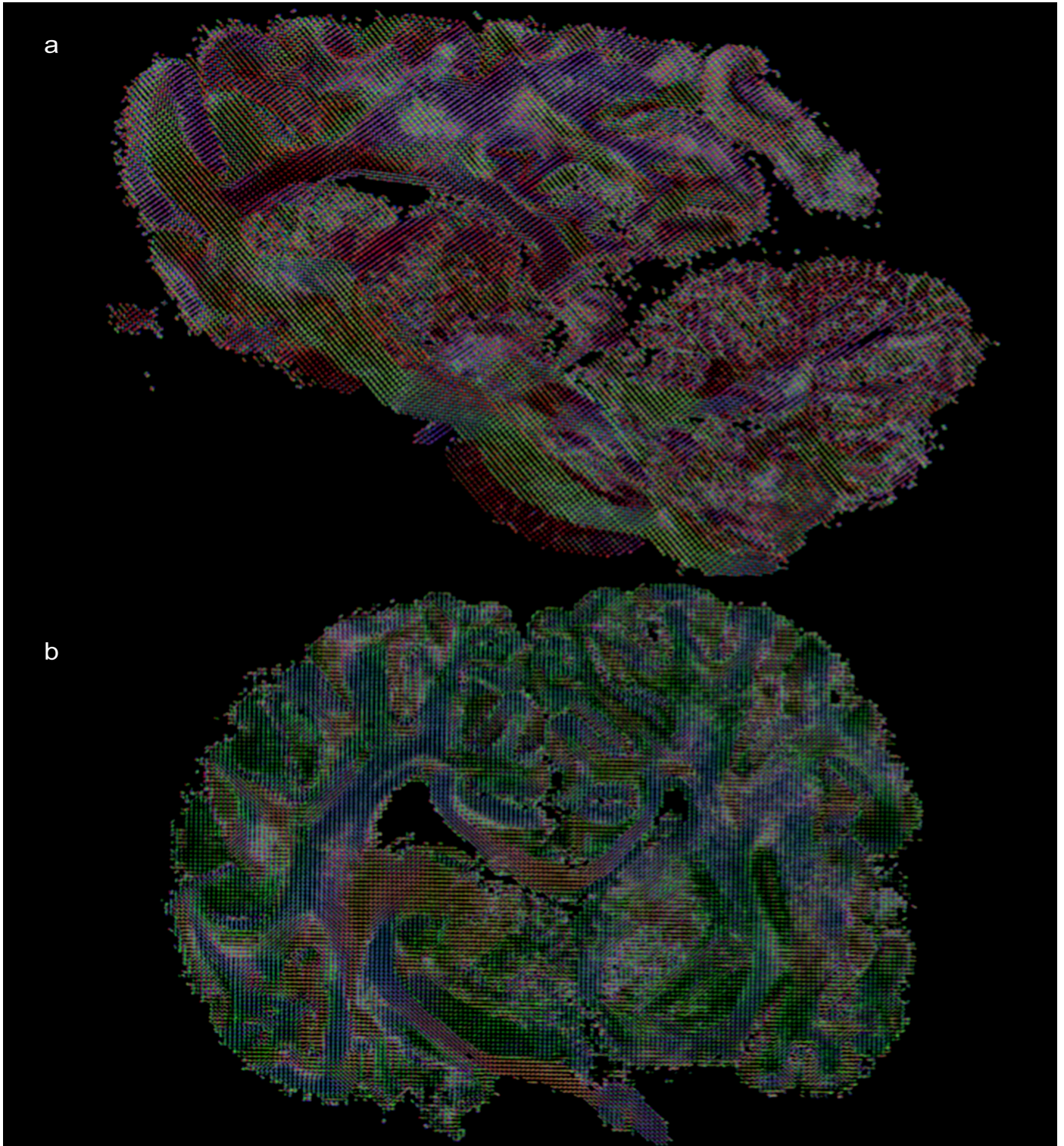


Figure 6.6: ODFs maps obtained from HARDI data acquired from the California sea lion brain using an analytical Q-ball model of spherical harmonic order 8 and Laplace-Beltrami regularization factor of 0.006. At the top, there is a sagittal view of the ODFs, and at the bottom it is a coronal view of the ODFs.

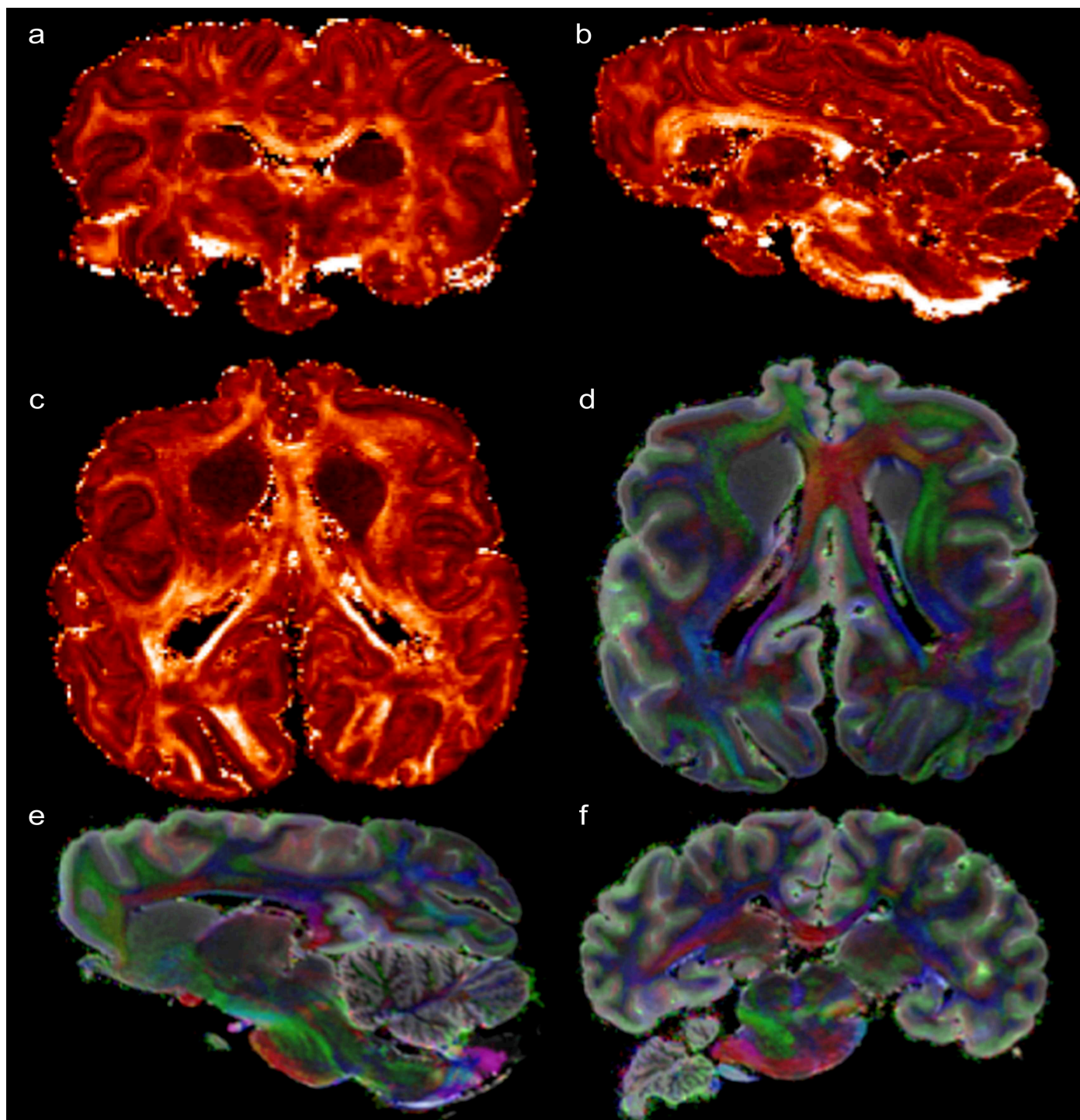


Figure 6.7: *GFA and CED maps of the California sea lion brain. The CED map is superimposed on the  $T_2$ -weighted  $600\mu\text{m}$  reference image obtained from averaging the two null  $b$ -values MR images. Images are showcased in the coronal (a,f), sagittal (b,e) and axial (c,d) views.*

map intra-cortical connectivity. As exhibited in Figure 6.9, directional information near and within the cerebral cortex reach sufficient angular resolution to detect the change in curvature of fibers as they are about to enter the cerebral cortex, and to track their radial trajectories within the cortical ribbon. Figures 6.9b and 6.9d also enable us to understand

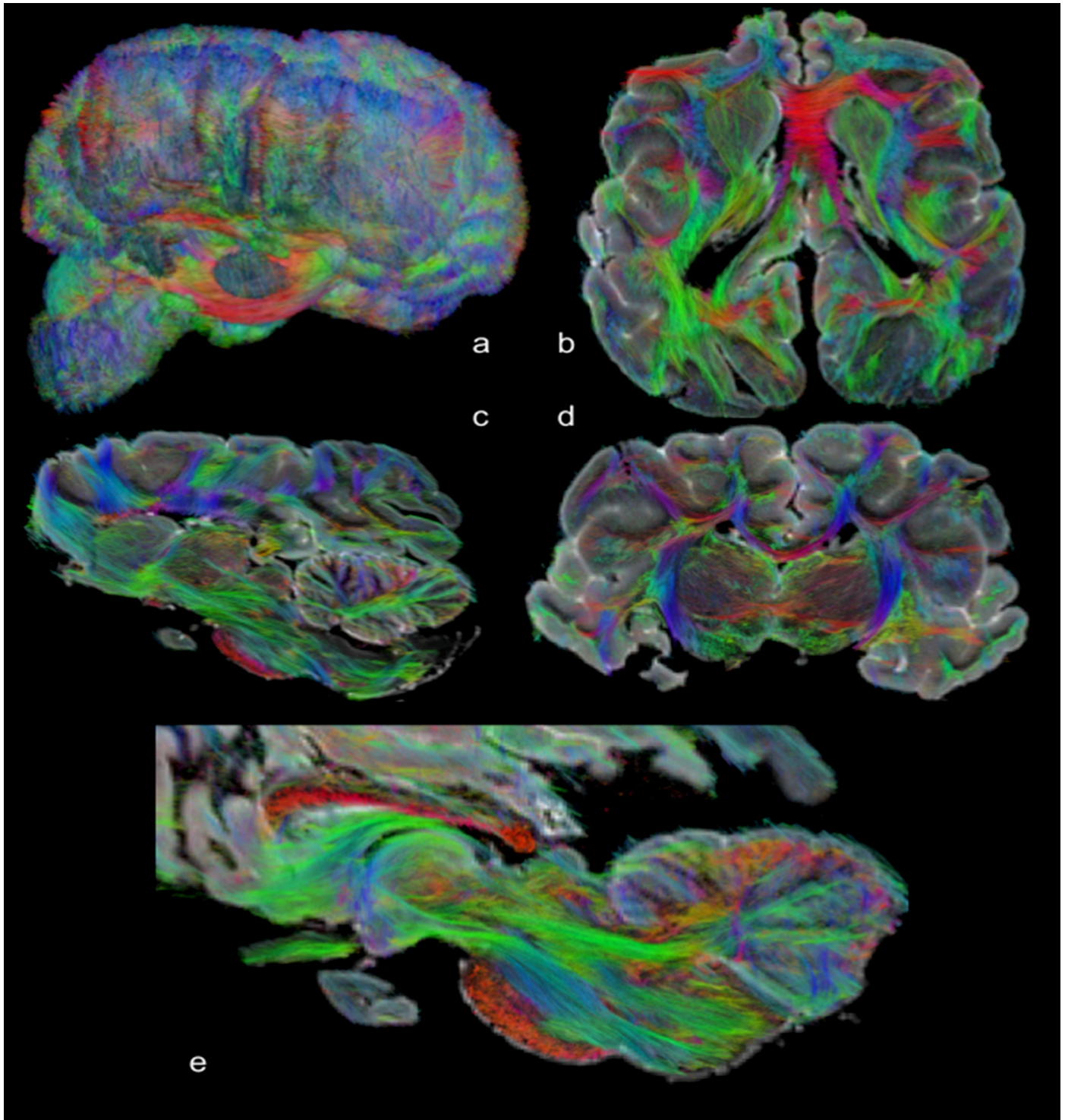


Figure 6.8: 3D rendering and tractograms of the California sea lion brain. (a) 3D rendering of the cortical surface in a coronal plane with the tractogram superimposed on. The tractogram is then superimposed on the 600 $\mu$ m  $T_2$ -weighted reference image in the axial (b), sagittal (c) and coronal (d) views. (e) Zoom in the brainstem and the cerebellum where a dense connectivity can be observed.

the differences in density of these fibers depending on the targeted region, with a density that can significantly vary at the walls of the sulci and at the top of the gyri. These mesoscopic information are promising for mapping the structural connectome of California sea lions, and more broadly of wildlife animals, in a more robust way than at the usual millimeter resolution. This meticulous analysis work will be an interesting research angle to develop in the continuation of the Neuro2Co project, as part of the collaboration with the ZooParc de Beauval and the INRAE teams.

As discussed in the Material and methods section and in order to facilitate the construction of the California sea lion white matter atlas, the high fiber density tractogram obtained from dMRI data was then analyzed using fiber clustering techniques. The latter were developed within the team as part of the Ginkgo toolbox and the applied algorithm results from the work of Guevara, Poupon, et al. 2011. We restricted the study to the longest fibers and set two thresholds to select the fibers belonging to the range of 50mm to 290mm so as to simplify the problem. That selection is based on the visual analysis of the histogram of fiber lengths (see Figure 6.10), thus discarding the short range connections between 0 and 50mm. This choice resulted in the selection of 15% of the streamlines (around 5 millions of fibers out of the 35 millions of fibers).

To further reduce the dimension of the problem, the selected fibers were separated into eight sets corresponding to eight sub-ranges: 50mm-80mm, 80mm-110mm, 110mm-140mm, 140mm-170mm, 170mm-200mm, 200mm-230mm, 230mm-260mm, 260mm-290mm. A clustering algorithm was then applied to each set, yielding at the end 17612 clusters embedding a slightly lower number of fibers than the 5 millions of input fibers. Some of the fibers were actually considered as outliers and discarded from the resulting clusters.

Figure 6.11 presents the obtained clusters by assigning them a locally specific color. The output clusters stand for groups of fibers which trajectories are coherent and correspond to sub-parts of projection, association or commissural bundles. This preliminary classification of the fibers led to automatically filter aberrant trajectories from the connectogram, and to build subsets of coherent fibers that can then be gathered to constitute fiber bundles. The largest and best known of which are described in neuroanatomy books and the others contributing to improving the knowledge about the structural connectivity of California sea lions. As a preliminary work, we were able to reconstruct some of these large bundles. Figure 6.12 showcases the corpus callosum as an example. Nevertheless, collaborating with biologists and veterinarians from ZooParc de Beauval and INRAE would be beneficial for deepening the exploration of the intra-subject fiber clustering in order to produce a first structural connectivity atlas of the California sea lion. Such an atlas would thus allow the study of anatomical-functional correlates linked to the specificities of the species, including for instance the singularity of the circuits controlling the two unilateral and bilateral sleep processes.

## 6.4 Conclusion

This chapter ends the second part of this manuscript dedicated to the investigation of the anatomical connectivities of a breeding animal, the Japanese quail, and eight wildlife animals raised in ZooParc de Beauval. The achieved work clearly demonstrates the potential of *ex vivo* ultra-high field diffusion MRI to explore the structural connectivity of these animal brains, as well as to characterize the microstructure of their cerebral tissues. A visual comparison of the generated fibers allowed the detection of similar connectomes between the bongo and the sitatunga, despite their significantly different brain volumes. This study also revealed the added value of the reached mesoscopic scale to better observe the intracortical connectivity of mammalian brains, and thus infer more reliable structural connectomes than *in vivo*, where the spatio-angular resolution remains limited to the millimeter scale. A substantial amount of work remains to



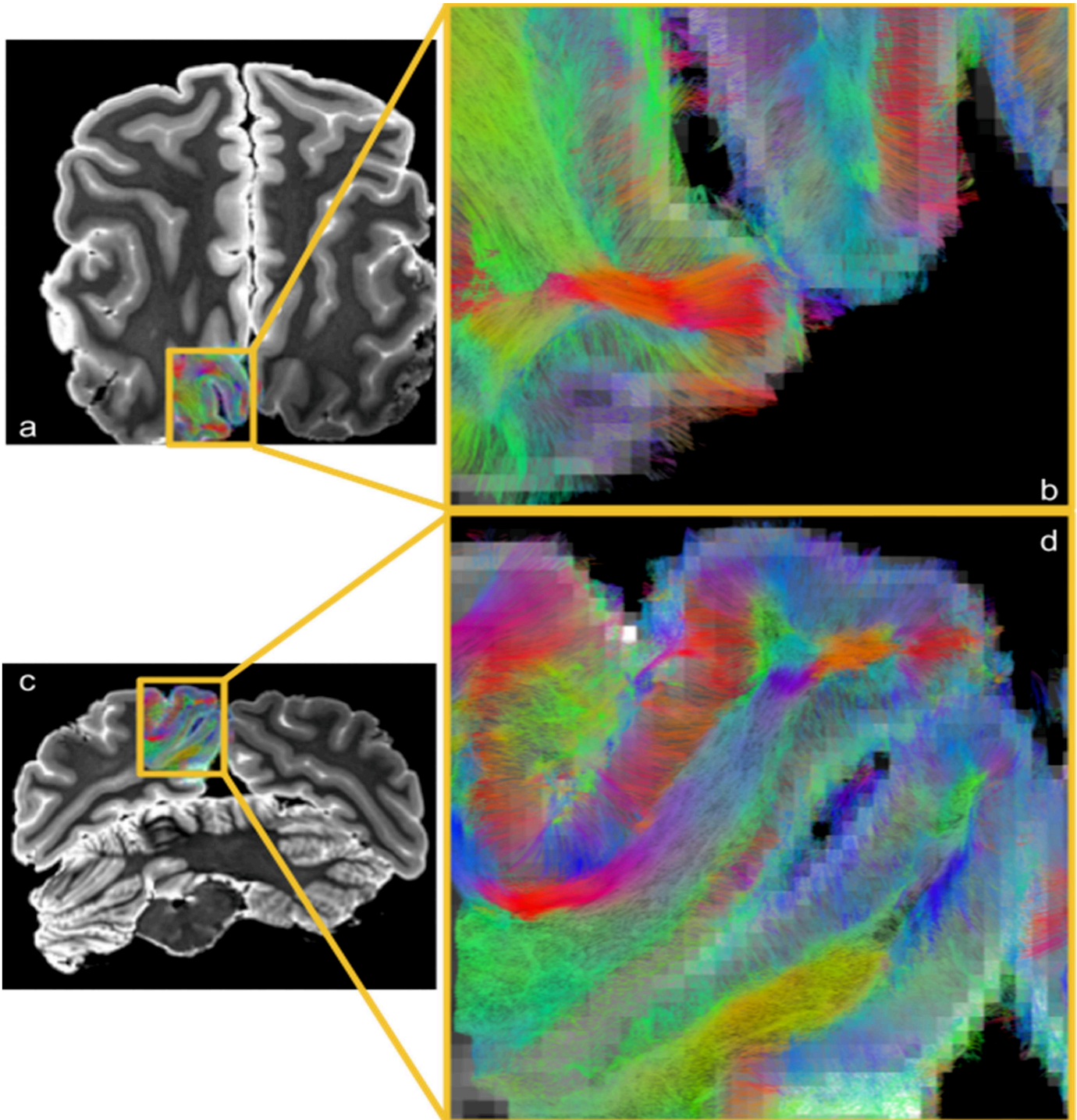


Figure 6.9: Zoom in the California sea lion tractogram highlighting cortical fibers.  $T_2$ -weighted reference image in the axial (a) and coronal (c) views, showing radial cortical fibers emerging from the subcortical white matter (b,d).

fully explore the acquired dataset, since the sanitary situation has limited interactions with our Neuro2Co partners. This work will be continued in the future thanks to the essential contribution of Dr E. Chaillou from INRAE and Dr B. Mulot from ZooParc de Beauval to include ethological analyses in the project.

The third and last part of this PhD work dives into the Chenonceau project, a multi-center work to establish a mesoscopic

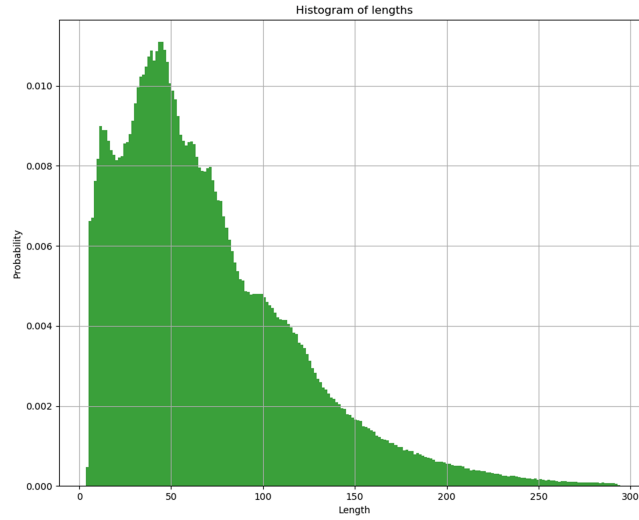


Figure 6.10: *Histogram of the fiber lengths (in millimeter) computed from the California sea lion tractogram.*

postmortem human brain MRI atlas using UHF diffusion-weighted and quantitative magnetic resonance imaging. The seventh chapter introduces the Chenonceau project and specimen. The eighth chapter focuses on the cerebral cortex of this human sample to explore its cyto- and myelo-architectonics, as well as its intracortical connectivity.

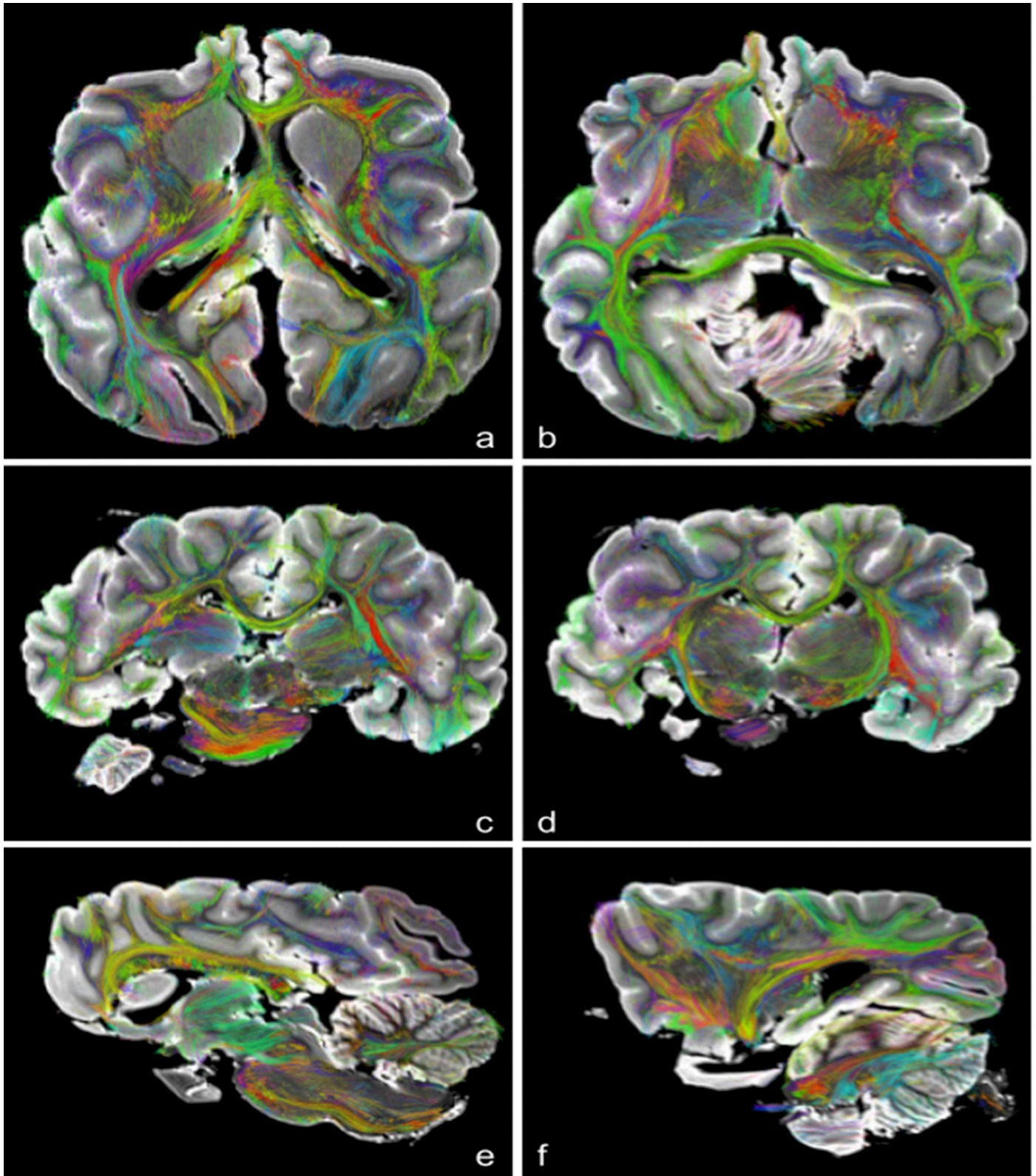


Figure 6.11: Images of the resulting intra-subject fiber clustering step performed on the California sea lion specimen. From the top to the bottom, there are pairs of clustering images in the axial (a,b), coronal (c,d) and sagittal (e,f) views. The represented fiber clusters belong to the range from 50mm to 290mm, which are the longest bundles readily observable. The intra-subject fiber clusters are superimposed on the 600 $\mu$ m  $T_2$ -weighted reference image.

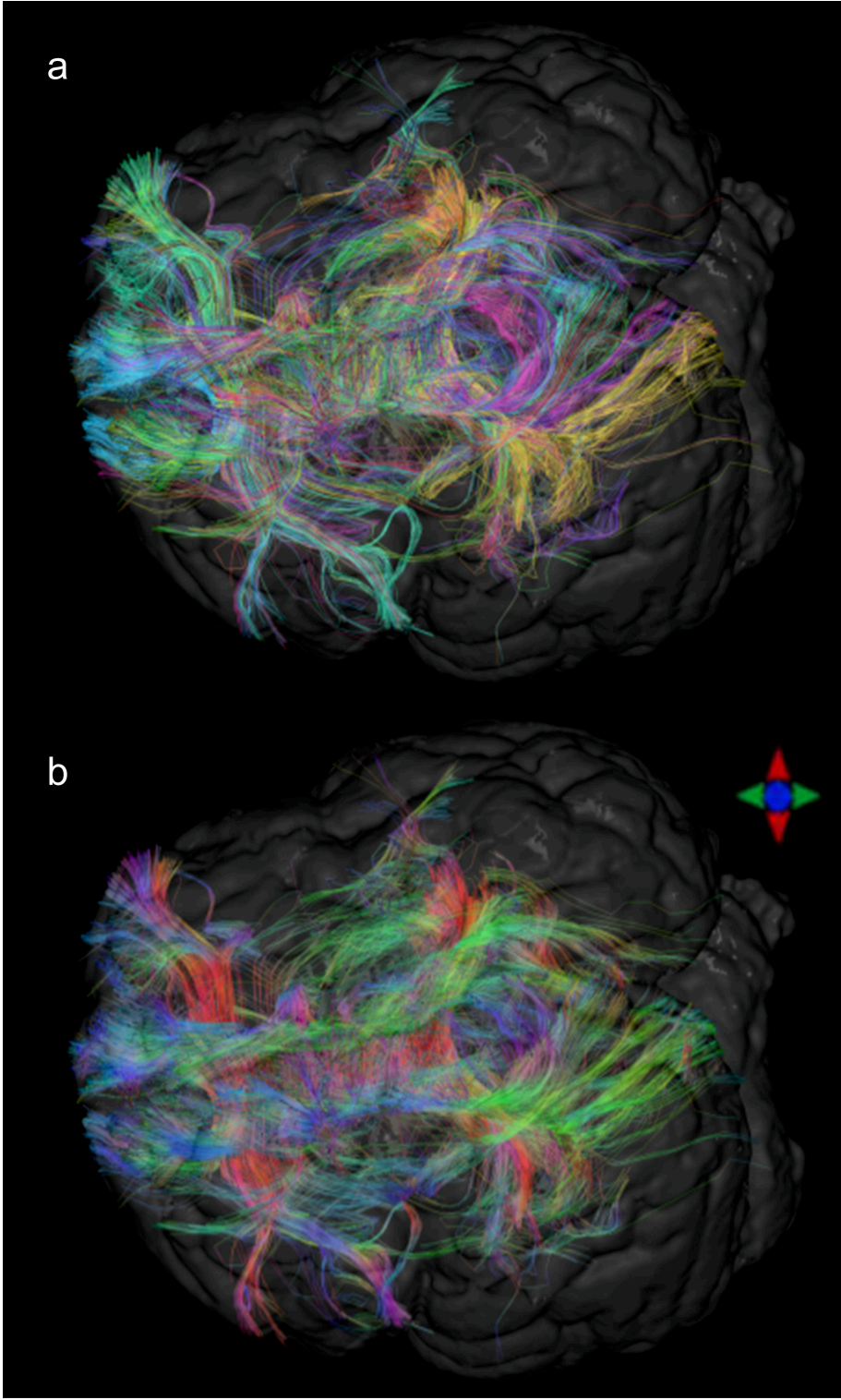


Figure 6.12: 3D rendering of the fiber clusters corresponding to the corpus callosum of the California sea lion. (a) Each cluster is represented in a distinct color. (b) The corpus callosum is represented using color-encoded directions defined by the colored cross.



## **Part III**

# **The human cerebral cortex in the Chenonceau project**



## Chapter 7

# Probing the human cortical cytoarchitecture and myeloarchitecture

Mapping the human brain structural and functional connectomes is a long ongoing process facing many methodological and technological challenges that need to be alleviated before reaching the final output (Sporns et al. 2005). It mostly relies on the improvement of functional magnetic resonance imaging (fMRI) and diffusion-weighted magnetic resonance imaging (dMRI) allowing to map *in vivo* the functional networks and to have access to the white matter connectivity using tractography methods. The Human Connectome Project (HCP), that started in 2010 (Van Essen, Ugurbil, et al. 2012), was specifically designed to provide an open and complete dataset of high-resolution anatomical, functional and diffusion MRI as well as magnetoencephalography on a large cohort of more than a thousand of healthy subjects. The latter were scanned using two dedicated 3T MRI systems equipped with the strongest diffusion gradients available on the market for clinical systems, as well as 7T MRI imaging systems. The community has largely taken ownership of this unique database, and many atlases have been produced or are currently under construction using the various imaging contrasts available. For instance, Glasser et al. 2016 has published a novel atlas of the cerebral cortex using proxies of myelin and task-related functional maps made up of 180 different cortical areas for each hemisphere.

Here, with the Chenonceau project that started in 2016 [Beaujoin 2018], we intended to create a unique mesoscopic MRI atlas of the human brain based on postmortem anatomical, diffusion-weighted and quantitative MR images. In the frame of this thesis, the obtained high spatial resolution dataset aims at exploring the microstructural features of the cortical ribbon, using local modeling of the diffusion process, relaxometry of the  $T_1$ ,  $T_2$ ,  $T_2^*$  times from quantitative MRI, tractography approaches to finely look at the connectivity within the cortex, multi-compartment models and clustering methods. This chapter presents the applied pipeline, from the brain sample preparation and acquisition protocols to the quantitative mappings of the whole brain.



## 7.1 Introduction to the Chenonceau project

The name of the project and the brain sample, Chenonceau, refers to a French castle located in the Centre-Val de Loire region. The chosen name pays tribute to the native place of the donor.

This section explains the human brain sample preparation process, as well as the design of the 3T, 7T and 11.7T acquisition protocols required for obtaining the anatomical, diffusion-weighted and quantitative dataset over the block-face, blocks and fields of view. Further details on the different components utilized to prepare the sample (containers, embedding gel, MRI bed) can be found in Beaujoin 2018 PhD thesis.

### 7.1.1 Ex vivo brain preparation process

A human brain specimen was obtained from the Body Donation program of the Anatomy Laboratory of Tours University (Pr C. Destrieux, Faculty of Medicine, CHU Bretonneau, Tours, France). This brain specimen was extracted from a 92-year-old male with a history of macular degeneration and early stages of cognitive disorders. The study was approved by the Local Ethical Committee and declared to the French national CODECOH procedure that supervises the preparation and conservation of human brain samples. The post mortem interval was of eight hours. As discussed in Chapter 4, best-quality fixation is obtained by combining immersion and perfusion techniques [Beach et al. 1987]. Therefore, the fixation process used both perfusion and immersion approaches and a 4% formalin buffer. The brain remained immersed in the formalin buffer for five months prior to the first MRI acquisitions. The immersion was ensured by levitation of the brain sample in the fixative bath so that the brain does not get deformed by the bottom of the container. The levitation protocol was devised by Pr C. Destrieux.

We chose to proceed the acquisition campaigns with preclinical MRI systems at 7T and 11.7T located in NeuroSpin. They reach ultra-high and extreme magnetic fields and are equipped with powerful gradient sets of 440mT/m and 780mT/m respectively. This choice was also motivated by all the benefits that bring a preclinical MRI scanner compared to a clinical MRI system. There are the strong gradient systems to obtain high angular resolutions, convert the gain in signal into spatial resolution, and cover a wide range of diffusion times. Moreover, the antenna loops get to be close to the scanned sampled, which increases the SNR and enhances spatial resolution. Since the acquisitions are performed postmortem, the effects of the fixation process must be taken into account. Reduced relaxation times entail a narrower acquisition window that is handled by strong gradient magnitudes. Diffusivity can be four times shorter which requires high b-values, namely more than 1000s/mm<sup>2</sup>, for dMRI sequences. It is for all these considerations that the preclinical systems outstrip the clinical ones for the Chenonceau project. As for the choice of the coil, volume coils were preferred over surface coils or cryogenic probes to favor homogeneous NMR signal and sensitivity across the entire field of view that was larger than the regular samples scanned on preclinical MRI systems. This choice was indeed made at the expense of a greater SNR that offers cryogenic probes, but it allows to presume constant Rician noise over the whole field of view.

However, a complete human brain does not fit into the coils of a preclinical MRI system, unlike a clinical one. Therefore, the brain sample had to be cut (see Figure 7.1) in order to fit in the largest volume coil available on these scanners (60mm inner diameter). Each hemisphere of the brain sample was cut into blocks (seven for the left hemisphere, six for the right hemisphere), that correspond to thick cuboid samples (4cmx4cmx20cm), as pictured in Figure 7.1. The cut was manually performed so as to minimize deformation and cerebral tissue loss. To ensure the samples integrity

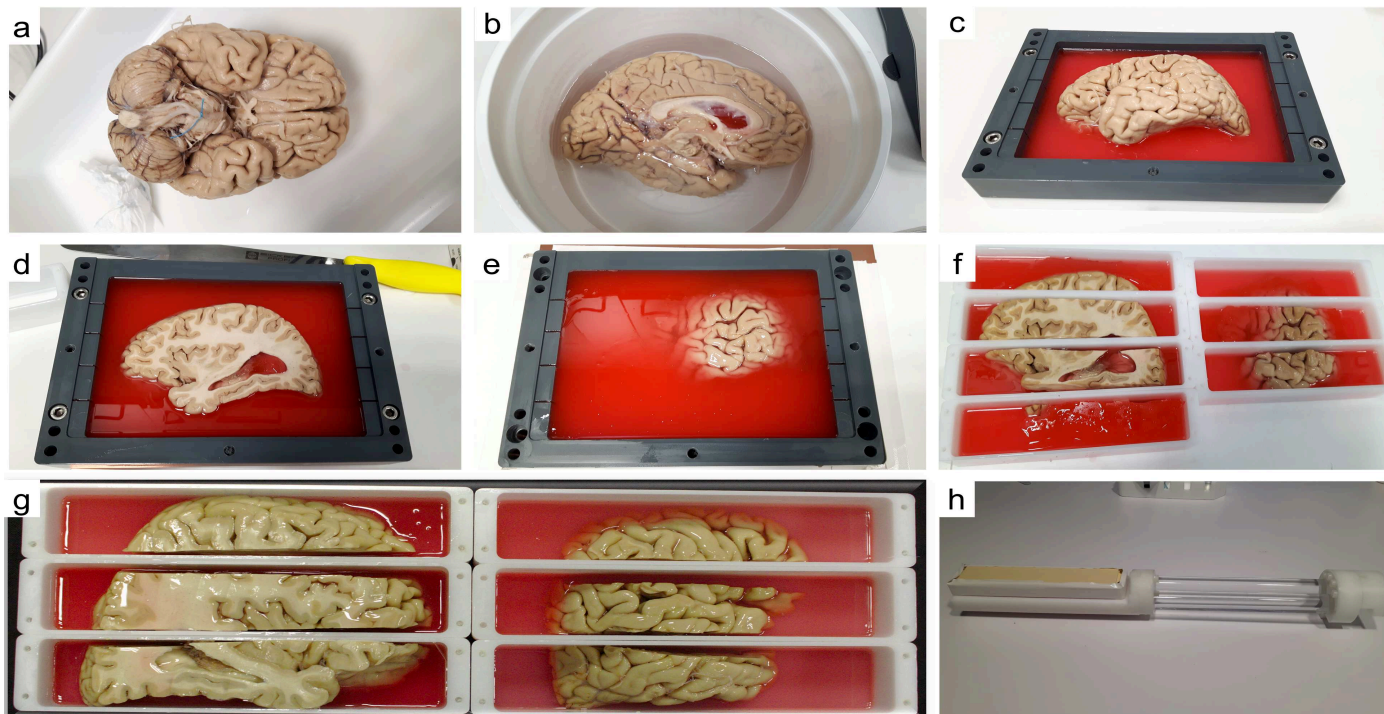


Figure 7.1: Photos of the cutting procedure of the brain sample. (a) Whole fixed brain. (b) Left-hemisphere part of the brain sample, which ventricle is filled with the fixing gel. (c) Left hemisphere surrounded by the sealing gel before further cuts. (d) Lateral part of the left hemisphere. (e) Medial part of the left hemisphere. (f) The seven blocks of the left hemisphere in their containers. (g) The six blocks of the right hemisphere in their containers. (h) A brain sample container placed inside the customized MRI bed, filled with gel and sealed with a screw-on lid.

throughout the years of the acquisition campaigns, they were stored in a fridge at 5°C. The formalin buffer was replaced by phosphate-buffered saline (PBS), that is monthly renewed, to maintain tissue hydration. An electrical sealing gel (Biz'gel, BizLine, France) was used to sustainably fix the blocks in their tailor-made plastic containers. This gel exhibits no significant NMR signal, a rapid reticulation at room temperature and a lasting conservation that excels the usually-employed agar-agar gel. No tissue breakdown has been observed over the past three years in that conservation state. For the scanning session, the imaged block has its PBS solution replaced with Fluorinert (FC-40, 3M, USA), an inert fluid that does not exhibit any NMR signal and preserves the hydration of the tissues.

Preliminary images were hence acquired before and right after the cutting procedure using a clinical 3T MRI scanner. The block-face anatomical MRI dataset, acquired before cutting the brain, serves as anatomical reference image for the intermediate diffeomorphic registration of the mesoscopic MRI data, as illustrated in Figure 7.2. The imaging protocol, before cutting the brain sample, involved a 3T Siemens MRI system (Prisma, Siemens, Erlangen, Germany), where T<sub>2</sub>-weighted scans at the semi-millimeter resolution were performed using a T2 SPACE sequence (500μm isotropic resolution, TE/TR = 105/700ms, matrix size = 512x512x320 slices, acceleration factor = 2, scan time = 20min). The aforementioned acquisition protocol was adjusted after the cutting step, still using a T2 SPACE sequence (400μm isotropic resolution, TE/TR = 103/700ms, matrix size = 512x208x512 slices, acceleration factor = 2, scan time = 52min).

Each block was scanned on the preclinical 11.7T MRI system during three to four sessions to acquire the fields of view (FOVs) with a size of about 40mmx42mmx56mm, and with an overlap of 1.6cm between each FOV. This overlap was essential to facilitate the registration process of the FOVs a posteriori. The combination of a letter and a number was

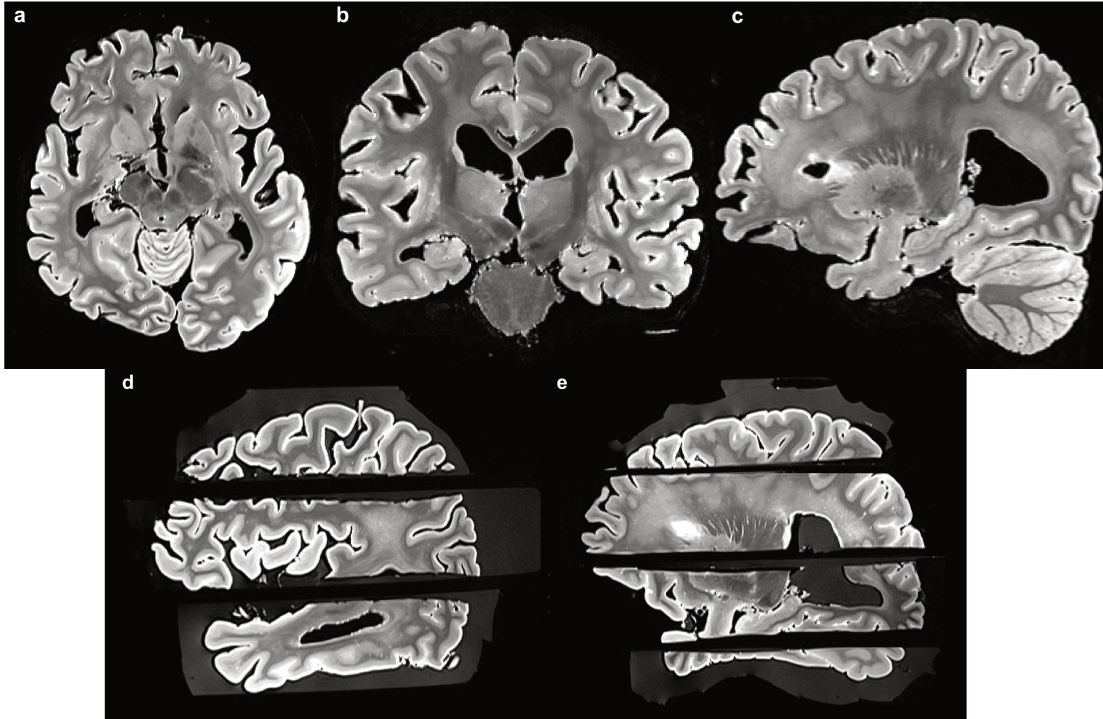


Figure 7.2: MRI images of the block-face acquired with the 3T Siemens clinical system. (a) Axial, (b) coronal, and (c) sagittal views of the whole brain sample before cutting (500µm isotropic resolution). (d, e) Sagittal view of the seven blocks composing the the left hemisphere (400µm isotropic resolution). Extra gel was removed from each container to avoid a calibration of the MRI system on the resonance frequency of the gel instead of that of the water. Images from Beaujoin 2018.

assigned to every FOV of the brain sample, from one to four in the posterior-anterior direction. Figure 7.3 illustrates the classification of the FOVs for both hemispheres. Short-term instabilities proper to *ex vivo* MRI are at once due to a temperature stabilization effect and a  $B_0$  drift, appearing within the first hours of scanning and hardly correctable. The former needs to be carefully taken into consideration as the diffusivity depends on it. That is why each brain block was first prepared many hours before scanning, and left waiting in the magnet room at least eight hours prior to scanning to preclude the unsatisfying output images.  $B_0$  drift can occur at the beginning of the scans and is related to the warm up of passive shims located close to the magnet tunnel. This unwanted proximity happens when larger tissue samples settle in the coil [Dyrby, Innocenti, et al. 2018]. The lengthy  $T_2$ -weighted anatomical MRI sequences were applied before the diffusion-weighted acquisitions to prevent  $B_0$  drift from spoiling the dMRI dataset. Moreover,  $T_2$ -weighted acquisitions allow to warm up the cerebral tissue so that it reaches a plateau temperature.

### 7.1.2 Anatomical and diffusion MRI protocol at 11.7T

The 11.7T acquisition protocol used in this thesis is the same one detailed in Beaujoin 2018. It lasts 108h per FOV and includes anatomical and diffusion-weighted sequences using the preclinical 11.7T Bruker BioSpec MRI scanner ( $G_{\max} = 780\text{mT/m}$ ,  $\text{slew-rate} = 9500\text{T/m/s}$ ). The two-year-long acquisition campaign (see Figure 7.6) was a team effort involving Dr J. Beaujoin, Alexandros Popov and myself.

The first step of calibrating the dMRI acquisition protocol was to determine the maximum echo time and b-values

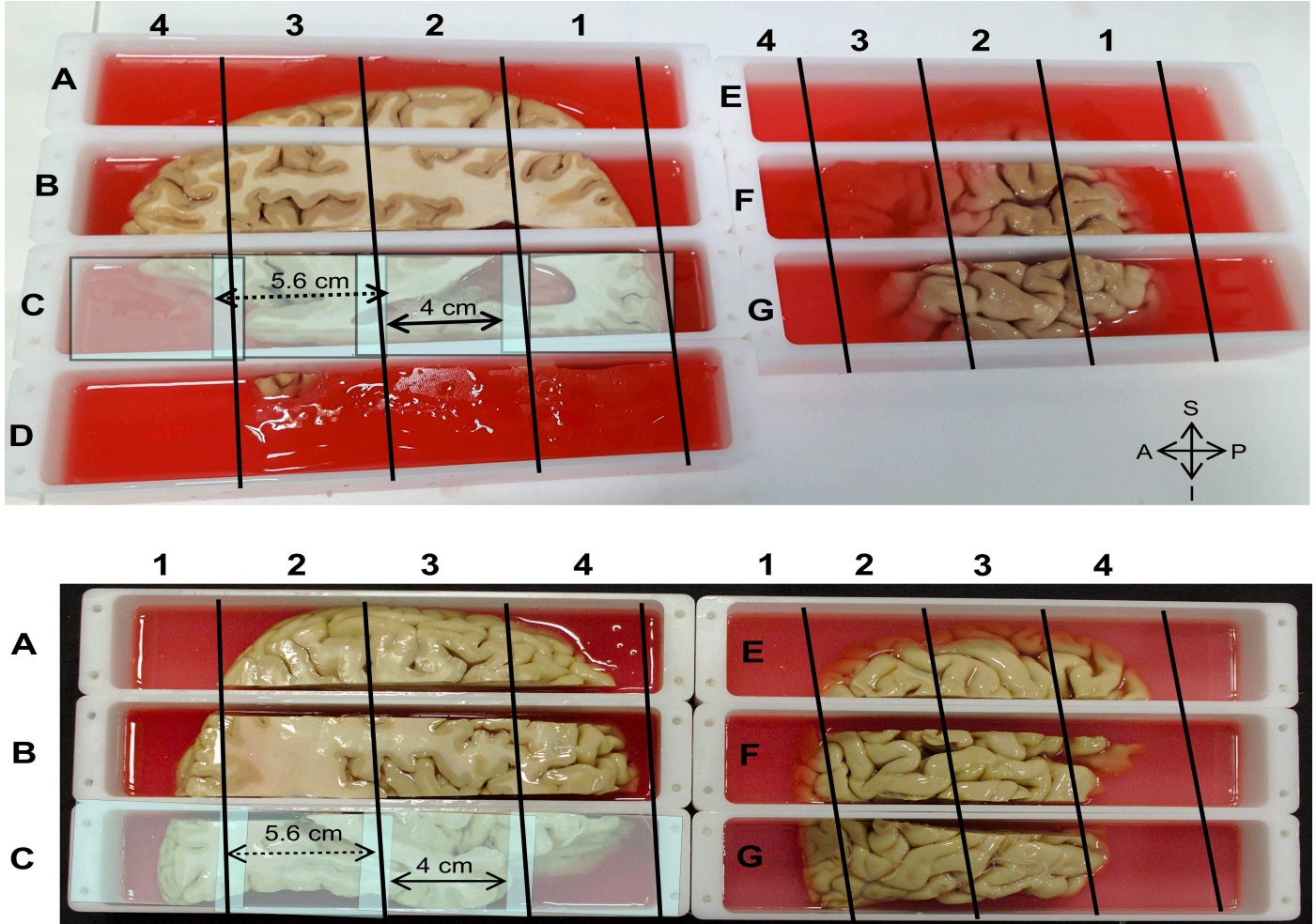


Figure 7.3: Classification of the fields of view from the human brain sample. The upper panel corresponds to the left hemisphere and the lower panel refers to the right hemisphere. The brain containers are identified by a letter, from A to G for the left hemisphere, from A to C then from E to G for the right hemisphere. The FOVs are numbered from one to four in the posterior-anterior direction. A = anterior. P = posterior. I = inferior. S = superior.

that could be used at 11.7T with a minimized signal loss. Consequently, we based our estimations on the computed histograms of the transverse relaxation time  $T_2$  and the mean diffusivity  $D$  of a hippocampus sample (see Figure 7.4). The scans on the hippocampus sample were also performed with the preclinical 11.7T system. The limited signal loss was guaranteed by the product  $e^{-\frac{TE}{T_2}} e^{-bD}$  being superior to 0.05 and equally distributed over both signal decays:

$$\begin{cases} e^{-\frac{TE_{max}}{T_2}} \geq \sqrt{0.05} \\ e^{-b_{max}D} \geq \sqrt{0.05} \end{cases} \quad (7.1)$$

The output is then:

$$\begin{cases} TE_{max} \leq 69ms \\ b_{max} \leq 9361s/mm^2 \end{cases} \quad (7.2)$$

Therefore, we were able to set the maximum echo time at 24.3ms in our protocol, which largely ensured a maximum

b-value at 8000s/mm<sup>2</sup>.

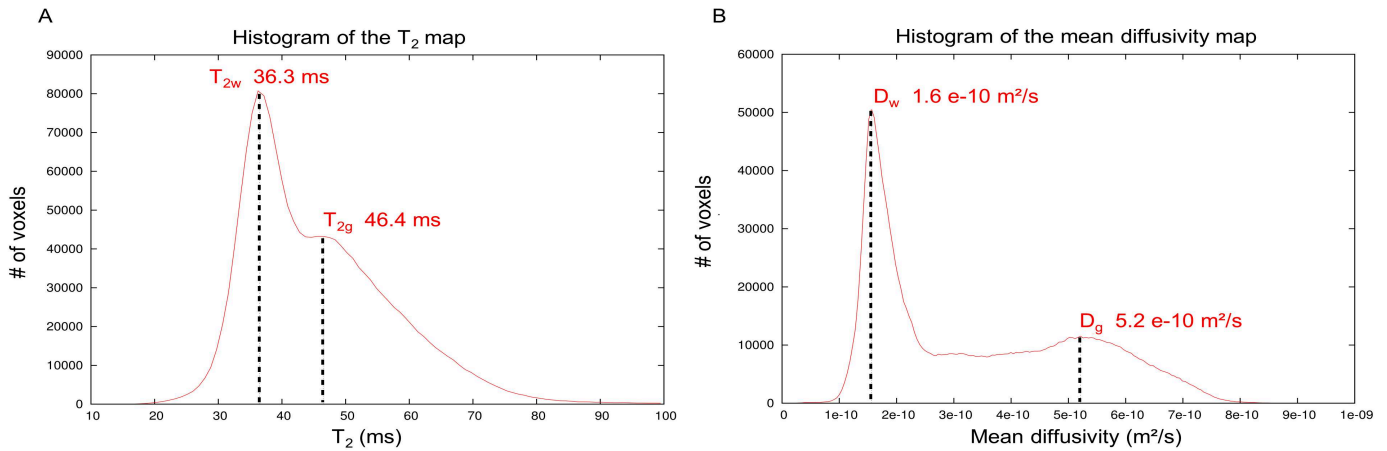


Figure 7.4: Histograms showing the distribution of the  $T_2$  relaxation time and mean diffusivity values of a hippocampus sample. (A)  $T_{2w}$  is assumed to be the characteristic  $T_2$  of the white matter and  $T_{2g}$  the characteristic  $T_2$  of the gray matter. (B)  $D_w$  is the mean diffusivity of the white matter and  $D_g$  is assumed to be the one characteristic of the gray matter. Image adapted from Beaujoin 2018.

The two anatomical sequences correspond to  $T_2$ -weighted sequences:

- a 2D SE sequence with a 150 $\mu$ m isotropic resolution (TE/TR = 16/6647ms, matrix size = 374x275x256 slices, 9 averages, flip angle = 90°, read bandwidth = 66kHz, scan time = 3h26min).
- a 3D MSME sequence with a 100 $\mu$ m isotropic resolution (TE/TR = 20/500ms, matrix size = 400x400x560 slices, 1 average, read bandwidth = 50kHz, scan time = 22h13min).

The left-sided images of Figure 7.5 portrays the anatomical MRI images of the left-hemisphere primary visual area at 100 $\mu$ m and 150 $\mu$ m isotropic resolutions.

The diffusion-weighted sequences include:

- a series of 3D segmented EPI PGSE sequences with a 200 $\mu$ m isotropic resolution (TE/TR = 24.3/250ms, 30 segments,  $\delta/\Delta = 5/12.3$ ms, 16  $b = 0$ s/mm<sup>2</sup> images,  $b = 1500/4500/8000$ s/mm<sup>2</sup> along 25/60/90 directions with the corresponding gradient strengths 289/500/666mT/m, 80 dummy scans).
- The 16  $b = 0$ s/mm<sup>2</sup> images were averaged to constitute a  $T_2$ -weighted reference image specific to the dMRI dataset.

The large number of segments applied in this protocol, i.e. 30 versus 3 to 6 in general, strongly attenuated susceptibility effects. The dMRI sequences were divided into multiple series of acquisitions in order to be properly managed by the reconstruction algorithm of the preclinical imaging software, ParaVision (Bruker, Germany). The memory limitation is indeed set to two gigabytes per scan. The right-sided images of Figure 7.5 depicts the raw dMRI images of the left-hemisphere primary visual area at four distinct b-values (0/1500/4500/8000s/mm<sup>2</sup>).

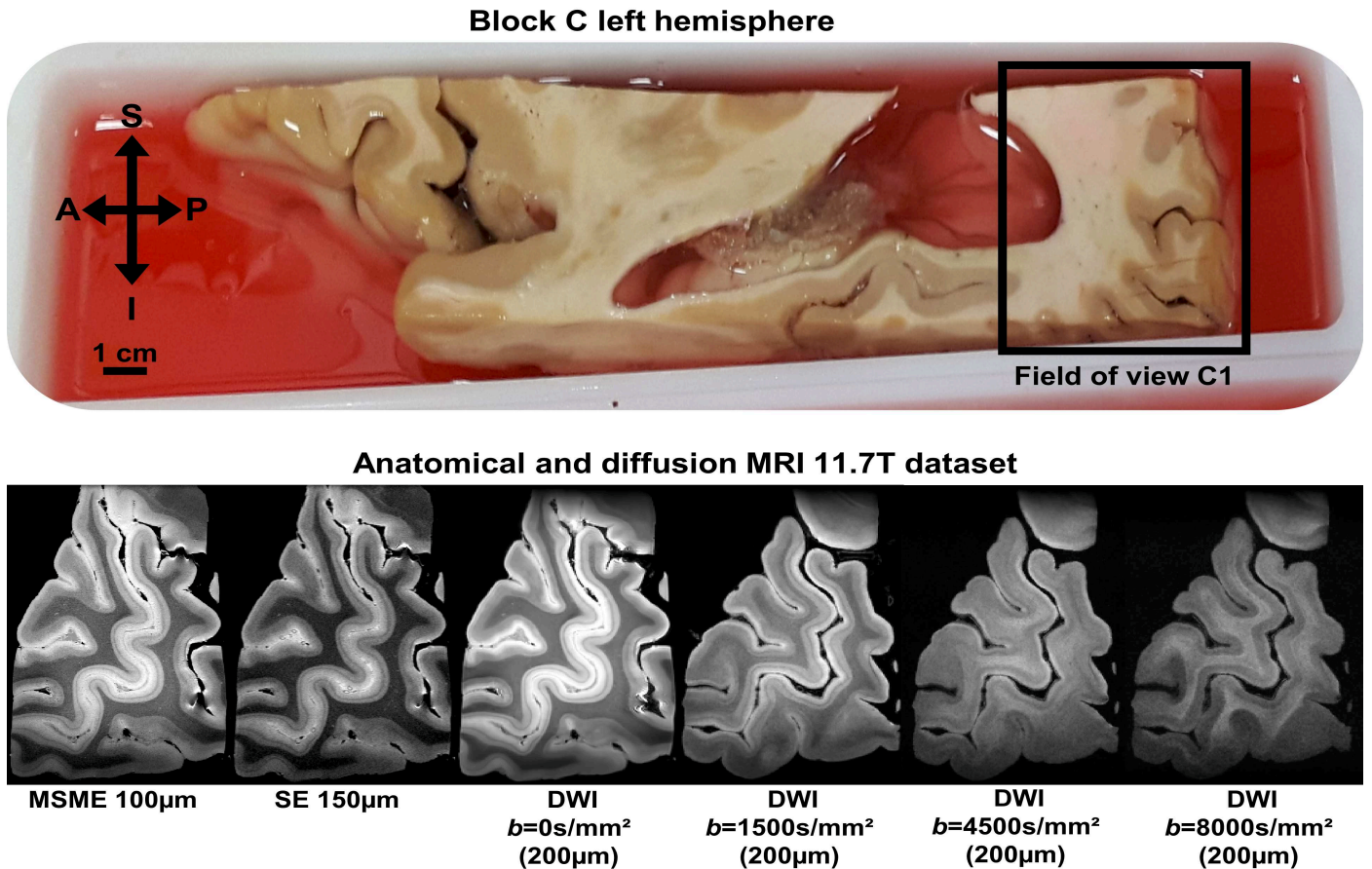


Figure 7.5: Anatomical and diffusion-weighted images from the left-hemisphere C1 field of view. At the top, sagittal view of the left-hemisphere C block including part of the occipital lobe from the Chenonceau brain. The scanned field of view C1 is framed in black. The red gel surrounding the sample is a sealing gel (Biz'gel, BizLine, France). From left to right, there are the raw  $T_2$ -weighted anatomical images at 100µm and 150µm isotropic resolutions. Then, there are the raw diffusion images at respectively  $b = 0/1500/4500/8000s/mm^2$ . All the FOVs are presented in the sagittal view. DWI = diffusion-weighted image. A = anterior. P = posterior. I = inferior. S = superior.

### 7.1.3 Quantitative MRI protocol at 7T

#### 7.1.3.1 Protocol tuning

The 7T MRI protocol was designed by me to provide a quantitative magnetic resonance imaging (qMRI) dataset of the Chenonceau brain with an isotropic resolution of 200µm, identical to the dMRI dataset for consistency between qMRI and dMRI data, as well as to facilitate the data registration. The acquisition campaign was realized over a year and a half (see Figure 7.6) using the preclinical 7T Bruker BioSpec MRI system ( $G_{max} = 440mT/m$ , slew-rate = 3440T/m/s). The 7T MRI system was selected instead of the preclinical 11.7T scanner due to the limited availability of the 11.7T imaging system. It was already booked for the first Chenonceau acquisition campaign for anatomical and diffusion-weighted data, plus other research studies at that time. Furthermore, it was beneficial for relaxometry to be performed at 7T rather than at 11.7T since the  $T_2$  and  $T_2^*$  relaxation times are longer at 7T. Hence, it provides a broader acquisition window to robustly compute the relaxation times of the Chenonceau brain.

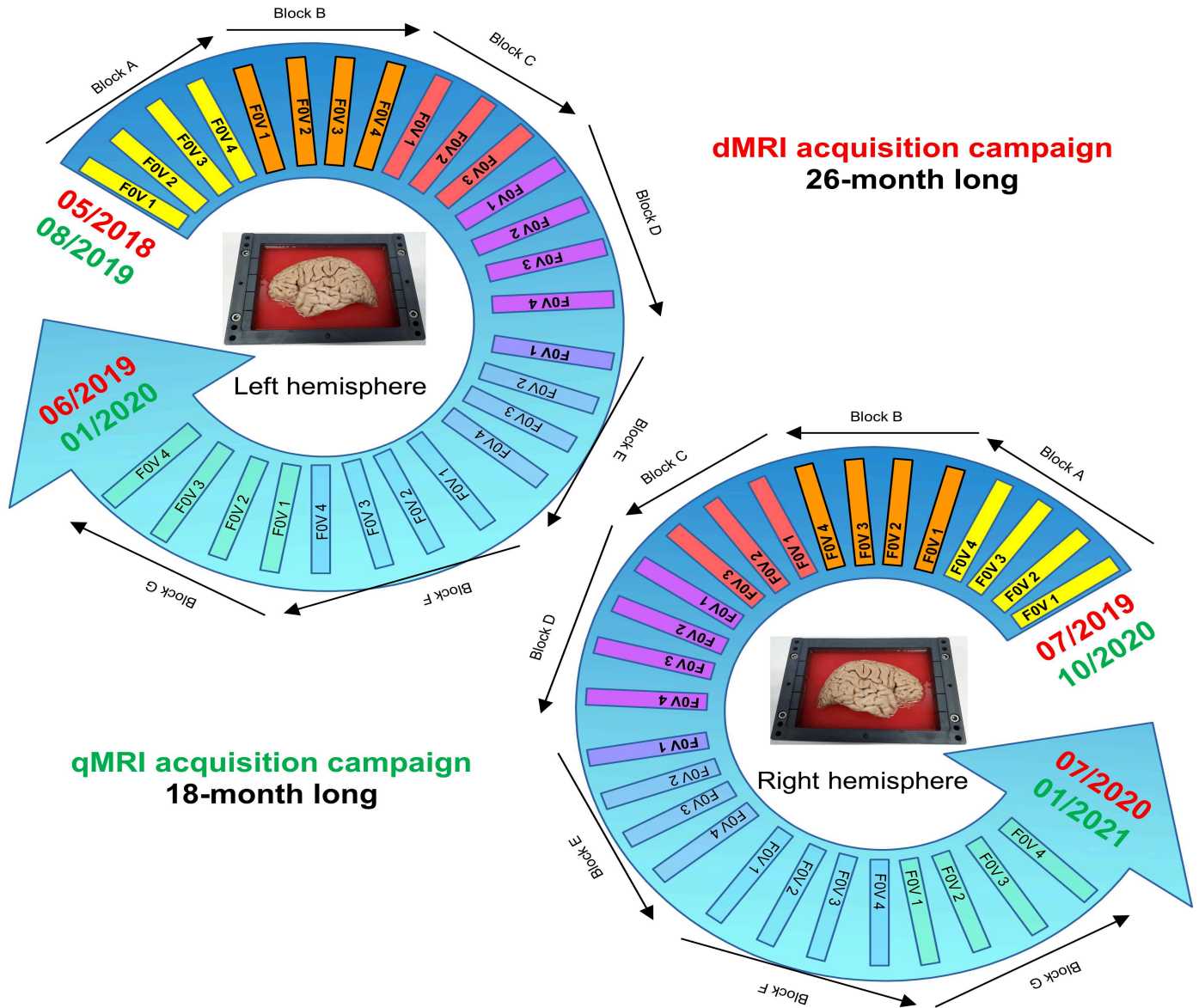


Figure 7.6: Schematic representation of the duration of the two acquisition campaigns. The drawing at the top refers to the acquisition campaign on the left hemisphere of the Chenonceau brain and the lower panel on the right hemisphere.

The first tests were conducted on a human sample of corpus callosum from a different specimen and they aimed at designing three sequences: 3D VFA FLASH sequence for  $T_1$  mapping, 3D MSME sequence for  $T_2$  mapping and 2D multi-gradient echo (MGE) sequence for  $T_2^*$  mapping. The MRI sequences incorporated in the protocol needed to last less than three days per FOV for a time constraint reason. The corpus callosum was placed in a customized hermetic container and immersed in Fluorinert during the scanning sessions.

The choice to avail the VFA FLASH and MSME sequences was validated at that stage due to the sufficient signal-to-noise ratios they offer (for the corpus callosum sample respectively 27.14 and 24.83) and no visible artifact. However, the test on the 2D MGE sequence was not conclusive due to a reconstruction error of the data made by the MRI system.

Thus, we decided to test the protocol directly on a field of view of the Chenonceau brain. The VFA FLASH and

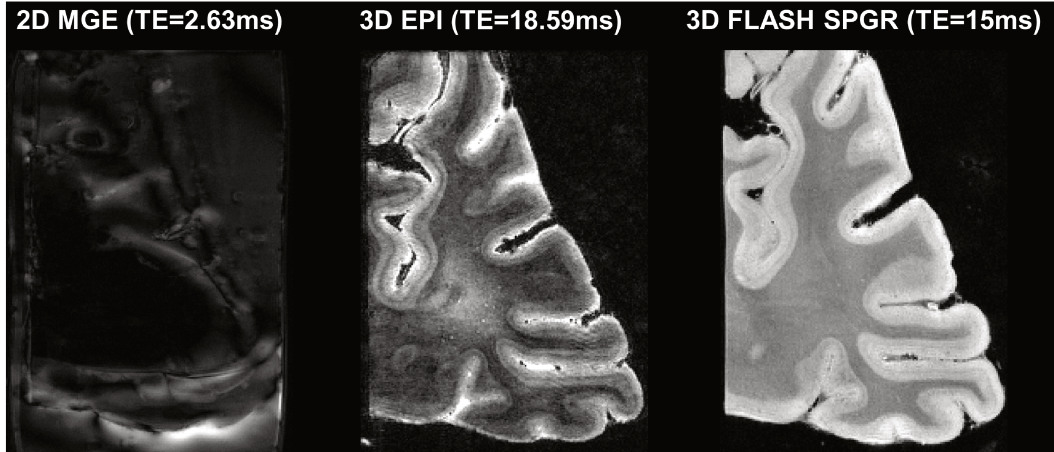


Figure 7.7: Series of  $T_2^*$ -weighted images on the right-hemisphere C1 field of view of the Chenonceau brain. The images are from the 2D MGE sequence, the 3D EPI sequence, and the 3D FLASH SPGR sequence.

MSME sequences met our expectations and the 2D MGE sequence was eventually inoperative for the  $T_2^*$  relaxometry, showing major distortions on the reconstructed images. Afterwards, we investigated a 3D EPI sequence to perform  $T_2^*$  relaxometry. It appeared that the output  $T_2^*$ -weighted images were not showing a satisfying SNR (below 5), and too many artifacts such as blurred images, major loss of signal due to susceptibility effects, and non-homogeneous NMR signal across the FOV. Consequently, we resorted to a 3D FLASH SPGR sequence that was validated since it showcased an enhanced SNR (over 6) and few artifacts. Figure 7.7 presents the output images of the  $T_2^*$ -weighted 2D MGE, 3D EPI and 3D FLASH SPGR sequences applied on the right-hemisphere C1 field of view of the Chenonceau brain.

The fixing gel in the brain containers was significantly visible on the first set of test images. Knowing that our sealing gel exhibits a resonance frequency close to that of the fat [Beaujoin 2018], we applied a fat saturation pulse for each MRI sequence that effectively suppressed the gel signal without affecting the value of the NMR signal.

$B_1^+$  mapping was likewise integrated in the imaging protocol to compute actual flip angle required for accurate  $T_1$  evaluation and correct  $B_1^+$  inhomogeneities that occur with the VFA FLASH sequences [Cheng et al. 2006; Cercignani et al. 2018]. The purpose was to select a MRI sequence that would be the best trade-off between rapidly image the FOVs and precisely map the  $B_1^+$  field distribution. We thus opted for the Boudreau et al. 2017 approach, based on a 3D EPI double-angle method. The computation of the  $B_1^+$  map is merely expressed in Equation (7.3):

$$B_1 \equiv \frac{\alpha_{corrected}}{\alpha} = \frac{\arccos\left(\frac{I_2}{2I_1}\right)}{\alpha} \quad (7.3)$$

where  $\alpha$  is the computed flip angle by the MRI scanner,  $\alpha_{corrected}$  is the exact local flip angle,  $I_1$  and  $I_2$  are the NMR signal intensities coming from the first (flip angle =  $\alpha$ ) and the second (flip angle =  $2\alpha$ ) acquisitions.

### 7.1.3.2 Description of the final protocol

After a series of imaging tests on human brain tissues to optimize the imaging parameters, we eventually setup the final 7T protocol, which lasts 72h for each field of view and includes :



- a series of 3D  $T_1$ -weighted variable flip angle (VFA) FLASH sequences [Trzasko et al. 2013] (TE/TR = 4.99/15ms, 65 angles, flip angles = 3-45°, matrix size = 280x212x204 slices, 1 average, read bandwidth = 50kHz, scan time = 12h30min). Measurement points were collected every 0.5° of the flip angle between 0° and 30°, then every 1.5° between 30° and 45°.
- a 3D  $T_2$ -weighted MSME sequence (TE/TR = 5.56-166.8/1000ms, 30 echoes, echo spacing = 5.56ms, matrix size = 280x212x204 slices, 3 averages, read bandwidth = 100kHz, scan time = 36h02min). A 10-minute time gap was fixed every five flip angles to prevent heating.
- a series of 3D  $T_2^*$ -weighted variable echo time FLASH SPGR sequences (TE/TR = 5-100/110.048ms, 10 echoes, flip angle = 50°, matrix size = 280x212x204 slices, 1 average, read bandwidth = 50kHz, scan time = 12h30min). Measurement points were collected at TE = 5/10/15/20/30/40/50/60/80/100ms.
- a dual flip-angle 3D EPI  $B_1^+$  mapping sequences [Cunningham et al. 2006; Boudreau et al. 2017] (TE/TR = 13.405/1500ms, flip angles = 30/60°, 1 average, 35 segments, signal type = spin echo, matrix size = 280x212x204 slices, read bandwidth = 300kHz, scan time = 5h56min).

Dummy scans were also added to the protocol in the same way as the 11.7T acquisition protocol to avoid non-homogeneous signal across the scanned FOV. Pauses of ten to twenty minutes were inserted between each series of MRI sequences, to preclude the brain block to heat during the scanning session.

Figure 7.8 illustrates the raw qMRI images of the right-hemisphere primary visual area at two distinct echo times ( $T_2$ -weighted and  $T_2^*$ -weighted sequences) or flip angles ( $T_1$ -weighted sequence).

#### 7.1.4 Expectations from the Chenonceau project

The Chenonceau project aims at investigating two major themes: the study of the structural connectivity of a human brain at unreachable spatial resolutions *in vivo*, and the study of the cerebral tissue microstructure.

- The first study explores the structural connectivity in different regions of the brain. The connectivity of the long white matter bundles and their endings is properly assessed. There is also the superficial subcortical connectivity with its U-shaped fibers that is captured. Last, the study dives into the connectivity of structures composed of gray matter: the basal ganglia, the cortical ribbon, and the small nuclei that remain invisible at low spatial resolution.
- The second study addresses the microstructure of the white matter, the cerebral cortex, and the deep structures. It tackles both the cytoarchitecture using diffusion-weighted magnetic resonance imaging, and the myeloarchitecture using quantitative magnetic resonance imaging, of the cited brain parts.

Two PhD students are currently involved in the project: Alexandros Popov who handles the white matter part of the Chenonceau brain, and myself taking interest in the laminar organization of the cerebral cortex from a cytoarchitectural and myeloarchitectural standpoint, as well as the cortico-cortical connectivity.

This introduction to the Chenonceau project reviewed the key parts of the brain collection, preparation and scanning at 11.7T then 7T. The next section explains the different steps of the pipeline used to generate the relaxometry and microstructural maps from the dMRI and qMRI dataset.

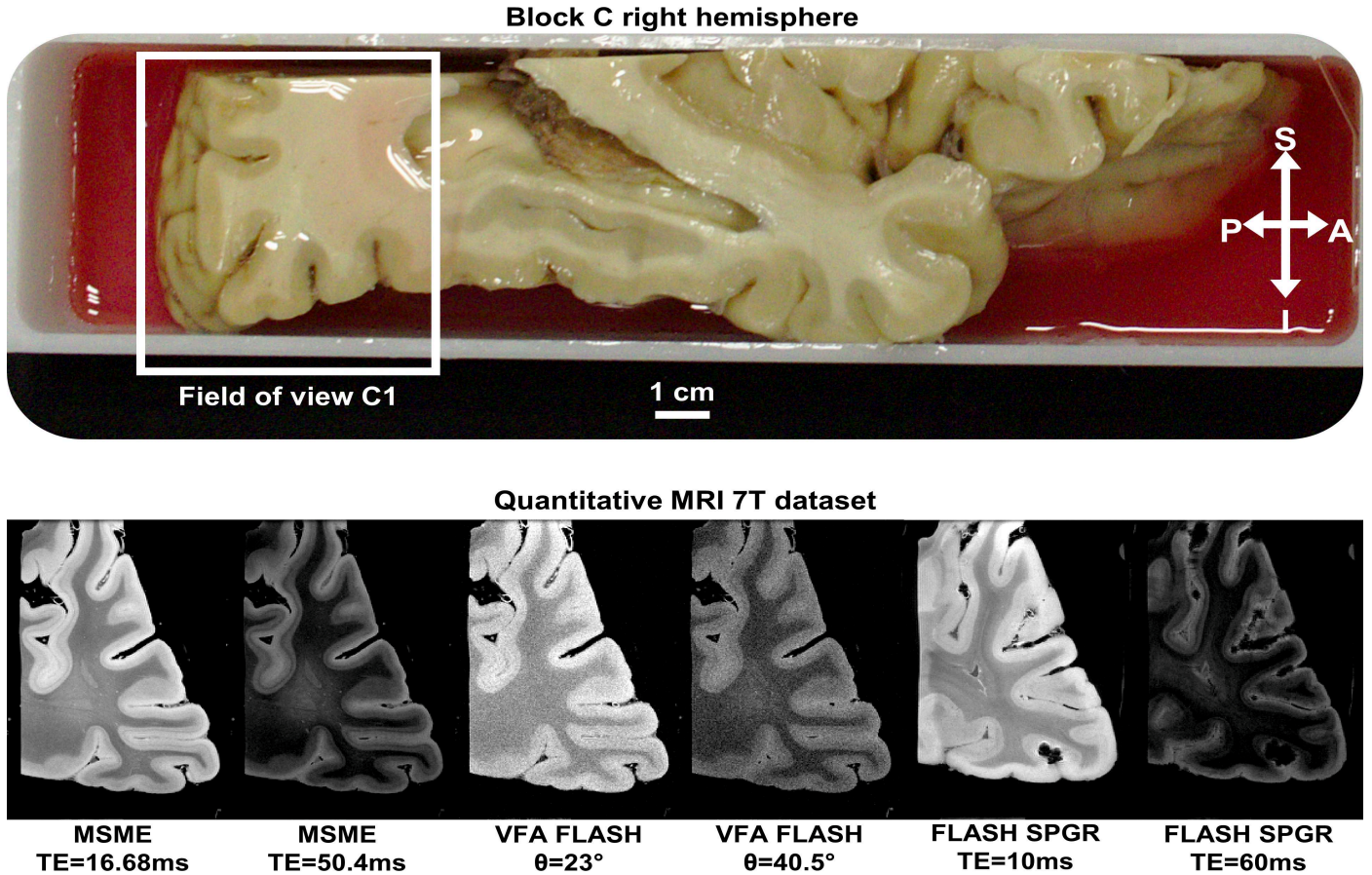


Figure 7.8: Relaxometric images from the right-hemisphere C1 field of view. Sagittal view of the right-hemisphere C block including part of the occipital lobe from the human brain sample. The scanned field of view C1 is framed in white (right hemisphere). The red gel surrounding the sample is a sealing gel (Biz'gel, BizLine, France). From left to right, there are pairs of raw quantitative images for the  $T_2$ -weighted MSME,  $T_1$ -weighted VFA FLASH and  $T_2^*$ -weighted variable echo time FLASH SPGR sequences. All the FOVs are presented in the sagittal view. A = anterior. P = posterior. I = inferior. S = superior.

## 7.2 Quantitative MRI mapping of the Chenonceau brain at 7T and 11.7T

This section focuses on the entire pipeline, pre- and post-processing, based on the use of the Ginkgo toolbox (<https://framagit.org/coupon/gkg>), that was developed to produce the  $T_1$ ,  $T_2$  and  $T_2^*$  relaxometry maps, as well as quantitative maps from the NODDI model of each field of view, before reconstructing the complete brain sample.

### 7.2.1 Pre-processing pipeline

All qMRI and dMRI data were denoised using a non-local means filter algorithm, considering the Rician nature of the noise [Condat 2010; Buades et al. 2011]. Details on the pre- and post-processing steps regarding the 11.7T dMRI dataset are given in Beaujoin 2018. They are likewise schematized in Figures 7.9 and 7.10, where the pre-processing pipeline (Figure 7.9) and the registration step (Figure 7.10) are showcased for the 7T and 11.7T MRI dataset. Figure

7.11 exhibits the output of the non-local means filter algorithm for every qMRI sequence in the left-hemisphere FOV A2. The contrasts of the images were preserved with no smoothing effect blurring them. We likewise observed a drastic increase of the SNR after using that filter, as summarized in Table 7.1. The latter presents the mean and the standard deviation of the SNR for each 7T MRI sequence before and after the non-local means filtering, according to the selected brain region: left hemisphere, right hemisphere and whole brain.

brain region	VFA FLASH	MSME	FLASH SPGR	EPI 60°	EPI 30°
left hemisphere (before filtering)	8.692 ±1.095	10.239 ±3.827	6.371 ±2.104	37.042 ±9.158	27.901 ±4.928
left hemisphere (after filtering)	86.626 ±25.574	87.563 ±85.996	38.727 ±30.165	356.726 ±229.899	385.950 ±193.225
right hemisphere (before filtering)	8.757 ±1.069	9.133 ±2.953	5.938 ±1.747	36.744 ±9.262	28.120 ±5.443
right hemisphere (after filtering)	82.196 ±14.08	86.343 ±48.397	40.900 ±33.501	422.367 ±214.503	389.014 ±155.518
whole brain (before filtering)	8.722 ±1.072	9.709 ±3.445	6.163 ±1.933	36.899 ±9.111	28.006 ±5.126
whole brain (after filtering)	84.504 ±20.780	93.936 ±80.548	39.769 ±31.483	388.179 ±222.765	387.418 ±174.323

Table 7.1: Table of the mean SNRs ( $\pm$  standard deviation) in the Chenonceau brain for each applied 7T qMRI sequence before and after the non-local means filtering, according to the selected brain region: left hemisphere, right hemisphere, whole brain.

The SNRs were calculated from the last echo for the  $T_2$ -weighted MSME and  $T_2^*$ -weighted FLASH SPGR sequences. As for the  $T_1$ -weighted variable flip angle (VFA) FLASH sequence, the measured SNR comes from the first flip angle at 3°. These measurement points correspond to the echo or flip angle that is the most affected by the noise which leads to the lowest level of signal-to-noise ratio that can be observed on the 7T qMRI images. The calculated SNRs pinpoint similar values for the left and right hemispheres as well as the entire brain, whatever 7T qMRI sequence considered. This observation evinces there are no significant differences between the signal-to-noise ratios of the fields of view, which advocates for the robustness of the blocks' preparation and acquisition procedure.

## 7.2.2 Relaxometry mapping

Quantitative  $T_1$  (qT1),  $T_2$  (qT2),  $T_2^*$  (qT2\*) and relative proton density (qPD) maps were computed using a robust fit for each of the  $T_1$ -weighted,  $T_2$ -weighted and  $T_2^*$ -weighted signal equations combined with a non-linear programming Nelder-Mead-based algorithm. The MWF map was obtained using a model fitting procedure [Kulikova et al. 2016] based on the  $T_1$ -weighted VFA FLASH and the  $T_2$ -weighted MSME sequences. Regarding the  $T_1$  and  $T_2$  contrasts to estimate the myelin water fraction, the NMR signals are considered to originate from two compartments: the parenchyma,  $par$ , composed of gray and white matters, and the myelin water,  $mw$ . We hypothesized in our model that no exchange exists between these two compartments.

$$\begin{cases} \frac{S_{MSME}(TE)}{S_0} = f_{par}\rho_{par}e^{-TE/T_{2par}} + f_{mw}\rho_{mw}e^{-TE/T_{2mw}} \\ \frac{S_{VFA}(TR,\alpha)}{S_0} = f_{par}\rho_{par}\sin(\alpha)\frac{1-e^{-TR/T_{1par}}}{1-\cos(\alpha)e^{-TR/T_{1par}}} + f_{mw}\rho_{mw}\sin(\alpha)\frac{1-e^{-TR/T_{1mw}}}{1-\cos(\alpha)e^{-TR/T_{1mw}}} \end{cases} \quad (7.4)$$

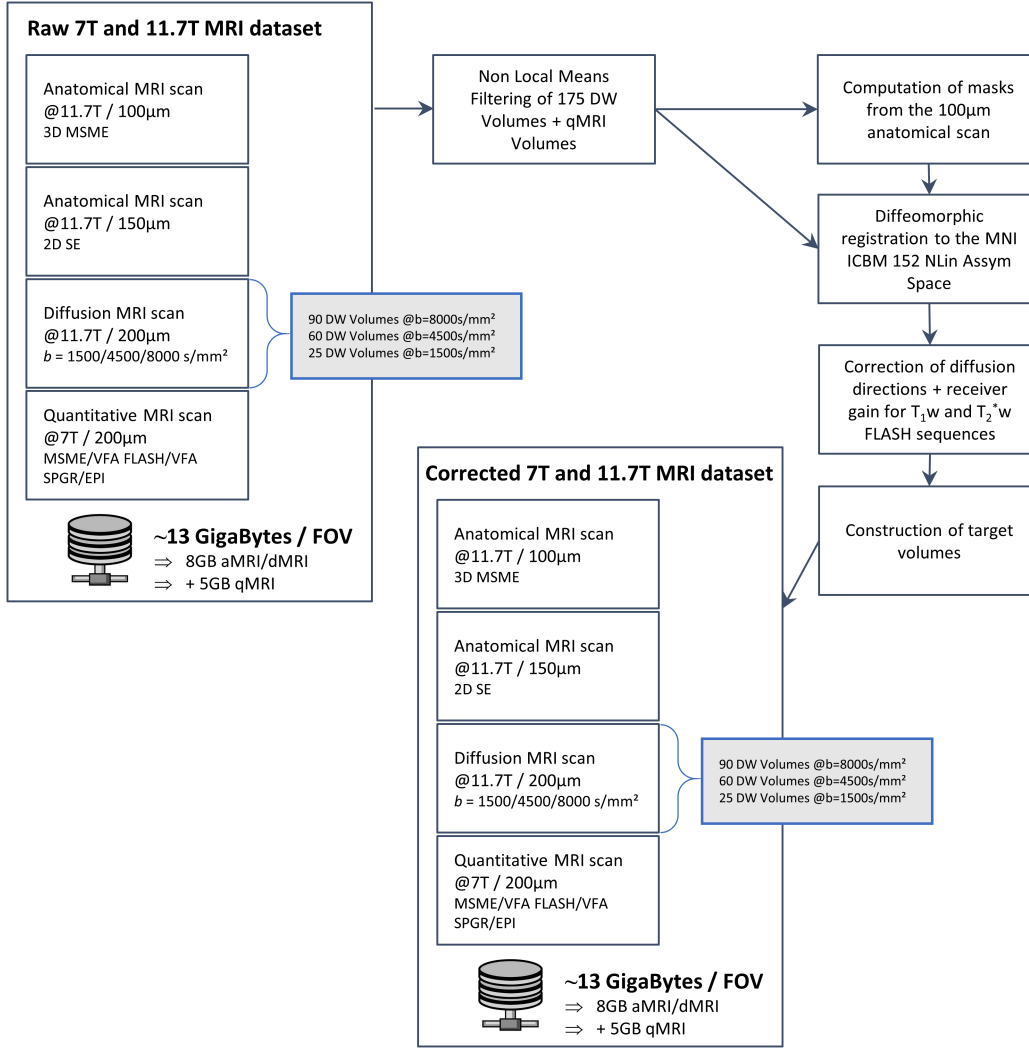


Figure 7.9: Schematic representation of the pre-processing pipeline of the Chenonceau project.

with the following constraints:

$$\begin{cases} f_{par} + f_{mw} = 1 \\ \forall f, 0 \leq f \leq 1 \end{cases} \quad (7.5)$$

$\alpha$  is the computed flip angle that varies from  $3^\circ$  to  $45^\circ$ .  $f_{par}$  and  $f_{mw}$  refer to the fractions of parenchyma and myelin water constituting the NMR signals.  $T_{1par}$ ,  $T_{2par}$ ,  $T_{1mw}$  and  $T_{2mw}$  are predetermined from literature [Birkl et al. 2016; Sengupta et al. 2018; Shatil et al. 2018], relaxometric measures performed on the brains of *ex vivo* mice at 11.7T, and the aforementioned fits of the  $T_1$ -weighted,  $T_2$ -weighted and  $T_2^*$ -weighted signal equations made out of the scanning of the Chenonceau's primary visual area.

Figure 7.12 showcases the qT1, qT2, qT2\* and MWF maps of the entire Chenonceau brain after the ANTs diffeomorphic registration of each FOV on the corresponding 3T block-face images, themselves being registered on the full brain reoriented in the MNI space. The diffeomorphic registration pipeline was entirely designed by Alexandros Popov.

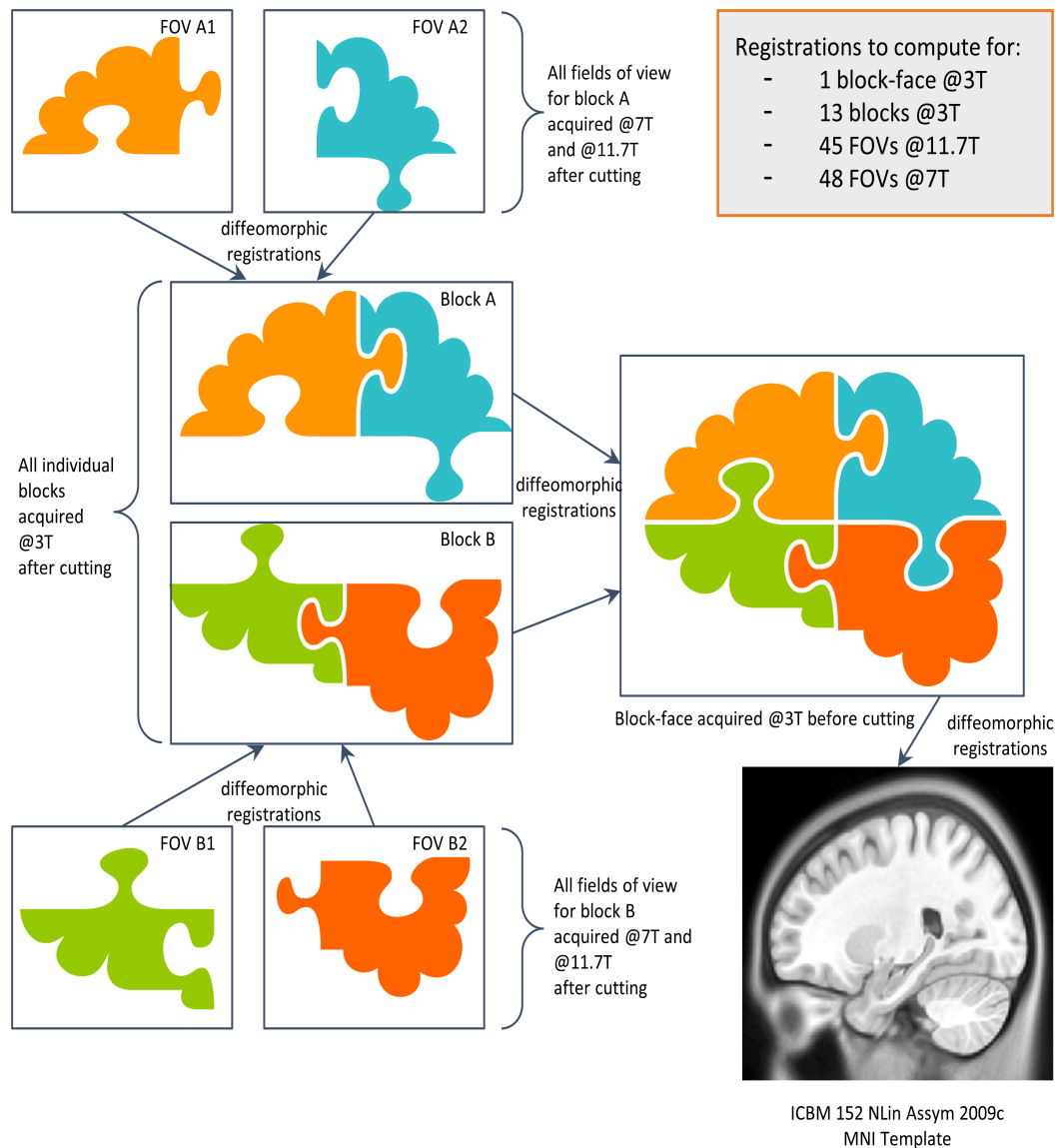


Figure 7.10: Schematic representation of the diffeomorphic registration step of the Chenonceau project.

It starts with the registration of each field of view on the corresponding block at  $400\mu\text{m}$  isotropic resolution, by taking into consideration the overlapping areas between the fields of view. This operation is realized for every reconstructed MR image from the acquisitions performed at 7T and 11.7T. Thus, on the example shown in Figure 7.12, it exists nine versions of the reconstructed block A, one for each anatomical MRI, qMRI, and dMRI sequence that was exploited in the pre- and post-processing pipelines:  $T_2$ -weighted SE and MSME,  $T_1$ -weighted VFA FLASH,  $T_2$ -weighted MSME,  $T_2^*$ -weighted FLASH SPGR, and  $T_2$ -weighted segmented EPI sequences for b-values at 0/1500/4500/8000s/mm<sup>2</sup>. Each block is likewise registered on the block-face that has a  $500\mu\text{m}$  isotropic resolution. Then, the block-face is registered on the ICBM 150 NLin Assymmetric 2009c MNI template. The latter was chosen as the MNI template space for the Chenonceau project because it is the common frame selected by HBP, the European flagship project for which the Chenonceau project takes part by supplying mesoscopic data to the HBP atlas.

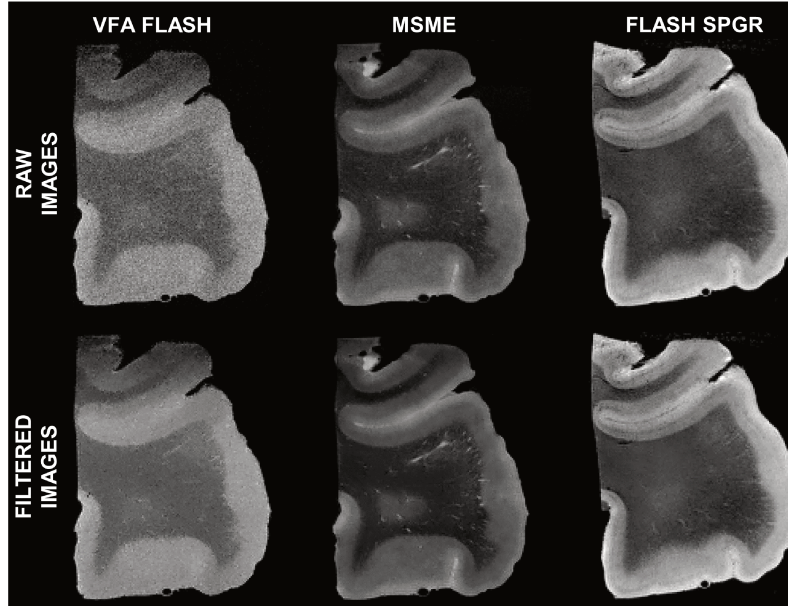


Figure 7.11: Images of the 7T data of a Chenonceau left-hemisphere field of view, A2, before (at the top) and after (at the bottom) the non-local means filtering of the Rician noise:  $T_1$ -weighted variable flip angle (VFA) FLASH sequence at  $\theta = 6^\circ$ ,  $T_2$ -weighted MSME sequence at  $TE = 66.72ms$ ,  $T_2^*$ -weighted variable echo time FLASH SPGR sequence at  $TE = 20ms$ . Slices are in the coronal view.

$B_1^+$  maps were generated for each field of view from the dual 3D EPI sequences using the double-angle method. They all presented similar values in the core area of the FOV, meaning the FOV minus the areas of overlap. This result can be explained by the use of a volume coil to acquire the MRI data, which allowed to suitably measure the NMR signal all over the field of view. Thus, considering Equation (7.3), we obtained that  $\alpha_{corrected} \simeq \alpha$ . The  $B_1^+$  maps were hence not integrated in the reconstruction of the complete  $qT_1$  map.

The two acquisition campaigns to scan the left and the right hemispheres were severely time-delayed. This was due to the inability to perform acquisitions for eight months caused by a technical problem on the 7T MRI scanner and the COVID-19 pandemic. Despite these two different timelines, it appeared that the NMR signal values and the relaxometry times were similar for both hemispheres when comparing their histograms. This observation correlates with the one made on the signal-to-noise ratio values (Table 7.1) and highlights the efficacy of the fixation and rehydration processes. The calculated relaxation times thus agree with literature [Birkel et al. 2016; Sengupta et al. 2018], as summarized in Table 7.2 that presents the measured mean and standard deviation of the relaxation times in the white matter and the cerebral cortex of the Chenonceau brain.

brain region	$T_1$ (ms)	$T_2$ (ms)	$T_2^*$ (ms)
white matter	199.25 $\pm$ 52.80	58.10 $\pm$ 15.11	27.97 $\pm$ 8.40
cerebral cortex	276.25 $\pm$ 78.15	64.61 $\pm$ 13.90	42.21 $\pm$ 12.43

Table 7.2: Table of the mean ( $\pm$  standard deviation) relaxation times in the Chenonceau brain for the white matter and the cerebral cortex at 7T.

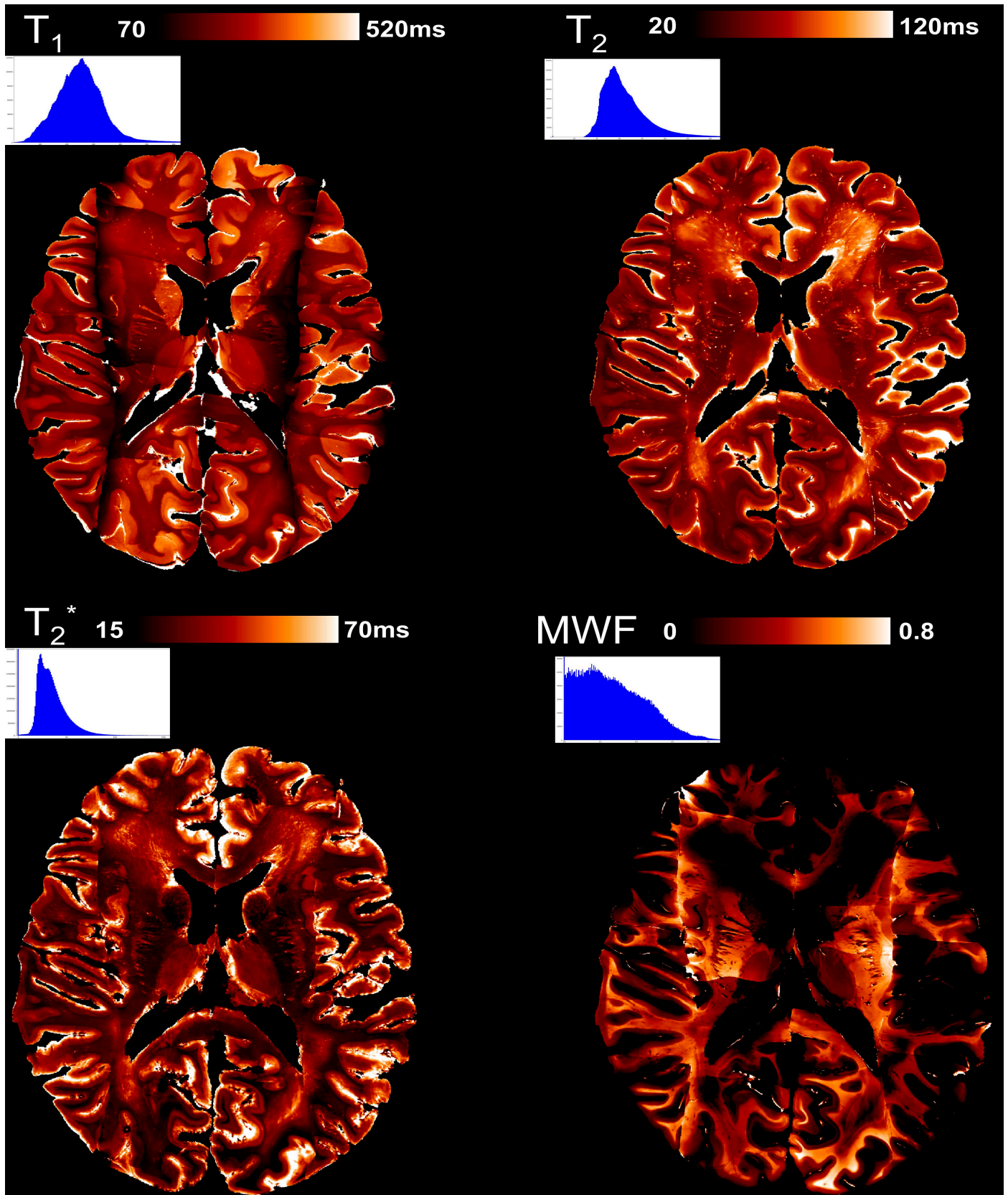


Figure 7.12: Quantitative  $T_1$ ,  $T_2$ ,  $T_2^*$  and myelin water fraction (MWF) maps and related histograms of the Chenonceau brain in the axial view. The brain was reoriented in the MNI space. The grayscale bars refer to the relaxation times ( $T_1$ ,  $T_2$ ,  $T_2^*$ ) or the fraction of myelin water measured in the entire ex vivo brain.

### 7.2.3 Quantitative mapping from the NODDI model

The multiple-shell dMRI dataset allowed to infer the microstructural NODDI model [Zhang, Schneider, et al. 2012; Zhang, Mi, et al. 2019] providing proxies of the neurite density given by the intracellular volume fraction ( $f_{\text{intra}}$ ) and the orientation dispersion (OD). The modeling was based on the  $T_2$ -weighted reference image, and the diffusion-weighted data at  $b = 4500\text{s/mm}^2$  and  $b = 8000\text{s/mm}^2$ . The local principal direction was initialized from the estimated DTI model. The parallel diffusivity of neurites was set to:  $d_{\parallel} = 4.2 * 10^{-10}\text{m}^2/\text{s}$ . The quantitative microstructural  $f_{\text{intra}}$  and OD maps are presented in Figure 7.13 which give an estimation of the parameters involved in the NODDI model. 3D diffeomorphic registrations on the 3T block-face images were also realized for the 11.7T dataset to enable the edition of the complete microstructural maps in the MNI space. These maps were indispensable to perform the cyto-clustering of the cortical ribbon as discussed in the next chapter.

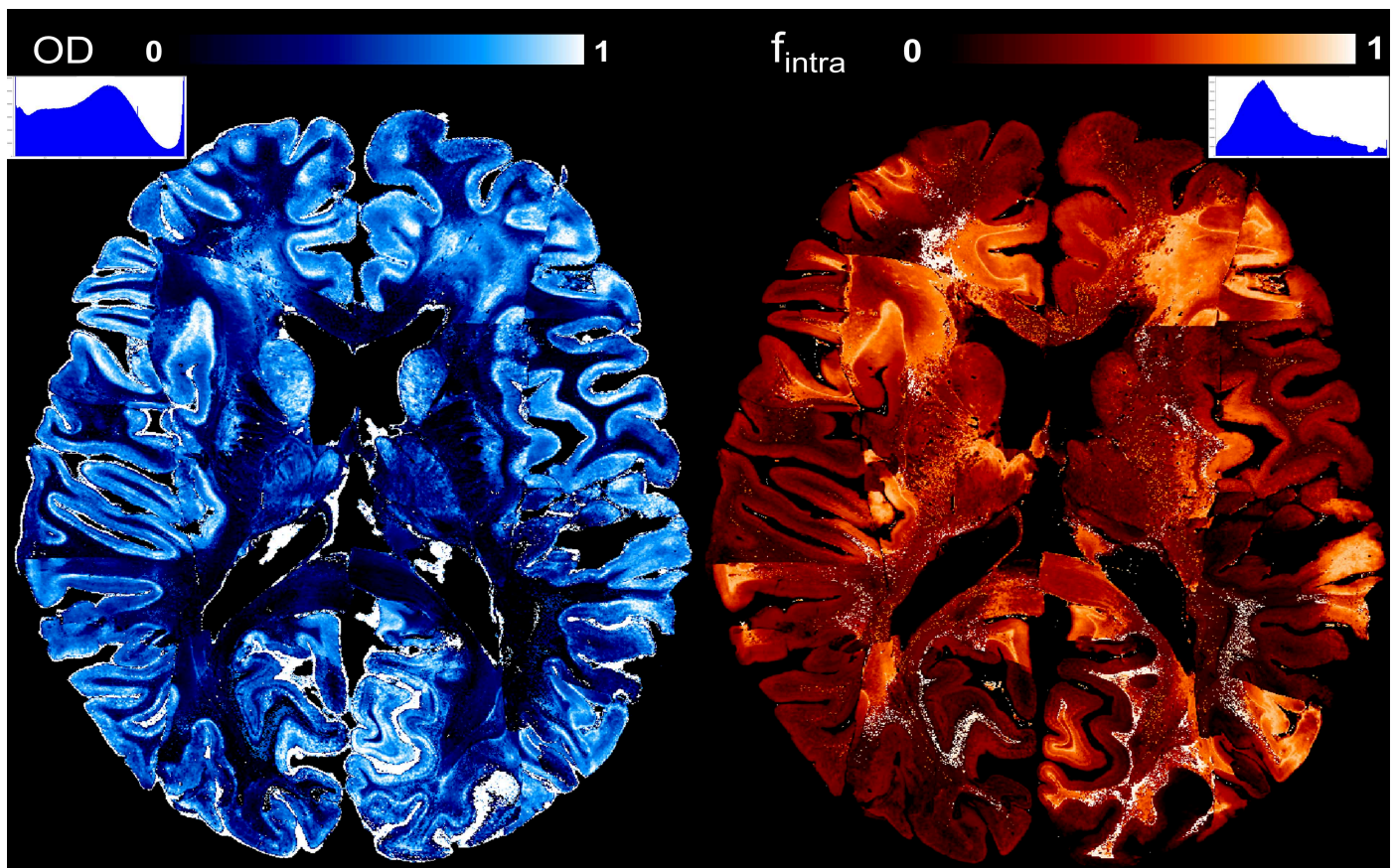


Figure 7.13: Quantitative maps and related histograms of the intracellular volume fraction ( $f_{\text{intra}}$ ) and orientation dispersion (OD) of the Chenonceau brain in the axial view. The brain was reoriented in the MNI space.

## 7.3 Conclusion

This introductory chapter to the Chenonceau project sums up the different steps that enabled the quantitative mapping on the entire postmortem human brain, from the fixation process that preserved the specimen's tissue to the post-processing pipeline that generated the maps. The two lengthy acquisition campaigns required specific MRI sequences



applied at 7T and 11.7T that led to this unique dMRI and qMRI dataset.

The following chapter addresses the cerebral cortex of the Chenonceau brain. From the previously described quantitative maps, we were able to segment the cortical layers and access to specific features of the cortical ribbon, namely its cytoarchitectonics, myeloarchitectonics and its structural connectivity. A comparison to histological analyses made on Chenonceau brain samples is also detailed in that next chapter.

# Chapter 8

## Focus on the Chenonceau cerebral cortex

The human cerebral cortex, which was detailed in Chapter 3, presents cytoarchitectural and myeloarchitectural features that can be explored with UHF quantitative and diffusion MRI. In the frame of the Chenonceau project, the cerebral cortex of an entire adult human brain was mapped and analyzed to obtain proxies of its cytoarchitecture and myeloarchitecture at the mesoscale. This last chapter depicts the process that led to the automatic segmentation of the cortical layers based on cytoarchitectural and myeloarchitectural information. Then, the structural intracortical connectivity is discussed. Last, a comparison to the 3D polarized light imaging (PLI) analyses conducted as ground truth to this study is detailed.

### 8.1 Inference of the laminar structure of the Chenonceau human cortex

#### 8.1.1 State of the art

Unveiling the cytoarchitecture and the myeloarchitecture of the human cerebral cortex is a major challenge that began long before Brodmann and it is still unresolved, as presented in Chapter 3. Diffusion and quantitative MRI both contribute to expand the amount of knowledge on that cerebral structure.

Diffusion MRI manifests sensitivity to radial and tangential orientations of axons and to the volume fraction of dendrites. Previous postmortem studies have validated the ability of dMRI to provide valuable insight about the gray matter microstructure like in the white matter [D'Arceuil and Crespigny 2007; D'Arceuil, Westmoreland, et al. 2007; Kleinnijenhuis, Zerbi, et al. 2013; Assaf 2017]. It indeed delivers relevant information on the cortical microstructure even with the use of scalar invariants stemming from conventional diffusion models (DTI, QBI, CSD, etc.) such as the fractional anisotropy (FA), the apparent diffusion coefficient (ADC), mean diffusivity (MD), the parallel and radial diffusivities [McNab, Jbabdi, et al. 2009; Miller, Stagg, et al. 2011; McNab, Polimeni, et al. 2013; Leuze et al. 2014; Aggarwal et al. 2015]. More advanced acquisition schemes using multiple-shell schemes and exploring q-space with large b-values or exploring time dependence with short to very long diffusion times are also beneficial for discriminating cortical areas [Fukutomi, Glasser, Murata, et al. 2019; Ganepola, Lee, et al. 2021]. Analyzing the cortical gray matter neurite morphology using diffusion MRI and NODDI provides valuable information regarding cytoarchitecture that are complementary to myeloar-

chitecture [Fukutomi, Glasser, Zhang, et al. 2018], and similar results to NODDI-based measures can be achieved with high b-value DTI [Fukutomi, Glasser, Murata, et al. 2019]. In Yi et al. 2019, the study results in exhibiting the sensitivity of the NODDI model to microglial density and the cellular changes associated with microglial activation, which could ameliorate clinical diagnostic accuracy. In Seehaus et al. 2015, strong relationships between myelin microstructure and DTI-based measures were found. It appears that high FA values correlate with high myelin density, while high MD values correspond to bimodal or diffuse orientation distributions and low myelin density.

Diffusion-weighted MRI was also applied on *in vivo* subjects to discriminate cortical layers [McNab, Polimeni, et al. 2013; Kleinnijhuis, Mourik, et al. 2015; Calamante et al. 2018; Ganepola, Nagy, et al. 2018], stressing the importance of high angular resolution [Heidemann et al. 2012; Nagy et al. 2013]. The latest biophysical model, soma and neurite density imaging (SANDI) [Palombo et al. 2020], is the intra-neurite model accommodating an approximate description of the contribution from water spins diffusing within cellular soma. It was devised to account for soma abundance in gray matter which enhances cortex modeling, and to manage high b-values ( $b \geq 3000s/mm^2$ ). But its application on living humans is restricted to 3T Connectom scanner, which remains scarce around the globe. The greatest hurdle to observe cortical lamination using dMRI is the spatial resolution [Assaf 2017]. However, the definition of high spatial resolution for *in vivo* MRI, namely  $1mm^3$  isotropic, is much lower than what can be reached postmortem. *Ex vivo* studies using ultra-high field dMRI are thus the preferred environment to achieve an accurate delineation of the cortical lamination.

Quantitative MRI also plays a key part in the *ex vivo* investigation of the cortical microstructure. The multiple MRI contrasts stemming from  $T_1$ ,  $T_2$  and  $T_2^*$  relaxation times, bring key information on human cortical myelination [Fatterpekar et al. 2002; Laule et al. 2006; Duyn et al. 2007; Geyer, Weiss, et al. 2011; Barazany et al. 2012; Cohen-Adad et al. 2012; De Martino et al. 2015]. *In vivo* studies [Dick et al. 2012; Deistung et al. 2013; Sereno et al. 2013; Lutti, Dick, et al. 2014; Marques et al. 2017; Trampel et al. 2017; Liu, Rubino, et al. 2019; Uddin et al. 2019] were conducted as well on that precise matter. In Edwards et al. 2018, a full review is made on MRI-based *in vivo* histology to probe the microstructure of the human isocortex. For instance,  $T_1$  relaxometry has been used as a proxy for cortical microstructure since it strongly depends on membrane composition [Koenig et al. 1990], plus  $T_1$  is sensitive to intracortical myelination [Bernhardt et al. 2018]. However, it is not a specific marker and may be affected by other factors [Winston et al. 2020]. To become more specific,  $T_1$  relaxometry has to be combined with multi-compartmental mapping of  $T_2$  relaxation time which allows the robust computation of myelin water fraction [MacKay et al. 1994; Kulikova et al. 2016; Ma et al. 2019; Dvorak et al. 2020; Piredda et al. 2020], and  $T_2^*$  relaxation time to provide further insight about iron content and myelin [Peters et al. 2007; Stüber et al. 2014; Sengupta et al. 2018] that are major complements to probe myeloarchitecture. Therefore, investigating myeloarchitecture is as relevant as probing cytoarchitecture to bring vital information on the functions of the cortex beyond the cellular composition [Timmler et al. 2019].

The need for automated segmentation of brain regions composed of gray matter was well addressed in Basukala et al. 2021, where quantitative susceptibility mapping allowed to segment the substantia nigra and the red nucleus in patients suffering from Parkinson's disease. This study points out a pertinent fact: the gold standard in segmentation remains manual segmentation by neuroanatomists and radiologists. Nevertheless, such a task would be daunting had it be performed on the human cerebral cortex, all the more as segmenting more than one cerebral cortex would be unfathomable. That is why automated segmentation of the human cerebral cortex is a reasonable solution to probe its cytoarchitecture and myeloarchitecture, offering no operator bias and potential consistency of the method. One should bear in mind that anatomical MRI is mandatory to apply automated segmentation [Dale et al. 1999; Kim, Singh, et al. 2005].

The existing *ex vivo* studies aiming at segmenting the cortex laminar structure [Aggarwal et al. 2015; Bastiani et al. 2016; Beaujoin et al. 2018; Little et al. 2021] usually focused on dMRI, or receptor autoradiography [Zilles, Palomero-

Gallagher, Grefkes, et al. 2002; Palomero-Gallagher and Zilles 2017; Palomero-Gallagher, Kedo, et al. 2020], and did not use relaxometric measurements, which could yet add valuable information in that purpose. Moreover, most of them do not target the cortical layers and just discriminate the cortex or cortical regions. The study of Calamante et al. 2018 did the diffusion-relaxometry combination but on three living patients from the HCP dataset. In Lifshits et al. 2018, partial volume effects in cortical layers imaging are explored through  $T_1$  relaxation mapping using high resolution IR MRI data. The study targeted clinically reachable spatial resolutions (0.43mm, 0.43mm, 1.5mm) to characterize cortical layers in the whole brain instead of laminar features such as myelin content. Resorting to low resolution  $T_1$  mapping precluded direct imaging of the layers that could be observed at high spatial resolution.

Here, we will present the method based on dMRI and qMRI data obtained at 7T and 11.7T with a 200 $\mu$ m isotropic resolution to automatically segment the cortical layers of the entire Chenonceau neocortex, related to cytoarchitectural and myeloarchitectural information.

### 8.1.2 Segmentation of the neocortex

From the resulting quantitative maps described in Chapter 7, we devised a contrast-based approach to separate the cortical ribbon of the neocortex from the rest of the Chenonceau brain. In Figure 8.1, we present the common approaches to parcel the brain using MRI-based data. The observation of the quantitative maps led to selection of the quantitative relative proton density (qPD) map generated from the series of  $T_1$ -weighted VFA FLASH sequences as the best contrast to proceed with. Figure 8.2 illustrates the different steps that produced the masking of the neocortex. The chosen qPD map, visible in Figure 8.2, showcased a clear contrast between PBS residuals, gray and white matters that allowed a k-means algorithm integrated in the Ginkgo toolbox (<https://framagit.org/coupon/gkg>) to partition the entire brain. Afterwards, a k-means clustering was applied on the qPD map to partition it based on its different intensity values. It necessitated 20 clusters to obtain a qualitative partition of the whole qPD map.

From there, the labels exclusively located in the isocortex were selected using a thresholding algorithm to constitute a pre-mask of the cortex. This pre-mask is then the input of the in-house region growing segmentation algorithm. The latter utilizes the voxels of the pre-mask as seeds to target all the remaining voxels that compose the neocortex and integrate them to the pre-mask to generate the final mask. When a region grows from a selected seed, only the borders of the growing seed will be kept to compose what we call the *front* of the growing region. The algorithm exploits the Ising model to regularize the segmentation process. It is likewise inspired by the process described in Mangin, Frouin, et al. 1995 to segment the cortex using topology preserving deformations. The created region growing segmentation algorithm is as follows:

1. Reading the qPD map and the pre-mask.
2. Definition of a bounding box of the MR image.
3. Reading the operator-dependent parameters which are the maximum iteration count of the front propagation (10000), the neighborhood type (26), the Ising factor (0.5) and the minimum modification count (2).
4. Computing of the variance, mean and standard deviation of the signal intensity in the pre-mask.
5. Propagating the front made of the pre-mask's voxels to perform region growing.
6. Looping over points placed in the current front.
7. Analysis of the proton density and the label values for the neighboring point.

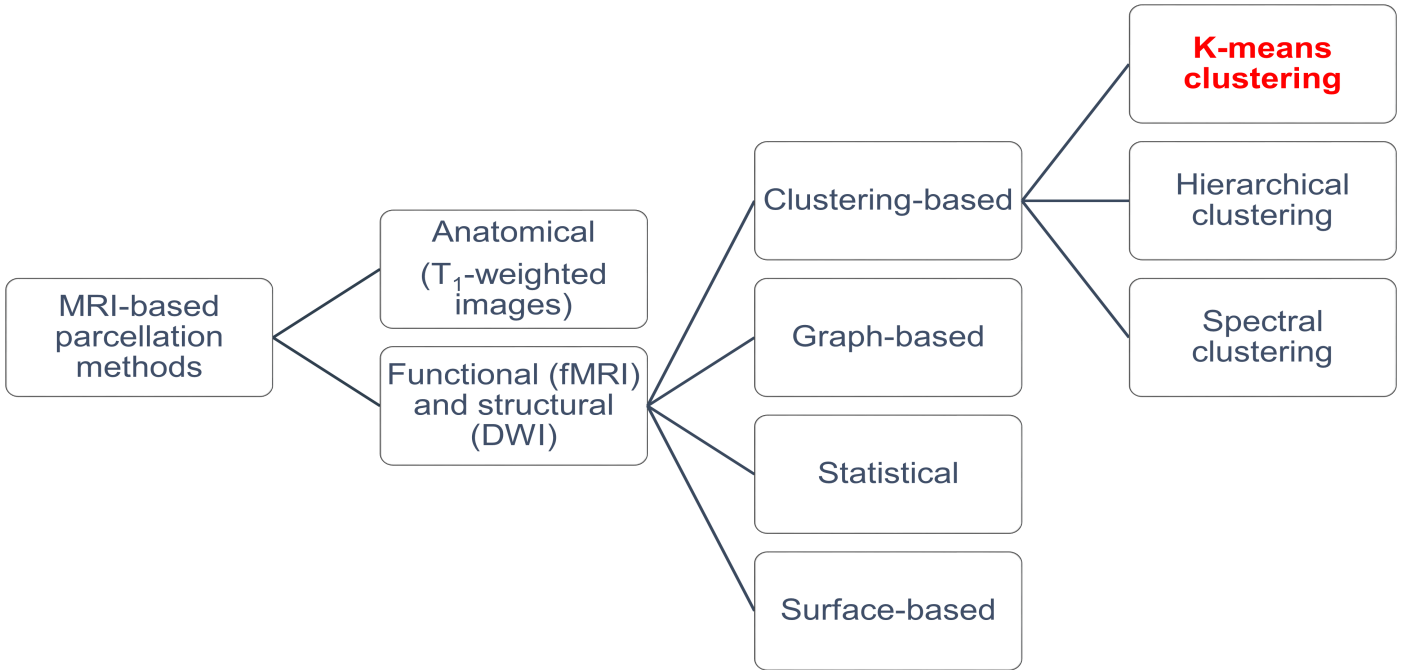


Figure 8.1: Hierarchical graph of the MRI-based approaches for brain parcellation. For the Chenonceau brain, we decided to proceed with *k*-means clustering for the segmentation of its isocortex. *fMRI* = functional magnetic resonance imaging. *DWI* = diffusion-weighted imaging. Graph adapted from Moghimi et al. 2021.

8. Calculation of the exposition (Equation (8.1)) and the variation of energy (Equation (8.2)) for the neighboring point presenting a different label from the current front. If the variation of energy is negative, the neighboring point is added to the current front.
9. Reiteration of the procedure.

$$exposition = \frac{(neighborIntensity - meanIntensity)^2}{intensityVariance} \quad (8.1)$$

where *neighborIntensity* is the signal value within the neighboring voxel, *meanIntensity* is the mean signal value of the current front, and *intensityVariance* is the variance of the signal value for the current front.

$$dU = isingFactor * min(exposition, 4.0) - isingFactor \quad (8.2)$$

with  $dU$ , the variation of energy and *isingFactor*, the Ising factor set by the operator to ensure regularization of the energy. Few manual corrections were needed to obtain the mask of the isocortex presented in Figure 8.2.

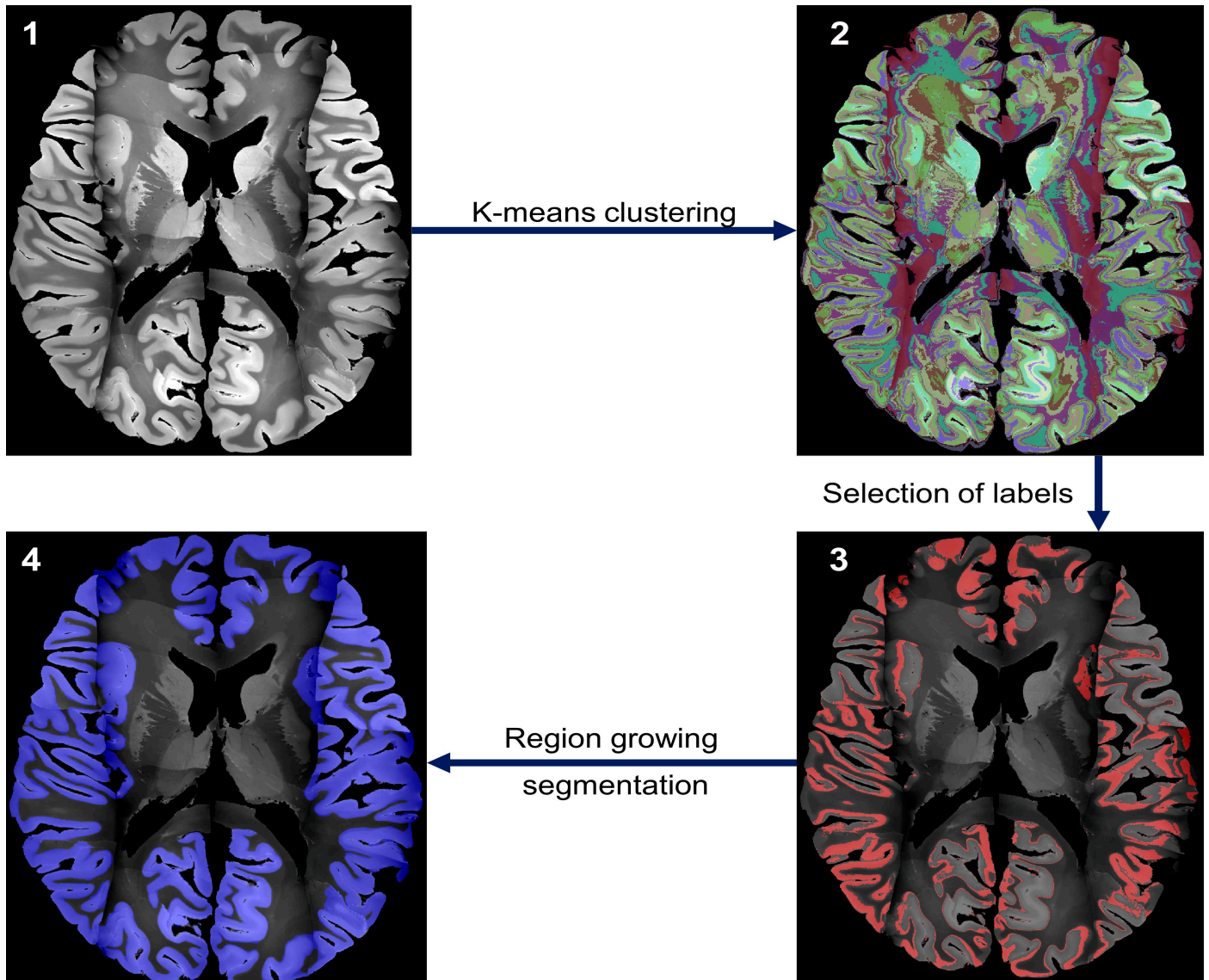


Figure 8.2: *Masking of the Chenonceau neocortex. Four steps led to that result: 1) selection of the quantitative relative proton density (qPD) map to mask the Chenonceau neocortex; 2) k-means clustering of the qPD map; 3) selection of the labels located in the neocortex using a thresholding algorithm; 4) application of the region growing segmentation algorithm to generate the cortex mask.*

### 8.1.3 Design of a method to segment cortical layers using multi-contrast clustering

The first attempt to reveal cyto-layers from dMRI data and myelo-layers from qMRI data was by defining at each voxel of the cortex mask a N-dimensional feature combining the pre-computed quantitative  $T_1$  (qT1),  $T_2$  (qT2),  $T_2^*$  (qT2\*), MWF, intracellular volume fraction ( $f_{\text{intra}}$ ) and orientation dispersion (OD) maps. N-dimension cluster maps as well as their associated posterior probability maps were established using a Gaussian mixture model for a number of components corresponding to the minimum of the Bayesian information criterion (BIC), thus defining a spatial parcellation of the cortical mantle. This procedure was the same one used in Beaujoin 2018 to characterize the laminar cortical structure in the primary visual cortex. The approach applied in this thesis is a direct N-dimensional extension of the approach originally proposed in Lifshits et al. 2018. It utilized  $T_1$  component probability maps to distinguish cortical layers for

which each layer was assigned a Gaussian distribution associated to a specific pair of mean and standard deviation  $T_1$  value. The CSF and the white matter had likewise their own  $T_1$  values from the probability maps. Therefore,  $T_1$  layers were revealed from the  $T_1$  histogram decomposition with a monotonic increasing mean  $T_1$  value when moving from the innermost to the outermost layers.

However, this approach was leveled off in the number of clusters that could be generated. We thus designed a new multi-contrast cortex layer clustering algorithm based on a k-means algorithm to automatically segment the cortex. To this aim, the vectors of intensity values corresponding to a subset of the multiple cytoarchitectural and myeloarchitectural proxies ( $qT1$ ,  $qT2$ ,  $qT2^*$ , MWF,  $f_{\text{intra}}$ , OD) within each voxel of the cortex are exploited to perform clustering and unveil the cortex laminar structure. We propose to adapt a progressive three-fold strategy by:

- first, applying the tool to cytoarchitectural proxies to segment cyto-layers.
- second, applying the tool to myeloarchitectural proxies to segment myelo-layers.
- third, investigating the added-value of a dual contribution from cytoarchitectural and myeloarchitectural proxies to segment layers combining cytoarchitecture and myeloarchitecture.

The multi-contrast cortical layer clustering algorithm illustrated in Figure 8.3 relies on five consecutive steps:

1. Reading the selected quantitative maps and the cortex mask.
2. Reading the operator-dependent parameters which are the maximum iteration count (10000) and the cluster count (10 to 15).
3. Computing minimum and maximum values for each MR contrast to normalize each contrast between -1 and +1.
4. Randomly seeding within the cortex mask using all the voxels within the cortex mask.
5. Computing the k-means clustering algorithm.

The resulting cluster maps were further enhanced using the Potts model to correct outliers [Potts 1952; Wu 1982] and to devise high resolution maps of the cortical layers in the neocortex. The work presented here is still preliminary but demonstrates the potential of the approach to map the laminar structure of the isocortex from both cytoarchitectural and myeloarchitectural standpoints.

#### 8.1.4 Segmentation of the laminar structure from cytoarchitectural information

The cyto-clustering maps were calculated from two Watson's NODDI-based parameters including the intracellular volume fraction ( $f_{\text{intra}}$ ) that stands for neurite density, and the orientation dispersion index  $\kappa$  (Equation (8.3)) that indicates the concentration of neurites around the main direction. The  $\kappa$  index was preferred over the orientation dispersion (OD) since the resulting maps using  $f_{\text{intra}}$  and OD exhibited a less coherent lamination. We willingly decided to not integrate DTI-based features such as the FA, MD or radial diffusivity since they would have provided redundant information already given by  $f_{\text{intra}}$  and  $\kappa$ , as well less sensitive to fiber coherence [Kleinnijenhuis, Zhang, et al. 2013]. Note that the NODDI model relying on the Bingham distribution could have been used to obtain two concentration factors along the main direction and perpendicular  $\kappa_1$ ,  $\kappa_2$  directions [Tariq et al. 2016].

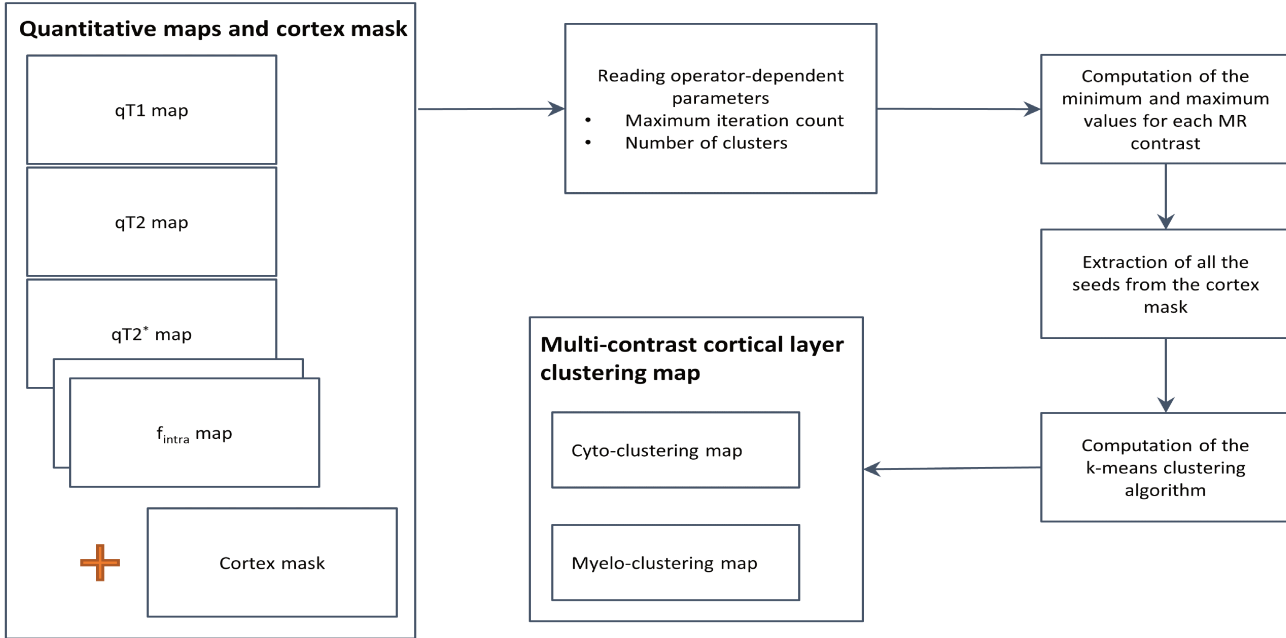


Figure 8.3: Schematic definition of the multi-contrast cortical layer clustering algorithm.

Figure 8.4 presents the cyto-clustering maps of two cortical regions of the Chenonceau isocortex obtained from  $f_{\text{intra}}$  and  $\kappa$  maps. The selected cortical regions are highlighted in blue on the qPD maps. The maps were corrected from outliers using the Potts model [Potts 1952; Wu 1982]. It required 10 clusters to parcel the neocortex for the samples of the primary visual cortex and the temporal cortex since a smaller number of clusters did not sufficiently segregate the isocortex. We could indeed notice one-layer cortical areas if less than 10 clusters were employed in the multi-contrast clustering algorithm, which must stem from parasitic intensity values generated by residual PBS.

$$OD = \frac{2}{\pi} \arctan\left(\frac{1}{\kappa}\right) \quad (8.3)$$

where  $OD$  is the orientation dispersion from the NODDI model.

Five layers were clearly visible for the V1 sample, while four layers stood out for in the temporal cortex. Layer I was likewise indicated in both cases, but its slimness made it hardly recognizable on the computed maps. As expected, cortical layers exhibit distinct thickness and organization for the two selected cortical regions. The granular aspects of the  $f_{\text{intra}}$  and  $\kappa$  maps reflected on the resulting cyto-clustering maps even after outlier corrections. Further work on improving the robustness of the estimation of NODDI parameters would be beneficial for enhancing the two quantitative maps. This results may suggest that the combination of the  $f_{\text{intra}}$  and  $\kappa$  maps is insufficient to account for the cortical cytoarchitecture. Additional corrections on the intensity values of the input images must be undertaken in order to smooth the output cortical layers and verify the efficacy of these two maps to infer cortical cytoarchitecture.



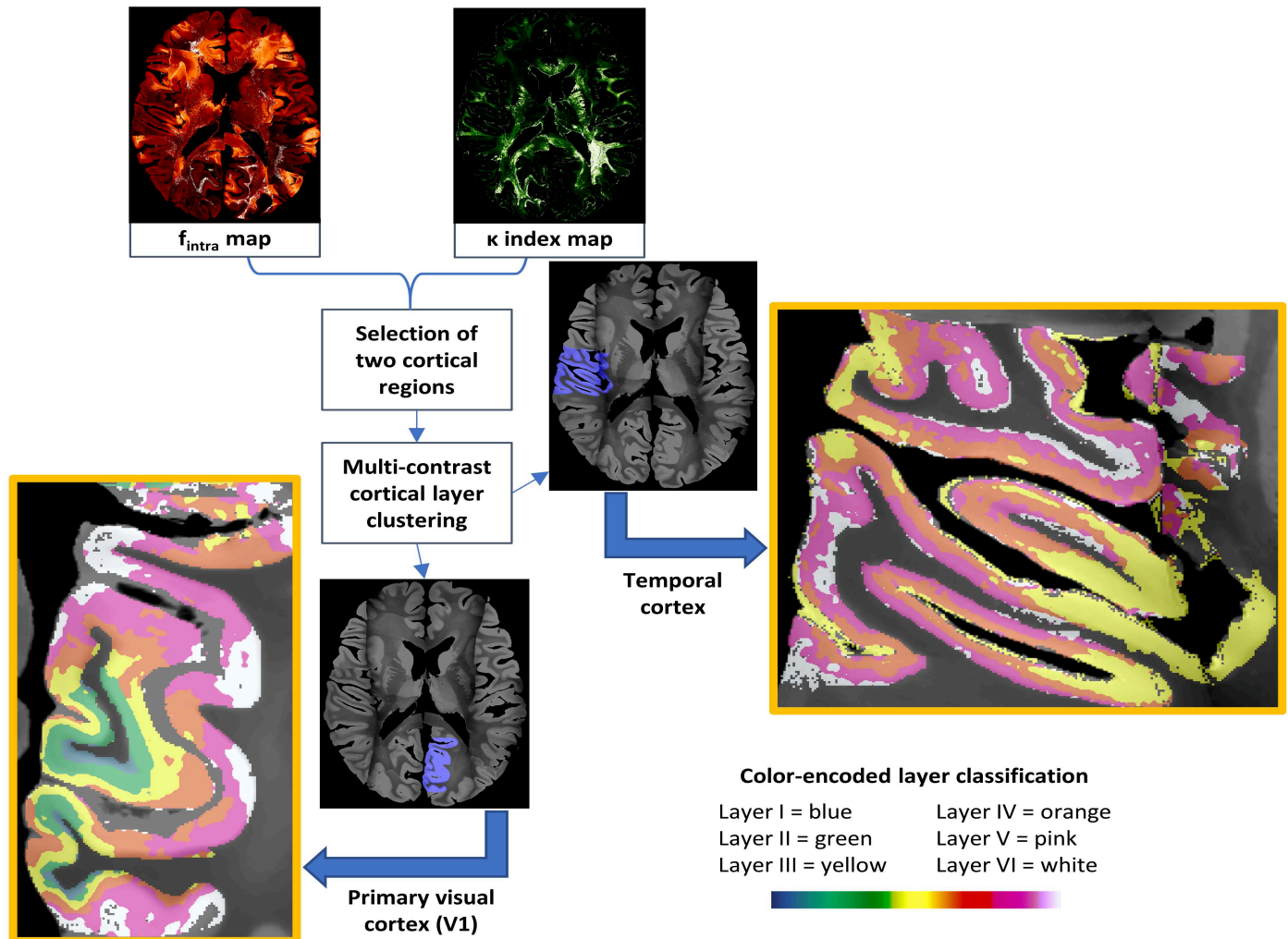


Figure 8.4: *Cyto-clustering maps of the Chenonceau neocortex. In the bottom left-hand corner, cyto-clustering map of a part of the primary visual cortex (V1). In the top right-hand corner, cyto-clustering map of a part of the temporal cortex. Both maps are presented after applying the Potts model to correct the outliers. The maps showcase 10 clusters to account for the extraneous intensity values embedded in them. Roman numbers were chosen to designate the cyto-layers so as to refer to the cytoarchitectonic nomenclature.*

### 8.1.5 Segmentation of the laminar structure from myeloarchitectural information

The myelo-clustering maps were computed as a combination of myelin water fraction (MWF) and  $qT2^*$  maps. Combinations of  $qT1$  and  $qT2^*$ , as well as  $qT1$ ,  $qT2$  and  $qT2^*$  were likewise tested but they did not generate a qualitative parcellation of the cortex mask. We also computed 10 clusters to properly segment the cortical ribbon in parts of the primary visual cortex and the temporal cortex.

Figure 8.5 shows the output of the multi-contrast cortical layer clustering algorithm using MWF and  $qT2^*$  maps. Afterwards, the discontinuous areas caused by intensity heterogeneity stemming from the Chenonceau puzzle reconstruction that needs to be improved, were manually corrected using a threshold algorithm that assembles selected labels. Finally, the Potts algorithm was applied to provide the final higher resolution map without deleterious outliers.

The layers of the myelo-clustering map were already visible before outliers correction unlike the cyto-clustering maps.

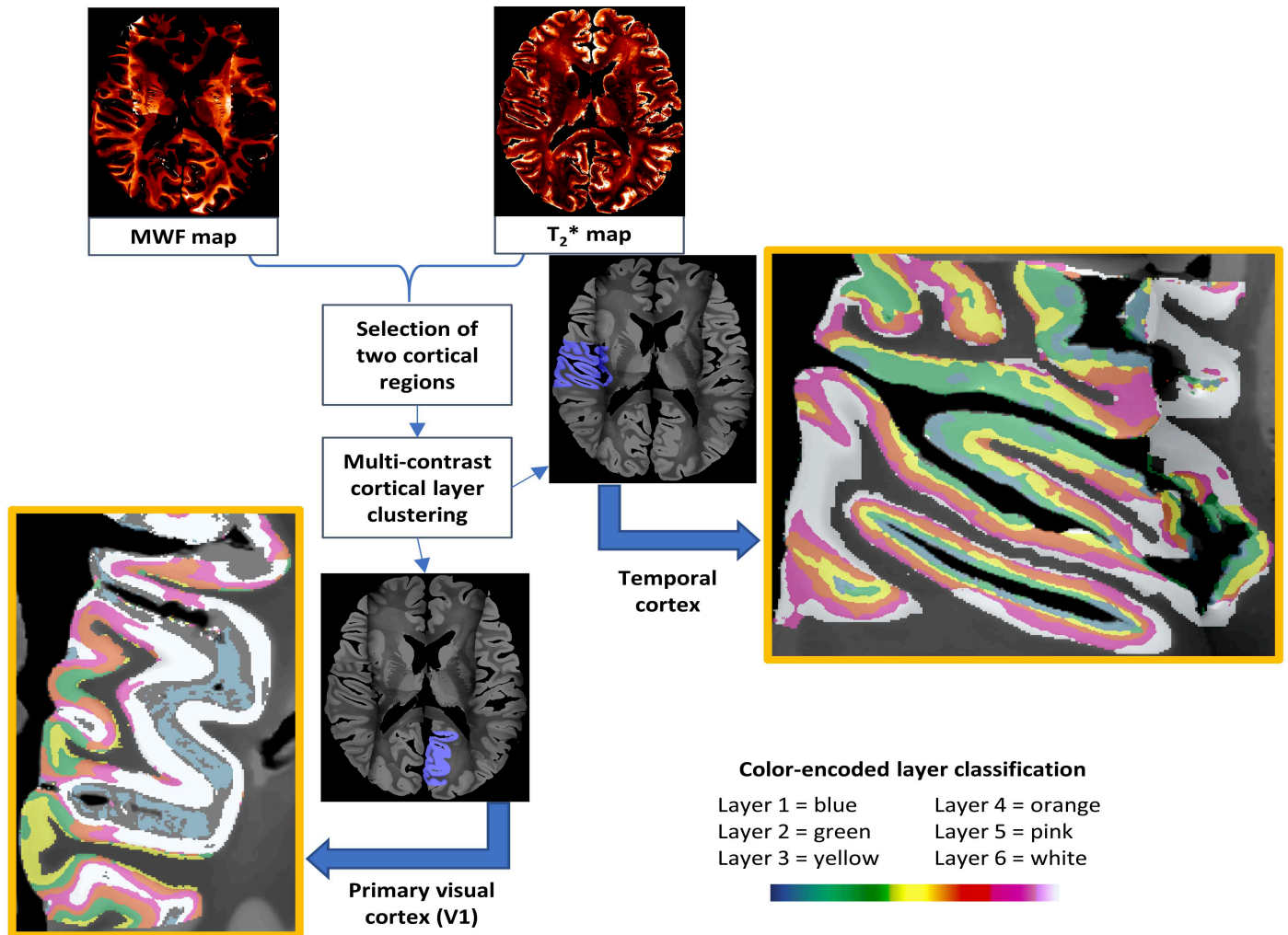


Figure 8.5: *Myelo-clustering maps of the Chenonceau neocortex. In the bottom left-hand corner, myelo-clustering map of a part of the primary visual cortex (V1). In the top right-hand corner, myelo-clustering map of a part of the temporal cortex. Both maps are presented after applying the Potts model to correct the outliers. The maps showcase 10 clusters to account for the parasitic intensity values embedded in them. Arabic numbers were chosen to designate the myelo-layers so as to refer to the myeloarchitectonic nomenclature.*

Moreover, six layers are noticeable for both cortical regions. The laminar organization of the myelo-clustering maps resembles to the one of the cyto-clustering map, however full correspondence was not always obtained throughout the brain sections. This disharmony in cortical layers may stem from the intensity heterogeneity that is observed in the overall input myeloarchitectural maps. It again results from a lack of intensity correction during Chenonceau puzzle reconstruction that should be improved in the future and could not be achieved in the frame of this thesis due to time constraints.

In the striate cortex (Brodmann area 17), the Gennari stripe was visible by denoting a specific layer separation between layers 4 and 5. It agrees with the previous MRI observations made using  $T_1$ -weighted sequences [Barbier et al. 2002; Fatterpekar et al. 2002; Clare et al. 2005; Barazany et al. 2012; Fracasso et al. 2016].

### 8.1.6 Segmentation of the laminar structure from cytoarchitectural and myeloarchitectural information

The combination of cytoarchitectural and myeloarchitectural information was performed by applying the multi-contrast clustering algorithm on the  $f_{\text{intra}}$ ,  $\kappa$ ,  $qT1$ ,  $qT2$  and  $qT2^*$  maps. This combination was the one offering the best results to parcel the neocortex. Strong similarities between cytoarchitectonics and myeloarchitectonics maps are well established in literature [Eickhoff et al. 2005; Amunts and Zilles 2015; Palomero-Gallagher and Zilles 2017]. Mixing the dMRI-based features and the qMRI-based features allowed to design layer-clustering maps as in Figure 8.6, and to highlight their commonalities in laminar features, namely cell density, myelination and iron content.

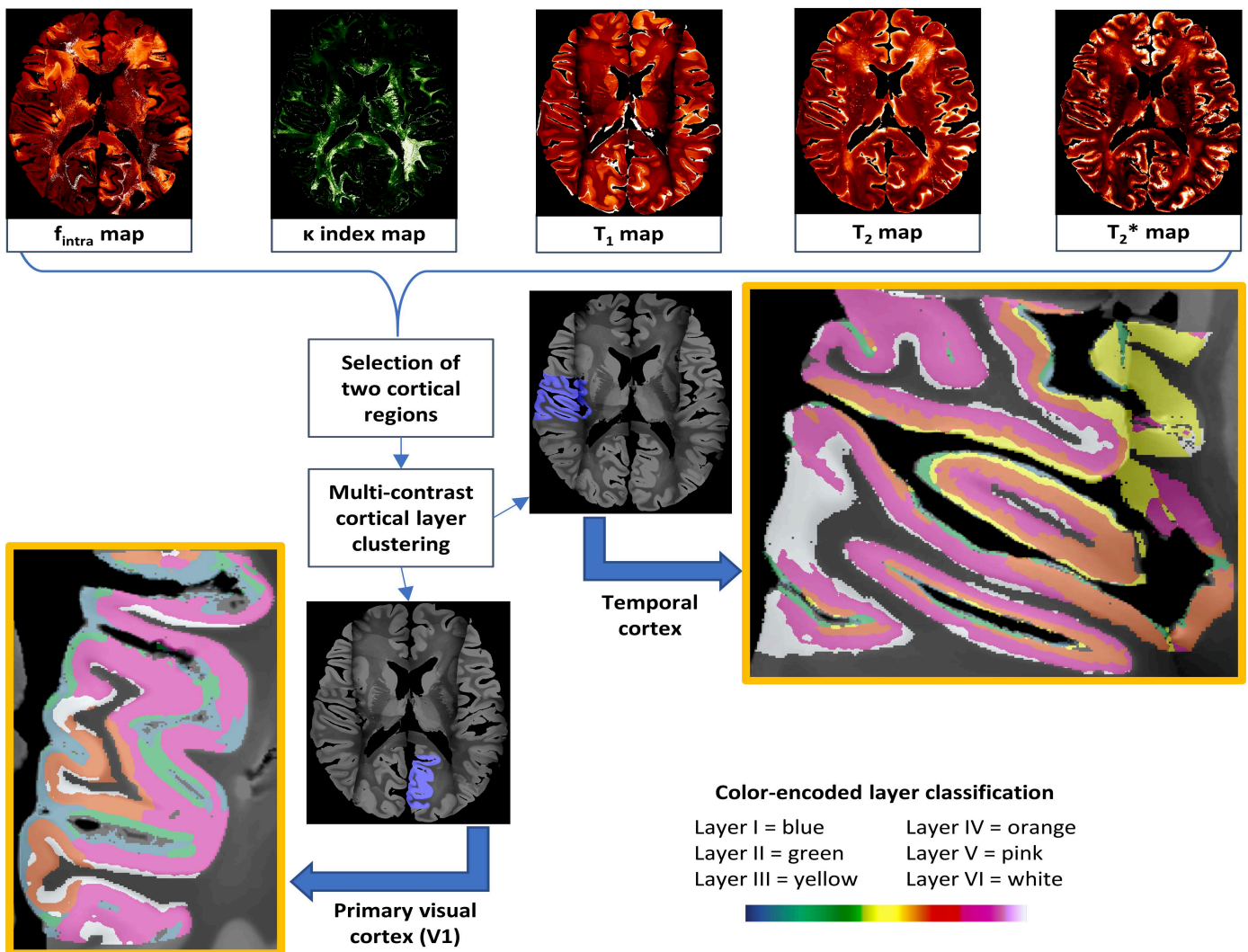


Figure 8.6: Layer-clustering maps of the Chenonceau neocortex. In the bottom left-hand corner, layer-clustering map of a part of the primary visual cortex (V1). In the top right-hand corner, layer-clustering map of a part of the temporal cortex. Both maps are presented after applying the Potts model to correct the outliers. The maps showcase 15 clusters to account for the multiplicity of intensity values embedded in them. Roman numbers were chosen to designate the cyto-layers so as to refer to the cytoarchitectonic nomenclature.

Our findings from combined NODDI-based parameters and relaxometric measures stood out cortical lamination by using

15 clusters in the clustering algorithm. We added clusters in the multi-contrast clustering algorithm in order to manage the multiplicity of intensity values issued from the combination of five quantitative parameters. We mostly observed six layers across brain slices for both occipital and temporal cortices. Furthermore, the combination of the five quantitative maps generated the smoothest and most continuous cortical layers compared to the cyto- and myelo-clustering maps. Demarcation at the Gennari stripe was noticed in V1.

There is still a substantial amount of work to improve the process that was not compatible with the timeframe of the PhD thesis, where two years were dedicated to acquire the unique Chenonceau dataset. The results presented here only establish a proof of concept that the inference of the cortex laminar structure is feasible. In addition, multiple validations of the various parameters used in the clustering method need to be performed such as the optimization of the needed number of clusters. The latter could have been done here, but it would be more valuable to investigate it after correcting between-FOVs intensity heterogeneities. However, these preliminary results are promising and pave the way to the establishment of a first atlas of the cortical cyto/myeloarchitecture using ultra-high field MRI at 7T and 11.7T.

We established in this section the access to this high resolution laminar structure of the isocortex, plus the diffusion MRI dataset can be exploited to map the structural connectivity of the neocortex. We now propose to investigate the potentiality of the Chenonceau mesoscopic 11.7T MRI dataset to map the inner connectivity of the isocortex.

## 8.2 Towards the inference of the inner connectivity of the isocortex

The myelinated fibers in the isocortex exhibit two main orientations: tangential and radial. The tangential fibers form laminae, while radial fibers are arranged in bundles, termed radii, which ascend from and descend to the subcortical white matter [Nieuwenhuys, Voogd, et al. 2007]. In order to explore the structural connectivity of the isocortex, a streamline regularized deterministic (SRD) tractography method [Perrin, Poupon, Cointepas, et al. 2005], available in the Ginkgo toolbox, was applied to the ODF map. The latter was computed from the HARDI diffusion MRI dataset acquired on the Chenonceau brain at  $b=4500\text{s/mm}^2$ , plus additional null b-value volumes for reference, along 60 uniformly distributed diffusion directions, and using the analytical Q-ball model with spherical harmonics order 8 and Laplace-Beltrami regularization factor 0.006.

A precise tuning of the SRD tractography method led to the following chosen parameters: forward step of  $50\mu\text{m}$ , fiber length range from 3mm to 300mm, aperture angle threshold of  $30^\circ$ , 1 random seed per voxel of the brain mask, discrete orientation set of 800 directions uniformly distributed over the unit sphere of the antipodally symmetric approach of Koay et al. 2011, GFA regularization factor of 0.090 corresponding to 99% of its cumulative histogram. The histogram of GFA values can be seen in Figure 8.7. The whole brain tractography process took one week to be processed and provided a dense tractogram composed of almost 150 millions of streamlines, as depicted in Figure 8.8.

A closer look at the cortical ribbon revealed a structured inner cortical connectivity as portrayed in Figure 8.9. The expected sharp turns are clearly visible when the fibers enter a gyrus and connect to sulci walls. Tangential fibers are also noticeable in the tractogram. A specific zoom in is realized on the left-hemisphere block F of the Chenonceau brain. This block was sent to our INM-1 partner (Pr Markus Axer, INM-1, Forschungszentrum, Jülich) to be further scanned using 3D polarized light imaging enabling the mapping of the myelinated axons at the microscopic scale for validation.

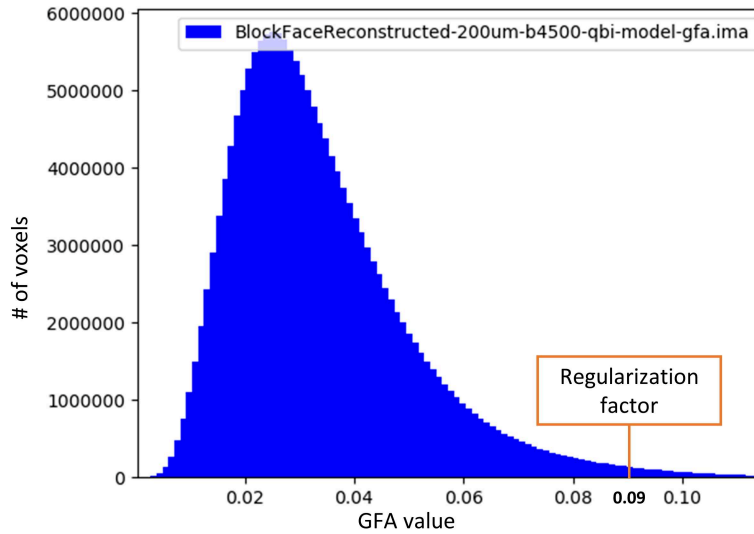


Figure 8.7: *GFA histogram of the Chenonceau brain issued from the aQBI model. The input for the GFA histogram computation was the 200 $\mu\text{m}$  diffusion-weighted image at  $b=4500\text{s}/\text{mm}^2$ . The value  $\text{GFA} = 0.090$  corresponds to 99% of the cumulative histogram.*

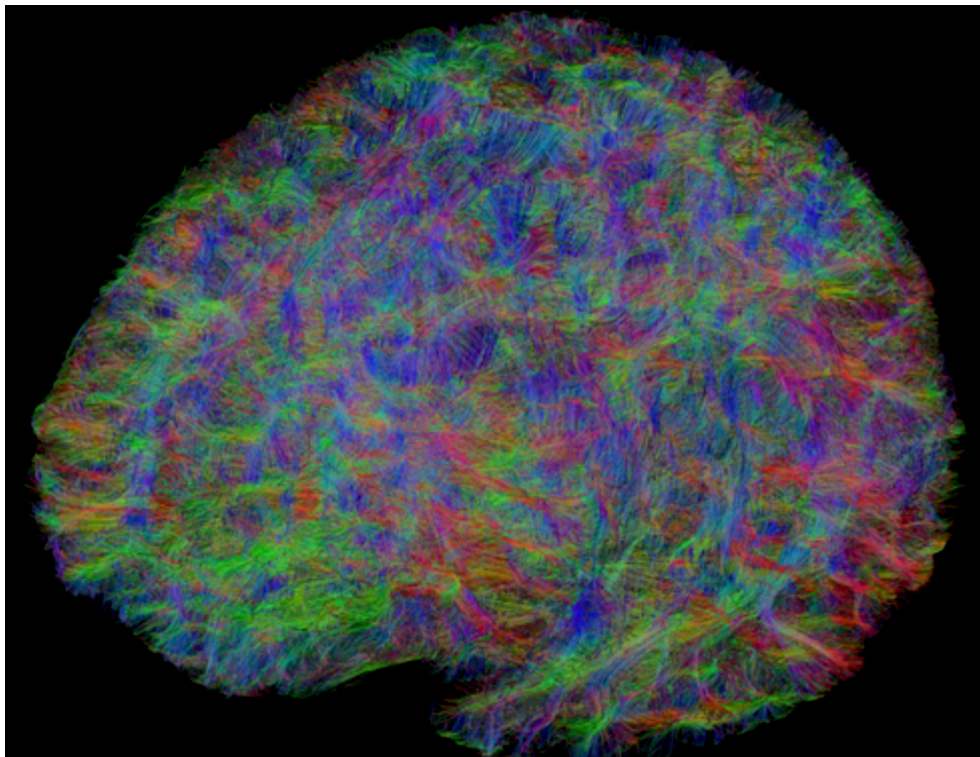


Figure 8.8: *The streamline regularized deterministic (SRD) dense tractogram of the Chenonceau brain. Only 1% of the 150 millions of generated fibers are represented here. The local directions of fibers are color-encoded.*

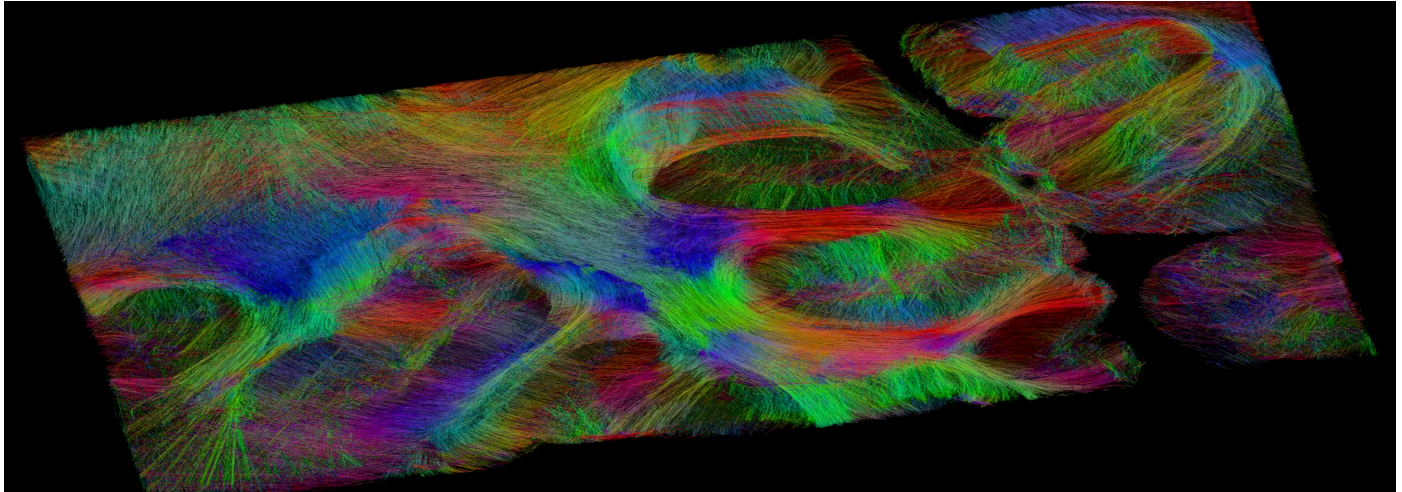


Figure 8.9: *Intracortical connectivity maps of the Chenonceau brain. Sample of the Chenonceau connectogram exhibiting cortical and subcortical U-shape white matter bundles.*

### 8.3 Comparison of 11.7T dMRI to 3D polarized light imaging

As stated in Dyrby, Innocenti, et al. 2018, interpretations of dMRI derived measures are far from a direct visualization of a specific microstructure but rather an indirect interpretation submitted to the limitation of diffusion local models and fiber tracking methods. The only acceptable ground truth to validate results on the cortical microstructure is thus histology [Palomero-Gallagher and Zilles 2017]. Regarding the context of the Chenonceau project, histology was at first planned on multiple brain blocks, but could not be performed prior the end of the two acquisition campaigns and the quality check of the collected data. Discussions with histologists led to the inability to gather histological sections from the Chenonceau brain due to both the fixation process applied in the project and the use of Fluorinert during the scans. They happened to be deleterious to immunostaining.

Consequently, we resorted to 3D polarized light imaging (PLI) that was performed by the research team of Pr M. Axer (INM-1, Forschungszentrum, Jülich, Germany). Two left-hemisphere blocks of the Chenonceau brain (blocks C and F) were sent from NeuroSpin (Gif-sur-Yvette, France) to their laboratory. The block F was the first one to be sliced into  $1.3\mu\text{m}$  in-plane sections with a  $50\mu\text{m}$  slice thickness. Polarized light imaging, an imaging technique pioneered by Pr M. Axer, relies on the exploitation of the birefringence of the myelin sheath to create contrast between axons of different directionality using a polarized light source and an optical microscope. The acquisition is performed on histological slices after sectioning the specimen. It can fully be made 3D by slightly tilting the slice with respect to the orthogonal plane to the light beam (see Axer et al. 2011 for more details). This imaging modality was considered as a validation tool of dMRI fiber orientation and tractography in Roebroek et al. 2018.

In Figure 8.10, we can observe output images of the Chenonceau brain from 3D PLI and tractography. The selected slice is around the parieto-occipital sulcus, where the precuneus and the cuneus are visible. Each color from either the tractogram or the polarized light image refers to a direction followed by the fibers. The intensity of the colors refers to the local density of white matter bundles. From this single 3D PLI slice, we can appreciate the radial and tangential fibers that populate the isocortex. Subcortical white matter bundles are also demarcated. A striking correspondence in fiber orientation and density stands out between the tractogram shown in Figure 8.10B and the 3D PLI slice presented in Figure 8.10C. The polarized light image has indeed a spatial resolution a hundred times higher than the dMRI-based

tractogram, and yet the diffusion-weighted signal obtained at a mesoscopic scale seems to mirror what can be observed at the microscopic scale. Considering polarized light imaging as ground truth to fiber organization as it was suggested in Roebroek et al. 2018, this resemblance suggests a validation of the designed tractogram to account for the actual fiber architecture in the human brain.

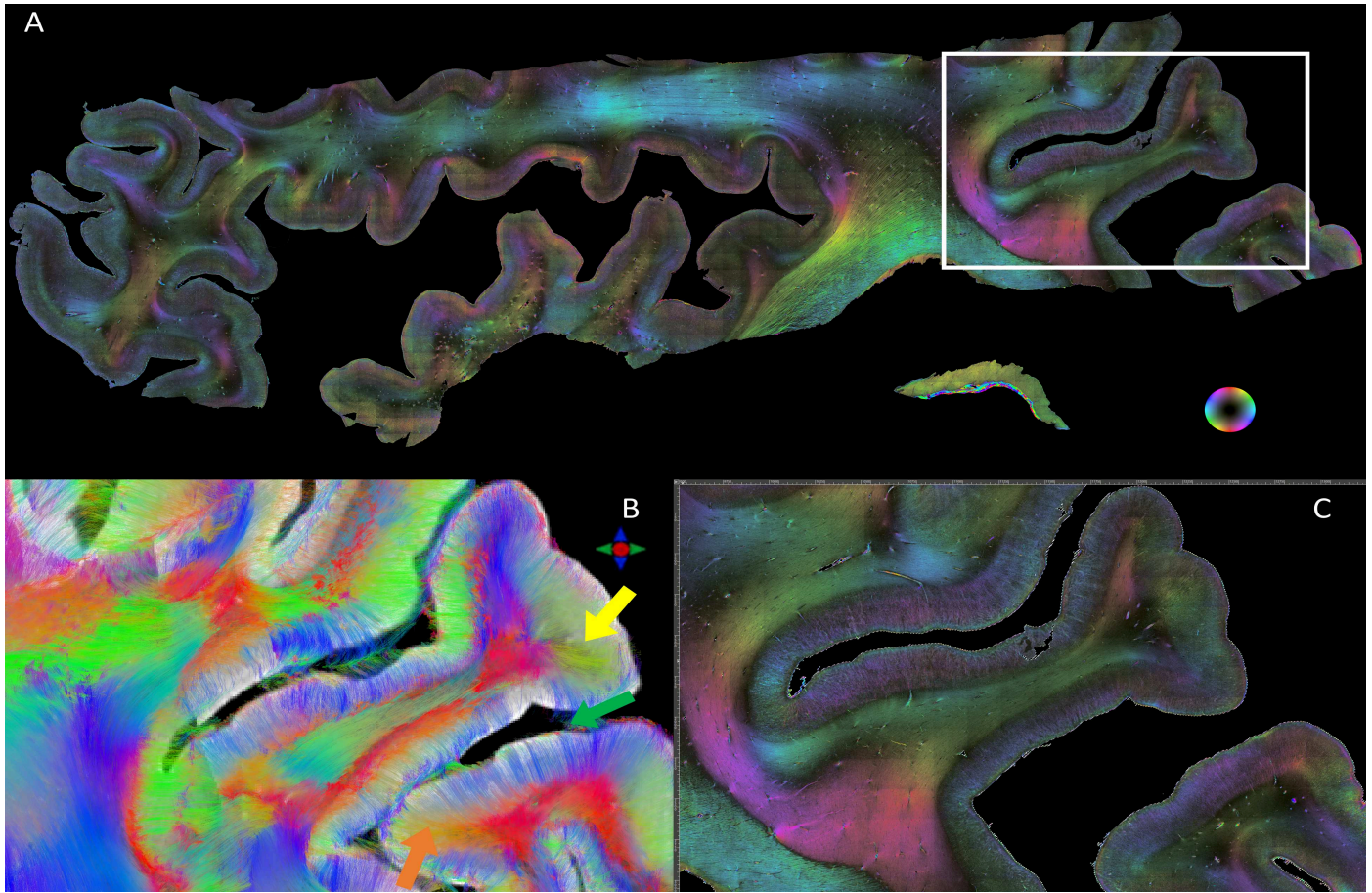


Figure 8.10: Comparison between the tractogram and the 3D polarized light image from a microscopic slice of the Chenonceau brain. (A) 1.3μm in-plane PLI slice that comes from the left-hemisphere block F. (B) Zoom in the connectivity map superimposed on the 200μm  $T_2$ -weighted reference image around the area of the left-hemisphere precuneus (yellow arrow) and cuneus (orange arrow). The parieto-occipital sulcus is likewise visible (green arrow). (C) Zoom in the full 3D PLI slice at the top (white frame) corresponding to the connectogram in (B). 3D polarized light image, courtesy of Axer, Amunts et al., Forschungszentrum, Jülich.

Figure 8.11 is a global presentation of all the imaging modalities and models that were applied for the Chenonceau project so far. The left-hemisphere block F is the chosen example with a special zoom in around the region of the parieto-occipital sulcus. The first line of the figure portrays the three 11.7T  $T_2$ -weighted anatomical MR images at 100μm, 150μm, and 200μm, the color-encoded diffusion direction (CED) map issued from the DTI model, and the corresponding FOV superimposed on the 500μm block-face image. The second line transcripts the 7T relaxometric maps (relative proton density,  $T_1$ ,  $T_2$  and  $T_2^*$ ) and the myelin water fraction (MWF) map. The third line illustrates the  $f_{\text{intra}}$  and  $\kappa$  index maps from the NODDI model, the generalized fractional anisotropy (GFA) map from the aQBI model, the streamline regularized deterministic tractogram and the 3D polarized light image. Therefore, Figure 8.10 offers a comparison of the MR-based images to the 3D polarized light image.

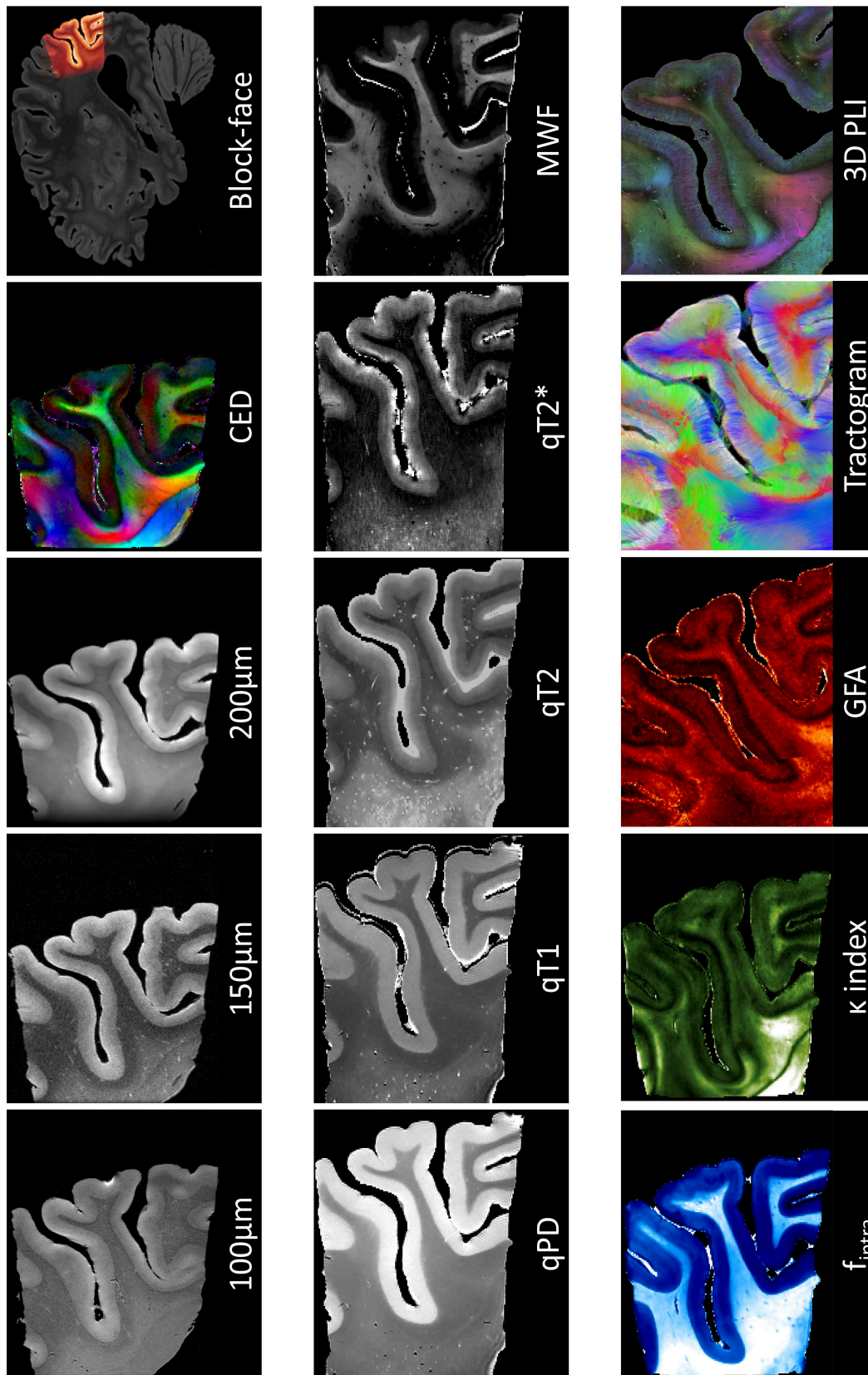


Figure 8.11: Global presentation of all the images and maps issued for the Chenonceau project so far. Images of the first column adapted from Beaujain 2018. 3D PLI image, courtesy of Axer, Amunts et al., Forschungszentrum, Jülich. All remaining images stem from this PhD work.



The high level of coherence between the tractograms obtained on the left-hemisphere block F using dMRI and PLI microscopy is promising and qualitatively assesses the high value of the Chenonceau 11.7T diffusion MRI dataset. Carefulness must remain to see tractography as a reliable tool for characterization of the cortical connectivity due to the existence of false-positives and the density of subcortical white matter beneath the infragranular layers of the cerebral cortex [Reveley et al. 2015; Jones, Alexander, et al. 2018]. This validation requires further quantitative evaluations that will be realized in the coming future. Nonetheless, it has already paved the way to many studies on the inner structural connectivity of the isocortex, which combine segmentation of the cortical layers to propose novel high resolution models of the human structural connectome.

Histology has been revived to compute human brain atlases. Mancini et al. 2020 presents a computational pipeline to design 3D consistent histology reconstructions of the human brain by adding MRI in the process. Nonetheless, as specified in this study, histology has three major issues: distortions of the sample caused by slicing the cerebral tissue, potential inhomogeneous staining in the sections, and the registration if distorted sections are also subject to sectioning artifacts.

The complete cytoarchitectonic atlas proposed in Amunts, Mohlberg, et al. 2020, which also takes part in the Human Brain Project (HBP), is the 3D reconstruction of stacked histological sections of 23 adult human brains. Knowing histology has its own biases and the cortical myeloarchitecture possess specificities that differ from cytoarchitecture, it will be interesting to compare the Jülich-Brain to the Chenonceau brain once its full reconstruction is finished.

## 8.4 Discussion

### 8.4.1 Comparison to existing studies

The automatic segmentation of the cerebral cortex to reveal its cytoarchitecture was discussed since the study of Schleicher et al. 1999. It suggested the use of quantitative data such as density profiles and grey level index to obtain an observer-independent procedure to identify cortical boundaries. Ever since, diffusion-weighted MRI has been the preferred approach to solve the automatic detection of gray matter lamination. In Dyrby, Baaré, et al. 2011, parallel layers were delineated in the cerebral cortex and hippocampus of *ex vivo* pigs using persistent angular structure magnetic resonance imaging (PAS-MRI) to perform multi-fiber reconstruction. We chose to resort to the robustness of high-field HARDI schemes to our study. Kleinnijenhuis, Zhang, et al. 2013 showcased variations of the fractional anisotropy (FA) across the cortical depth for the primary visual cortex at 11.7T. However, DTI-based features are less sensitive to microstructural changes than HARDI-based ones, such as generalized fractional anisotropy (GFA) that was utilized in this thesis.

So far, myelin mapping techniques in cortex on living subjects are meant to parcel into macroscopic myeloarchitectonic areas the cortical ribbon or to investigate the development of the isocortex with age [Edwards et al. 2018]. However, *ex vivo* myelin mapping can go a step further by reaching sufficient SNR and spatio-angular resolution to analyze cortical laminae, as it can be challenging *in vivo* [Trampel et al. 2017]. This thesis work undertook that path by computing myelin water fraction maps of the Chenonceau brain that were useful in creating myelo-clustering maps.

The recent work of Bastiani et al. 2016 also aimed at an automatic segmentation of the human cerebral cortex using high-resolution dMRI data. Despite a 340 $\mu$ m spatial resolution, the study was suffering from partial volume effects especially for the molecular layer I. The Chenonceau dMRI and qMRI dataset at ultra-high field is positioned at an isotropic 200 $\mu$ m spatial resolution evincing as well high angular diffusion resolution (175 directions at  $b=1500/4500/8000$ s/mm<sup>2</sup>)

that seems to alleviate these partial volume effects since layer I was detected in our computed myelo- and layer-clustering maps.

Finally, intracortical connectivity was not fully explored to be able to compare our results to the latest studies [Girard et al. 2020; Shamir et al. 2021]. Further work need to be conducted on that topic to further investigate and map *ex vivo* the cortical laminar connectivity at the mesoscale.

### 8.4.2 Limitations and future improvements

The presented PhD work on the Chenonceau neocortex exhibits some limitations due to the lack of time to fully explore the entire cortical ribbon. Only two cortical regions were investigated to apply the multi-contrast cortical layer clustering algorithm since intensity heterogeneity prevented us to generate complete cortical layer clustering maps without applying an excessive number of clusters. If we had decided to do so, manual corrections would have been mandatory making the clustering algorithm much more operator-dependent that it already is. We indeed chose to apply 10 clusters for the cyto- and myelo-clustering maps, and 15 clusters for the layer-clustering maps. These choices were empirical in order to suppress extraneous intensity values that must come from residual PBS laid on the cerebral cortex. Consequently, there is room for improvement in the Chenonceau images to profit by all the microstructural information they enclose.

In the frame of this thesis, we were unable to investigate the hippocampal allocortex, which is another component of the superficial gray matter, due to a lack of time to pursue this idea. It will be interesting to analyze the added-value of the qMRI data in the studying of the human hippocampus and compare the results to the findings made in Beaujoin et al. 2018.

Furthermore, the sanitary situation prevented us from having enough time to compare the intracortical connectogram to the cyto-clustering, myelo-clustering, and layer-clustering maps of the neocortex. Such a comparison would be pertinent to investigate connectivity in the cortical layers in the same way Amunts and Zilles 2015 did present that both cytoarchitecture and myeloarchitecture reflect different aspects of connectivity.

Cutting the Chenonceau brain to collect the anatomical, diffusion and quantitative MRI data obviously entailed slight brain tissue losses that would have not occurred if the brain had not been sliced. In Kim, Sakaie, et al. 2021, four complete adult human brains were scanned *ex vivo* with a 170 $\mu$ m isotropic resolution. However, the study was limited to anatomical imaging and required three coronal slabs to fully cover the specimen. The study of Sébille et al. 2019 consisted in acquired diffusion-weighted data at ultra-high field (11.7T) of a *ex vivo* macaque brain. The acquisition performance relied on Gadolinium-soaking to reduce  $T_1$  values and improve SNR. Such a protocol could have not been applied on the Chenonceau brain due to the cutting procedure that may have undermined Gadolinium-soaking, plus  $T_1$  relaxometry would have been precluded by the modification of the actual  $T_1$  values in the cerebral cortex. Besides,  $T_1$  relaxation time remained stable along the 7T acquisition campaign as well as the  $T_1$  contrast. The fixation process for the Chenonceau brain must have delayed or suppressed the reduced differences between  $T_1$  and  $T_2$  values.

The brain cutting may have been a risky strategy to compose the unique 7T and 11.7T MRI dataset after two years of dual acquisition campaigns, but it seems to have paid off by the richness of the acquired data that pave the way to better understand the human ultrastructure. A major issue that remains on the Chenonceau dataset is its intensity heterogeneity that impacted the results of the reconstructed quantitative maps. Simple corrections will be performed in the coming future to make the most of the 7T and 11.7T MRI dataset.

Waehnert et al. 2014 realized the modeling of cortical laminae by computing 20 intracortical laminae. This approach

would be pertinent using the unique dMRI and qMRI Chenonceau dataset, however this work was out of the scope of this PhD thesis. It would be the motivation of the PhD work of Anas Bachiri, member of the Ginkgo team.

Recently, optical coherence tomography (OCT) was used to quantitatively measure myelin content and neuron density in the human brain [Chang et al. 2021]. This imaging modality was suggested in Roebroek et al. 2018 to validate dMRI-based tractography and collected cytoarchitectural and myeloarchitectural information. Comparison to histology showed a linear relationship with the myelin content across different regions of the human brain, while the neuron density only slightly modulate the overall tissue scattering properties. We could then consider OCT to validate the 7T quantitative Chenonceau dataset to observe any correlation with OCT studies conducted on the Chenonceau brain. Such a possibility could only enhance the usefulness of the Chenonceau qMRI dataset.

## 8.5 Conclusion

This final chapter detailed the state of the art regarding the automated methods to discriminate cortical layers in the human cerebral cortex. The issue is well addressed for the basal ganglia that have a simpler structure than the cerebral cortex, but the challenge remains for the latter. We described here our approach to automatically segment the isocortex of the Chenonceau brain that resulted in three types of maps: a cyto-clustering map, a myelo-clustering map and a layer-clustering map that combines cytoarchitectural and myeloarchitectural information. We likewise described the exploration of the cortico-cortical connectivity in the Chenonceau neocortex and correlated our findings with the 3D polarized light imaging histological section of the same brain sample. The matching in fiber architecture for the two distinct MR imaging modalities is promising for further quantitative validation of our Chenonceau 11.7T dMRI dataset and subsequent tractogram. Similar validation could be undertaken for the Chenonceau 7T qMRI dataset with the gold standard histological validation or with more recent techniques such as optical coherence tomography.

# Chapter 9

## Conclusion

### 9.1 Conclusion and contributions

The principal goal of this thesis was to investigate the structural connectivity, the cytoarchitecture and the myeloarchitecture of *ex vivo* animal and human brains at the mesoscopic scale. Anatomical, diffusion and quantitative magnetic resonance imaging at ultra-high field was here the exclusive combination of imaging modalities to achieve that goal. The contributions of all MRI sequences were put on an equal footing to make the most of the information they were providing to establish proxies of these cartographies. The main point was to highlight the possibility of collecting microstructural information on complete *ex vivo* animal or human brains with an imposed spatial resolution: the mesoscale. This thesis sets precedent to future *ex vivo* or *in vivo* studies of the cerebral tissue microstructure at the mesoscopic scale. The main contributions of this work are summarized hereafter.

#### 9.1.1 Structural connectivity atlas of the Japanese quail

A first structural connectivity atlas of the Japanese quail (*Coturnix japonica*) was designed from diffusion-weighted and anatomical MRI acquisitions at 11.7T on a cohort of 21 subjects. The atlas exhibits a 200 $\mu$ m isotropic resolution and is composed of 34 labeled white matter bundles that reflect the structural connectivity of the two lines of quails scanned in this study: the short tonic immobility (STI) and the long tonic immobility (LTI) quails. Analyses of diffusion-based features along the white matter bundles revealed differences in the connectivity patterns characterizing the two lines, which are divergent on their emotionality trait. Results pave the way to a better understanding of the link between behaviors and the underlying anatomical substrates. This work was submitted to the journal *Brain Structure and Function* (see Appendix A) and is currently under review.

### 9.1.2 Structural connectivity of wildlife animals

The structural connectivities of eight animals that lived in the ZooParc de Beauval (Beauval zoo, Saint-Aignan, France) were investigated with a similar approach to the one used for the Japanese quails to compare their socio-emotional circuits that dictate their behaviors. The key idea was to analyze commonalities and differences between preys and predators among the scanned postmortem specimens. Anatomical and diffusion-weighted MRI sequences were applied at ultra-high field to settle mesoscopic datasets. Tractography approaches and clustering methods were used to stand out typical white matter bundles such as the corpus callosum or the corticospinal tract. An emphasis was put on the California sea lion to illustrate the scope of brain exploration that offers the anatomical and diffusion MRI dataset. This work has established the methodological bases to provide a robust approach in order to map the structural connectivity of all animals. It is now requiring a collaborative work with biologists and ethologists to investigate the functional circuits of interest.

### 9.1.3 Inference of the cytoarchitecture and myeloarchitecture of the human cortical ribbon

As part of HBP, the Chenonceau project aimed at designing a mesoscopic atlas of the *ex vivo* human brain using UHF MRI. It is in that objective that two parallel acquisition campaigns were performed for two years on two preclinical MRI systems: one at 7T for quantitative MRI, and the other at 11.7T for anatomical and diffusion-weighted MRI. The substantial amount of data led to a unique dataset that offers multiple MR contrasts at 100 $\mu$ m, 150 $\mu$ m, and 200 $\mu$ m isotropic resolutions. These contrasts allowed the quantitative mapping of  $T_1$ ,  $T_2$  and  $T_2^*$  relaxation times, myelin water fraction (MWF), and proxies of neurites using the NODDI model. Dedicated pre- and post-processing pipelines on the whole brain specimen were developed and made available on the Ginkgo toolbox <https://framagit.org/coupon/gkg>.

The unique diffusion and quantitative MRI dataset acquired at mesoscopic resolution on the Chenonceau brain paves the way to exploring the human cerebral cortex with a level of detail never achieved before in magnetic resonance imaging. In particular, it has been possible to accomplish a fine segmentation of the cortical ribbon by combining the various imaging modalities available, and by exploiting the additional information provided by diffusion MRI on the cytoarchitectonic side and by the quantitative MRI on the myeloarchitectonic side. The exploitation of this extensive dataset through the use of clustering methods has thus made it possible to study the laminar structure of the Chenonceau neocortex. Last, advanced tractography techniques has offered the possibility to better understand the structural intracortical connectivity. This work is under preparation for publication.

### 9.1.4 Contributions of this thesis

**The Neuro2Co project** It is a French project directed by Dr E. Chaillou (Unité de Physiologie de la Reproduction et des Comportements, INRAE, CNRS, IFCE, Université de Tours, Nouzilly, France) that firstly aims at investigating the socio-emotional circuits in two types of animal models: breeding and wildlife animals. The anatomical and diffusion-weighted MRI acquisitions performed during this thesis at ultra-high field on nine animal species constitute a unique and diverse dataset. The latter is meant to correlate structural connectivity, with cognitive functions and ethological observations. This PhD work has so far enabled the design of the first structural connectivity atlas of the Japanese quail. It has likewise set the methodological bases to explore the structural connectivity of any animal brain in order to access its socio-emotional circuit and improve animal well-being.

Secondly, the project fosters the transmission of neuroscientific knowledge to middle school students eager to discover neuroscience. The project was funded by the Centre-Val de Loire regional council. Researchers, PhD students and teachers collaborate to facilitate the learning of software used by the neuroscientific community to analyze MR images. This thesis work contributed in providing MR images of Japanese quails and wildlife animals from the ZooParc de Beauval on which the students could train on. Teaching sessions were likewise organized to present the work progress to the students and collaborators of the project.

**The European Human Brain Project (HBP)** It is a large European flagship project aiming at the establishment of a multimodal, multiscale atlas of the human brain, from the microscale to the macroscale, involving more than a hundred of landmark institutions in the fields of neuroscience, neuroimaging, biology, clinics and computer science. This ten-year long project that began in 2013 involves European research centers in order to investigate the singularity of the human brain, to advance therapeutic solutions for brain diseases, and to develop state-of-the-art neuromorphic computers. This thesis work is part of the HBP contributed to enrich the HBP Human Brain Atlas with postmortem mesoscopic anatomical, quantitative and diffusion MRI data acquired throughout the Chenonceau project.

**The FibrAtlasII-III project** It is a French ANR project conducted by Pr C. Destrieux (INSERM iBrain U1253 unit, CHU Bretonneau, Faculté de Médecine de Tours, France) in partnership with the NeuroSpin/BAOBAB/Ginkgo research team. The project aims at validating tractography approaches via the MRI acquisition campaign of senior healthy volunteers. The participants agreed to give their bodies to science. That way, their brains were scanned *in vivo* using magnetic resonance imaging, then Klingler's dissection was performed on the same *ex vivo* brains once the participants have passed away.

The Chenonceau project, and by extension this thesis work, takes part of the FibrAtlasII-III project. The resulting dMRI dataset led to the structural connectivity map of the Chenonceau brain which provides insights to accurately investigate the connectivity of the scanned and dissected brains partaking in the FibrAtlasII-III project.

## 9.2 Upcoming work

The forthcoming work on the Chenonceau atlas address two further challenges:

- establishing a mesoscopic structural connectome using the mesoscopic Chenonceau 11.7T anatomical and diffusion MRI dataset to develop a novel AI-based global tractography method with anatomical and microstructural constraints. This question is covered by the PhD work of Alexandros Popov.
- going beyond the conventional analytical models, such as NODDI, DTI, CSD and aQBI, to extract orientational and cytoarchitectural information from dMRI. The selected approach consists in using large scale simulations with machine learning to devise novel realistic computational models able to better decode the brain tissue ultrastructure. This issue is handled by two PhD work. On the one hand, the work of Alexis Brullé is focused on the modeling of white matter microstructure. On the other hand, the work of Anas Bachiri deals with the cortex cytoarchitecture.

### 9.2.1 Towards a mesoscopic structural connectome of the Chenonceau atlas

Several examples of fiber inference were given in the frame of this thesis, to illustrate the richness of the Chenonceau diffusion MRI dataset to investigate its structural connectivity and tissue ultrastructure. The current methods used to perform fiber tracking were based on conventional deterministic and probabilistic streamlining approaches known to lack robustness and to generate many false positiveness. Despite the very high spatial and angular resolutions reached at 11.7T with 780mT/m gradient magnitudes significantly improves the situation, the blind principle of streamline reconstructions undoubtedly suffers from much limitations at this fine scale.

Global spin-glass-based approaches have already been proposed by the research team to investigate the structural connectivity and tissue ultrastructure of the human brain [Teillac et al. 2017]. The inference of the global set of connections from ODFs maps is by essence an ill-posed problem that requires the use of a global framework to obtain an optimal solution. This can be achieved by designing a Markovian framework that would rely on the representation of fibers as connected spin-glasses. Their positions and orientations stem from the optimization of a global energy associated to the whole set of spins. Such a spin-glass-based Markovian framework allows it to generate the set of connections in a competitive process. Therefore, the global coherence of the entire set of reconstructed fibers is preserved, unlike the streamlining approaches that generate fibers independently. Moreover, the Markovian framework facilitates the addition of further regularization constraints to better take into account anatomical and microstructural information. That way, it precludes solutions corresponding to local minimum of the global energy. Regarding the Chenonceau mesoscopic dataset, a major challenge is linked to the massive amount of data, hundreds of Gigabytes, that entails using a non-standard workstation to process the data. Conventional solutions would take years to process the unprecedented spatial resolution of the Chenonceau dataset, whereas it would only take a day for a millimeter dMRI dataset. Consequently, high performance computing approaches are mandatory to address that challenge.

Furthermore, energy minimization is currently performed using a Metropolis-Hastings algorithm. Nonetheless, this optimization framework is worth being replaced by novel approaches that would stem from artificial intelligence, for instance reinforcement learning. This approach is currently investigated by the PhD work of Alexandros Popov. The study is conducted in the frame of the joint French-German AIDAS institute created by CEA and the Forschungszentrum Jülich.

### 9.2.2 Towards new computational models of tissue ultrastructure

Up to recently, the modeling of local diffusion process was exclusively relying on the design of analytical models. Most ODF reconstruction algorithms utilize the decomposition of the diffusion NMR signal into adequate orthogonal function basis. Thus, the computation of impulse responses of white matter bundles involved in the water diffusion process is facilitated. It also allows to efficiently deconvolve the acquired diffusion NMR signal attenuation to get the orientational profile of the propagator. Similarly, existing microstructural models providing insight about the tissue cytoarchitecture rely on multi-compartmental models. The latter assume no exchange between compartments to get analytical close forms of the contribution corresponding to each compartment. The modeling scheme uses standard functions on the sphere such as Watson's distribution. The main drawback of ODF and microstructural analytical models is the lack of resolution. There is indeed no solution to the diffusion, or heat, equation out of simple geometries including spheres, cylinders and ellipsoids. Fibers and cells are usually represented by oversimplified geometry shapes. That strategy turns to drastically reduce the ability of the diffusion analytical models to represent the complexity of the local tissue configurations.

New models have recently been introduced to go beyond these limitations. The Ginkgo research team has released a

new framework, MEDUSA [Ginsburger et al. 2019], relying on large-scale simulations to model cellular environments allowing to represent cell membranes with realistic geometric shapes. The goal is to simulate the diffusion process of water molecules using Monte-Carlo simulations, and to simulate as well the attenuation of the diffusion NMR signal for any type of diffusion sequence: PGSE, OGSE, b-tensor, etc. The novel framework requires the use of high performance computing facilities to create sizeable dictionaries of realistic virtual brain samples together with their diffusion NMR signature. MEDUSA paves the way to the design of computational models of tissue microstructure using machine or deep learning tools. We believe that such approaches may offer more suitable frameworks to develop immersive models able to map finer details of the tissue ultrastructure.

Two PhD theses have started on that topic:

- a thesis targeting the development of a computational model of white matter microstructure by Alexis Brullé.
- a thesis focused on the development of a computational model of cortex cytoarchitecture by Anas Bachiri.

It is likely that a computational model of the cortex cytoarchitecture containing robust information of the geometric details regarding the cortical cell populations would enhance the cytoarchitectural mapping of cortical layers and areas. This is a promising approach to further investigate the abundant information embedded in the Chenonceau 11.7T MRI dataset.

### 9.2.3 On the importance of validating computational models

The design of computational models of tissue microstructure requires validation to assess the ability of the method to deliver reliable measures. This strategy involves the use of alternative modalities and immunohistochemistry seems to be the most appropriate modality to achieve this goal. To this aim, a new consortium has been created in the frame of *Simulation Numérique* collaborative translational program (PTC). It is funded by CEA and gathers the NeuroSpin/BAOBAB/Ginkgo team, the Laboratoire des Maladies Neurodégénératives (Dr T. Delzescaux and Dr C. Jan, Université Paris-Saclay, CEA, CNRS, MIRCen, Fontenay-aux-Roses, France), the INSERM U1253 iBrain unit (Pr C. Destrieux, Service des Dons du Corps, CHU Bretonneau, Faculté de Médecine de Tours, France), and the CEA/TGCC team.

The project will involve the analyses of multiple small samples of the adult human cerebral cortex (1 cmx1 cmx1 cm) using different stainings to tag somas, astrocytes, microglia and myelin. The protocol will produce 3D histological images of the brain samples with a spatial resolution close to 5 $\mu$ m. From these histological images, the neurons will be individually segmented [You 2015; You et al. 2019] and a deep learning algorithm will provide morphological information on the segmented cell population: number, mean radius, or even orientation.

These valuable data will be important input to the MEDUSA simulator, complementary to literature, for creating realistic cortical tissue phantoms.





# Appendix A

## Communications

### Journal publications

- R. Yebga Hot, M. Siwiaszczyk, I. Uszynski, S.A. Love, F. Andersson, L. Calandreau, F. Poupon, J. Beaujoin, B. Herlin, F. Boumezbeur, B. Mulot, E. Chaillou, C. Poupon, Characterization of the emotionality trait of the Japanese quail using ultra-high field diffusion MRI and connectivity mapping at 11.7T - Submitted to *Brain Structure and Function*
- M. Siwiaszczyk, R. Yebga Hot, M. Morisse, L. Calandreau, D. Barrière, J. Beaujoin, B. Mulot, F. Andersson, C. Poupon, S. Love, E. Chaillou, Quail (*Coturnix japonica*) brain MRI template and whole-brain atlas, doi: <https://doi.org/10.5281/zenodo.4700523>

### Conference publications

- A. Popov, R. Yebga Hot, J. Beaujoin, I. Uszynski, F. Boumezbeur, F. Poupon, C. Destrieux, C. Poupon, CHENON-CEAU: An entire ex vivo human brain 11.7T anatomical and diffusion MRI dataset at the mesoscopic scale. Abstract #1596. *Organization for Human Brain Mapping (2021)* - Poster presentation
- A. Popov, R. Yebga Hot, J. Beaujoin, I. Uszynski, F. Boumezbeur, F. Poupon, C. Destrieux, C. Poupon, Chenon-ceau: An entire ex vivo human brain 11.7T anatomical and diffusion MRI dataset at the mesoscopic scale. Abstract #0214. *International Society for Magnetic Resonance in Medicine (2021)* - Oral presentation (*Summa cum laude*)
- R. Yebga Hot, A. Popov, J. Beaujoin, G. Perez, F. Poupon, J.-F. Mangin, I. Lima Maldonado, C. Destrieux, C. Poupon, *Ex vivo* mapping of the cyto- and the myeloarchitecture of the human cerebral cortex using ultra-high field MRI (7T and 11.7T). Abstract #L01.74. *European Society for Magnetic Resonance in Medicine (2020)* - Poster and oral presentations
- R. Yebga Hot, A. Popov, J. Beaujoin, G. Perez, F. Poupon, J.-F. Mangin, I. Lima Maldonado, C. Destrieux, C. Poupon, *Ex vivo* mapping of the cyto- and myeloarchitecture of the human cerebral cortex using UHF MRI. Abstract #1770. *Organization for Human Brain Mapping (2020)* - Poster presentation

- R. Yebga Hot, A. Popov, J. Beaujoin, G. Perez, F. Poupon, J.-F. Mangin, I. Lima Maldonado, C. Destrieux, C. Poupon, *Ex vivo* mapping of the cyto- and the myeloarchitecture of the human cerebral cortex using ultra-high field MRI (7T and 11.7T). Abstract #3777. *International Society for Magnetic Resonance in Medicine (2020)* - Poster presentation
- R. Yebga Hot, A. Popov, J. Beaujoin, G. Perez, F. Poupon, I. Lima Maldonado, J.-F. Mangin, C. Destrieux, C. Poupon, *Ex vivo* mapping of the cyto- and myeloarchitecture of the human cerebral cortex using ultra-high field MRI. *Journées jeunes chercheurs Société Française de Physique Médicale / Groupement de Recherche Mi2b (2019)* - Oral presentation
- J. Beaujoin, A. Popov, R. Yebga Hot, F. Poupon, J.-F. Mangin, C. Destrieux, C. Poupon, CHENONCEAU: towards a novel mesoscopic (100/200 $\mu$ m) post-mortem human brain MRI atlas at 11.7T. Abstract #Th671. *Organization for Human Brain Mapping (2019)* - Poster presentation
- R. Yebga Hot, M. Siwiaszczyk, J. Beaujoin, D.A. Barrière, I. Uszynski, S.A. Love, L. Calandreau, B. Mulot, E. Chaillou, C. Poupon, A novel 11.7T ultra-high field diffusion MRI structural connectivity atlas of the Japanese quail. Abstract #Th749. *Organization for Human Brain Mapping (2019)* - Poster presentation
- J. Beaujoin, A. Popov, R. Yebga Hot, F. Poupon, J.-F. Mangin, C. Destrieux, C. Poupon, CHENONCEAU: towards a novel mesoscopic (100/200 $\mu$ m) post mortem human brain MRI atlas at 11.7T. Abstract #0654. *International Society for Magnetic Resonance in Medicine (2019)* - Oral presentation (*Summa cum laude*)
- R. Yebga Hot, M. Siwiaszczyk, J. Beaujoin, D.A. Barrière, I. Uszynski, S.A. Love, L. Calandreau, B. Mulot, E. Chaillou, C. Poupon, A novel 11.7T ultra-high field dMRI connectivity atlas of the Japanese quail. Abstract #0995. *International Society for Magnetic Resonance in Medicine (2019)* - Oral presentation
- M. Siwiaszczyk, R. Yebga Hot, C. Poupon, L. Calandreau, B. Mulot, S.A. Love, E. Chaillou, Impact de la sélection d'un comportement de peur sur l'anatomie de l'encéphale de caille. Utilisation de l'imagerie par résonance magnétique (IRM) ex vivo. Abstract #hal-02786926. *31e Colloque Biotechnocentre (2018)* - Poster presentation

# Bibliography

- Gennari, F. (1782).** *De peculiari structura cerebri nonnullisque ejus morbis.* Google-Books-ID: z2NEAAAACAAJ. Ex Regio Typographeo. 120 pp. (Cited on page 31).
- Baillarger, J. G. F. (1840).** *Recherches sur la structure de la couche corticale des circonvolutions du cerveau.* chez J.-B. Baillière (Cited on page 31).
- Vogt, O. and Vogt, C. (1903).** “Zur anatomischen Gliederung des Cortex cerebri”. In: *J Psychol Neurol* 2.4, pp. 160–180 (Cited on pages 34, 37).
- Campbell, A. (1905).** *Histological studies on the localization of cerebral function.* Histological studies on the localization of cerebral function. Pages: Pp. 360. Oxford, England: Univ. Press. Pp. 360 (Cited on page 37).
- Elliot Smith, G. (1907).** “A New Topographical Survey of the Human Cerebral Cortex, being an Account of the Distribution of the Anatomically Distinct Cortical Areas and their Relationship to the Cerebral Sulci”. In: *Journal of Anatomy and Physiology* 41 (Pt 4), pp. 237–254 (Cited on page 37).
- Brodmann, K. (1909).** *Vergleichende Lokalisationslehre der Grosshirnrinde in ihren Prinzipien dargestellt auf Grund des Zellenbaues.* In collab. with Wellcome Library. Leipzig : Barth. 346 pp. (Cited on page 13).
- Cajal, S. R. (1911).** “Histologie du systeme nerveux de l’Homme et des verte be s.” In: *Maloine (Paris)* 2, pp. 891–942 (Cited on page 81).
- Vogt, C. and Vogt, O. (1919).** “Allgemeinere Ergebnisse unserer Hirnforschung”. In: *J Psychol Neurol (Leipz)* 25, pp. 279–468 (Cited on pages 28, 31, 37).
- Economo, C. von and Koskinas, G. N. (1925).** *Die cytoarchitektonik der hirnrinde des erwachsenen menschen,* OCLC: 14723058. Wien und Berlin: J. Springer (Cited on page 37).
- Frisch, R. and Stern, O. (1933).** “Über die magnetische Ablenkung von Wasserstoffmolekülen und das magnetische Moment des Protons. I”. In: *Springer* 85.2, pp. 4–16 (Cited on page 47).
- Klingler, J. (1935).** *Erleichterung der makroskopischen Präparation des Gehirns durch den Gefrierprozess.* Orell Füssli (Cited on page 81).
- Rabi, I. I., Zacharias, J. R., Millman, S., and Kusch, P. (1938).** “A New Method of Measuring Nuclear Magnetic Moment”. In: *Physical Review* 53.4. Publisher: American Physical Society, pp. 318–318 (Cited on page 47).
- Bloch, F. (1946).** “Nuclear Induction”. In: *Physical Review* 70.7. Publisher: American Physical Society, pp. 460–474 (Cited on pages 47, 49).
- Purcell, E. M., Torrey, H. C., and Pound, R. V. (1946).** “Resonance Absorption by Nuclear Magnetic Moments in a Solid”. In: *Physical Review* 69.1. Publisher: American Physical Society, pp. 37–38 (Cited on page 47).
- Hahn, E. L. (1950).** “Spin Echoes”. In: *Physical Review* 80.4. Publisher: American Physical Society, pp. 580–594 (Cited on page 52).
- Potts, R. B. (1952).** “Some generalized order-disorder transformations”. In: *Mathematical Proceedings of the Cambridge Philosophical Society* 48.1. Publisher: Cambridge University Press, pp. 106–109 (Cited on pages 156, 157).

- Carr, H. Y. and Purcell, E. M. (1954).** "Effects of Diffusion on Free Precession in Nuclear Magnetic Resonance Experiments". In: *Physical Review* 94.3. Publisher: American Physical Society, pp. 630–638 (Cited on page 69).
- Stämpfli, R. (1954).** "A new method for measuring membrane potentials with external electrodes". In: *Experientia* 10.12, pp. 508–509 (Cited on page 20).
- Jerison, H. J. (1955).** "Brain to Body Ratios and the Evolution of Intelligence". In: *Science* 121.3144. Publisher: American Association for the Advancement of Science, pp. 447–449 (Cited on page 119).
- Torrey, H. C. (1956).** "Bloch Equations with Diffusion Terms". In: *Physical Review* 104.3. Publisher: American Physical Society, pp. 563–565 (Cited on page 58).
- Mountcastle, V. B. (1957).** "Modality and topographic properties of single neurons of cat's somatic sensory cortex". In: *Journal of Neurophysiology* 20.4. Publisher: American Physiological Society, pp. 408–434 (Cited on page 30).
- Carr, H. Y. (1958).** "Steady-State Free Precession in Nuclear Magnetic Resonance". In: *Physical Review* 112.5. Publisher: American Physical Society, pp. 1693–1701 (Cited on page 61).
- Meiboom, S. and Gill, D. (1958).** "Modified Spin-Echo Method for Measuring Nuclear Relaxation Times". In: *Review of Scientific Instruments* 29.8. Publisher: American Institute of Physics, pp. 688–691 (Cited on page 69).
- Klingler, J. and Gloor, P. (1960).** "The connections of the amygdala and of the anterior temporal cortex in the human brain". In: *Journal of Comparative Neurology* 115.3, pp. 333–369 (Cited on page 81).
- Wilson, W. O., Abbott, U. K., and Abplanalp, H. (1961).** "Evaluation of Coturnix (Japanese Quail) as Pilot Animal for Poultry". In: *Poultry Science* 40.3, pp. 651–657 (Cited on page 76).
- Hodgkin, A. L. (1964).** "conduction of the nervous impulse". In: Publisher: Liverpool University Press (Cited on page 20).
- Phillips, R. E. (1964).** "'Wildness' in the Mallard duck: Effects of brain lesions and stimulation on 'escape behavior' and reproduction". In: *Journal of Comparative Neurology* 122.2. \_eprint: <https://onlinelibrary.wiley.com/doi/pdf/10.1002/cne.9012202> pp. 139–155 (Cited on page 105).
- Stejskal, E. O. and Tanner, J. E. (1965).** "Spin Diffusion Measurements: Spin Echoes in the Presence of a Time-Dependent Field Gradient". In: *The Journal of Chemical Physics* 42.1. Publisher: American Institute of Physics, pp. 288–292 (Cited on page 58).
- Ernst, R. R. and Anderson, W. A. (1966).** "Application of Fourier Transform Spectroscopy to Magnetic Resonance". In: *Review of Scientific Instruments* 37.1. Publisher: American Institute of Physics, pp. 93–102 (Cited on page 53).
- Karten, H. J. and Hodos, W. (1967).** *A stereotaxic atlas of the brain of the pigeon (Columba livia) by Harvey J. Karten and William Hodos.* OCLC: 38230345. Baltimore: Johns Hopkins Press (Cited on page 80).
- Look, D. C. and Locker, D. R. (1970).** "Time Saving in Measurement of NMR and EPR Relaxation Times". In: *Review of Scientific Instruments* 41.2. Publisher: American Institute of Physics, pp. 250–251 (Cited on page 69).
- Lauterbur, P. C. (1973).** "Image Formation by Induced Local Interactions: Examples Employing Nuclear Magnetic Resonance". In: *Nature* 242.5394. Number: 5394 Publisher: Nature Publishing Group, pp. 190–191 (Cited on page 47).
- Gallup, G. G. (1977).** "Tonic Immobility: the Role of Fear and Predation". In: *The Psychological Record* 27.1, pp. 41–61 (Cited on page 77).
- Mansfield, P. (1977).** "Multi-planar image formation using NMR spin echoes". In: *Journal of Physics C: Solid State Physics* 10.3. Publisher: IOP Publishing, pp. L55–L58 (Cited on pages 47, 61).
- Bilo, D. (1978).** "Wind stimuli control vestibular and optokinetic reflexes in the pigeon." In: (Cited on page 98).
- Jacobson, M. and Hirose, G. (1978).** "Origin of the retina from both sides of the embryonic brain: a contribution to the problem of crossing at the optic chiasma". In: *Science* 202.4368. Publisher: American Association for the Advancement of Science Section: Reports, pp. 637–639 (Cited on page 9).

- Galaburda, A. and Sanides, F. (1980).** "Cytoarchitectonic organization of the human auditory cortex". In: *Journal of Comparative Neurology* 190.3, pp. 597–610 (Cited on page 37).
- Duvernoy, H. M., Delon, S., and Vannson, J. L. (1981).** "Cortical blood vessels of the human brain". In: *Brain Research Bulletin* 7.5, pp. 519–579 (Cited on pages 39, 41, 43).
- Jacob, J. and Ziswiler, V. (1982).** "The uropygial gland. In: Farner DS, King JR, Parkes KC (eds). *Avian Biology*". In: *Academic press, New-York* 6, pp. 199–324 (Cited on page 78).
- Kuenzel, W. J. (1982).** "Transient aphagia produced following bilateral destruction of the lateral hypothalamic area and quinto-frontal tract of chicks". In: *Physiology & Behavior* 28.2, pp. 237–244 (Cited on page 98).
- Wu, F. Y. (1982).** "The Potts model". In: *Reviews of Modern Physics* 54.1, pp. 235–268 (Cited on pages 156, 157).
- Thickman, D. I., Kundel, H. L., and Wolf, G. (1983).** "Nuclear magnetic resonance characteristics of fresh and fixed tissue: the effect of elapsed time." In: *Radiology* 148.1, pp. 183–185 (Cited on page 78).
- Ehrlich, D. and Mills, D. (1985).** "Myelogenesis and estimation of the number of axons in the anterior commissure of the chick (*Gallus gallus*)". In: *Cell and Tissue Research* 239.3, pp. 661–666 (Cited on page 98).
- Phillips, R. E. and Youngren, O. M. (1986).** "Unilateral kainic acid lesions reveal dominance of right archistriatum in avian fear behavior". In: *Brain Research* 377.2, pp. 216–220 (Cited on page 105).
- Savage-Rumbaugh, S., McDonald, K., Sevcik, R. A., Hopkins, W. D., and Rubert, E. (1986).** "Spontaneous symbol acquisition and communicative use by pygmy chimpanzees (*Pan paniscus*)". In: *Journal of Experimental Psychology: General* 115.3. Place: US Publisher: American Psychological Association, pp. 211–235 (Cited on page 75).
- Beach, T. G., Tago, H., Nagai, T., Kimura, H., McGeer, P. L., and McGeer, E. G. (1987).** "Perfusion-fixation of the human brain for immunohistochemistry: comparison with immersion-fixation". In: *Journal of Neuroscience Methods* 19.3, pp. 183–192 (Cited on pages 55, 134).
- Hukkanen, V. and R oytt , M. (1987).** "Autolytic changes of human white matter: An electron microscopic and electrophoretic study". In: *Experimental and Molecular Pathology* 46.1, pp. 31–39 (Cited on page 54).
- Wang, H. Z., Riederer, S. J., and Lee, J. N. (1987).** "Optimizing the precision in T1 relaxation estimation using limited flip angles". In: *Magnetic Resonance in Medicine* 5.5. \_eprint: <https://onlinelibrary.wiley.com/doi/pdf/10.1002/mrm.1910050502>, pp. 399–416 (Cited on page 69).
- Kuenzel, W. J. and Masson, M. (1988).** *A stereotaxic atlas of the brain of the chick (Gallus domesticus)*. Johns Hopkins University Press (Cited on page 80).
- Le Bihan, D., Delannoy, J., and Levin, R. L. (1989).** "Temperature mapping with MR imaging of molecular diffusion: application to hyperthermia." In: *Radiology* 171.3. Publisher: Radiological Society of North America, pp. 853–857 (Cited on page 56).
- Clarke, S. and Miklossy, J. (1990).** "Occipital cortex in man: Organization of callosal connections, related myelo- and cytoarchitecture, and putative boundaries of functional visual areas". In: *Journal of Comparative Neurology* 298.2, pp. 188–214 (Cited on page 37).
- Koenig, S. H., Brown, R. D., Spiller, M., and Lundbom, N. (1990).** "Relaxometry of brain: Why white matter appears bright in MRI". In: *Magnetic Resonance in Medicine* 14.3, pp. 482–495 (Cited on page 152).
- Abeles, M. (1991).** *Corticonics: Neural Circuits of the Cerebral Cortex*. Google-Books-ID: v46SDOLJrLcC. Cambridge University Press. 298 pp. (Cited on page 34).
- Jones, R. B., Mills, A. D., and Faure, J. M. (1991).** "Genetic and experiential manipulation of fear-related behavior in Japanese quail chicks (*Coturnix coturnix japonica*)". In: *Journal of Comparative Psychology (Washington, D.C.:* 1983) 105.1, pp. 15–24 (Cited on page 76).

- Mills, A. D. and Faure, J. M. (1991).** "Divergent selection for duration of tonic immobility and social reinstatement behavior in Japanese quail (*Coturnix coturnix japonica*) chicks". In: *Journal of Comparative Psychology (Washington, D.C.: 1983)* 105.1, pp. 25–38 (Cited on page 76).
- Vallortigara, G. and Andrew, R. J. (1991).** "Lateralization of response by chicks to change in a model partner". In: *Animal Behaviour* 41.2, pp. 187–194 (Cited on page 103).
- Le Bihan, D., Turner, R., Douek, P., and Patronas, N. (1992).** "Diffusion MR imaging: clinical applications." In: *American Journal of Roentgenology* 159.3. Publisher: American Roentgen Ray Society, pp. 591–599 (Cited on page 67).
- Tovi, M. and Ericsson, A. (1992).** "Measurements of T1 and T2 over time in formalin-fixed human whole-brain specimens". In: *Acta Radiologica (Stockholm, Sweden: 1987)* 33.5, pp. 400–404 (Cited on page 56).
- Buxton, R. B. (1993).** "The diffusion sensitivity of fast steady-state free precession imaging". In: *Magnetic Resonance in Medicine* 29.2. \_eprint: <https://onlinelibrary.wiley.com/doi/pdf/10.1002/mrm.1910290212>, pp. 235–243 (Cited on page 61).
- Callaghan, P. T. (1993).** *Principles of Nuclear Magnetic Resonance Microscopy*. Google-Books-ID: yjrjT\_W5hygC. Clarendon Press. 520 pp. (Cited on pages 59, 61, 63).
- Insko, E. K. and Bolinger, L. (1993).** "Mapping of the Radiofrequency Field". In: *Journal of Magnetic Resonance, Series A* 103.1, pp. 82–85 (Cited on page 69).
- Basser, P. J., Mattiello, J., and LeBihan, D. (1994).** "MR diffusion tensor spectroscopy and imaging". In: *Biophysical Journal* 66.1, pp. 259–267 (Cited on pages 62, 76, 79).
- Collins, D., Neelin, P., Peters, T., and Evans, A. (1994).** "Automatic 3D intersubject registration of MR volumetric data in standardized Talairach space." In: *Journal of Computer Assisted Tomography* 18.2, pp. 192–205 (Cited on page 37).
- Jones, R. B., Mills, A. D., Faure, J.-M., and Williams, J. B. (1994).** "Restraint, fear, and distress in Japanese quail genetically selected for long or short tonic immobility reactions". In: *Physiology & Behavior* 56.3, pp. 529–534 (Cited on page 76).
- MacKay, A., Whittall, K., Adler, J., Li, D., Paty, D., and Graeb, D. (1994).** "In vivo visualization of myelin water in brain by magnetic resonance". In: *Magnetic Resonance in Medicine* 31.6, pp. 673–677 (Cited on page 152).
- Chabriat, H., Vahedi, K., et al. (1995).** "Clinical spectrum of CADASIL: a study of 7 families". In: *The Lancet* 346.8980, pp. 934–939 (Cited on page 45).
- Mangin, J.-F., Frouin, V., Bloch, I., Régis, J., and López-Krahe, J. (1995).** "From 3D magnetic resonance images to structural representations of the cortex topography using topology preserving deformations". In: *Journal of Mathematical Imaging and Vision* 5.4, pp. 297–318 (Cited on page 153).
- Rogers, L. J. (1995).** "The development of brain and behaviour in the chicken." In: *The development of brain and behaviour in the chicken*. Publisher: CAB INTERNATIONAL (Cited on page 103).
- Ester, M., Kriegel, H.-P., and Xu, X. (1996).** "A Density-Based Algorithm for Discovering Clusters in Large Spatial Databases with Noise". In: p. 6 (Cited on page 83).
- Pierpaoli, C., Jezzard, P., Basser, P. J., Barnett, A., and Di Chiro, G. (1996).** "Diffusion tensor MR imaging of the human brain." In: *Radiology* 201.3. Publisher: Radiological Society of North America, pp. 637–648 (Cited on page 79).
- Pierpaoli, C. and Basser, P. J. (1996).** "Toward a quantitative assessment of diffusion anisotropy". In: *Magnetic Resonance in Medicine* 36.6. \_eprint: <https://onlinelibrary.wiley.com/doi/pdf/10.1002/mrm.1910360612>, pp. 893–906 (Cited on page 65).
- Stollberger, R. and Wach, P. (1996).** "Imaging of the active B1 field in vivo". In: *Magnetic Resonance in Medicine* 35.2, pp. 246–251 (Cited on page 69).

- Ebisu, T. et al. (1997).** “Hemorrhagic and nonhemorrhagic stroke: diagnosis with diffusion-weighted and T2-weighted echo-planar MR imaging.” In: *Radiology* 203.3. Publisher: Radiological Society of North America, pp. 823–828 (Cited on page 67).
- Mills, A. D., Crawford, L. L., Domjan, M., and Faure, J. M. (1997).** “The behavior of the Japanese or domestic quail *Coturnix japonica*.” In: *Neuroscience & Biobehavioral Reviews* 21.3, pp. 261–281 (Cited on page 76).
- Mountcastle, V. B. (1997).** “The columnar organization of the neocortex.” In: *Brain* 120.4, pp. 701–722 (Cited on pages 30, 31).
- Braitenberg, V. and Schüz, A. (1998).** *Anatomy of the Cortex: Statistics and Geometry*. Google-Books-ID: Mfvu-CAAAQBAJ. Springer Science & Business Media. 244 pp. (Cited on page 20).
- Poupon, C., Mangin, J. -F., Frouin, V., Régis, J., Poupon, F., Pachot-Clouard, M., Le Bihan, D., and Bloch, I. (1998).** “Regularization of MR diffusion tensor maps for tracking brain white matter bundles”. In: *Medical Image Computing and Computer-Assisted Intervention — MICCAI’98*. Ed. by W. M. Wells, A. Colchester, and S. Delp. Lecture Notes in Computer Science. Berlin, Heidelberg: Springer, pp. 489–498 (Cited on page 65).
- Yamauchi, H., Fukuyama, H., Nagahama, Y., Katsumi, Y., Dong, Y., Hayashi, T., Konishi, J., and Kimura, J. (1998).** “Atrophy of the Corpus Callosum, Cortical Hypometabolism, and Cognitive Impairment in Corticobasal Degeneration”. In: *Archives of Neurology* 55.5. Publisher: American Medical Association, pp. 609–614 (Cited on page 42).
- Conturo, T. E., Lori, N. F., Cull, T. S., Akbudak, E., Snyder, A. Z., Shimony, J. S., McKinstry, R. C., Burton, H., and Raichle, M. E. (1999).** “Tracking neuronal fiber pathways in the living human brain”. In: *Proceedings of the National Academy of Sciences* 96.18. Publisher: National Academy of Sciences Section: Physical Sciences, pp. 10422–10427 (Cited on page 65).
- Dale, A. M., Fischl, B., and Sereno, M. I. (1999).** “Cortical Surface-Based Analysis: I. Segmentation and Surface Reconstruction”. In: *NeuroImage* 9.2, pp. 179–194 (Cited on page 152).
- Gelman, N., Gorell, J. M., Barker, P. B., Savage, R. M., Spickler, E. M., Windham, J. P., and Knight, R. A. (1999).** “MR Imaging of Human Brain at 3.0 T: Preliminary Report on Transverse Relaxation Rates and Relation to Estimated Iron Content”. In: *Radiology* 210.3. Publisher: Radiological Society of North America, pp. 759–767 (Cited on page 70).
- Mori, S., Crain, B. J., Chacko, V. P., and Zijl, P. C. M. V. (1999).** “Three-dimensional tracking of axonal projections in the brain by magnetic resonance imaging”. In: *Annals of Neurology* 45.2. \_eprint: [https://onlinelibrary.wiley.com/doi/pdf/10.1002/1546-8249\(199902\)45:2<3265::AID-ANA213E3.0.CO;2-3](https://onlinelibrary.wiley.com/doi/pdf/10.1002/1546-8249(199902)45:2<3265::AID-ANA213E3.0.CO;2-3), pp. 265–269 (Cited on page 65).
- Poupon, C. (1999).** “Détection des faisceaux de fibres de la substance blanche pour l’étude de la connectivité anatomique cérébrale”. These de doctorat. Paris, ENST (Cited on page 66).
- Schleicher, A., Amunts, K., Geyer, S., Morosan, P., and Zilles, K. (1999).** “Observer-Independent Method for Microstructural Parcellation of Cerebral Cortex: A Quantitative Approach to Cytoarchitectonics”. In: *NeuroImage* 9.1, pp. 165–177 (Cited on page 166).
- Barkovich, A. J. and Kuzniecky, R. I. (2000).** “Gray matter heterotopia”. In: *Neurology* 55.11. Publisher: Wolters Kluwer Health, Inc. on behalf of the American Academy of Neurology Section: Views & Reviews, pp. 1603–1608 (Cited on page 43).
- Fischl, B. and Dale, A. M. (2000).** “Measuring the thickness of the human cerebral cortex from magnetic resonance images”. In: *Proceedings of the National Academy of Sciences of the United States of America* 97.20, pp. 11050–11055 (Cited on pages 23, 41).
- Lansberg, M. G., Albers, G. W., Beaulieu, C., and Marks, M. P. (2000).** “Comparison of diffusion-weighted MRI and CT in acute stroke”. In: *Neurology* 54.8. Publisher: Wolters Kluwer Health, Inc. on behalf of the American Academy of Neurology Section: Articles, pp. 1557–1561 (Cited on page 67).



- LeDoux, J. (2000).** "Emotion Circuits in the Brain". In: *Annual Review of Neuroscience* 23.1, pp. 155–184 (Cited on page 105).
- Medina, L. and Reiner, A. (2000).** "Do birds possess homologues of mammalian primary visual, somatosensory and motor cortices?" In: *Trends in Neurosciences* 23.1, pp. 1–12 (Cited on page 105).
- Richard, S., Davies, D. C., and Faure, J. M. (2000).** "The role of fear in one-trial passive avoidance learning in Japanese quail chicks genetically selected for long or short duration of the tonic immobility reaction". In: *Behavioural Processes* 48.3, pp. 165–170 (Cited on page 105).
- Richard, S. (2000).** "Bases neuroanatomiques des comportements de peur chez la caille japonaise". thesis. Rennes, Agrocampus Ouest (Cited on page 103).
- Schachter, M., Does, M. D., Anderson, A. W., and Gore, J. C. (2000).** "Measurements of Restricted Diffusion Using an Oscillating Gradient Spin-Echo Sequence". In: *Journal of Magnetic Resonance* 147.2, pp. 232–237 (Cited on pages 69, 119).
- Wedeen, V. J., Reese, T. G., Tuch, D. S., Weigel, M. R., Dou, J.-G., Weisskoff, R. M., and Chessler, D. (2000).** "Mapping Fiber Orientation Spectra in Cerebral White Matter with Fourier-Transform Diffusion MRI". In: p. 1 (Cited on pages 62–64).
- Wu, C.-C., Russell, R. M., and Karten, H. J. (2000).** "Ontogeny of the tectorotundal pathway in chicks (*Gallus gallus*): Birthdating and pathway tracing study". In: *Journal of Comparative Neurology* 417.1. \_eprint: <https://onlinelibrary.wiley.com/doi/pdf/10.1002/cne.10000>, pp. 115–132 (Cited on page 98).
- Schellinger, P. D. et al. (2001).** "Stroke magnetic resonance imaging within 6 hours after onset of hyperacute cerebral ischemia". In: *Annals of Neurology* 49.4. \_eprint: <https://onlinelibrary.wiley.com/doi/pdf/10.1002/ana.95>, pp. 460–469 (Cited on page 67).
- Barbier, E. L., Marrett, S., Danek, A., Vortmeyer, A., Gelderen, P. v., Duyn, J., Bandettini, P., Grafman, J., and Koretsky, A. P. (2002).** "Imaging cortical anatomy by high-resolution MR at 3.0T: Detection of the stripe of Gennari in visual area 17". In: *Magnetic Resonance in Medicine* 48.4, pp. 735–738 (Cited on page 159).
- Fatterpekar, G. M., Naidich, T. P., Delman, B. N., Aguinaldo, J. G., Gultekin, S. H., Sherwood, C. C., Hof, P. R., Drayer, B. P., and Fayad, Z. A. (2002).** "Cytoarchitecture of the Human Cerebral Cortex: MR Microscopy of Excised Specimens at 9.4 Tesla". In: *American Journal of Neuroradiology* 23.8, pp. 1313–1321 (Cited on pages 152, 159).
- Fink, J. N., Kumar, S., Horkan, C., Linfante, I., Selim, M. H., Caplan, L. R., and Schlaug, G. (2002).** "The Stroke Patient Who Woke Up". In: *Stroke* 33.4. Publisher: American Heart Association, pp. 988–993 (Cited on page 67).
- Lyamin, O. I., Mukhametov, L. M., Chetyrbok, I. S., and Vassiliev, A. V. (2002).** "Sleep and wakefulness in the southern sea lion". In: *Behavioural Brain Research* 128.2, pp. 129–138 (Cited on page 119).
- Schüz, A. and Miller, R. (2002).** *Cortical Areas: Unity and Diversity*. Google-Books-ID: PibbUUpipH8C. CRC Press. 533 pp. (Cited on pages 25, 32).
- Tuch, D. S. (2002).** "Diffusion MRI of complex tissue structure". Accepted: 2005-08-23T19:22:31Z Journal Abbreviation: Diffusion magnetic resonance imaging of complex tissue structure. Thesis. Massachusetts Institute of Technology (Cited on pages 62–64).
- Westin, C. -F., Maier, S. E., Mamata, H., Nabavi, A., Jolesz, F. A., and Kikinis, R. (2002).** "Processing and visualization for diffusion tensor MRI". In: *Medical Image Analysis* 6.2, pp. 93–108 (Cited on page 61).
- Zilles, K., Palomero-Gallagher, N., Grefkes, C., Scheperjans, F., Boy, C., Amunts, K., and Schleicher, A. (2002).** "Architectonics of the human cerebral cortex and transmitter receptor fingerprints: reconciling functional neuroanatomy and neurochemistry". In: *European Neuropsychopharmacology* 12.6, pp. 587–599 (Cited on pages 37, 152).

- Behrens, T. E. J., Woolrich, M. W., Jenkinson, M., Johansen-Berg, H., Nunes, R. G., Clare, S., Matthews, P. M., Brady, J. M., and Smith, S. M. (2003). "Characterization and propagation of uncertainty in diffusion-weighted MR imaging". In: *Magnetic Resonance in Medicine* 50.5, pp. 1077–1088 (Cited on pages 64, 66).
- Deoni, S. C. L., Rutt, B. K., and Peters, T. M. (2003). "Rapid combined T1 and T2 mapping using gradient recalled acquisition in the steady state". In: *Magnetic Resonance in Medicine* 49.3, pp. 515–526 (Cited on page 69).
- Jansons, K. M. and Alexander, D. C. (2003). "Persistent angular structure: new insights from diffusion magnetic resonance imaging data". In: *Inverse Problems* 19.5, pp. 1031–1046 (Cited on page 64).
- Liu, C., Bammer, R., and Moseley, M. E. (2003). "Generalized Diffusion Tensor Imaging (GDTI): A Method for Characterizing and Imaging Diffusion Anisotropy Caused by Non-Gaussian Diffusion". In: *Israel Journal of Chemistry* 43.1. \_eprint: <https://onlinelibrary.wiley.com/doi/pdf/10.1560/HB5H-6XBR-1AW1-LNX9>, pp. 145–154 (Cited on page 64).
- Parker, G. J. M., Haroon, H. A., and Wheeler-Kingshott, C. A. M. (2003). "A framework for a streamline-based probabilistic index of connectivity (PICO) using a structural interpretation of MRI diffusion measurements". In: *Journal of Magnetic Resonance Imaging* 18.2, pp. 242–254 (Cited on pages 66, 76, 110).
- Parsons, E. C., Does, M. D., and Gore, J. C. (2003). "Modified oscillating gradient pulses for direct sampling of the diffusion spectrum suitable for imaging sequences". In: *Magnetic Resonance Imaging. Proceedings of the Sixth International Meeting on Recent Advances in MR Applications to Porous Media* 21.3, pp. 279–285 (Cited on page 61).
- Thompson, P. M. and Toga, A. W. (2003). "Cerebral Cortex Diseases and Cortical Localization". In: *eLS*. American Cancer Society (Cited on page 42).
- Aoki, I., Wu, Y.-J. L., Silva, A. C., Lynch, R. M., and Koretsky, A. P. (2004). "In vivo detection of neuroarchitecture in the rodent brain using manganese-enhanced MRI". In: *NeuroImage* 22.3, pp. 1046–1059 (Cited on page 76).
- Bernstein, M. A., King, K. F., and Zhou, X. J. (2004). *Handbook of MRI Pulse Sequences*. Google-Books-ID: d6PLHcyejEIC. Elsevier. 1041 pp. (Cited on page 70).
- Corouge, I., Gouttard, S., and Gerig, G. (2004). "Towards a shape model of white matter fiber bundles using diffusion tensor MRI". In: *2004 2nd IEEE International Symposium on Biomedical Imaging: Nano to Macro (IEEE Cat No. 04EX821)*. 2004 2nd IEEE International Symposium on Biomedical Imaging: Nano to Macro (IEEE Cat No. 04EX821), 344–347 Vol. 1 (Cited on page 81).
- Kövari Enikő, Gold Gabriel, Herrmann François R., Canuto Alessandra, Hof Patrick R., Michel Jean-Pierre, Bouras Constantin, and Giannakopoulos Panteleimon (2004). "Cortical Microinfarcts and Demyelination Significantly Affect Cognition in Brain Aging". In: *Stroke* 35.2. Publisher: American Heart Association, pp. 410–414 (Cited on page 44).
- Pfefferbaum, A., Sullivan, E. V., Adalsteinsson, E., Garrick, T., and Harper, C. (2004). "Postmortem MR imaging of formalin-fixed human brain". In: *NeuroImage* 21.4, pp. 1585–1595 (Cited on pages 55, 56, 77).
- Reiner, A. et al. (2004). "Revised nomenclature for avian telencephalon and some related brainstem nuclei". In: *Journal of Comparative Neurology* 473.3. \_eprint: <https://onlinelibrary.wiley.com/doi/pdf/10.1002/cne.20118>, pp. 377–414 (Cited on page 105).
- Van Der Linden, A., Van Meir, V., Tindemans, I., Verhoye, M., and Balthazart, J. (2004). "Applications of manganese-enhanced magnetic resonance imaging (MEMRI) to image brain plasticity in song birds". In: *NMR in Biomedicine* 17.8. \_eprint: <https://onlinelibrary.wiley.com/doi/pdf/10.1002/nbm.936>, pp. 602–612 (Cited on page 77).
- Zilles, K. (2004). "CHAPTER 27 - Architecture of the Human Cerebral Cortex: Regional and Laminal Organization". In: *The Human Nervous System (Second Edition)*. Ed. by G. Paxinos and J. K. Mai. San Diego: Academic Press, pp. 997–1055 (Cited on pages 24, 32).
- Assaf, Y. and Basser, P. J. (2005). "Composite hindered and restricted model of diffusion (CHARMED) MR imaging of the human brain". In: *NeuroImage* 27.1, pp. 48–58 (Cited on pages 64, 66).

- Clare, S. and Bridge, H. (2005).** "Methodological issues relating to in vivo cortical myelography using MRI". In: *Human Brain Mapping* 26.4, pp. 240–250 (Cited on page 159).
- Diekamp, B., Regolin, L., Güntürkün, O., and Vallortigara, G. (2005).** "A left-sided visuospatial bias in birds". In: *Current Biology* 15.10, R372–R373 (Cited on page 79).
- Eickhoff, S., Walters, N. B., Schleicher, A., Kril, J., Egan, G. F., Zilles, K., Watson, J. D. G., and Amunts, K. (2005).** "High-resolution MRI reflects myeloarchitecture and cytoarchitecture of human cerebral cortex". In: *Human Brain Mapping* 24.3, pp. 206–215 (Cited on page 160).
- Jensen, J. H., Helpert, J. A., Ramani, A., Lu, H., and Kaczynski, K. (2005).** "Diffusional kurtosis imaging: The quantification of non-gaussian water diffusion by means of magnetic resonance imaging". In: *Magnetic Resonance in Medicine* 53.6, pp. 1432–1440 (Cited on page 64).
- Kalenscher, T., Windmann, S., Diekamp, B., Rose, J., Güntürkün, O., and Colombo, M. (2005).** "Single Units in the Pigeon Brain Integrate Reward Amount and Time-to-Reward in an Impulsive Choice Task". In: *Current Biology* 15.7, pp. 594–602 (Cited on page 98).
- Kim, J. S., Singh, V., Lee, J. K., Lerch, J., Ad-Dab'bagh, Y., MacDonald, D., Lee, J. M., Kim, S. I., and Evans, A. C. (2005).** "Automated 3-D extraction and evaluation of the inner and outer cortical surfaces using a Laplacian map and partial volume effect classification". In: *NeuroImage* 27.1, pp. 210–221 (Cited on page 152).
- Mori, S., Wakana, S., Zijl, P. C. M. v., and Nagae-Poetscher, L. M. (2005).** *MRI Atlas of Human White Matter*. Google-Books-ID: ItwRYlvFNLIC. Elsevier. 249 pp. (Cited on page 81).
- Neary, D., Snowden, J., and Mann, D. (2005).** "Frontotemporal dementia". In: *The Lancet Neurology* 4.11, pp. 771–780 (Cited on page 42).
- Perrin, M., Poupon, C., Cointepas, Y., et al. (2005).** "Fiber tracking in q-ball fields using regularized particle trajectories". In: *Information Processing in Medical Imaging: Proceedings of the ... Conference* 19, pp. 52–63 (Cited on pages 80, 85, 112, 121, 161).
- Perrin, M., Poupon, C., Rieul, B., Leroux, P., Constantinesco, A., Mangin, J.-F., and Lebihan, D. (2005).** "Validation of q-ball imaging with a diffusion fibre-crossing phantom on a clinical scanner". In: *Philosophical Transactions of the Royal Society of London. Series B, Biological Sciences* 360.1457, pp. 881–891 (Cited on pages 66, 110).
- Sporns, O., Tononi, G., and Kötter, R. (2005).** "The Human Connectome: A Structural Description of the Human Brain". In: *PLOS Computational Biology* 1.4, e42 (Cited on pages 66, 133).
- Yong-Hing, C. J., Obenaus, A., Stryker, R., Tong, K., and Sarty, G. E. (2005).** "Magnetic resonance imaging and mathematical modeling of progressive formalin fixation of the human brain". In: *Magnetic Resonance in Medicine* 54.2, pp. 324–332 (Cited on page 56).
- Cheng, H.-L. M. and Wright, G. A. (2006).** "Rapid high-resolution T1 mapping by variable flip angles: Accurate and precise measurements in the presence of radiofrequency field inhomogeneity". In: *Magnetic Resonance in Medicine* 55.3, pp. 566–574 (Cited on pages 69, 141).
- Cunningham, C. H., Pauly, J. M., and Nayak, K. S. (2006).** "Saturated double-angle method for rapid B1+ mapping". In: *Magnetic Resonance in Medicine* 55.6, pp. 1326–1333 (Cited on pages 69, 142).
- De Groof, G., Verhoye, M., Van Meir, V., Tindemans, I., Leemans, A., and Van der Linden, A. (2006).** "In vivo diffusion tensor imaging (DTI) of brain subdivisions and vocal pathways in songbirds". In: *NeuroImage* 29.3, pp. 754–763 (Cited on page 77).
- Faure, J.-M., Arnould, C., Beaumont, C., Guémené, D., Leterrier, C., D. Mills, A., and Richard, S. (2006).** "Consequences of selection for fear in Japanese quail". In: *Archiv für Geflügelkunde* 70, S216–222 (Cited on page 76).

- Laule, C., Leung, E., Li, D. K., Trabouisee, A. L., Paty, D. W., MacKay, A. L., and Moore, G. R. (2006).** "Myelin water imaging in multiple sclerosis: quantitative correlations with histopathology". In: *Multiple Sclerosis Journal* 12.6, pp. 747–753 (Cited on page 152).
- Mori, S. and Zhang, J. (2006).** "Principles of Diffusion Tensor Imaging and Its Applications to Basic Neuroscience Research". In: *Neuron* 51.5, pp. 527–539 (Cited on pages 57, 76, 110).
- Özarslan, E., Shepherd, T. M., Vemuri, B. C., Blackband, S. J., and Mareci, T. H. (2006).** "Resolution of complex tissue microarchitecture using the diffusion orientation transform (DOT)". In: *NeuroImage* 31.3, pp. 1086–1103 (Cited on page 64).
- Sullivan, E. V. and Pfefferbaum, A. (2006).** "Diffusion tensor imaging and aging". In: *Neuroscience & Biobehavioral Reviews*. Methodological and Conceptual Advances in the Study of Brain-Behavior Dynamics: A Multivariate Lifespan Perspective 30.6, pp. 749–761 (Cited on page 67).
- Sun, S.-W., Liang, H.-F., Le, T. Q., Armstrong, R. C., Cross, A. H., and Song, S.-K. (2006).** "Differential sensitivity of in vivo and ex vivo diffusion tensor imaging to evolving optic nerve injury in mice with retinal ischemia". In: *NeuroImage* 32.3, pp. 1195–1204 (Cited on page 76).
- Thelwall, P. E., Shepherd, T. M., Stanisz, G. J., and Blackband, S. J. (2006).** "Effects of temperature and aldehyde fixation on tissue water diffusion properties, studied in an erythrocyte ghost tissue model". In: *Magnetic Resonance in Medicine* 56.2, pp. 282–289 (Cited on pages 55, 56).
- Behrens, T. E. J., Berg, H. J., Jbabdi, S., Rushworth, M. F. S., and Woolrich, M. W. (2007).** "Probabilistic diffusion tractography with multiple fibre orientations: What can we gain?" In: *NeuroImage* 34.1, pp. 144–155 (Cited on pages 76, 110).
- Boissy, A. et al. (2007).** "Emotions and cognition: a new approach to animal welfare". In: *Animal Welfare* 16.2, pp. 37–43 (Cited on page 75).
- Chao, Y.-P., Yang, C.-Y., Cho, K.-H., Yeh, C.-H., Chou, K.-H., Chen, J.-H., and Lin, C.-P. (2007).** "The Development of Brain Connectivity Browser by Tractography of QBI". In: *2007 29th Annual International Conference of the IEEE Engineering in Medicine and Biology Society*. 2007 29th Annual International Conference of the IEEE Engineering in Medicine and Biology Society. ISSN: 1558-4615, pp. 2094–2097 (Cited on page 66).
- D'Arceuil, H. and Crespigny, A. de (2007).** "The effects of brain tissue decomposition on diffusion tensor imaging and tractography". In: *NeuroImage* 36.1, pp. 64–68 (Cited on pages 55, 56, 77, 151).
- D'Arceuil, H. E., Westmoreland, S., and Crespigny, A. J. de (2007).** "An approach to high resolution diffusion tensor imaging in fixed primate brain". In: *NeuroImage* 35.2, pp. 553–565 (Cited on pages 77, 151).
- Descoteaux, M., Angelino, E., Fitzgibbons, S., and Deriche, R. (2007).** "Regularized, fast, and robust analytical Q-ball imaging". In: *Magnetic Resonance in Medicine* 58.3, pp. 497–510 (Cited on page 64).
- Duyn, J. H., Gelderen, P. van, Li, T.-Q., Zwart, J. A. de, Koretsky, A. P., and Fukunaga, M. (2007).** "High-field MRI of brain cortical substructure based on signal phase". In: *Proceedings of the National Academy of Sciences* 104.28, pp. 11796–11801 (Cited on page 152).
- Hazard, D., Couty, M., and Guémené, D. (2007).** "Characterization of CRF, AVT, and ACTH cDNA and pituitary-adrenal axis function in Japanese quail divergently selected for tonic immobility". In: *American Journal of Physiology-Regulatory, Integrative and Comparative Physiology* 293.3. Publisher: American Physiological Society, R1421–R1429 (Cited on page 76).
- Jespersen, S. N., Kroenke, C. D., Østergaard, L., Ackerman, J. J. H., and Yablonskiy, D. A. (2007).** "Modeling dendrite density from magnetic resonance diffusion measurements". In: *NeuroImage* 34.4, pp. 1473–1486 (Cited on page 61).

- Jian, B., Vemuri, B. C., Özarslan, E., Carney, P. R., and Mareci, T. H. (2007).** “A novel tensor distribution model for the diffusion-weighted MR signal”. In: *NeuroImage* 37.1, pp. 164–176 (Cited on page 64).
- LeDoux, J. (2007).** “The amygdala”. In: *Current Biology* 17.20, R868–R874 (Cited on page 105).
- Nieuwenhuys, R., Voogd, J., and Huijzen, C. v. (2007).** *The Human Central Nervous System: A Synopsis and Atlas*. Google-Books-ID: vAiFe7gZLhoC. Springer Science & Business Media. 967 pp. (Cited on pages 34, 161).
- Orosz, S. E. and Bradshaw, G. A. (2007).** “Avian Neuroanatomy Revisited: From Clinical Principles to Avian Cognition”. In: *Veterinary Clinics of North America: Exotic Animal Practice*. Neuroanatomy and Neurodiagnostics 10.3, pp. 775–802 (Cited on page 105).
- Peters, A. M., Brookes, M. J., Hoogenraad, F. G., Gowland, P. A., Francis, S. T., Morris, P. G., and Bowtell, R. (2007).** “T2\* measurements in human brain at 1.5, 3 and 7 T”. In: *Magnetic Resonance Imaging*. Proceedings of the International School on Magnetic Resonance and Brain Function 25.6, pp. 748–753 (Cited on pages 70, 152).
- Tournier, J.-D., Calamante, F., and Connelly, A. (2007).** “Robust determination of the fibre orientation distribution in diffusion MRI: Non-negativity constrained super-resolved spherical deconvolution”. In: *NeuroImage* 35.4, pp. 1459–1472 (Cited on page 64).
- Wu, Y.-C. and Alexander, A. L. (2007).** “Hybrid diffusion imaging”. In: *NeuroImage* 36.3, pp. 617–629 (Cited on page 63).
- Alexander, D. C. (2008).** “A general framework for experiment design in diffusion MRI and its application in measuring direct tissue-microstructure features”. In: *Magnetic Resonance in Medicine* 60.2, pp. 439–448 (Cited on page 66).
- Assaf, Y., Blumenfeld-Katzir, T., Yovel, Y., and Basser, P. J. (2008).** “Axciliber: A method for measuring axon diameter distribution from diffusion MRI”. In: *Magnetic Resonance in Medicine* 59.6, pp. 1347–1354 (Cited on page 66).
- Descoteaux, M., Deriche, R., Knosche, T. R., and Anwander, A. (2008).** “Deterministic and Probabilistic Tractography Based on Complex Fibre Orientation Distributions”. In: *IEEE Transactions on Medical Imaging* 28.2, pp. 269–286 (Cited on page 64).
- Ghosh, A., Descoteaux, M., and Deriche, R. (2008).** “Riemannian Framework for Estimating Symmetric Positive Definite 4th Order Diffusion Tensors”. In: *Medical Image Computing and Computer-Assisted Intervention – MICCAI 2008*. Ed. by D. Metaxas, L. Axel, G. Fichtinger, and G. Székely. Lecture Notes in Computer Science. Berlin, Heidelberg: Springer, pp. 858–865 (Cited on page 64).
- Guevara, P., Perrin, M., Cathier, P., Cointepas, Y., Riviere, D., Poupon, C., and Mangin, J.-F. (2008).** “Connectivity-based parcellation of the cortical surface using q-ball imaging”. In: *2008 5th IEEE International Symposium on Biomedical Imaging: From Nano to Macro*. 2008 5th IEEE International Symposium on Biomedical Imaging: From Nano to Macro. ISSN: 1945-8452, pp. 903–906 (Cited on page 67).
- Hazard, D., Couty, M., Richard, S., and Guémené, D. (2008).** “Intensity and duration of corticosterone response to stressful situations in Japanese quail divergently selected for tonic immobility”. In: *General and Comparative Endocrinology* 155.2, pp. 288–297 (Cited on page 76).
- Hazard, D., Leclaire, S., Couty, M., and Guémené, D. (2008).** “Genetic differences in coping strategies in response to prolonged and repeated restraint in Japanese quail divergently selected for long or short tonic immobility”. In: *Hormones and Behavior* 54.5, pp. 645–653 (Cited on pages 76, 105).
- Huss, D., Poynter, G., and Lansford, R. (2008).** “Japanese quail (*Coturnix japonica*) as a laboratory animal model”. In: *Lab Animal* 37, pp. 513–519 (Cited on page 76).
- Jouvent, E., Mangin, J.-F., Porcher, R., Viswanathan, A., O’Sullivan, M., Guichard, J.-P., Dichgans, M., Bousser, M.-G., and Chabriat, H. (2008).** “Cortical changes in cerebral small vessel diseases: a 3D MRI study of cortical morphology in CADASIL”. In: *Brain* 131.8, pp. 2201–2208 (Cited on page 45).

- Poirier, C., Vellema, M., Verhoye, M., Van Meir, V., Wild, J. M., Balthazart, J., and Van Der Linden, A. (2008).** “A three-dimensional MRI atlas of the zebra finch brain in stereotaxic coordinates”. In: *NeuroImage* 41.1, pp. 1–6 (Cited on page 80).
- Rogers, L. J. (2008).** “Development and function of lateralization in the avian brain”. In: *Brain Research Bulletin*. Special Issue: Brain Mechanisms, Cognition and Behaviour in Birds 76.3, pp. 235–244 (Cited on page 103).
- Rosas, H. D., Salat, D. H., Lee, S. Y., Zaleta, A. K., Pappu, V., Fischl, B., Greve, D., Hevelone, N., and Hersch, S. M. (2008).** “Cerebral cortex and the clinical expression of Huntington’s disease: complexity and heterogeneity”. In: *Brain* 131.4, pp. 1057–1068 (Cited on page 42).
- Saint-Dizier, H. (2008).** “Les réponses de peur chez la caille japonaise : approches neurobiologique et comportementale.” thesis. Tours (Cited on pages 103, 105, 106).
- Chabriat, H., Joutel, A., Dichgans, M., Tournier-Lasserre, E., and Bousser, M.-G. (2009).** “CADASIL”. In: *The Lancet Neurology* 8.7, pp. 643–653 (Cited on page 45).
- Dawe, R. J., Bennett, D. A., Schneider, J. A., Vasireddi, S. K., and Arfanakis, K. (2009).** “Postmortem MRI of human brain hemispheres: T2 relaxation times during formaldehyde fixation”. In: *Magnetic Resonance in Medicine* 61.4, pp. 810–818 (Cited on pages 56, 57).
- Economo, C. von and Triarhou, L. (2009).** *Cellular Structure of the Human Cerebral Cortex*. Journal Abbreviation: Cellular Structure of the Human Cerebral Cortex Publication Title: Cellular Structure of the Human Cerebral Cortex (Cited on pages 26, 27, 29).
- Fillard, P., Poupon, C., and Mangin, J.-F. (2009).** “A Novel Global Tractography Algorithm Based on an Adaptive Spin Glass Model”. In: *Medical Image Computing and Computer-Assisted Intervention – MICCAI 2009*. Ed. by G.-Z. Yang, D. Hawkes, D. Rueckert, A. Noble, and C. Taylor. Lecture Notes in Computer Science. Berlin, Heidelberg: Springer, pp. 927–934 (Cited on page 62).
- Johansen-Berg, H. and Behrens, T. E. J. (2009).** *Diffusion MRI: From Quantitative Measurement to In-vivo Neuroanatomy*. Google-Books-ID: UTvMIAEACAAJ. Elsevier/Academic Press. 490 pp. (Cited on page 42).
- Martinez-Garcia, F., Novejarque, A., and Lanuza, E. (2009).** “15 The Evolution of the Amygdala in Vertebrates”. In: *Evolutionary neuroscience*, p. 313 (Cited on pages 105, 109).
- McNab, J. A., Jbabdi, S., Deoni, S. C. L., Douaud, G., Behrens, T. E. J., and Miller, K. L. (2009).** “High resolution diffusion-weighted imaging in fixed human brain using diffusion-weighted steady state free precession”. In: *NeuroImage* 46.3, pp. 775–785 (Cited on pages 61, 77, 151).
- Naidich, T. P., Duvernoy, H. M., Delman, B. N., Sorensen, A. G., Kollias, S. S., and Haacke, E. M. (2009).** *Duvernoy’s Atlas of the Human Brain Stem and Cerebellum: High-Field MRI, Surface Anatomy, Internal Structure, Vascularization and 3 D Sectional Anatomy*. Google-Books-ID: Fx7wlnVxwfUC. Springer Science & Business Media. 872 pp. (Cited on page 15).
- Saint-Dizier, H., Constantin, P., Davies, D. C., Leterrier, C., Lévy, F., and Richard, S. (2009).** “Subdivisions of the arcopallium/posterior pallial amygdala complex are differentially involved in the control of fear behaviour in the Japanese quail”. In: *Brain Research Bulletin* 79.5, pp. 288–295 (Cited on page 105).
- Shepherd, T. M., Thelwall, P. E., Stanisz, G. J., and Blackband, S. J. (2009).** “Aldehyde fixative solutions alter the water relaxation and diffusion properties of nervous tissue”. In: *Magnetic Resonance in Medicine* 62.1, pp. 26–34 (Cited on pages 55, 77).
- Wichman, A., Freire, R., and Rogers, L. J. (2009).** “Light exposure during incubation and social and vigilance behaviour of domestic chicks”. In: *Laterality* 14.4. Publisher: Routledge \_eprint: <https://doi.org/10.1080/13576500802440616>, pp. 381–394 (Cited on page 103).

- Zilles, K. and Amunts, K. (2009). "Receptor mapping: Architecture of the human cerebral cortex". In: *Current Opinion in Neurology* 22.4, pp. 331–339 (Cited on page 37).
- Alexander, D. C., Hubbard, P. L., Hall, M. G., Moore, E. A., Ptito, M., Parker, G. J. M., and Dyrby, T. B. (2010). "Orientationally invariant indices of axon diameter and density from diffusion MRI". In: *NeuroImage* 52.4, pp. 1374–1389 (Cited on page 66).
- Amunts, K., Lenzen, M., Friederici, A. D., Schleicher, A., Morosan, P., Palomero-Gallagher, N., and Zilles, K. (2010). "Broca's Region: Novel Organizational Principles and Multiple Receptor Mapping". In: *PLOS Biology* 8.9. Publisher: Public Library of Science, e1000489 (Cited on page 37).
- Condat, L. (2010). "A Simple Trick to Speed Up and Improve the Non-Local Means" (Cited on page 143).
- De Groof, G. D. and Linden, A. V. d. (2010). "Love songs, bird brains and diffusion tensor imaging". In: *NMR in Biomedicine* 23.7. \_eprint: <https://analyticalsciencejournals.onlinelibrary.wiley.com/doi/pdf/10.1002/nbm.1551>, pp. 873–883 (Cited on page 77).
- Lutti, A., Hutton, C., Finsterbusch, J., Helms, G., and Weiskopf, N. (2010). "Optimization and validation of methods for mapping of the radiofrequency transmit field at 3T". In: *Magnetic Resonance in Medicine* 64.1, pp. 229–238 (Cited on pages 68, 69).
- Moser, E. (2010). "Ultra-high-field magnetic resonance: Why and when?" In: *World Journal of Radiology* 2.1, pp. 37–40 (Cited on page 53).
- Ochfeld, E., Newhart, M., Molitoris, J., Leigh, R., Cloutman, L., Davis, C., Crinion, J., and Hillis, A. E. (2010). "Ischemia in Broca Area Is Associated With Broca Aphasia More Reliably in Acute Than in Chronic Stroke". In: *Stroke* 41.2. Publisher: American Heart Association, pp. 325–330 (Cited on page 45).
- Oishi, K., Faria, A. V., Zijl, P. C. M. v., and Mori, S. (2010). *MRI Atlas of Human White Matter*. Google-Books-ID: v8MWjTpVUAYC. Academic Press. 266 pp. (Cited on page 81).
- Stanic, K., Montecinos, H., and Caprile, T. (2010). "Subdivisions of chick diencephalic roof plate: Implication in the formation of the posterior commissure". In: *Developmental Dynamics* 239.10. \_eprint: <https://anatomypubs.onlinelibrary.wiley.com/> pp. 2584–2593 (Cited on page 98).
- Avants, B. B., Tustison, N. J., Song, G., Cook, P. A., Klein, A., and Gee, J. C. (2011). "A reproducible evaluation of ANTs similarity metric performance in brain image registration". In: *NeuroImage* 54.3, pp. 2033–2044 (Cited on page 80).
- Axer, M., Amunts, K., Grässel, D., Palm, C., Dammers, J., Axer, H., Pietrzyk, U., and Zilles, K. (2011). "A novel approach to the human connectome: Ultra-high resolution mapping of fiber tracts in the brain". In: *NeuroImage* 54.2, pp. 1091–1101 (Cited on pages 107, 163).
- Buades, A., Coll, B., and Morel, J.-M. (2011). "Non-Local Means Denoising". In: *Image Processing On Line* 1, pp. 208–212 (Cited on pages 79, 112, 143).
- Calandreau, L., Favreau-Peigné, A., et al. (2011). "Higher inherent fearfulness potentiates the effects of chronic stress in the Japanese quail". In: *Behavioural Brain Research* 225.2, pp. 505–510 (Cited on pages 76, 105).
- Drobnjak, I., Zhang, H., Hall, M. G., and Alexander, D. C. (2011). "The matrix formalism for generalised gradients with time-varying orientation in diffusion NMR". In: *Journal of Magnetic Resonance* 210.1, pp. 151–157 (Cited on page 61).
- Duijn, S. v., Nabuurs, R. J. A., Rooden, S. v., Maat-Schieman, M. L. C., Duinen, S. G. v., Buchem, M. A. v., Weerd, L. v. d., and Natté, R. (2011). "MRI artifacts in human brain tissue after prolonged formalin storage". In: *Magnetic Resonance in Medicine* 65.6, pp. 1750–1758 (Cited on page 56).

- Dyrby, T. B., Baaré, W. F. C., Alexander, D. C., Jelsing, J., Garde, E., and Søgaard, L. V. (2011).** “An ex vivo imaging pipeline for producing high-quality and high-resolution diffusion-weighted imaging datasets”. In: *Human Brain Mapping* 32.4, pp. 544–563 (Cited on pages 77, 166).
- Geyer, S., Weiss, M., Reimann, K., Lohmann, G., and Turner, R. (2011).** “Microstructural Parcellation of the Human Cerebral Cortex – From Brodmann’s Post-Mortem Map to in vivo Mapping with High-Field Magnetic Resonance Imaging”. In: *Frontiers in Human Neuroscience* 5 (Cited on page 152).
- Guevara, P., Poupon, C., Rivière, D., Cointepas, Y., Descoteaux, M., Thirion, B., and Mangin, J.-F. (2011).** “Robust clustering of massive tractography datasets”. In: *NeuroImage* 54.3, pp. 1975–1993 (Cited on pages 3, 67, 81, 82, 113, 125).
- Jbabdi, S. and Johansen-Berg, H. (2011).** “Tractography: Where Do We Go from Here?” In: *Brain Connectivity* 1.3. Publisher: Mary Ann Liebert, Inc., publishers, pp. 169–183 (Cited on page 66).
- Kastler, B. and Vetter, D. (2011).** *Comprendre l’IRM: Manuel d’auto-apprentissage*. Google-Books-ID: mBHTNw3eR34C. Elsevier Masson. 407 pp. (Cited on pages 50, 51, 53, 54).
- Koay, C. G., Hurley, S. A., and Meyerand, M. E. (2011).** “Extremely efficient and deterministic approach to generating optimal ordering of diffusion MRI measurements”. In: *Medical Physics* 38.8. \_eprint: <https://aapm.onlinelibrary.wiley.com/doi/pdf/10.1118/1.3598001> pp. 4795–4801 (Cited on pages 121, 161).
- Miller, K. L., Stagg, C. J., et al. (2011).** “Diffusion imaging of whole, post-mortem human brains on a clinical MRI scanner”. In: *NeuroImage* 57.1, pp. 167–181 (Cited on pages 56, 61, 77, 112, 151).
- Reisert, M., Mader, I., Anastasopoulos, C., Weigel, M., Schnell, S., and Kiselev, V. (2011).** “Global fiber reconstruction becomes practical”. In: *NeuroImage* 54.2, pp. 955–962 (Cited on pages 66, 76, 110).
- Tournier, J.-D., Mori, S., and Leemans, A. (2011).** “Diffusion Tensor Imaging and Beyond”. In: *Magnetic Resonance in Medicine* 65.6, pp. 1532–1556 (Cited on page 79).
- Vellema, M., Verschueren, J., Van Meir, V., and Van der Linden, A. (2011).** “A customizable 3-dimensional digital atlas of the canary brain in multiple modalities”. In: *NeuroImage* 57.2, pp. 352–361 (Cited on pages 80, 82).
- Yendiki, A. et al. (2011).** “Automated Probabilistic Reconstruction of White-Matter Pathways in Health and Disease Using an Atlas of the Underlying Anatomy”. In: *Frontiers in Neuroinformatics* 5 (Cited on page 81).
- Zhang, H., Hubbard, P. L., Parker, G. J. M., and Alexander, D. C. (2011).** “Axon diameter mapping in the presence of orientation dispersion with diffusion MRI”. In: *NeuroImage* 56.3, pp. 1301–1315 (Cited on page 66).
- Barazany, D. and Assaf, Y. (2012).** “Visualization of Cortical Lamination Patterns with Magnetic Resonance Imaging”. In: *Cerebral Cortex* 22.9. Publisher: Oxford Academic, pp. 2016–2023 (Cited on pages 152, 159).
- Catani, M. and Schotten, M. T. d. (2012).** *Atlas of Human Brain Connections*. Google-Books-ID: nROILZ9HwEgC. OUP Oxford. 533 pp. (Cited on page 81).
- Cohen-Adad, J., Polimeni, J. R., Helmer, K. G., Benner, T., McNab, J. A., Wald, L. L., Rosen, B. R., and Mainero, C. (2012).** “T<sup>2\*</sup> mapping and B<sub>0</sub> orientation-dependence at 7T reveal cyto- and myeloarchitecture organization of the human cortex”. In: *NeuroImage* 60.2, pp. 1006–1014 (Cited on page 152).
- Dick, F., Tierney, A. T., Lutti, A., Josephs, O., Sereno, M. I., and Weiskopf, N. (2012).** “In Vivo Functional and Myeloarchitectonic Mapping of Human Primary Auditory Areas”. In: *Journal of Neuroscience* 32.46. Publisher: Society for Neuroscience Section: Articles, pp. 16095–16105 (Cited on page 152).
- Duyn, J. H. (2012).** “The future of ultra-high field MRI and fMRI for study of the human brain”. In: *NeuroImage*. 20 YEARS OF fMRI 62.2, pp. 1241–1248 (Cited on page 70).
- Garyfallidis, E., Brett, M., Correia, M. M., Williams, G. B., and Nimmo-Smith, I. (2012).** “QuickBundles, a Method for Tractography Simplification”. In: *Frontiers in Neuroscience* 6 (Cited on pages 67, 82).



- Heidemann, R. M., Anwander, A., Feiweier, T., Knösche, T. R., and Turner, R. (2012).** “k-space and q-space: Combining ultra-high spatial and angular resolution in diffusion imaging using ZOOPPA at 7T”. In: *NeuroImage* 60.2, pp. 967–978 (Cited on page 152).
- Jouvent, E., Mangin, J.-F., Duchesnay, E., et al. (2012).** “Longitudinal changes of cortical morphology in CADASIL”. In: *Neurobiology of Aging* 33.5, 1002.e29–1002.e36 (Cited on page 45).
- Li, S. P. and Padhani, A. R. (2012).** “Tumor response assessments with diffusion and perfusion MRI”. In: *Journal of Magnetic Resonance Imaging* 35.4, pp. 745–763 (Cited on page 67).
- Miller, K. L., McNab, J. A., Jbabdi, S., and Douaud, G. (2012).** “Diffusion tractography of post-mortem human brains: Optimization and comparison of spin echo and steady-state free precession techniques”. In: *NeuroImage* 59.3, pp. 2284–2297 (Cited on page 61).
- Neher, P. F., Stieltjes, B., Reisert, M., Reicht, I., Meinzer, H.-P., and Fritzsche, K. H. (2012).** “MITK global tractography”. In: *Medical Imaging 2012: Image Processing*. Medical Imaging 2012: Image Processing. Vol. 8314. International Society for Optics and Photonics, p. 83144D (Cited on page 66).
- Stikov, N., Levesque, I. R., Tardif, C. L., Barral, J. K., and Pike, G. B. (2012).** “Validation of T1 Mapping Techniques: Are Phantom Studies Sufficient?” In: p. 1 (Cited on page 69).
- Van Essen, D. C., Ugurbil, K., et al. (2012).** “The Human Connectome Project: A data acquisition perspective”. In: *NeuroImage*. Connectivity 62.4, pp. 2222–2231 (Cited on page 133).
- Zhang, H., Schneider, T., Wheeler-Kingshott, C. A., and Alexander, D. C. (2012).** “NODDI: Practical in vivo neurite orientation dispersion and density imaging of the human brain”. In: *NeuroImage* 61.4, pp. 1000–1016 (Cited on pages 3, 64, 66, 115, 149).
- Assayag, O., Grieve, K., Devaux, B., Harms, F., Pallud, J., Chretien, F., Boccara, C., and Varlet, P. (2013).** “Imaging of non-tumorous and tumorous human brain tissues with full-field optical coherence tomography”. In: *NeuroImage: Clinical* 2, pp. 549–557 (Cited on page 33).
- Boulay, J., Chaillou, E., Bertin, A., Constantin, P., Arnould, C., Leterrier, C., and Calandreau, L. (2013).** “A higher inherent trait for fearfulness is associated with increased anxiety-like behaviours and diazepam sensitivity in Japanese quail”. In: *Behavioural Brain Research* 237, pp. 124–128 (Cited on page 76).
- Calandreau, L., Bertin, A., Favreau-Peigné, A., Richard, S., Constantin, P., Lansade, L., Arnould, C., and Leterrier, C. (2013).** “Impact of high and low anxiety trait on object habituation and discrimination: Evidence from selected lines of Japanese quail”. In: *Behavioural Brain Research* 250, pp. 299–303 (Cited on page 76).
- Deistung, A., Schäfer, A., Schweser, F., Biedermann, U., Turner, R., and Reichenbach, J. R. (2013).** “Toward in vivo histology: A comparison of quantitative susceptibility mapping (QSM) with magnitude-, phase-, and R2\*-imaging at ultra-high magnetic field strength”. In: *NeuroImage* 65, pp. 299–314 (Cited on page 152).
- Destrez, A., Deiss, V., Lévy, F., Calandreau, L., Lee, C., Chaillou-Sagon, E., and Boissy, A. (2013).** “Chronic stress induces pessimistic-like judgment and learning deficits in sheep”. In: *Applied Animal Behaviour Science* 148.1, pp. 28–36 (Cited on page 75).
- Geyer, S. and Turner, R. (2013).** *Microstructural Parcellation of the Human Cerebral Cortex: From Brodmann’s Post-Mortem Map to in Vivo Mapping with High-Field Magnetic Resonance Imaging*. Google-Books-ID: fbBGAAAAQBAJ. Springer Science & Business Media. 261 pp. (Cited on page 56).
- Güntürkün, O., Verhoye, M., De Groof, G., and Van der Linden, A. (2013).** “A 3-dimensional digital atlas of the ascending sensory and the descending motor systems in the pigeon brain”. In: *Brain Structure and Function* 218.1, pp. 269–281 (Cited on pages 80, 98).

- Ianuș, A., Siow, B., Drobnjak, I., Zhang, H., and Alexander, D. C. (2013). "Gaussian phase distribution approximations for oscillating gradient spin echo diffusion MRI". In: *Journal of Magnetic Resonance* 227, pp. 25–34 (Cited on page 61).
- Kleinnijenhuis, M., Zhang, H., Wiedermann, D., Küsters, B., Norris, D., and Cappellen van Walsum, A.-M. van (2013). "Detailed laminar characteristics of the human neocortex revealed by NODDI and histology". In: *Human brain mapping*, pp. 3815–3815 (Cited on pages 156, 166).
- Kleinnijenhuis, M., Zerbi, V., Küsters, B., Slump, C. H., Barth, M., and Cappellen van Walsum, A.-M. van (2013). "Layer-specific diffusion weighted imaging in human primary visual cortex in vitro". In: *Cortex* 49.9, pp. 2569–2582 (Cited on page 151).
- Mangin, J. -F., Fillard, P., Cointepas, Y., Le Bihan, D., Frouin, V., and Poupon, C. (2013). "Toward global tractography". In: *NeuroImage. Mapping the Connectome* 80, pp. 290–296 (Cited on page 66).
- McNab, J. A., Polimeni, J. R., et al. (2013). "Surface based analysis of diffusion orientation for identifying architectonic domains in the in vivo human cortex". In: *NeuroImage* 69, pp. 87–100 (Cited on pages 151, 152).
- Nagy, Z., Alexander, D. C., Thomas, D. L., Weiskopf, N., and Sereno, M. I. (2013). "Using High Angular Resolution Diffusion Imaging Data to Discriminate Cortical Regions". In: *PLOS ONE* 8.5, e63842 (Cited on page 152).
- Nilsson, M., Westen, D. van, Ståhlberg, F., Sundgren, P. C., and Lätt, J. (2013). "The role of tissue microstructure and water exchange in biophysical modelling of diffusion in white matter". In: *Magnetic Resonance Materials in Physics, Biology and Medicine* 26.4, pp. 345–370 (Cited on page 61).
- Özarlan, E., Koay, C. G., and Basser, P. J. (2013). "Simple Harmonic Oscillator Based Reconstruction and Estimation for One-Dimensional q-Space Magnetic Resonance (1D-SHORE)". In: *Excursions in Harmonic Analysis, Volume 2: The February Fourier Talks at the Norbert Wiener Center*. Ed. by T. D. Andrews, R. Balan, J. J. Benedetto, W. Czaja, and K. A. Okoudjou. Applied and Numerical Harmonic Analysis. Boston: Birkhäuser, pp. 373–399 (Cited on page 64).
- Sereno, M. I., Lutti, A., Weiskopf, N., and Dick, F. (2013). "Mapping the Human Cortical Surface by Combining Quantitative T1 with Retinotopy". In: *Cerebral Cortex* 23.9, pp. 2261–2268 (Cited on page 152).
- Trzasko, J. D., Mostardi, P. M., Riederer, S. J., and Manduca, A. (2013). "Estimating T1 from Multichannel Variable Flip Angle SPGR Sequences". In: *Magnetic resonance in medicine : official journal of the Society of Magnetic Resonance in Medicine / Society of Magnetic Resonance in Medicine* 69.6 (Cited on pages 69, 142).
- Baron, C. A. and Beaulieu, C. (2014). "Oscillating gradient spin-echo (OGSE) diffusion tensor imaging of the human brain". In: *Magnetic Resonance in Medicine* 72.3. \_eprint: <https://onlinelibrary.wiley.com/doi/pdf/10.1002/mrm.24987>, pp. 726–736 (Cited on page 61).
- Blausen, B. (2014). "Medical gallery of Blausen Medical 2014". In: *WikiJournal of Medicine* 1.2 (Cited on page 9).
- Favreau-Peigné, A. et al. (2014). "Emotionality Modulates the Effect of Chronic Stress on Feeding Behaviour in Birds". In: *PLOS ONE* 9.2. Publisher: Public Library of Science, e87249 (Cited on page 76).
- Foxley, S., Jbabdi, S., Clare, S., Lam, W., Ansorge, O., Douaud, G., and Miller, K. (2014). "Improving diffusion-weighted imaging of post-mortem human brains: SSFP at 7T". In: *NeuroImage* 102, pp. 579–589 (Cited on page 61).
- Guio, F. D., Reyes, S., Vignaud, A., Duering, M., Ropele, S., Duchesnay, E., Chabriat, H., and Jouvent, E. (2014). "In Vivo High-Resolution 7 Tesla MRI Shows Early and Diffuse Cortical Alterations in CADASIL". In: *PLOS ONE* 9.8. Publisher: Public Library of Science, e106311 (Cited on page 45).
- Leuze, C. W. U., Anwander, A., Bazin, P.-L., Dhital, B., Stüber, C., Reimann, K., Geyer, S., and Turner, R. (2014). "Layer-specific intracortical connectivity revealed with diffusion MRI". In: *Cerebral Cortex (New York, N.Y.: 1991)* 24.2, pp. 328–339 (Cited on page 151).

- Lutti, A., Dick, F., Sereno, M. I., and Weiskopf, N. (2014).** “Using high-resolution quantitative mapping of R1 as an index of cortical myelination”. In: *NeuroImage*. In-vivo Brodmann Mapping of the Human Brain 93, pp. 176–188 (Cited on page 152).
- Phillips, K. A., Bales, K. L., et al. (2014).** “Why Primate Models Matter”. In: *American journal of primatology* 76.9, pp. 801–827 (Cited on page 75).
- Stüber, C. et al. (2014).** “Myelin and iron concentration in the human brain: A quantitative study of MRI contrast”. In: *NeuroImage* 93, pp. 95–106 (Cited on page 152).
- Wahnert, M. D., Dinse, J., Weiss, M., Streicher, M. N., Wahnert, P., Geyer, S., Turner, R., and Bazin, P. -L. (2014).** “Anatomically motivated modeling of cortical laminae”. In: *NeuroImage*. In-vivo Brodmann Mapping of the Human Brain 93, pp. 210–220 (Cited on page 167).
- Aggarwal, M., Nauen, D. W., Troncoso, J. C., and Mori, S. (2015).** “Probing region-specific microstructure of human cortical areas using high angular and spatial resolution diffusion MRI”. In: *NeuroImage* 105, pp. 198–207 (Cited on pages 151, 152).
- Amunts, K. and Zilles, K. (2015).** “Architectonic Mapping of the Human Brain beyond Brodmann”. In: *Neuron* 88.6, pp. 1086–1107 (Cited on pages 37, 160, 167).
- Baer, J., Lansford, R., and Cheng, K. (2015).** “Chapter 22 - Japanese Quail as a Laboratory Animal Model”. In: *Laboratory Animal Medicine (Third Edition)*. Ed. by J. G. Fox, L. C. Anderson, G. M. Otto, K. R. Pritchett-Corning, and M. T. Whary. Boston: Academic Press, pp. 1087–1108 (Cited on page 76).
- Calabrese, E., Badea, A., Coe, C. L., Lubach, G. R., Shi, Y., Styner, M. A., and Johnson, G. A. (2015).** “A diffusion tensor MRI atlas of the postmortem rhesus macaque brain”. In: *NeuroImage* 117, pp. 408–416 (Cited on page 110).
- Calabrese, E., Badea, A., Cofer, G., Qi, Y., and Johnson, G. A. (2015).** “A Diffusion MRI Tractography Connectome of the Mouse Brain and Comparison with Neuronal Tracer Data”. In: *Cerebral Cortex* 25.11, pp. 4628–4637 (Cited on page 110).
- De Martino, F., Moerel, M., Xu, J., Moortele, P.-F. van de, Ugurbil, K., Goebel, R., Yacoub, E., and Formisano, E. (2015).** “High-Resolution Mapping of Myeloarchitecture In Vivo: Localization of Auditory Areas in the Human Brain”. In: *Cerebral Cortex* 25.10, pp. 3394–3405 (Cited on page 152).
- Descoteaux, M. (2015).** “High Angular Resolution Diffusion Imaging (HARDI)”. In: (Cited on pages 63, 65).
- Guesdon, V., Meurisse, M., Chesneau, D., Picard, S., Lévy, F., and Chaillou, E. (2015).** “Behavioral and endocrine evaluation of the stressfulness of single-pen housing compared to group-housing and social isolation conditions”. In: *Physiology & Behavior* 147, pp. 63–70 (Cited on page 75).
- James, J. S., Radhakrishnan, A., Thomas, B., Madhusoodanan, M., Kesavadas, C., Abraham, M., Menon, R., Rathore, C., and Vilanilam, G. (2015).** “Diffusion tensor imaging tractography of Meyer’s loop in planning resective surgery for drug-resistant temporal lobe epilepsy”. In: *Epilepsy Research* 110, pp. 95–104 (Cited on page 67).
- Jonckers, E., Güntürkün, O., Groof, G. D., Linden, A. V. d., and Bingman, V. P. (2015).** “Network structure of functional hippocampal lateralization in birds”. In: *Hippocampus* 25.11, pp. 1418–1428 (Cited on page 103).
- Kleinnijenhuis, M., Mourik, T. van, Norris, D. G., Ruiters, D. J., Cappellen van Walsum, A.-M. van, and Barth, M. (2015).** “Diffusion tensor characteristics of gyrencephaly using high resolution diffusion MRI in vivo at 7T”. In: *NeuroImage* 109, pp. 378–387 (Cited on page 152).
- Ogura, Y., Izumi, T., Yoshioka, M., and Matsushima, T. (2015).** “Dissociation of the neural substrates of foraging effort and its social facilitation in the domestic chick”. In: *Behavioural Brain Research* 294, pp. 162–176 (Cited on page 98).
- Reveley, C., Seth, A. K., Pierpaoli, C., Silva, A. C., Yu, D., Saunders, R. C., Leopold, D. A., and Ye, F. Q. (2015).** “Superficial white matter fiber systems impede detection of long-range cortical connections in diffusion MR tractography”. In: *Proceedings of the National Academy of Sciences* 112.21, E2820–E2828 (Cited on page 166).

- Seehaus, A., Roebroek, A., Bastiani, M., Fonseca, L., Bratzke, H., Lori, N., Vilanova, A., Goebel, R., and Galuske, R. (2015).** “Histological validation of high-resolution DTI in human post mortem tissue”. In: *Frontiers in Neuroanatomy* 9. Publisher: Frontiers (Cited on page 152).
- Standring, S. (2015).** *Gray’s Anatomy E-Book: The Anatomical Basis of Clinical Practice*. Google-Books-ID: b7FVCgAAQBAJ. Elsevier Health Sciences. 2256 pp. (Cited on pages 10, 12, 22, 25, 28, 35).
- Watrin, F., Manent, J.-B., Cardoso, C., and Represa, A. (2015).** “Causes and Consequences of Gray Matter Heterotopia”. In: *CNS Neuroscience & Therapeutics* 21.2, pp. 112–122 (Cited on page 43).
- You, Z. (2015).** *Cellular morphometric analysis: from microscopic scale to whole mouse brains*. In collab. with M. Vandenberghe, Y. BALBASTRE, N. Souedet, A.-S. Herard, and T. Delzescaux. Series: Micro-, Meso- and Macro-Dynamics of the Brain Published: 23ème Colloque Médecine et Recherche en Neurosciences de la Fondation IPSEN: “Micro-, meso- and macrodynamics” (Cited on page 173).
- Zilles, K., Palomero-Gallagher, N., and Amunts, K. (2015).** “Cytoarchitecture and Maps of the Human Cerebral Cortex”. In: *Brain Mapping*. Ed. by A. W. Toga. Waltham: Academic Press, pp. 115–135 (Cited on page 25).
- Bastiani, M. et al. (2016).** “Automatic Segmentation of Human Cortical Layer-Complexes and Architectural Areas Using Ex vivo Diffusion MRI and Its Validation”. In: *Frontiers in Neuroscience* 10 (Cited on pages 152, 166).
- Birkel, C., Langkammer, C., Golob-Schwarzl, N., Leoni, M., Haybaeck, J., Goessler, W., Fazekas, F., and Ropele, S. (2016).** “Effects of formalin fixation and temperature on MR relaxation times in the human brain”. In: *NMR in Biomedicine* 29.4, pp. 458–465 (Cited on pages 54, 56, 145, 147).
- Bouhrara, M., Reiter, D. A., Celik, H., Fishbein, K. W., Kijowski, R., and Spencer, R. G. (2016).** “Analysis of mcDESPO- and CPMG-derived parameter estimates for two-component nonexchanging systems”. In: *Magnetic Resonance in Medicine* 75.6. \_eprint: <https://onlinelibrary.wiley.com/doi/pdf/10.1002/mrm.25801>, pp. 2406–2420 (Cited on page 69).
- Colgan, N. et al. (2016).** “Application of neurite orientation dispersion and density imaging (NODDI) to a tau pathology model of Alzheimer’s disease”. In: *NeuroImage* 125, pp. 739–744 (Cited on page 64).
- Conn, P. M. (2016).** *Conn’s Translational Neuroscience*. Google-Books-ID: oFGNCwAAQBAJ. Academic Press. 778 pp. (Cited on page 20).
- De Groof, G., George, I., Touj, S., Stacho, M., Jonckers, E., Cousillas, H., Hausberger, M., Güntürkün, O., and Van der Linden, A. (2016).** “A three-dimensional digital atlas of the starling brain”. In: *Brain Structure and Function* 221.4, pp. 1899–1909 (Cited on pages 80, 82).
- Drobnjak, I., Zhang, H., Ianuş, A., Kaden, E., and Alexander, D. C. (2016).** “PGSE, OGSE, and sensitivity to axon diameter in diffusion MRI: Insight from a simulation study”. In: *Magnetic Resonance in Medicine* 75.2. \_eprint: <https://onlinelibrary.wiley.com/doi/pdf/10.1002/mrm.25631>, pp. 688–700 (Cited on page 61).
- Fracasso, A., Veluw, S. J. van, Visser, F., Luijten, P. R., Spliet, W., Zwanenburg, J. J. M., Dumoulin, S. O., and Petridou, N. (2016).** “Lines of Baillarger in vivo and ex vivo: Myelin contrast across lamina at 7T MRI and histology”. In: *NeuroImage* 133, pp. 163–175 (Cited on page 159).
- Gao, Y. et al. (2016).** “A 3D high resolution ex vivo white matter atlas of the common squirrel monkey (*saimiri sciureus*) based on diffusion tensor imaging”. In: *Medical Imaging 2016: Image Processing*. Medical Imaging 2016: Image Processing. Vol. 9784. International Society for Optics and Photonics, 97843K (Cited on page 110).
- Glasser, M. F. et al. (2016).** “A multi-modal parcellation of human cerebral cortex”. In: *Nature* 536.7615, pp. 171–178 (Cited on page 133).
- Knöchel, C. et al. (2016).** “Cortical thinning in bipolar disorder and schizophrenia”. In: *Schizophrenia Research* 172.1, pp. 78–85 (Cited on page 44).

- Kodiweera, C., Alexander, A. L., Harezlak, J., McAllister, T. W., and Wu, Y.-C. (2016).** “Age effects and sex differences in human brain white matter of young to middle-aged adults: A DTI, NODDI, and q-space study”. In: *NeuroImage* 128, pp. 180–192 (Cited on page 64).
- Kulikova, S., Hertz-Pannier, L., Dehaene-Lambertz, G., Poupon, C., and Dubois, J. (2016).** “A New Strategy for Fast MRI-Based Quantification of the Myelin Water Fraction: Application to Brain Imaging in Infants”. In: *PLOS ONE* 11.10, e0163143 (Cited on pages 144, 152).
- Pohmann, R., Speck, O., and Scheffler, K. (2016).** “Signal-to-noise ratio and MR tissue parameters in human brain imaging at 3, 7, and 9.4 tesla using current receive coil arrays”. In: *Magnetic Resonance in Medicine* 75.2. \_eprint: <https://onlinelibrary.wiley.com/doi/pdf/10.1002/mrm.25677>, pp. 801–809 (Cited on page 53).
- Tariq, M., Schneider, T., Alexander, D. C., Gandini Wheeler-Kingshott, C. A., and Zhang, H. (2016).** “Bingham–NODDI: Mapping anisotropic orientation dispersion of neurites using diffusion MRI”. In: *NeuroImage* 133, pp. 207–223 (Cited on pages 65, 156).
- Van Essen, D. C. and Glasser, M. F. (2016).** “The Human Connectome Project: Progress and Prospects”. In: *Cerebrum: the Dana Forum on Brain Science* 2016 (Cited on page 66).
- Assaf, Y. (2017).** “Imaging laminar structures in the gray matter with diffusion MRI”. In: *NeuroImage* (Cited on pages 151, 152).
- Bhuiyan, P. S., Rajgopal, L., and Shyamkishore, K. (2017).** *Inderbir Singh’s Textbook of Human Neuroanatomy: (Fundamental & Clinical)*. Google-Books-ID: GrpEDwAAQBAJ. JP Medical Ltd. 295 pp. (Cited on page 15).
- Boudreau, M., Tardif, C. L., Stikov, N., Sled, J. G., Lee, W., and Pike, G. B. (2017).** “B1 mapping for bias-correction in quantitative T1 imaging of the brain at 3T using standard pulse sequences”. In: *Journal of Magnetic Resonance Imaging* 46.6, pp. 1673–1682 (Cited on pages 69, 141, 142).
- Cechetto, D. F. and Weishaupt, N. (2017).** *The Cerebral Cortex in Neurodegenerative and Neuropsychiatric Disorders: Experimental Approaches to Clinical Issues*. Google-Books-ID: JsAOCAAAQBAJ. Academic Press. 342 pp. (Cited on page 44).
- Di Donato, I. et al. (2017).** “Cerebral Autosomal Dominant Arteriopathy with Subcortical Infarcts and Leukoencephalopathy (CADASIL) as a model of small vessel disease: update on clinical, diagnostic, and management aspects”. In: *BMC Medicine* 15.1, p. 41 (Cited on page 45).
- Güntürkün, O., Stacho, M., and Ströckens, F. (2017).** “The Brains of Reptiles and Birds”. In: pp. 171–221 (Cited on page 80).
- Hanics, J., Teleki, G., Alpár, A., Székely, A. D., and Csillag, A. (2017).** “Multiple amygdaloid divisions of arcopallium send convergent projections to the nucleus accumbens and neighboring subpallial amygdala regions in the domestic chicken: a selective pathway tracing and reconstruction study”. In: *Brain Structure and Function* 222.1, pp. 301–315 (Cited on pages 105, 106).
- Heule, R. and Bieri, O. (2017).** “Rapid and robust variable flip angle T1 mapping using interleaved two-dimensional multislice spoiled gradient echo imaging”. In: *Magnetic Resonance in Medicine* 77.4, pp. 1606–1611 (Cited on page 69).
- Marques, J. P., Khabipova, D., and Gruetter, R. (2017).** “Studying cyto and myeloarchitecture of the human cortex at ultra-high field with quantitative imaging: R1, R2\* and magnetic susceptibility”. In: *NeuroImage* 147, pp. 152–163 (Cited on page 152).
- Palomero-Gallagher, N. and Zilles, K. (2017).** “Cortical layers: Cyto-, myelo-, receptor- and synaptic architecture in human cortical areas”. In: *NeuroImage* (Cited on pages 30, 153, 160, 163).
- Prabhakar, H. (2017).** *Essentials of Neuroanesthesia*. Google-Books-ID: YELQDAAAQBAJ. Academic Press. 1068 pp. (Cited on pages 12, 13, 19).

- Teillac, A., Beaujoin, J., Poupon, F., Mangin, J.-F., and Poupon, C. (2017).** “A Novel Anatomically-Constrained Global Tractography Approach to Monitor Sharp Turns in Gyri”. In: *Medical Image Computing and Computer Assisted Intervention MICCAI 2017*. Ed. by M. Descoteaux, L. Maier-Hein, A. Franz, P. Jannin, D. L. Collins, and S. Duchesne. Lecture Notes in Computer Science. Springer International Publishing, pp. 532–539 (Cited on pages 76, 110, 172).
- Trampel, R., Bazin, P.-L., Pine, K., and Weiskopf, N. (2017).** “In-vivo magnetic resonance imaging (MRI) of laminae in the human cortex”. In: *NeuroImage* (Cited on pages 152, 166).
- Tsougos, I. (2017).** *Advanced MR Neuroimaging : From Theory to Clinical Practice*. CRC Press (Cited on pages 58, 67).
- Xin, Q., Ogura, Y., Uno, L., and Matsushima, T. (2017).** “Selective contribution of the telencephalic arcopallium to the social facilitation of foraging efforts in the domestic chick”. In: *European Journal of Neuroscience* 45.3. \_eprint: <https://onlinelibrary.wiley.com/doi/pdf/10.1111/ejn.13475>, pp. 365–380 (Cited on page 105).
- Zucchelli, M., Descoteaux, M., and Menegaz, G. (2017).** “NODDI-SH: a computational efficient NODDI extension for fODF estimation in diffusion MRI”. In: *arXiv:1708.08999 [physics]*. arXiv: 1708.08999 (Cited on page 65).
- Beaujoin, J. (2018).** “Post mortem inference of the human brain microstructure using ultra-high field magnetic resonance imaging with strong gradients”. These de doctorat. Université Paris-Saclay (ComUE) (Cited on pages xxxiv, xxxviii, 3, 59, 66, 133, 134, 136, 138, 141, 143, 155, 165).
- Beaujoin, J., Palomero-Gallagher, N., Boumezeur, F., Axer, M., Bernard, J., Poupon, F., Schmitz, D., Mangin, J.-F., and Poupon, C. (2018).** “Post-mortem inference of the human hippocampal connectivity and microstructure using ultra-high field diffusion MRI at 11.7 T”. In: *Brain Structure and Function* 223.5, pp. 2157–2179 (Cited on pages 152, 167).
- Bernhardt, B. C., Fadaie, F., Vos de Wael, R., Hong, S.-J., Liu, M., Guiot, M. C., Rudko, D. A., Bernasconi, A., and Bernasconi, N. (2018).** “Preferential susceptibility of limbic cortices to microstructural damage in temporal lobe epilepsy: A quantitative T1 mapping study”. In: *NeuroImage. Microstructural Imaging* 182, pp. 294–303 (Cited on page 152).
- Bertin, A. et al. (2018).** “Incubation temperature affects the expression of young precocial birds’ fear-related behaviours and neuroendocrine correlates”. In: *Scientific Reports* 8.1. Number: 1 Publisher: Nature Publishing Group, p. 1857 (Cited on page 105).
- Calamante, F., Jeurissen, B., Smith, R. E., Tournier, J.-D., and Connelly, A. (2018).** “The role of whole-brain diffusion MRI as a tool for studying human in vivo cortical segregation based on a measure of neurite density”. In: *Magnetic Resonance in Medicine* 79.5, pp. 2738–2744 (Cited on pages 152, 153).
- Cercignani, M., Dowell, N. G., and Tofts, P. S. (2018).** *Quantitative MRI of the Brain: Principles of Physical Measurement, Second edition*. Google-Books-ID: VXFQDwAAQBAJ. CRC Press. 361 pp. (Cited on pages 68, 70, 141).
- De Cocker, L. J., Lindenholz, A., Zwanenburg, J. J., Kolk, A. G. van der, Zwartbol, M., Luijten, P. R., and Hendrikse, J. (2018).** “Clinical vascular imaging in the brain at 7T”. In: *NeuroImage. Neuroimaging with Ultra-high Field MRI: Present and Future* 168, pp. 452–458 (Cited on page 67).
- Dyrby, T. B., Innocenti, G. M., Bech, M., and Lundell, H. (2018).** “Validation strategies for the interpretation of microstructure imaging using diffusion MRI”. In: *NeuroImage. Microstructural Imaging* 182, pp. 62–79 (Cited on pages 54, 55, 70, 136, 163).
- Edwards, L. J., Kirilina, E., Mohammadi, S., and Weiskopf, N. (2018).** “Microstructural imaging of human neocortex in vivo”. In: *NeuroImage. Microstructural Imaging* 182, pp. 184–206 (Cited on pages 152, 166).
- Fukutomi, H., Glasser, M. F., Zhang, H., Autio, J. A., Coalson, T. S., Okada, T., Togashi, K., Van Essen, D. C., and Hayashi, T. (2018).** “Neurite imaging reveals microstructural variations in human cerebral cortical gray matter”. In: *NeuroImage. Microstructural Imaging* 182, pp. 488–499 (Cited on page 152).

- Ganepola, T., Nagy, Z., Ghosh, A., Papadopoulo, T., Alexander, D. C., and Sereno, M. I. (2018).** “Using diffusion MRI to discriminate areas of cortical grey matter”. In: *NeuroImage*. Microstructural Imaging 182, pp. 456–468 (Cited on page 152).
- Goulas, A., Zilles, K., and Hilgetag, C. C. (2018).** “Cortical Gradients and Laminar Projections in Mammals”. In: *Trends in Neurosciences* 41.11, pp. 775–788 (Cited on page 115).
- Hamaide, J., Lukacova, K., Verhoye, M., and Linden, A. V. d. (2018).** “Predict future learning accuracy by the structural properties of the brain, an in vivo longitudinal MRI study in songbirds”. In: *bioRxiv*. Publisher: Cold Spring Harbor Laboratory Section: New Results, p. 477679 (Cited on page 77).
- Ji, E., Samuel, S., Leboyer, M., Guevara, M., Guevara, P., Poupon, C., Grigis, A., and Houenou, J. (2018).** “T145. ALTERATIONS IN SUPERFICIAL WHITE MATTER IN THE FRONTAL CORTEX IN SCHIZOPHRENIA: A DWI STUDY USING A NOVEL ATLAS”. In: *Schizophrenia Bulletin* 44 (Suppl 1), S172 (Cited on page 44).
- Jones, D. K., Alexander, D. C., et al. (2018).** “Microstructural imaging of the human brain with a ‘super-scanner’: 10 key advantages of ultra-strong gradients for diffusion MRI”. In: *NeuroImage*. Microstructural Imaging 182, pp. 8–38 (Cited on page 166).
- Kalaria, R. N. (2018).** “The pathology and pathophysiology of vascular dementia”. In: *Neuropharmacology*. Cerebral Ischemia 134, pp. 226–239 (Cited on page 44).
- Lifshits, S., Tomer, O., Shamir, I., Barazany, D., Tsarfaty, G., Rosset, S., and Assaf, Y. (2018).** “Resolution considerations in imaging of the cortical layers”. In: *NeuroImage*. Pushing the spatio-temporal limits of MRI and fMRI 164, pp. 112–120 (Cited on pages 153, 155).
- Lormant, F., Cornilleau, F., Constantin, P., Meurisse, M., Lansade, L., Leterrier, C., Lévy, F., and Calandreau, L. (2018).** “A trait for a high emotionality favors spatial memory to the detriment of cue-based memory in Japanese quail”. In: *Behavioural Processes* 157, pp. 256–262 (Cited on page 76).
- Menant, O. et al. (2018).** “First evidence of neuronal connections between specific parts of the periaqueductal gray (PAG) and the rest of the brain in sheep: placing the sheep PAG in the circuit of emotion”. In: *Brain Structure and Function* 223.7, pp. 3297–3316 (Cited on page 75).
- Moore, K. L. and Dalley, A. F. (2018).** *Clinically Oriented Anatomy*. Google-Books-ID: 9CvvDwAAQBAJ. Wolters kluwer india Pvt Ltd. 1470 pp. (Cited on page 14).
- Puelles, L., Martinez-de-la-Torre, M., Martinez, S., Watson, C., and Paxinos, G. (2018).** *The Chick Brain in Stereotaxic Coordinates and Alternate Stains: Featuring Neuromeric Divisions and Mammalian Homologies*. Google-Books-ID: 8OR8DwAAQBAJ. Academic Press. 324 pp. (Cited on pages 80, 98).
- Roebroek, A., Miller, K. L., and Aggarwal, M. (2018).** “Ex vivo diffusion MRI of the human brain: Technical challenges and recent advances”. In: *NMR in Biomedicine* 0.0, e3941 (Cited on pages 163, 164, 168).
- Sengupta, S., Fritz, F. J., Harms, R. L., Hildebrand, S., Tse, D. H. Y., Poser, B. A., Goebel, R., and Roebroek, A. (2018).** “High resolution anatomical and quantitative MRI of the entire human occipital lobe ex vivo at 9.4T”. In: *NeuroImage*. Neuroimaging with Ultra-high Field MRI: Present and Future 168, pp. 162–171 (Cited on pages 70, 145, 147, 152).
- Shatil, A. S., Uddin, M. N., Matsuda, K. M., and Figley, C. R. (2018).** “Quantitative Ex Vivo MRI Changes due to Progressive Formalin Fixation in Whole Human Brain Specimens: Longitudinal Characterization of Diffusion, Relaxometry, and Myelin Water Fraction Measurements at 3T”. In: *Frontiers in Medicine* 5 (Cited on page 145).
- Siless, V., Chang, K., Fischl, B., and Yendiki, A. (2018).** “AnatomiCuts: Hierarchical clustering of tractography streamlines based on anatomical similarity”. In: *NeuroImage* 166, pp. 32–45 (Cited on page 82).
- Uszynski, I. (2018).** “Identification et caractérisation des faisceaux de substance blanche en IRM : développements précliniques”. These de doctorat. Université Grenoble Alpes (ComUE) (Cited on page 110).

- Avila, N. L., Lebenberg, J., Rivière, D., Auzias, G., Fischer, C., Poupon, F., Guevara, P., Poupon, C., and Mangin, J.-F. (2019).** “Inference of an Extended Short Fiber Bundle Atlas Using Sulcus-Based Constraints for a Diffeomorphic Inter-subject Alignment”. In: *Computational Diffusion MRI*. Ed. by E. Bonet-Carne, F. Grussu, L. Ning, F. Sepehrband, and C. M. W. Tax. Mathematics and Visualization. Cham: Springer International Publishing, pp. 323–333 (Cited on page 67).
- Barrière, D. A. et al. (2019).** “The SIGMA rat brain templates and atlases for multimodal MRI data analysis and visualization”. In: *Nature Communications* 10.1. Number: 1 Publisher: Nature Publishing Group, pp. 1–13 (Cited on pages 76, 110).
- Beul, S. F. and Hilgetag, C. C. (2019).** “Neuron density fundamentally relates to architecture and connectivity of the primate cerebral cortex”. In: *NeuroImage* 189, pp. 777–792 (Cited on page 115).
- Constantinides, V. C., Paraskevas, G. P., Paraskevas, P. G., Stefanis, L., and Kapaki, E. (2019).** “Corticobasal degeneration and corticobasal syndrome: A review”. In: *Clinical Parkinsonism & Related Disorders* 1, pp. 66–71 (Cited on page 42).
- Fukutomi, H., Glasser, M. F., Murata, K., et al. (2019).** “Diffusion Tensor Model links to Neurite Orientation Dispersion and Density Imaging at high b-value in Cerebral Cortical Gray Matter”. In: *Scientific Reports* 9.1, pp. 1–12 (Cited on pages 151, 152).
- Ginsburger, K., Matuschke, F., Poupon, F., Mangin, J.-F., Axer, M., and Poupon, C. (2019).** “MEDUSA: A GPU-based tool to create realistic phantoms of the brain microstructure using tiny spheres”. In: *NeuroImage* 193, pp. 10–24 (Cited on page 173).
- Liu, H., Rubino, C., et al. (2019).** “Myelin Water Atlas: A Template for Myelin Distribution in the Brain”. In: *Journal of Neuroimaging* 0.0 (Cited on pages 70, 152).
- Ma, Y.-J., Searleman, A. C., Jang, H., Wong, J., Chang, E. Y., Corey-Bloom, J., Bydder, G. M., and Du, J. (2019).** “Whole-Brain Myelin Imaging Using 3D Double-Echo Sliding Inversion Recovery Ultrashort Echo Time (DESIRE UTE) MRI”. In: *Radiology*, p. 190911 (Cited on page 152).
- Prabhakar, H., Mahajan, C., and Kapoor, I. (2019).** *Essentials of Geriatric Neuroanesthesia*. Google-Books-ID: LnGdDwAAQBAJ. CRC Press. 458 pp. (Cited on page 41).
- Sarrazin, S. et al. (2019).** “Higher in vivo Cortical Intracellular Volume Fraction Associated with Lithium Therapy in Bipolar Disorder: A Multicenter NODDI Study”. In: *Psychotherapy and Psychosomatics* 88.3. Publisher: Karger Publishers, pp. 171–176 (Cited on page 44).
- Sébille, S. B., Rolland, A.-S., Welter, M.-L., Bardinnet, E., and Santin, M. D. (2019).** “Post mortem high resolution diffusion MRI for large specimen imaging at 11.7T with 3D segmented echo-planar imaging”. In: *Journal of Neuroscience Methods* 311, pp. 222–234 (Cited on pages 77, 167).
- Timmler, S. and Simons, M. (2019).** “Grey matter myelination”. In: *Glia* 0.0 (Cited on page 152).
- Turner, R. (2019).** “Myelin and Modeling: Bootstrapping Cortical Microcircuits”. In: *Frontiers in Neural Circuits* 13 (Cited on pages 32, 34).
- Tustison, N. J. et al. (2019).** “Longitudinal Mapping of Cortical Thickness Measurements: An Alzheimer’s Disease Neuroimaging Initiative-Based Evaluation Study”. In: *Journal of Alzheimer’s Disease* 71.1. Publisher: IOS Press, pp. 165–183 (Cited on page 41).
- Uddin, M. N., Figley, T. D., Solar, K. G., Shatil, A. S., and Figley, C. R. (2019).** “Comparisons between multi-component myelin water fraction, T1w/T2w ratio, and diffusion tensor imaging measures in healthy human brain structures”. In: *Scientific Reports* 9.1, p. 2500 (Cited on page 152).



- Yi, S. Y., Barnett, B. R., Torres-Velázquez, M., Zhang, Y., Hurley, S. A., Rowley, P. A., Hernando, D., and Yu, J.-P. J. (2019). "Detecting Microglial Density With Quantitative Multi-Compartment Diffusion MRI". In: *Frontiers in Neuroscience* 13 (Cited on page 152).
- You, Z., Balbastre, Y., Bouvier, C., Hérard, A.-S., Gipchtein, P., Hantraye, P., Jan, C., Souedet, N., and Delzescaux, T. (2019). "Automated Individualization of Size-Varying and Touching Neurons in Macaque Cerebral Microscopic Images". In: *Frontiers in Neuroanatomy* 13. Publisher: Frontiers (Cited on page 173).
- Zhang, W., Mi, L., Thompson, P. M., and Wang, Y. (2019). "A Geometric Framework for Feature Mappings in Multimodal Fusion of Brain Image Data". In: *Information Processing in Medical Imaging*. Ed. by A. C. S. Chung, J. C. Gee, P. A. Yushkevich, and S. Bao. Lecture Notes in Computer Science. Springer International Publishing, pp. 617–630 (Cited on pages 3, 149).
- Zikidi, K., Gajwani, R., Gross, J., Gumley, A. I., Lawrie, S. M., Schwannauer, M., Schultze-Lutter, F., Fracasso, A., and Uhlhaas, P. J. (2019). "Grey-matter abnormalities in clinical high-risk participants for psychosis". In: *Schizophrenia Research* (Cited on page 44).
- Amunts, K., Mohlberg, H., Bludau, S., and Zilles, K. (2020). "Julich-Brain: A 3D probabilistic atlas of the human brain's cytoarchitecture". In: *Science*. Publisher: American Association for the Advancement of Science Section: Report (Cited on page 166).
- Assaf, Y., Bouznach, A., Zomet, O., Marom, A., and Yovel, Y. (2020). "Conservation of brain connectivity and wiring across the mammalian class". In: *Nature Neuroscience* 23.7. Number: 7 Publisher: Nature Publishing Group, pp. 805–808 (Cited on page 110).
- Behroozi, M. et al. (2020). "Event-related functional MRI of awake behaving pigeons at 7T". In: *Nature Communications* 11.1. Number: 1 Publisher: Nature Publishing Group, p. 4715 (Cited on page 80).
- Bryant, K. L., Li, L., Eichert, N., and Mars, R. B. (2020). "A comprehensive atlas of white matter tracts in the chimpanzee". In: *PLOS Biology* 18.12. Publisher: Public Library of Science, e3000971 (Cited on page 110).
- Dvorak, A. V. et al. (2020). "Multi-spin echo T2 relaxation imaging with compressed sensing (METRICS) for rapid myelin water imaging". In: *Magnetic Resonance in Medicine* n/a (n/a). \_eprint: <https://onlinelibrary.wiley.com/doi/pdf/10.1002/mrm.2819> (Cited on page 152).
- Girard, G. et al. (2020). "On the cortical connectivity in the macaque brain: A comparison of diffusion tractography and histological tracing data". In: *NeuroImage* 221, p. 117201 (Cited on pages 110, 115, 167).
- Gong, T., Tong, Q., He, H., Sun, Y., Zhong, J., and Zhang, H. (2020). "MTE-NODDI: Multi-TE NODDI for disentangling non-T2-weighted signal fractions from compartment-specific T2 relaxation times". In: *NeuroImage*, p. 116906 (Cited on page 65).
- Guevara, M., Guevara, P., Román, C., and Mangin, J.-F. (2020). "Superficial white matter: A review on the dMRI analysis methods and applications". In: *NeuroImage* 212, p. 116673 (Cited on page 67).
- Kamiya, K., Hori, M., and Aoki, S. (2020). "NODDI in clinical research". In: *Journal of Neuroscience Methods* 346, p. 108908 (Cited on page 64).
- Lormant, F., Cornilleau, F., Constantin, P., Meurisse, M., Lansade, L., Leterrier, C., Lévy, F., and Calandreau, L. (2020). "Research Note: Role of the hippocampus in spatial memory in Japanese quail". In: *Poultry Science* 99.1, pp. 61–66 (Cited on page 76).
- Mancini, M., Casamitjana, A., Peter, L., Robinson, E., Crampsie, S., Thomas, D. L., Holton, J. L., Jaunmuktane, Z., and Iglesias, J. E. (2020). "A multimodal computational pipeline for 3D histology of the human brain". In: *Scientific Reports* 10.1. Number: 1 Publisher: Nature Publishing Group, p. 13839 (Cited on page 166).

- Nazeri, A., Schifani, C., Anderson, J. A. E., Ameis, S. H., and Voineskos, A. N. (2020).** “In vivo imaging of gray matter microstructure in major psychiatric disorders: Opportunities for clinical translation”. In: *Biological Psychiatry: Cognitive Neuroscience and Neuroimaging* (Cited on page 64).
- Nieuwenhuys, R. and Broere, C. A. J. (2020).** “A detailed comparison of the cytoarchitectonic and myeloarchitectonic maps of the human neocortex produced by the Vogt–Vogt school”. In: *Brain Structure and Function*. Company: Springer Distributor: Springer Institution: Springer Label: Springer Publisher: Springer Berlin Heidelberg, pp. 1–17 (Cited on page 38).
- Palombo, M., Ianus, A., Guerreri, M., Nunes, D., Alexander, D. C., Shemesh, N., and Zhang, H. (2020).** “SANDI: A compartment-based model for non-invasive apparent soma and neurite imaging by diffusion MRI”. In: *NeuroImage* 215, p. 116835 (Cited on pages 115, 152).
- Palomero-Gallagher, N., Kedo, O., Mohlberg, H., Zilles, K., and Amunts, K. (2020).** “Multimodal mapping and analysis of the cyto- and receptorarchitecture of the human hippocampus”. In: *Brain Structure and Function* (Cited on page 153).
- Perez, E. C. et al. (2020).** “Object and food novelty induce distinct patterns of c-fos immunoreactivity in amygdala and striatum in domestic male chicks (*Gallus gallus domesticus*)”. In: *Behavioural Brain Research* 381, p. 112453 (Cited on page 75).
- Piredda, G. F. et al. (2020).** “Fast and high-resolution myelin water imaging: Accelerating multi-echo GRASE with CAIPIRINHA”. In: *Magnetic Resonance in Medicine* n/a (n/a). \_eprint: <https://onlinelibrary.wiley.com/doi/pdf/10.1002/mrm.28427> (Cited on page 152).
- Shaaban, C. E. and Molad, J. (2020).** “Cerebral small vessel disease: Moving closer to hemodynamic function”. In: *Neurology* 94.21. Publisher: Wolters Kluwer Health, Inc. on behalf of the American Academy of Neurology Section: Editorial, pp. 909–910 (Cited on page 45).
- Stacho, M., Herold, C., Rook, N., Wagner, H., Axer, M., Amunts, K., and Güntürkün, O. (2020).** “A cortex-like canonical circuit in the avian forebrain”. In: *Science* 369.6511. Publisher: American Association for the Advancement of Science Section: Research Article (Cited on page 105).
- Triarhou, L. C. (2020).** “Pre-Brodmann pioneers of cortical cytoarchitectonics I: Theodor Meynert, Vladimir Betz and William Bevan-Lewis”. In: *Brain Structure and Function* (Cited on pages 36, 37).
- Winston, G. P. et al. (2020).** “Microstructural Imaging in Temporal Lobe Epilepsy: Diffusion Imaging Changes Relate to Reduced Neurite Density”. In: *NeuroImage: Clinical*, p. 102231 (Cited on page 152).
- Basukala, D., Mukundan, R., Lim, A., Hurrell, M. A., Keenan, R. J., Dalrymple-Alford, J. C., Anderson, T. J., Myall, D. J., and Melzer, T. R. (2021).** “Automated segmentation of substantia nigra and red nucleus using quantitative susceptibility mapping images: Application to Parkinson’s disease”. In: *Computers & Electrical Engineering* 91, p. 107091 (Cited on page 152).
- Bergamino, M., Walsh, R. R., and Stokes, A. M. (2021).** “Free-water diffusion tensor imaging improves the accuracy and sensitivity of white matter analysis in Alzheimer’s disease”. In: *Scientific Reports* 11.1. Number: 1 Publisher: Nature Publishing Group, p. 6990 (Cited on page 67).
- Chang, S. et al. (2021).** “Measuring myelin content and cell density in the human brain using optical coherence tomography”. In: *Optical Techniques in Neurosurgery, Neurophotonics, and Optogenetics*. Optical Techniques in Neurosurgery, Neurophotonics, and Optogenetics. Vol. 11629. International Society for Optics and Photonics, 116291J (Cited on page 168).
- Cimflova, P. et al. (2021).** “MRI Diffusion-Weighted Imaging to Measure Infarct Volume: Assessment of Manual Segmentation Variability”. In: *Journal of Neuroimaging* n/a (n/a). \_eprint: <https://onlinelibrary.wiley.com/doi/pdf/10.1111/jon.12850> (Cited on page 67).

- Costalunga, G., Kobylkov, D., Rosa-Salva, O., Vallortigara, G., and Mayer, U. (2021).** “Light-incubation effects on lateralisation of single unit responses in the visual Wulst of domestic chicks”. In: *Brain Structure and Function* (Cited on page 103).
- Ganepola, T., Lee, Y., Alexander, D. C., Sereno, M. I., and Nagy, Z. (2021).** “Multiple b-values improve discrimination of cortical gray matter regions using diffusion MRI: an experimental validation with a data-driven approach”. In: *Magnetic Resonance Materials in Physics, Biology and Medicine* (Cited on page 151).
- Kim, S., Sakaie, K., Blümcke, I., Jones, S., and Lowe, M. J. (2021).** “Whole-brain, ultra-high spatial resolution ex vivo MRI with off-the-shelf components”. In: *Magnetic Resonance Imaging* 76, pp. 39–48 (Cited on page 167).
- Little, G. and Beaulieu, C. (2021).** “Automated Cerebral Cortex Segmentation Based Solely on Diffusion Tensor Imaging for Investigating Cortical Anisotropy”. In: *NeuroImage*, p. 118105 (Cited on page 152).
- Moghim, P., Dang, A. T., Netoff, T. I., Lim, K. O., and Atluri, G. (2021).** “A Review on MR Based Human Brain Parcellation Methods”. In: *arXiv:2107.03475 [q-bio]*. arXiv: 2107.03475 (Cited on page 154).
- Prevost, V. H., Yung, A., Morris, S. R., Vavasour, I. M., Samadi-Bahrami, Z., Moore, G. R. W., Laule, C., Mackay, A., and Kozlowski, P. (2021).** “Temperature dependence and histological correlation of inhomogeneous magnetization transfer and myelin water imaging in ex vivo brain”. In: *NeuroImage* 236, p. 118046 (Cited on page 70).
- Rahmanzadeh, R. et al. (2021).** “Myelin and axon pathology in multiple sclerosis assessed by myelin water and multi-shell diffusion imaging”. In: *Brain* (awab088) (Cited on page 67).
- Shamir, I. and Assaf, Y. (2021).** “An MRI-Based, Data-Driven Model of Cortical Laminar Connectivity”. In: *Neuroinformatics* 19.2, pp. 205–218 (Cited on pages 115, 167).
- Smaers, J. B. et al. (2021).** “The evolution of mammalian brain size”. In: *Science Advances* 7.18. Publisher: American Association for the Advancement of Science Section: Research Article, eabe2101 (Cited on pages 119, 120).



**Titre:** IRM de diffusion et quantitative à très haut champ et forts gradients pour l'exploration de la connectivité, de la cytoarchitecture, et de la myéloarchitecture du cerveau de l'animal à l'homme à l'échelle mésoscopique

**Mots clés:** neuroimagerie, IRM à très haut champ, IRM quantitative, IRM de diffusion, microstructure du cortex cérébral, connectivité structurelle

**Résumé:** La neuroimagerie fait face à deux grands défis: cartographier le connectome du cerveau humain et comprendre l'organisation cellulaire des aires corticales reliant les connexions cérébrales. Des limites méthodologiques et technologiques font encore obstacle à la production de cartes à haute résolution dépassant la résolution millimétrique *in vivo*. L'utilisation conjointe de très hauts champs magnétiques (>7T) et de gradients puissants (>300mT/m) permet de dépasser ces limites. Cette thèse a pour but d'explorer cette piste et de démontrer qu'il est possible d'obtenir des cartographies de résolution mésoscopique à partir de cerveaux scannés *ex vivo* aussi bien chez l'animal que chez l'homme. Les appareils d'IRM cliniques étant encore dépourvus de cette double technologie, la stratégie adoptée a donc reposé sur l'utilisation de deux imageurs précliniques à 7T et 11,7T, équipés de puissants gradients à 440mT/m et 780mT/m respectivement. Ils ont permis de produire des cartographies du cerveau à l'échelle mésoscopique dans le cadre de trois études complémentaires. Le développement de protocoles dédiés incluant des séquences d'imagerie anatomique, pondérées en diffusion et quantitatives a permis de cartographier les structures cérébrales les plus fines, d'en étudier la connectivité structurelle, et d'en caractériser la cytoarchitecture et la myéloarchitecture. Ces travaux ont nécessité le développement de chaînes de traitement spécifiques pour reconstruire et analyser les cartographies ciblées. Les connectivités structurelles liées aux circuits socio-émotionnels d'animaux d'élevage et sauvages ont d'abord été étudiées à partir de protocoles comprenant des séquences IRM pondérées en  $T_2$  et en diffusion. La première des espèces étudiées fut la caille japonaise, un oiseau d'élevage dont le caractère émotionnel peut être caractérisé par sa réponse spécifique face à des situations de peur appelée immobilité tonique. Une cohorte de 21 sujets a été formée pour valider l'hypothèse que sa propension à exprimer la peur

se reflète dans son connectome. L'étude menée en collaboration avec l'INRAE Val de Loire (Nouzilly, France) portait sur deux lignées: les caillies à courte (STI) et longue (LTI) immobilités toniques. Les données de diffusion ont permis d'établir un premier atlas de connectivité structurelle de la caille japonaise qui a révélé l'existence de différences structurelles entre les deux lignées au niveau de plusieurs faisceaux de fibres dont certains participant au circuit socio-émotionnel. La deuxième étude portait sur l'exploration des cerveaux de 8 animaux sauvages provenant du ZooParc de Beauval (Saint-Aignan, France). Leurs cartes de connectivité structurelle ont été générées et l'étiquetage des faisceaux de substance blanche impliqués dans leurs circuits socio-émotionnels a été réalisé. Ces deux premières études ont été des tremplins pour l'acquisition de données mésoscopiques sur un cerveau humain scanné *ex vivo*, afin d'en cartographier sa connectivité intracorticale. L'étude du cortex cérébral humain *in vivo* visant l'échelle mésoscopique reste ardue mais prometteuse pour mieux comprendre les pathologies cérébrales associées aux lésions du cortex, qu'elles soient neurodégénératives, psychiatriques ou neurodéveloppementales. Pour cette étude *ex vivo*, un cerveau humain entier a été mis à disposition par le CHU de Bretonneau (Tours, France) après son extraction et sa fixation. Après avoir été découpé en 13 blocs de taille compatible avec le diamètre du tunnel des IRM précliniques, ce cerveau a pu être scanné avec un protocole incluant de nombreuses séquences d'IRM anatomique, de diffusion (11,7T) et quantitative (7T). Deux campagnes d'acquisition IRM ont pu être menées en parallèle pendant 2 ans. Dans le cadre de ce travail de thèse, une étude visant à la caractérisation fine du ruban cortical a été conduite après reconstruction du puzzle complet, dont l'objectif principal visait la segmentation des couches corticales le constituant.

**Title:** Ultra-high field diffusion and quantitative MRI with strong gradients to explore the connectivity, cytoarchitecture and myeloarchitecture of animal and human brains at the mesoscale

**Keywords:** neuroimaging, ultra-high field MRI, quantitative MRI, diffusion MRI, cerebral cortex microstructure, structural connectivity

**Abstract:** Mapping the structural connectome and probing the cytoarchitecture of the cortical areas involved in cerebral connections are two of the greatest challenges that face the neuroimaging community. Methodological and technological issues still stand in the way of producing high-resolution maps, namely below the millimeter scale, on living subjects. Ultra-high magnetic fields (>7T) and powerful gradient sets (>300mT/m) are potent tools related to MRI that can overcome these hurdles. This thesis has the purpose of mapping human and non-human brains post-mortem based on the combined use of the cited tools. Since clinical MRI systems do not offer this combination yet, the chosen approach was to scan brain samples with two preclinical systems (7T and 11.7T) equipped with strong gradients (440mT/m and 780mT/m) that enabled to produce cartographies at the mesoscopic scale in the frame of three complementary studies. Anatomical MRI, diffusion MRI (dMRI) and quantitative MRI (qMRI) as well as the brain fixation process were instrumental in these studies to finely map cerebral structures and connections, and collect cytoarchitectural and myeloarchitectural information as well. Dedicated post-processing pipelines were developed to map and analyze the substantial amount of data. The structural connectivities related to the socio-emotional circuits of breeding and wildlife animals were firstly investigated using  $T_2$ -weighted MRI and dMRI protocols. The breeding species was the Japanese quail, a bird which emotionality trait can be characterized through its specific response facing fearful situations called tonic immobility. A cohort of 21 subjects was formed to validate if its propensity to

express fearfulness is reflected in its connectome. The study, in collaboration with INRAE Val de Loire (Nouzilly, France), consisted in investigating two lines of Japanese quails: the short (STI) and the long tonic immobility (LTI) lines. The 200-micron dMRI dataset led to a first structural connectivity atlas of the Japanese quail which revealed the existence of structural differences between the connectivity patterns characterizing the two lines. Then, 8 wildlife animals that lived in the ZooParc de Beauval (Saint-Aignan, France) were scanned at a submillimeter resolution. Their structural connectivity maps were generated and the labeling of the white matter bundles involved in their socio-emotional circuits was done. These two studies were stepping stones in observing the structural intracortical connectivity of the human cerebral cortex. The investigation of the human cerebral cortex at the mesoscale remains challenging but promising to better understand psychiatric, neurodegenerative and neurodevelopmental pathologies associated with cortex damage. In this *ex vivo* study, an entire human brain was provided by the Bretonneau University Hospital (Tours, France) after its extraction and fixation. The MRI dataset stems from two acquisition campaigns performed at 7T for qMRI and at 11.7T for anatomical MRI and dMRI, which lasted 2 years. The human brain sample was cut into 13 blocks in order to fit in the tunnels of the preclinical MRI scanners. For this thesis, the 200-micron qMRI and dMRI dataset enabled an automatic segmentation of the cortical layers inferred from MRI-based information. This segmentation aimed at better understanding the cytoarchitecture and myeloarchitecture of the human cerebral cortex.

